New insight into the Adsorptive Removal of Organic and Inorganic Pollutants from Aqueous set up with tailored cellulosic and polymer-based biomaterials: Modeling and Ecotoxicological assessment

A Thesis Submitted in Partial Fulfillment of
the Requirements for the Degree of

Doctor of Philosophy

by

Tasrin Shahnaz

Roll No: 176106114

Under the supervision of

Dr. Selvaraju Narayanasamy

DEPARTMENT OF BIOSCIENCES AND BIOENGINEERING

INDIAN INSTITUTE OF TECHNOLOGY GUWAHATI

ASSAM

JULY 2022

TH-3150_176106114

INDIAN INSTITUTE OF TECHNOLOGY GUWAHATI

DEPARTMENT OF BIOSCIENCES AND BIOENGINEERING

GUWAHATI-781039

DECLARATION

I, hereby declare that the matter embodied in this thesis entitled "**New insight into the Adsorptive Removal of Organic and Inorganic Pollutants from Aqueous set up with tailored cellulosic and polymer based biomaterials: Modeling and Ecotoxicological assessment**" is the result of investigations carried out by me under the supervision of **Dr. Selvaraju Narayanasamy**, Department of Biosciences and Bioengineering, Indian Institute of Technology Guwahati, Guwahati, India for the award of the degree of Doctor of Philosophy. This work has not been submitted elsewhere for any degree, diploma, associateship or membership etc. of any Institute or University to the best of my knowledge and belief.

IIT Guwahati

18.07.2022

Tasrin Shahnaz

Roll No. 176106114

TH-3150_176106114

INDIAN INSTITUTE OF TECHNOLOGY GUWAHATI
DEPARTMENT OF BIOSCIENCES AND BIOENGINEERING
GUWAHATI-781039

Dr. Selvaraju Narayanasamy
Associate Professor
Department of Biosciences and Bioengineering

Tel. No.: +91-361-2583210
Fax No.: +91-361-2582249
E-mail: selva@iitg.ac.in

CERTIFICATE

This is to certify that the thesis entitled "**New insight into the Adsorptive Removal of Organic and Inorganic Pollutants from Aqueous set up with tailored cellulosic and polymer based biomaterials: Modeling and Ecotoxicological assessment**" being submitted to the **Indian Institute of Technology Guwahati** by **TASRIN SHAHNAZ** for the award of the degree of **Doctor of Philosophy** in **Biosciences and Bioengineering,** is a bonafide record of research work carried out by her. The contents of this thesis have not been submitted to any other University or Institute for the award of any degree or diploma.

Tasrin Shahnaz
IIT Guwahati
18.07.2022

Dr. Selvaraju Narayanasamy
(Thesis supervisor)

TH-3150_176106114

ACKNOWLEDGEMENT

As the journey of my research has been coming to an end, I would like to take the opportunity here to express my heartfelt gratitude to all the people who made this journey possible. Experiencing this phase of my career is indeed a great part that has the contribution of numerous people and their guidance, support and utmost beliefs on me that shaped me and changed me into a better person.

First, I express my sincere gratitude to my research advisor **Dr. Selvaraju Narayanasamy,** Associate Professor, Department of Biosciences and Bioengineering, Indian Institute of Technology Guwahati for his guidance, advice, tremendous encouragement, patience, valuable discussion, and continuous moral support throughout my PhD journey. I am humbled and genuinely grateful to have him as my thesis supervisor. I am indebted for his kind, positive attitude and for placing confidence and trust in me to be his student. I am also grateful to him for letting me pursue my ideas and I am privileged to be a part of his research team.

I owe my gratitude to ex-Department HOD **Prof. Kannan Pakshirajan and Prof. Latha Rangan** for their administrative capability. I would like to thank the current HOD **Prof. Rakhi Chaturvedi** for providing Departmental facilities. It is by their cooperation only that I can complete my PhD.

I would like to acknowledge my Doctoral committee: **Dr. Soumen Kumar Maiti**, Chairman of the Doctoral Committee and members **Dr. Cota Navin Gupta**, **Dr. Pankaj Kalita** for their intellectual support, encouragement and valuable suggestions.

I would like to acknowledge the **Ministry of Human Resource Development** (MHRD, Government of India) for providing me with the fellowship during my PhD tenure.

I owe my gratitude to **Central Instrument Facility (CIF)** and **Department Central Instrument Facility (DCIF, BSBE)** and the respective technical staff for providing the Instruments facilities. I want to express my thanks to our office staff members for their help and support. I wish to acknowledge all the research scholars of the Department of Biosciences and Bioengineering and all the other departments and centres of IIT Guwahati for their help.

TH-3150_176106114

I extend my sincere acknowledgement towards my institute **IIT Guwahati**, a beautiful place amidst natural beauty that provided me with the opportunity to embark on this finest learning experience with world-class facilities.

I will take the opportunity to express my sincere thanks to all my past and present lab members of the Biochemical and Bioenvironmental Engineering Lab. My special thanks to my senior **Dr. Chandi Patra** for his endless help and support throughout my PhD journey. He has a major contribution to various project works and other non-technical works by giving his valuable time wholeheartedly. I am also grateful to my senior **Dr. Abhishek Ajmani** and **Dr. Shravan Kumar** for their help and support during my early days. I express my sincere thank to my lab junior **Mr. Vishnu Priyan V.** for coordinating many research work and helping me. I am extending my gratitude to **Mr. Ajit Kumar, Mr. Harish Kumar R., Mr. Ragavan C.** and **Mr. Jyotiprakash R**. for their cooperation and support. I am thankful to **Mr. Fazil SMM** for his innumerable support, for extending his helping hand in many work. I thank all the previous M. Tech students **Mr. Vivek Sharma, Mr. Rajmohan Medisetti**, **Mr. Rishabh Gupta**, **Mr. Nitesh Kumar**, **Ms. Anjali J., Mr. Bedadeep D., Mr. Nirvesh Patel and Ms. Ghurupreya R.** All their support has been an integral part of this journey.

I would like to acknowledge my friends for their valuable suggestions, moral support, assistance and contribution. My special and wholehearted thanks to **Ms. Pratibha** for her selfless motivation, help and support. I am thankful to **Ms. Priyanka** for all her innumerable support and kind gestures. I express my gratitude to **Ms. Heena, Ms. Khyati, Mrs. Tanmayee, Ms. Tinka, Ms. Udangshree** for all their help. I am also extending my thanks to all my friends and juniors.

I am deeply grateful to my family **Maa, Abba, Maina and Tasmim** for their unconditional love, support, patience, motivation and blessings in carrying out my PhD. I am thankful to both my grandparents whom I lost during my PhD tenure and relatives for their blessings in this journey. I will take the opportunity to thank my best friend **Ridip** for his unconditional help, moral support, strength, guidance, suggestion and affection throughout my PhD journey. Their faith and unconditional sacrifices for me always pushed me beyond my limit to achieve the best in life.

TH-3150_176106114

I am equally thankful to **Mimi, Koli, Pui, Sunu, Munu, Locopoco, Yippee, Pokora, Samosa, Jhalmuri** and all the campus dogs and cats for their unconditional affection. Spending time with them is the best therapy during some of the toughest times.

Above all, I am grateful to **God** for finding me capable of fulfilling this extremely difficult task and providing me continuous motivation, positive energy and support. I am thankful to **God** for blessing me with the completion of my Doctoral work.

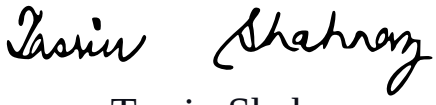

Tasrin Shahnaz

TH-3150_176106114

CONTENTS

Abstract

The significance of water as a resource for the survival of humanity is incomparable. With the rapid advancement in various technologies, the demand for water usage has been augmented exponentially. From the industry domain to fulfilling the basic necessity for the people, water conservation with proper qualitative allocation has been at the forefront of all activities. While the swift developments in the technological industries have been a boon for appeasing the hefty consumer demand in the market, it leaves a deterrent impact on the environment. To eradicate the grave danger to the aquatic environment, the treatment of wastewater is crucial and imperative. The first study of the thesis work examines the efficiency of the removal of hexavalent chromium using physicochemically activated lignocellulosic biomass from *Acacia auriculiformis* (Fabaceae family). The treatment involved sulphuric acid activation followed by pyrolysis resulting in chemically modified activated carbon. Further, it was complexed with a chelating agent i.e. EDTA. Acid treatment and complexation with chelating agents improvised the biosorbent's sorption capacity towards chromium species. Adsorption parameters like pH, adsorbent dosage, temperature, and initial metal concentration were optimised in the batch study. The optimised data were further equilibrated using detailed two-parameter and three-parameter isotherm models, kinetics, and thermodynamic models to determine the nature of the sorbent–sorbate interaction. In the next work cellulose, which is the major component of lignocellulose, was explored by converting it to nano size that further significantly enhances the specific surface area and minimises the intraparticle diffusion distance. Despite their ability to adsorb various pollutants, the challenge in scaling up the process lies in the agglomeration and disintegration of cellulosic material in the aqueous media. In the past decade, various studies have been reported to overcome these difficulties by using polymer matrices as support which provide high mechanical strength and stability under different environmental conditions to improve the adsorption efficiency of the cellulosic base material. A fundamental understanding of cellulose fibre composite with tailor-made personalization has contributed to a diverse range of high-end engineering applications. In this study, nanocellulose was synthesized from cellulose via the top-down method and chemical polymerization of pyrrole to make nanocellulose embedded

polypyrrole composite (NCPPY). This modification provides superior properties, enhanced functionality, and application in dye removal. This work may serve as an alternative to the conventional method for removing dye from industrial effluent, providing an essential, fascinating field of cellulose-based nanocomposite application. The goal is to study the application of the composite for the removal of direct blue 6 and bromophenol blue in unary and binary systems. The results showed satisfactory removal of the dyes with 99.18, 96.32 and 98.77% for direct blue, bromophenol blue and binary systems respectively. To provide evidence about the clarity of the effluent after treatment with the synthesized adsorbent, seed toxicity was performed where root length and % germination was used as key metric. Though various approaches to adsorption have been studied for the development of biological adsorbents with high selectivity and binding capacity, less attention has been given to the simultaneous removal of more than one category of pollutant. This NCPPY composite was used to remove both heavy metal chromium [Cr(VI)] and Congo red dye (CR) in a simulated binary mixture. The process was statistically modelled using response surface methodology (RSM) to study the influence of Cr(VI) and CR concentration, temperature, and adsorbent dosage on adsorption of Cr(VI)/CR. Apart from adsorption isotherms, kinetics and thermodynamics models the effect of co-existing ions using different common salts and heavy metals like iron, copper, and zinc were also studied. Again cellulose was utilised to adsorb pharmaceutical pollutants viz. an antibiotic Ciprofloxacin (CPXO) and an anti-inflammatory agent Diclofenac (DCF). However, this time as an approach toward green nanotechnology, the cellulose was extracted from *Cyperus rotundus*, a widely distributed perennial grass (weed) species found in tropical and warmer temperate areas throughout the world and was scaled down to nano-cellulose and named Grass Nano Cellulose (GNC). The adsorbent GNC was characterised using various microscopic, elemental, and spectroscopic analyses to monitor the physicochemical alterations of the surface before and after adsorption. The size of the converted nanocellulose was found to be 40-50 nm. An extended toxicity study was performed using plant seeds and zebrafish. The experimental findings implied the feasibility of GNC for the efficient removal of CPXO and DCF and reduced toxicity of the treated pollutant on model organisms. GNC showed excellent efficiency for these emerging pollutants with greater adsorptive capacity and could be commercialised with its high and cheap

availability as well as the conversion to the final product. Further, the GNC was functionalized using ferrous sulphate and ferric chloride co-precipitation on its surface rendering magnetic GNC (MGNC). The magnetisation step facilitates the easy retrieval of the sample after adsorption. A fundamental understanding of MGNC was obtained through characterization, to fabricate an effective biosorbent for a rare earth element cerium [Ce(III)]. The vibrating sample magnetometer showed the ferromagnetic behaviour of the prepared adsorbent MGNC whereas the crystallinity of MGNC was confirmed by the X-ray Diffraction pattern. Isotherm, kinetics, and thermodynamics study further support the favourability of the present work. This work is expected to provide a novel approach to studying and developing a more effective waste removal method.

In the past few years with a variety of fibres in addition to the traditional fibres, the textile industry has undergone a tremendous modernisation with the heavy production of dyes and pigments in their effluent annually. In this final study, this grass-extracted cellulose has been used for a very toxic dye Basic Fuchsine, from simulated wastewater in both static and continuous adsorptive mode. Experimental conditions were optimised and isotherm, kinetics, and thermodynamics of the process were analysed for batch mode. Further, in continuous mode, a fixed column was used to study the real-time behaviour of the adsorbent towards the adsorbate. The data derived were fitted in models like Yoon, Thomas, Adams and BDST and found that maximum adsorption capacity to be 318.45 mg/g with a maximum of 97% removal efficiency. Additionally, the probable mechanism of the dye adsorption onto the adsorbate was discussed. Results indicated that cellulose derived from grass exhibited an exceptionally good adsorption capacity towards aqueous basic fuchsine and can be used as an efficient and economically feasible adsorbent substance for the exclusion of the dye from contaminated water.

ABBREVIATIONS

A_{rp}	Redlich-Peterson model constant
AES	Atomic Emission Spectroscopy
APS	Ammonium persulfate
ANOVA	Analysis of variance
BB	Bromophenol Blue
BF	Basic fuchsine
BET	Brunauer-Emmett-Teller
B_{rp}	Redlich-Peterson constant
BDST	Bed depth service time
C	Boundary thickness constant in Intraparticle diffusion kinetics
CCD	Central Composite Design
C_e	Concentration of adsorbate at equilibrium
C_i	Initial concentration of adsorbate
C_0	Influent adsorbate concentration
C_t	Effluent adsorbate concentration
CPXO	Ciprofloxacin
CPPY	Cellulose Polypyrrole
Ce(III)	Cerium
C_{ad}	Concentration after desorption
C_{de}	Concentration after adsorption
DCF	Diclofenac
Co^{+2}	Cobalt ion
$CaCl_2$	Calcium chloride
CO_3^{-2}	Carbonate ion
C_p	Equilibrium concentration of DB 6

C_q	Equilibrium concentration of BB
CR	Congo Red
Cr(VI)	Hexavalent Chromium
$Cr_2O_7^{-2}$	Dichromate ion
CrO_4^{-2}	Chromate ion
Cu^{+2}	Copper ion
DB 6	Direct Blue 6
DPC	1,5-diphenylcarbazide
DSC	Differential Scanning Calorimetry
EDS	Energy-dispersive X-ray spectroscopy
E_{DR}	Mean biosorption energy
EDTA	Ethylenediaminetetra acetic acid
F	Flow rate of adsorbate in the column
Fe^{+3}	Ferric ion
FTIR	Fourier transforms infrared spectroscopy
GC	Grass cellulose
GNC	Grass nanocellulose
g	Gram
g	Redlich-Peterson constant
% G	Germination percentage
h	Hours
H_2SO_4	Sulfuric acid
H_3PO_4	Phosphoric acid
HCl	Hydrochloride acid
$HCrO_4^-$	Hydrogen chromate ion
J	Joule
K	Kelvin
K_1	Pseudo-First order rate constant

K_2	Pseudo-Second order rate constant
KH_2PO_4	Potassium dihydrogen phosphate
$K_2Cr_2O_7$	Potassium dichromate
K_a	Rate constant of packed bed column
K_{AB}	Kinetics constant
K_{DR}	Mean free energy of adsorption
K_{TH}	Thomas model constant
K_{YN}	Yoon-Nelson rate constant
K_{rp}	Redlich-Peterson constant
K_F	Freundlich adsorption constant
K_H	Halsey isotherm constants
K_{id}	Intra-Particle Diffusion rate constant
kJ	Kilojoule
K_L	Langmuir energy constant
l	*l* is the thickness of well in the 96-well plate
L	Litre
m	Mass
m	Meter
mg	Milligram
mL	Mililitre
mol	Mole
MGNC	Magnetic Grass nanocellulose
$MgNO_3$	Magnesium nitrate
m_{total}	Amount of adsorbate sent to the packed bed column
N	Normal (concentration)
N_0	Adsorption capacity in BDST
1/n	Freundlich biosorption intensity
N_{AB}	Saturation constant

n_H	Halsey isotherm constant
NC	Nanocellulose
NCPPY	Nanocellulose Polypyrrole
NaCl	Sodium Chloride
NaClO	Sodium Hypochlorite
$NaHCO_3$	Sodium bicarbonate
NaOH	Sodium Hydroxide
Ni^{+2}	Nickel ion
nm	Nanometer
NO_3^{-2}	Nitrate ion
OEHHA	Office of Environmental Health Hazard Assessment
OVAT	One-variable-at-a-time
Pa	Pascal
ppb	parts per billion
Pb^{+2}	Lead ion
PHG	Public Health Goal
PO_4^{-3}	Phosphate ion
PY	Pyrrole
PPY	Polypyrrole
Q_{DR}	Dubinin-Radushkevich maximum adsorption capacity
q_e	Amount of pollutants adsorbed by adsorbent at equilibrium
q_m	Maximum adsorption capacity
q_{total}	Adsorbate adsorption amount
Q_0	Adsorption capacity of adsorbent
Q_e	Adsorption capacity of adsorbent at equilibrium
Q_L	Langmuir maximum adsorption capacity
Q_{rp}	Redlich-Peterson maximum adsorption capacity
Q_t	Adsorption capacity at a specific time ’t’

Q_{total}	Maximum column capacity
R	Universal gas constant (8.314 J/mol/K)
R^2	Coefficient of determination
R_a	Roughness average
R_q	Root mean square roughness
R_t	Maximum height of the roughness
R_p	Maximum roughness peak height
RAA	Raw plant biomass *Acacia auriculiformis*
R_L	Separation factor
R%	Removal percentage of adsorbate
RSM	Response Surface Methodology
rpm	Rotations per minute
SAA	Sulfuric acid-activated
SAAC	Sulfuric acid-activated chelated
SO_4^{-2}	Sulphate ion
t	Breakthrough time
T	Temperature
TGA	Thermogravimetric Analysis
u	Superficial velocity
USEPA	United States Environmental Protection Agency
UV	Ultraviolet
V	Volume
V_{eff}	Effective volume of packed bed column effluent
Vis	Visible
W	Total dry weight of the adsorbent used in packed bed column
$W_{\lambda 1p,q}$	Total absorbance of the mixture solution at 590 for DB 6
$W_{\lambda 2p,q}$	Total absorbance of the mixture solution at 545 nm BB
W_a	Waviness average

W_{max}	Waviness maximum height
WHO	World Health Organisation
Y%	Yield rate
Zn^{+2}	Zinc ion
$ZnSO_4$	Zinc sulfate
Z	Adsorbent bed height
ΔG°	Gibb's free energy
ΔH°	Change in enthalpy
ΔS°	Change in entropy
α	Elovich constant
β	Elovich constant
ε	Polyani potential
$\varepsilon_{\lambda 1p}$, $\varepsilon_{\lambda 1q}$, $\varepsilon_{\lambda 2p}$, $\varepsilon_{\lambda 2q}$	Molar absorption coefficients
θ	Fractional coverage of sorption site
ρ	Density of investigated solution
τ	Time needed for 50% adsorbate breakthrough

LIST OF TABLES

LIST OF FIGURES

CHAPTER 1
INTRODUCTION AND REVIEW OF LITERATURE

1. INTRODUCTION

1.1. Background

With the rapid development of industries worldwide, pollution from effluents is a major threat that the environment is facing (US EPA). Heavy metals are found naturally on the earth. They become concentrated as a result of human activities and can enter the plant, animal and human tissues via inhalation, diet and manual handling. Then they can bind to and interfere with the functioning of vital cellular components. Dyes are commonly used in papermaking, textile, food, printing, cosmetic and leather industries that provide a wide range of colourants due to their broad and subtle structural differences. These dyes and their by-products such as sulfonated aromatic amines are mostly toxic and even carcinogenic. About 50,000 tons per year of dyes are released into the water bodies without any prior treatment (Elwakeel et al., 2016). Antibiotics and anti-inflammatory drugs have been potentially used in both humans and animals for the therapeutic purpose to treat various infectious diseases. Pharmaceutical manufacturers and health care release massive amounts of these drug residues into their effluent that eventually get into the aquatic environment and enter the food chain. Though in trace amounts, these micropollutants leave adverse health effects on plants and animals with human beings topping the list (Gulen et al., 2020). Antibiotic-resistant microbes are a major threat to the medical sector globally by changing the ecological balance and posing substantial risks as they have been detected in the aquatic system for the past few decades. Rare Earth Elements (REEs) consist of the 15 elements of the Lanthanide series, plus Scandium and Yttrium. Cerium is the most abundant of REEs in the earth's crust (Silva et al., 2019). Due to their exceptional physicochemical properties, cerium compounds have wide applications in electronics, catalysis, optics, fuel cells and metallurgy (Fakhri et al., 2017). Cerium ions from industrial processing plants as well as mining sites are prone to gradually accumulate in the ecosystem, causing a significant increase in cerium levels in humans, animals and soil particles (Huang et al., 2021, Bian et al., 2021). In the aquatic organism, cerium ions can provoke severe damage to the cell membranes and can negatively affect, the functioning of their nervous system and reproduction. That being the case, it's highly important to alleviate the environmental and health hazards associated with cerium

polluted aquatic environment. To circumvent this global issue of water pollution, it is imperative to engage in research to have a solution for treating the industrial effluent with cost-effective and more importantly having a synergistic effect on a wide range of pollutants (Chu et al., 2020, Stylianou et al., 2021, Fauda et al., 2021, Li et al., 2014, Sauceda et al., 2016).

Research spanning more than seventy years in the field of bioremediation has led to the growth and widespread use of various novel technologies. Among them, one alternative option to expensive methods is adsorption which is an efficient method to remove pollutants from water. However, common sorbents, like plant biomass, activated carbon and clay materials suffer from relatively low sorption capacity (Hu et al., 2019, Fayazi et al., 2015). To overcome this fundamental issue some new classes of materials have been explored but they still show low selectivity, unsatisfactory regeneration and recyclability (Zhou et al., 2013). Indeed, besides efficient absorption characteristics concerning adsorption capacity and reaction kinetics, the materials should also avoid secondary pollution, exhibit easy separation from clean water, lightweight and simple desorptivity for high recyclability. In the era of cross-disciplinary knowledge, people are synthesizing materials with advanced properties by merging nanotechnology, chemical engineering, and biotechnology but they too suffer from low reusability as well as selectivity. In the practical scenario, the actual concern is not only one pollutant or two, there are different types of toxic products that cause water pollution driving almost all the industries to look for a better solution that has low economic consequences. Biopolymers like cellulose, chitosan and starch have excellent potential in the preparation of aerogels due to their excellent biodegradability and biocompatibility (Yuan et al., 2017, Lu et al., 2012, Sinchinga et al., 2022, Meneses et al., 2022, Brandes et al., 2019, Noreen et al., 2020, Medri et al., 2020). Cellulose is a natural polymer available in abundance from plant biomass, and bacterial sources and is of very low cost when purchased. Scaling down cellulose to nanocellulose enhances their biocompatibility, recyclability and their availability owing to their production from natural resources (Shahnaz et al., 2020). With the evolution of soft material synthesis and engineering, some potential polymers are used to convert to a more advanced form addressed as hydrogel with properties like biocapacity and biodegradability (Chang et al., 2017,

Curvello et al., 2019, Yue et al., 2019). Hydrogels are physicochemically modified materials, with a three-dimensional cross-linked network that can retain a much larger amount of liquid than its weight. Industries like cosmetics, food additives, drug delivery systems, tissue engineering, the biomedical application have already started using hydrogels owing to their massive potential. Hydrogels can be further freeze-dried to form aerogel, which is very light with a highly porous morphology and large surface area (Sharma et al., 2020, Yao et al., 2018). Aerogels are prepared from hydrogel in which the liquid phase is replaced by gas.

In this thesis work, plans to synthesize plant-based modified adsorbents that could be effectively used for heavy metals, dyes, antibiotics and rare earth elements with high removal capacity has been proposed. This work will mainly be focused on the synthesis, characterization and application required for wastewater remediation. A tailor-made sample could be a promising solution for environmental remediation in the long run as they are subjected to personalized improvisation during synthesis with enhanced physicochemical properties.

1.2. Review of Literature

Heavy metals are one such menacing component of industrial effluents responsible for polluting the aqueous ecosystem (Hong et al., 2019, Carolin et al., 2017, Yap et al., 2020, Mironyuk et al., 2020, Choi et al., 2008, Kharrazi et al., 2020, Jumima et al., 2020). For almost sixty years, relevant research in this field is devoted to eliminating metals from industrially produced wastewater causing soil and water pollution (Saravanan et al., 2019). Chromium is yet another heavy metal that is redox-active; exists primarily in hexavalent i.e. Cr(VI) and trivalent i.e. Cr(III) oxidation forms (Nakkeeran et al, 2018, Banerjee et al., 2018). Chromium contamination in water (from industrial effluents) results in various health hazards to living beings viz. severe chronic disorders, kidney stress, gastro-intestinal distress, etc. along with several mutagenic and carcinogenic effects (Ntuli et al., 2019, Pakade et al., 2016). Owing to its carcinogenic potential, various government agencies like the United States Environmental Protection Agency (USEPA) has established the tolerance level for Cr(VI) in drinkable water as 50 ppb (parts per billion). Similarly, the Office of Environmental Health Hazard Assessment (OEHHA) has established the Public Health Goal (PHG) for total chromium in potable water as 2.5 ppb (Patra et al., 2019,

Ajmani et al., 2019). Industrially opted conventional methods for Cr(VI) elimination from wastewater have their setbacks and limitations viz. the major shortcomings being; heavy machinery, infrastructure and labour costs, incomplete reduction of Cr(VI) to Cr(III), low sensitivity towards dilute solutions, non-sustainable and non-recyclable. Hence biosorption has been intensively studied and exploited for the bioremediation of heavy metals like chromium from wastewater before being dumped into water bodies (Pradhan et al., 2019, Pakade et al., 2016, Maremeni et al., 2018). Adsorption is a sorbate-sorbent interaction phenomenon where the amount of sorbate molecules gradually decreases, significantly owing to the individual surface properties and the various interactions between the sorbate and sorbent molecule. Activated carbon has been the most preferred adsorbent for over a decade for the removal of heavy metals due to its scalable and efficient sorption capacities (Gupta et al., 2013). Some of its surface properties include elevated surface area, variable surface chemistry, excellent porosity and strength, etc. have been exploited for the sorption of Cr(VI) species (Wang et al., 2009, Dakiky et al., 2002). Complexation of adsorbents with chelating agents (ligands) elevates their adsorption capacity owing to the enhancement of surface functional groups. Complexation provides specific donor functional groups to metal species, to form stable metal-chelate complexes. The interaction mechanism is based on various coordination bonds with the metal ion (Yu et al., 2019). Ethylene-diamine-tetra-acetic acid (EDTA) has found its suitability as a complexing agent due to its excellent metal-binding capacity, biodegradability and reusability (Naghipour et al., 2016).

The impact of dyes on water bodies threatens aquatic living forms by lowering the dissolved oxygen and light penetration, inhibiting the photosynthesis process as well as terrestrial organisms causing various problems nausea, skin ulceration, kidney damage, and anaemia to name a few. The production of $8*10^5$ tons of synthetic dyes globally per year is accompanied by the accumulation of a high concentration of coloured discharge into the river streams (Li et al., 2020, Marrakchi et al., 2020, Amiralian et al., 2020, Kalme et al., 2007, Gupta et al., 2011, Sirajudheen et al., 2020). Various literature has confirmed the presence of toxic dye compounds and has suggested various treatment methods (Atia et al., 2005, Zhao et al., 2021, Sun et al., 2017). Anionic dye, bromophenol Blue belongs to the triphenylmethane family and direct blue 6

belongs to azo dye. Both are widely used in various applications such as pH indicators, determination of trace quantity of metals, multiple industries such as paper, textile, biological staining, etc.

Over 100 thousand different types of dye used in the industries include Basic Fuchsine ($C_{20}H_{20}ClN_3$) with an intricate aromatic molecular form of most of the industrially used dyes makes it challenging to remediate wastewater polluted with dyes from textile and other dyestuff industries. Discharging these types of toxic dyes cause a detrimental impact on the aquatic lives in the forms of discolouration and generation of foul-smelling water, as well as the hindrance in the penetration of sunlight that leads to the disruption in the aquatic ecosystem. In addition to these dangers, there are risks involved as far as human health is concerned. Skin diseases while coming to contact with the polluted water, digestive disorders from consuming the contaminated water, with cancer being one of the consequences (Eshaq and ElMetwally, 2019; Katheresan et al., 2018; Santoso et al., 2020; Yang, 2008).

An abundantly available natural polymer, cellulose with general formula $(C_6H_{10}O_5)_n$ consists of repeating units of glucose monomers twisted to 180° to each other linked by β(1,4) glycosidic linkages. The oxygen atom of one glucose unit electrostatically attracts the hydrogen atom of the neighbouring glucose unit which leads to interchain hydrogen bonding and is responsible for the linear chain of cellulose. Apart from interchain hydrogen bonds, Van der Waal's forces are essential for cellulose stiffness. In addition to this, plenty of hydroxyl groups in cellulose moiety pave the way to surface modifications, which improve stability, dye adsorption capacity and sustainability (Xu et al., 2017, Priya et al., 2022, wang et al., 2020, Ares et al., 2019, Hong et al., 2019). It is insoluble in water due to the presence of high molecular weight and the presence of long-chain. The hydrophilic nature of cellulose makes it a poor barrier for water molecules. In this regard, polypyrrole (PPY) has been employed as an interesting alternative due to its hydrophobic nature (Shahnaz et al., 2020). Polypyrrole is the organic polymer formed by polymerization, which is generally the oxidation of pyrrole rings (C_4H_5N). Conductive polymers such as polypyrrole (PPY), polyacetylene, polyaniline, and polythiophene are used in various fields including microelectronics, composite materials, optical devices, gas sensors, rechargeable batteries, antistatic coatings as well as an adsorbent for the removal of heavy metals. Although

these polymers have been broadly used in various fields, their capacity to form hydrogen bonds is relatively low and they have weak mechanical strength and relatively poor film formation. The mechanical integrity can be enhanced by coating cellulose nanoparticles with polypyrrole composite, which leads to active electrostatic forces between -NH group of Polypyrrole and hydroxyl groups of cellulose moiety. The cellulose-based adsorbent has been used for the treatment of wastewater as an alternative to some of the cost and energy-intensive methodology based on commercially used activated carbon-based adsorption. This field has now set a new benchmark to understand the fibres of plant-origin cellulose and their probable modification for advanced engineering applications. Among them one is the scaling down to nanoscale cellulose with tailor-made functionalities with significant importance to be given to the preparation, surface functionalization and fabrication with other polymers (Archin et al. 2019; Liu et al. 2020). Nanocellulose is a star candidate in many areas of research owing to its versatile advantages including renewable raw material availability, mechanical strength, high surface area, low density, biodegradability, and biocompatibility. Nanocellulose derived from cellulose using acid/base hydrolysis, enzymatic or mechanical breakdown is a promising biopolymer for various advanced applications like tissue engineering, sensor base, shock and sound absorber, adsorption, paper-making, composites, packaging, electronic devices, coatings, biomedicine, automotive parts to name a few (Beyki et al. 2016; Li et al. 2018; Pires et al. 2019). But the presence of hydroxyl group in large quantities often causes flocculation of nanocellulose in nonpolar solvents. To overcome this problem, numerous chemical augmentation is being tested to improve its functionality. One approach is polymers grafted on nanocellulose surfaces through polymerization techniques i.e. the "grafting-from" techniques. The polymer grafting-from method also denoted surface-initiated (SI) polymerization, is based on the initiation and subsequent propagation of the monomer through reactive moieties on the surface. Polypyrrole was selected owing to its special characteristics of environmental stability, easy production, low cost, non-toxicity and hygroscopic nature (Al-Gheethi et al., 2022). Extensive studies on this polymer justify its stability, low cost and eco-friendly nature (Wang et al., 2020).

Apart from all these pollutants yet another category of emerging contaminants is the pharmaceutical waste. Antibiotics and anti-inflammatory drugs have been potentially used in

both humans and animals for the therapeutic purpose to treat various infectious diseases (Gulen and Demircivi et al., 2020, Hu et al., 2017). Pharmaceutical manufacturers and health care release a massive amount of these drug residues in their effluent that eventually get into the aquatic environment and enter the food chain (Gong et al., 2021, Fan et al., 2021, Du et al., 2021, Ma et al., 2021, Gustafsson et al., 2015). Though in trace amounts these micropollutants leave adverse health effects on plants and animals with human beings on top of the list (Lu et al., 2020). Antibiotic-resistant microbes are a major threat to the medical sector globally which changes the ecological balance and poses substantial risk as they are being detected in the aquatic system for the past few decades. A very commonly prescribed drug is Ciprofloxacin which is a second-generation antibiotic from the fluoroquinolone family that is used in skin, sinus, urinary, respiratory, bone, joint, diarrhoea, gastrointestinal tract infection treatment owing to its broad-spectrum activity (Bizi and El Bachra, 2020). This leads to the widespread occurrence of this drug in water bodies with a very high concentration of up to 31 mgL^{-1} in pharma-effluent and 2.5-6.5 mgL^{-1} in surface water (Avci et al., 2020). Another emerging contaminant of the clinical field used commonly is the anti-inflammatory agent Diclofenac to treat inflammation and rheumatoid arthritis (Ares et al., 2019). Among NSAIDs, this drug has the highest acute toxicity with EC_{50} values of less than 100 mgL^{-1} (Alvarez et al., 2015). Detection of diclofenac in wastewater is found at a concentration up to 0.002 mgL^{-1} and due to this trace occurrence, it has been listed as a priority contaminant by 2013/39/EU Directive (Graouer-Bacart et al., 2003) with global consumption of about 940 tons estimated on annual basis. This drug is also a major component of personal care products (Zhao et al., 2017) which is why its presence is increasing in waste effluent even from households and finally bioaccumulating in nature. Therefore, effective and fast removal of these residues before their release into water bodies or soil is very important. Mechanical removal processes are indeed required but have their limitation because of the trace occurrence of micropollutants. A very efficient technique Advanced Oxidation Process (AOP) degrade bioaccumulating contaminants but also has shortcomings in producing intermediates of acute toxicity. Therefore, an alternative to conventional techniques is finding their way to modern research that enables the manufacturing of bio-origin material (Patra et al., 2020) that can adsorb the micropollutants till their threshold

limit (Cantarella et al., 2019). Adsorption is a comparatively simple and economic method for the removal of micropollutants from wastewater (Gupta et al., 2013) with few gaps that need to be fulfilled. Among various components used to produce adsorbent, nano-dimensioned materials are in attendance for their enhanced and unique physicochemical properties like a high surface area to volume ratio, size, shape, composition, and electronic properties that vary from the bulk material. Cellulosic fibres naturally are good adsorbing agents due to their abundant functional groups and sheet-like arrangement (Blanco et al., 2018). When this property is improved by enhancing extra surface area by scaling down to nanocellulose this could be a great candidate for the adsorption process (Phanthong et al., 2018). Nanocellulose is a very potent candidate in modern research owing to its versatile application in many areas because of its advantages including the availability of raw material, high surface area, low density, strength, biodegradability and biocompatibility to name a few. This is a very promising biopolymer and has diversified applications. *Cyprus rotundas*, a herbaceous plant that grows pretty much everywhere and does not require much attention still play a very important role in the ecosystem. Though it is very easily accessible researchers around the globe are working on improving the quality and cultivation of this plant (Kian et al., 2019).

The last category of pollutant that was included in the present work is Rare Earth Elements (REEs). REEs consists of the 15 elements of the Lanthanide series (from Lanthanum to Lutetium), plus Scandium and Yttrium. Among them, cerium is the most abundant of REEs in the earth's crust (Silva et al., 2019, Allahkarami and Rezai, 2019). Due to their exceptional physicochemical properties, cerium compounds have wide applications in electronics, catalysis, optics, fuel cells and metallurgy (Fakhri et al., 2017, Kilbourn, 2011, Dahle and Arai, 2015). Cerium ions from industrial processing plants as well as mining sites are prone to gradually accumulate in the ecosystem, causing a significant increase in cerium levels in humans, animals and soil particles (Lin et al., 2017, Dashtian and Zare-Dorabei, 2017). In aquatic organisms, cerium ions can provoke severe damage to the cell membranes and can negatively affect, the functioning of their nervous system and reproduction. That being the case, it's highly important to alleviate the environmental and health hazards associated with a cerium-polluted aquatic environment. Reverse-osmosis, Ion exchange, precipitation, membrane separation,

electrochemical treatment, solvent extraction and adsorption are the most preferred techniques for the removal of cerium ions from contaminated water (Allahkarami and Rezai, 2019). Amongst all these techniques, adsorption is highly recommended, due to the relative simplicity of process design and operation. Commonly employed solid adsorbents for the water treatment process includes activated carbon, bentonite, silica, zeolite, etc (Chua et al., 2021, Feng et al., 2021). However, the utility of these adsorbents is constrained due to the high cost and difficulty in separation from wastewater (Han et al., 2020). Inefficiency in the retrieval of adsorbents from wastewater will result in undesirable secondary pollution. Therefore, it's crucial to fabricate cost-effective adsorbents that can be separated from wastewater with relative ease. In recent years, research focus has shifted towards, the development of eco-friendly adsorption systems for the removal of pollutants from wastewater (Adeniyi and Ighalo, 2019). A lot of research has reported species of fungi, bacteria, algae and plant-derived materials as efficient biosorbents for wastewater treatment (Peng et al., 2018, Li et al., 2020). Biosorbents are superior to conventional adsorbents in terms of cost, eco-friendliness and ease of disposal. In association with cellulose, plant cell walls also contain hemicellulose and lignin. The lignocellulosic material of the plant cell wall must be pre-treated to eliminate lignin and hemicellulose to yield cellulose. When cellulose fibres undergo mechanical shearing or acid hydrolysis in a controlled manner, they render elongated fibrillar or rod-like crystalline particles that are defect-free and have at least one dimension in the nanoscale range (Chu et al., 2020). This material is called grass nanocellulose (GNC), it possesses a large surface, low density, and high tensile strength and it can be chemically modified using facile approaches (Ibrahim et al., 2019, Amiralian et al., 2020). Thus, GNC can be utilized to fabricate effective biosorbents for the removal of cerium ions from wastewater. Recently, as a result of advancements in the field of nanotechnology, magnetic nanoparticles have garnered plenty of attention and it's being studied by a lot of researchers. This is because they possess the ability to display high magnetization under the influence of an external magnetic field. Magnetic nanoparticles such as magnetite (Fe_3O_4) have been used in numerous bioengineering and biomedical applications such as magnetic resonance imaging, biosensors, cancer treatment with magnetic induction hyperthermia and targeted drug delivery (Supramaniam et al., 2018). Magnetite can be incorporated into the nanocellulose

matrix to render nanocellulose-based magnetite nanocomposites which have been widely applied in bioseparation (Benmassaoud et al., 2017). These biosorbents can be easily retrieved from water after the biosorption process, by applying an external magnetic field. Thus, the secondary pollution caused by the biosorbent during the wastewater treatment process will be significantly minimized.

The natural properties of cellulose are the added benefit with a highly fibrous structure for this material making it one of the best choices for adsorptive removal. It has an abundant functional group on the surface which easily binds to most of the sites on pollutant which further enhance the adsorption capacity. From the economic as well as the environmental impact perspective, the use of cellulose is an excellent choice. The cellulose used in this study is derived from grass (*Cyperus rotundas*). The nature of growing anywhere is easily accessible. The biocompatibility, as well as the bio-degradability, makes this material more adept for use. The process is cost-friendly due to the ease of obtaining the raw material (Shahnaz et al., 2021). Though this material is available in a copious form and easily acquirable, there are not significant numbers of studies reporting it in the use of bio-based removal of pollutants. Fig. 1.1 is the various categories of pollutants used in the present study.

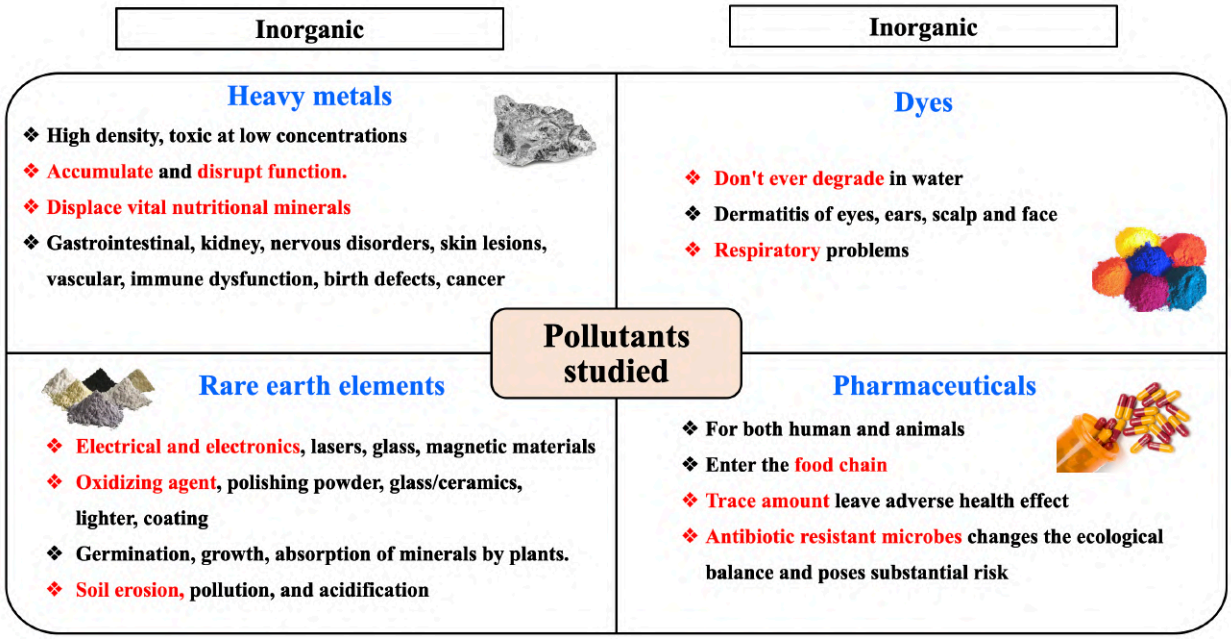

Fig. 1.1: Various categories pollutants studied in the thesis work

1.3. Theoretical aspects

1.3.1. Adsorption isotherm models

Isotherm models analyze the sorbate-sorbent interaction behaviour in an aqueous solution at constant temperatures. Owing to the influence of the experimental data on the various isotherms, it was decisive in evaluating the distribution of sorbate molecules over the sorbent's surface (Nekouei et al., 2015).

1.3.1.1. Langmuir adsorption isotherm

According to the Langmuir adsorption isotherm, the adsorbate molecules will form a uniform singular layer over the homogenous adsorbent's surface, owing to negligible hindrance between the sorbate and sorbent molecules. Langmuir isotherm model can be non-linearly represented as:

$$q_e = \frac{Q_L K_l C_e}{1 + K_l C_e} \tag{1.1}$$

q_e (mgg^{-1}) represents the experimentally obtained equilibrium biosorption capacity, Q_L (mgg^{-1}) defines the theoretical maximal biosorption capacity, C_e (mgl^{-1}) presents the equilibrated concentration of metal sorbate molecules, K_l (lmg^{-1}) presents a dimensionless coefficient known as separation factor (R_L). K_l predicts the acceptability of the adsorption process and its relation with the separation factor (R_L) can be represented as:

$$R_L = \frac{1}{1 + K_l C_i} \tag{1.2}$$

C_i (mgl^{-1}) refers to the initial adsorbate concentration. K_l values between 0 to1 suggest the favourability of the Langmuir isotherm towards the sorbate-sorbent interaction (Langmuir, 1918).

1.3.1.2. Freundlich adsorption isotherm

Freundlich isotherm model is pertinent to sorbate and adsorbent interactions which results in sorbate multilayer formation over the adsorbent. This interaction involves the non-uniform and spatial distribution of adsorption heat over heterogeneous adsorbent surfaces. Freundlich isotherm model can be non-linearly represented as:

$$q_e = K_f C_e^{1/n} \quad (1.3)$$

K_f (mgg^{-1}) represents Freundlich constant; 1/n relates to adsorption intensity (Freundlich, 1939).

1.3.1.3. Dubinin-Radushkevich Isotherm model

Dubinin-Radushkevich isotherm model relates to the micro-pore filling as opposed to layer-on-layer adsorption on pore surfaces. Unlike Langmuir isotherm, D-R isotherm is inconsiderate to the homogenous surface or constant adsorption potential. This model predicts the adsorption process as either physisorption or chemisorption. The non-linear representation of the D-R isotherm can be represented as:

$$q_e = Q_{DR} \exp^{-K_{DR}\varepsilon^2} \quad (1.4)$$

Q_{DR} (mgg^{-1}) represents D-R adsorption capacity. Polanyi potential (ε) can be represented in the equation; $\varepsilon = RTln(1 + \frac{1}{C_e})$. K_{DR} (mol^2J^{-2}) is a constant that represents the mean free energy for sorbate-sorbent interaction (Dubinin, 1960). Mean biosorption energy (E_{DR}) can be evaluated using K_{DR} and thus can be represented as:

$$E_{DR} = \frac{1}{\sqrt{2K_{DR}}} \quad (1.5)$$

R represents temperature in Kelvin (K) and universal gas constant (8.314 $Jmol^{-1}K^{-1}$) respectively. If K_{DR}<8 $kJmol^{-1}$, then the sorbate-sorbent interaction directs to physisorption, whereas for K_{DR}>16 $kJmol^{-1}$, it's chemisorption.

1.3.1.4. Redlich-Peterson Isotherm model

Three parameter Redlich-Peterson isotherm is a countenance of both Freundlich and Langmuir isotherm (Redlich et al., 1959). This model fulfils the inaccuracies of these two parameter isotherms and represents the adsorption equilibria over a broad range of sorbate concentrations which is mathematically represented as:

$$Q_e = \frac{Q_{rp} B_{rp} C_e}{1 + B_{rp} C_e^g} \quad (1.6)$$

Here, Q_{rp} and B_{rp} are Redlich-Peterson parameters; g is an exponent (value varies from 0 to 1). When g=1, the Redlich-Peterson model equation follows the Langmuir isotherm model equation, and when $1/Q_{rp}B_{rp}=0$, it behaves like the Freundlich isotherm model.

1.3.1.5. Halsey isotherm model

Another commonly employed isotherm is Halsey which signifies multilayer adsorption and heteroporosity for the adsorbent surface and also how it interacts with the sorbate molecules. The model can be represented as:

$$ln q_e = \left(\frac{1}{n_H}\right) ln K_H - \left(\frac{1}{n_H}\right) ln 1/C_e \quad (1.7)$$

K_H and n are evaluated as Halsey isotherm model constant and Halsey isotherm model exponent respectively (Halsey, 1948).

1.3.2. Kinetic Models

1.3.2.1. Pseudo-first order kinetics

Pseudo-first order describes the initial phase of a sorbate-sorbent interaction. It is in this phase where the uptake rate of sorbate molecules by the adsorbent directly corresponds to the intensity of the available sites on the adsorbent. Pseudo-first order can be represented as:

$$\frac{dq_t}{dt} = K_1(q_e - q_t) \quad (1.8)$$

q_t (mgg^{-1}) represents the extent of adsorbate molecules adsorbed by the sorbent at a time 't' and q_e (mgg^{-1}) represents the saturated biosorption of sorbate molecules onto the sorbent's surface. K_1 (min^{-1}) presents a pseudo-first-order rate constant (Anirudhan et al., 2012, Noreen et al., 2020, Hachemaoui et al., 2020, Naushad et al., 2014, Kumar et al., 2016, Rigueto et al., 2021).

1.3.2.2. Pseudo-second order kinetics

Pseudo-second order model directly relates the uptake rate of the sorbate molecules by the sorbent's surface with the squared difference between the adsorbed sorbate concentration at a time 't' and the concentration adsorbed at the equilibrium phase. Pseudo-second order kinetics can be expressed as:

$$\frac{dq_t}{dt} = K_2(q_e - q_t)^2 \quad (1.9)$$

K_2 ($gmg^{-1}min^{-1}$) here represents the pseudo-second-order kinetic rate constant (Ho et al., 1999, Alqadami et al., 2016, Ameh et al., 2022, Chandrasekaran et al., 2020, Ballav et al., 2018, Chafyq et al., 2021).

1.3.2.3. Intra-particle diffusion

Adsorption occurs in 3 steps for porous adsorbents viz. external mass transfer involving the transfer of sorbate molecules from the liquid phase to the surface of the sorbent; intra-particle diffusion of the sorbate species to the pores of the adsorbent; and adsorption onto the pore surface. Intra-particle diffusion accounts for the rate-limiting step of the adsorption process since adsorption within the pores occurs at a very high rate. The mathematical representation of intra-particle diffusion is as follows:

$$Q_t = K_{id} t^{1/2} + C \tag{1.10}$$

C represents the boundary thickness constant and K_{id} ($mgg^{-1}min^{-0.5}$) represents the intra-particle diffusion rate constant (Yang et al., 2008, Albadarin et al., 2017, Ngwabebhoh et al., 2019, Lonappan et al., 2018, wu et al., 2009).

1.3.2.4. Elovich model

The Elovich equation is widely used in adsorption kinetics, which describes the chemical adsorption mechanism in nature. Mathematically it is represented as:

$$q_t = \frac{1}{\beta} ln\,\alpha\beta + \frac{1}{\beta} ln\,t \tag{1.11}$$

Where q_t (mgg^{-1}) represents the extent of adsorbate molecules adsorbed by the sorbent at a time 't'. Elovich constants are denoted by α and β (Tran et al., 2019, Shahnaz et al., 2022, Wu et al., 2009).

1.3.3. Thermodynamics analysis

The energy and enthalpy change distribution for sorbate-sorbent interaction was determined by evaluating the change in Gibb's free energy (ΔG^0) and change in enthalpy (ΔH^0). The spontaneity nature of the sorption process was determined by evaluating change in entropy (ΔS^0). The mathematical representation of the above said is as follows:

$$\Delta G^\circ = -RTln(k_a) \tag{1.12}$$

$$\ln(k_a) = \frac{(-\Delta H^\circ)}{RT} + \frac{(\Delta S^\circ)}{R} \quad (1.13)$$

k_a (lgm^{-1}) represents the distribution co-efficient and can be represented as:

$$k_a = \frac{Q_e}{C_e} * \frac{v_1}{v_2} \quad (1.14)$$

v_1 and v_2 represent the coefficient activities of the sorbate species adsorbed and sorbate in solution at equilibrium, respectively (Nekouei et al., 2015, Kumar et al., 2020, Mishra et al., 2020). The ratio for v_1 and v_2 though can be considered as one for dilute solutions and hence the equation can be converted to:

$$k_a = C_e \overset{lim}{\rightarrow} 0 \frac{Q_e}{C_e} \quad (1.15)$$

1.3.4. Continuous column models

Theoretical models underlying continuous mode have been proposed by many investigators. These continuous column models provide important information hidden beneath the experimental data and are highly useful for the determination of maximum adsorption capacity. (Mthombeni et al., 2018, Iheanacho et al., 2018, Hussein et al., 2022). Further, these models play important role in designing the column reactor on a large scale. Various important continuous column models, fundamental assumptions and mathematical denotations have been discussed in detail below.

1.3.4.1. Thomas model

Thomas model is a widely used model in packed bed column performance which follows Langmuir assumption without axial dispersion. It also defines the adsorption process to be in line with reversible second-order kinetics. The equation can be mathematically represented as:

$$\ln(\frac{C_0}{C_t}\text{-}1) = \frac{K_{TH} * Q_0 * W}{F} - K_{TH} * C_0 * t \quad (1.16)$$

Where, K_{TH} ($mLmin^{-1}mg^{-1}$) and Q_0 (mgg^{-1}) are the Thomas model constant and the adsorption capacity of the adsorbent, respectively; F ($mLmin^{-1}$) represents the flow rate of adsorbate in the column; W (g) is the weight of adsorbent in the fixed bed column; and C_0/C_t denotes the ratio of influent to an effluent concentration of dye solution (Javanbakht and Rafiee, 2022). From the

linear plot drawn for ln ((C_0/C_t)-1) versus t using linear regression form, unknown values of K_{TH} and Q_0 of the Thomas equation were determined by slope and intercept, respectively (Javanbakht et al., 2022, Sapana et a;., 2019, Patel et al., 2022).

1.3.4.2. Adams Bohart model

Adams-Bohart model assumes that equilibrium is not instantaneous and the extent of the adsorption process is proportional to the extent of adsorbent surface active sites or the residual adsorptive capacity of the adsorbent. This model defines the fundamental equation by using surface reaction theory. Adams-Bohart model can be applied to evaluate the performance of the dynamic column that explains the initial breakthrough curve C_t/C_0 against t for the fixed bed column. The linear expression can be presented mathematically as:

$$\ln(\frac{C_t}{C_0})=K_{AB}*C_0*t - K_{AB}*N_{AB}*\frac{Z}{u} \quad (1.17)$$

where influent and effluent BF concentrations are C_0 (mgL^{-1}) and C_t (mgL^{-1}) respectively; adsorbent bed height is Z (cm); superficial velocity u ($cmmin^{-1}$) that were derived by dividing the flow rate of the column by the cross-sectional area of the bed. The plot between $\ln(C_t/C_0)$ versus t was used to evaluate unknown parameters K_{AB} ($Lmg^{-1}min^{-1}$) (kinetics constant) and N_{AB} (mgL^{-1}) (saturation constant) from the slope and the intercept respectively (Chu et al., 2020, Lai et al., 2021).

1.3.4.3. Yoon Nelson model

This model is known to be the simplest theoretical model for evaluating column performance as it does not consider the physical properties of the adsorption bed and adsorbate used. It assumes that the possibility of adsorption and adsorbate breakthrough on the adsorbent surface could be the probable reason for the reduced adsorption rate. This approach has been fitted to the dynamic adsorption of BF on to aqueous solution using *GC.* mathematical equation (18) as shown below:

$$\ln(\frac{C_t}{C_0 - C_t})=K_{YN}*t - K_{YN}*\tau \quad (1.18)$$

Here, K_{YN} (min^{-1}) and τ (min) are the rate constant and time needed for 50% adsorbate breakthrough respectively whereas t represents the processing time (Biswas and Mishra, 2015).

The slope and intercept of the plot linearized between $\ln C_t/(C_0-C_t)$ and t give the values of K_{YN} and τ (Yin et al., 2022, Gong et al., 2021, Juela et al., 2021, Farias et al., 2021)

1.3.4.4. Bed Depth Service time model

This model is an extension of the laboratory scale set up to apply to the pilot scale with the same dynamic behaviour of the packed bed column. BDST also neglects external mass transfer and intraparticle mass transfer resistance while explaining the physical adsorption. BDST model can be represented as it describes the correlation between the processing time (t) and column bed height (Z):

$$t=\left(\frac{N_0 Z}{C_0 u}\right)-\left(\frac{1}{C_0 K_a}\right)\ln\left(\frac{C_0}{C_b}-1\right) \quad (1.19)$$

C_0 and C_b represent the influent and breakthrough dye concentration respectively, K_a is the rate constant of the packed bed column ($Lmg^{-1}min^{-1}$), u indicates the linear velocity ($cmmin^{-1}$) and N_0 represents the adsorption capacity (mgL^{-1}) (Lai et al., 2021, Feizi et al., 2021, Elwakeel et al., 2009).

1.4. Problem statement and related objectives

With the expanded knowledge published on wastewater treatment over a few decades, it is observed that a major trait of a potent adsorbent is to be able to counter various categories of pollutants. It is an added benefit if the adsorbent is of biological origin and thereby the biodegradability of the used adsorbent is possible at ease. The well-studied biological materials like lignocellulosic and cellulosic materials pave the way for easy chemical modification with high chemical stability. However, the challenge is in the scaling up of the adsorption process where despite their ability to adsorb various pollutants, agglomeration and disintegration of cellulosic material in the aqueous media is very common. Here comes the integration of polymeric materials as a support to overcome these difficulties which provide high mechanical strength and stability under different environmental conditions to improve the adsorption efficiency of the cellulosic base material. Another important property is the understanding of the cost-efficiency of an adsorbent. Thus it is imperative to know the regenerative cycles and principles behind them. The static and flow adsorptive process needs proper optimization of various influencing parameters which is included in the present study. Along with this in real industrial wastewater, there will be multiple contaminants with various ions and salts. Hence the influence of all these factors is equally important in the selective elimination of a pollutant by an adsorbent. Toxicity endpoint analysis of the adsorbed wastewater is the study to understand the efficacy of the adsorbent once it remediates successfully. Phytotoxicity and acute fish toxicity assays are two key measures to check the viability of the after-remediation process. So, from the discussion mentioned above the research work has been designed with the following objectives:

1. Synthesis of tailored material with enhanced biosorption capacity.
2. Design the experiments with different pollutants like heavy metals, dye, antibiotics and rare earth elements etc.
3. Significance of important parameters and their possible interaction in both batch and continuous mode.
4. Desorption and recyclability studies.
5. Toxicity endpoint studies with biological model system viz. Photo and fish toxicity.

1.5. Outline of the thesis

Based on the above-discussed objectives the thesis work has been divided into the following 8 chapters.

Chapter 1: General introduction and theoretical background

Chapter 2: A comparative study of raw, acid modified and EDTA complexed *Acacia auriculiformis* biomass for removal of hexavalent chromium

Chapter 3: Facile preparation of nanocellulose embedded polypyrrole for dye removal: unary and binary process optimization and seed toxicity

Chapter 4: Surface modification of nanocellulose using polypyrrole for the adsorptive removal of Congo red dye and chromium in binary mixture

Chapter 5: Use of Nanocellulose extracted from grass for adsorption abatement of Ciprofloxacin and Diclofenac removal with phyto, and fish toxicity studies

Chapter 6: Magnetic nanocellulose from *Cyperus rotundas* grass in the absorptive removal of rare earth element cerium (III): Toxicity studies and interpretation

Chapter 7: *Cyperus rotundus* as a new cellulose source for remediation of Basic Fuchsine dye: A static and flow adsorptive approach

Chapter 8: Summary and Conclusion

Chapter 2
A comparative study of raw, acid modified and EDTA complexed *Acacia auriculiformis* biomass for removal of hexavalent chromium

The work embodied in this chapter is published in

TASRIN SHAHNAZ, Chandi Patra, Vivek Sharma, and Selvaraju Narayanasamy*, Biosorption of Chromium from simulated wastewater using activated and chelated *Acacia auriculiformis* as a plausible biosorbent, **Chemistry and Ecology, 2020, (Taylor & Francis, SCI IF: 2.381)**

TH-3150_176106114

Abstract

The current study deals with the removal of hexavalent chromium from simulated solution using *Acacia auriculiformis* shells and their different modified forms as potent biosorbents. The raw plant biomass (RAA) was acid-modified with sulphuric acid and named sulphuric acid activated carbon (SAA) and was further complexed with ethylene-diamine-tetra-acetic acid (SAAC) to further modify its sorption capacity. Adsorption parameters like pH, adsorbent dosage, temperature and initial metal concentration were optimized in a batch study using the one-variable-at-a-time method. The optimized data were further equilibrated using isotherm, kinetic and thermodynamic models to determine the nature of sorbent-sorbate interaction. Langmuir isotherm showed the best fit for the three adsorbents with Langmuir maximum adsorption capacities being 91.48, 117.75 and 145.72 mgg^{-1} for RAA, SAA and SAAC respectively at pH 2. From the correlation coefficients of the fitted kinetic models, it was observed that sorbent-sorbate interaction followed pseudo-second-order and chemisorption in nature. Thermodynamic analysis verifies endothermic interaction with an elevated degree of randomness about the sorbent-sorbate interaction. The adsorbents were regenerated for 4 cycles and the biosorbents proved potent for efficient sorption of Cr(VI). For SAAC the removal efficiency decreased from 57.51% to 26.81% after the 4th cycle which is more than twice and thrice as compared to SAA and RAA.

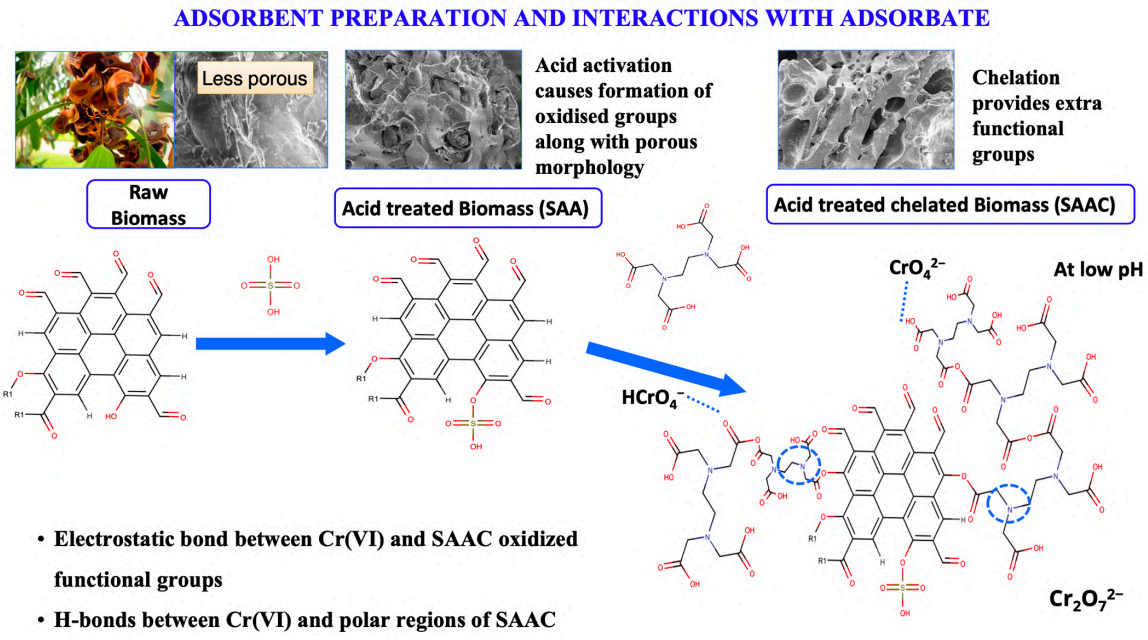

Scheme 2.1: Graphical representation

TH-3150_176106114

2.1. Materials and methods

2.1.1. Preparation of sorbate solution

A stock solution (1000 mgl^{-1}) of Cr(VI) aqueous solution was prepared by adding 2.828 g $K_2Cr_2O_7$ in 1000 ml distilled water (Milli-Q). The experimental solutions from 100 to 1000 mgl^{-1} concentrations were prepared by diluting the stock solution in distilled water. All chemicals and reagents thus used were of analytical grade and obtained from HiMedia Labs (India).

2.1.2. Preparation of biosorbents

2.1.3. Biosorbent preparation

Acacia auriculiformis was collected from the IIT Guwahati Campus located at 26˚11’14’’N91˚41’30’’E. It was then washed with a soap solution for removing soil and dirt particulates and allowed to dry at 333K for two days in a hot air oven. The biosorbent was then disintegrated into small pieces, crushed and pulverized using a blender and sieved through five different ranges (<0.075 mm, 0.15 mm, 0.30 mm, 0.45 mm, 0.60 mm). The prepared powdered biosorbent; RAA (Raw *Acacia auriculiformis)* was stored in an airtight plastic container for further use.

2.1.4. Sulfuric acid treatment and activation

The dried powdered biomass (RAA) was acid treated with sulfuric acid (98%) in the ratio of 1:2 (weight of biomass in g: volume of acid in ml) and allowed to react for 24 hours in a fume hood. The acid-treated biomass was then pyrolysed in a muffle furnace at 673 K for 1.5 hours. Acid-activated biomass was then soaked with 1.5% sodium bicarbonate for a day and then it was washed thoroughly with distilled water to remove the residual acid. Once pH≅7 is achieved, the acid-activated biomass; SAA (Sulfuric acid-treated *Acacia auriculiformis*) was oven-dried and stored in airtight containers (Asfaram et al., 2015).

2.1.5. Complexation with a chelating agent

Once acid activation of raw biomass is achieved, SAA was complexed with Ethylene-diamine-tetra-acetic acid (EDTA). Sulphuric acid-activated samples (SAA) were complexed with 1M EDTA in the proportion of 1:2 (SAA in g: EDTA in mL) and mixed uniformly for 48 hours at room temperature. Once the mixture is uniform, it was washed repeatedly via centrifugation at 5000 rpm, till clear supernatant is obtained. The pellet thus obtained was

TH-3150_176106114

acid-activated/complexed biosorbent; SAAC. It was oven-dried and stored in airtight containers.

2.1.6. Characterization

The surface morphology and topological properties of the samples were characterised through field emission scanning electron microscopy (FESEM) (Zeiss, Sigma, Germany). For surface, elemental analysis, energy dispersive X-ray spectrometry (EDX) (Zeiss, Sigma, Germany) was performed. Functional groups attributed to Cr(VI) species biosorption were recognised using Fourier transform infrared spectrometry (FTIR) (Spectrum Two, PerkinElmer, USA) in the range of 4000-400 cm^{-1}. Total pore analysis and average surface (Brunauer-Emmett-Teller/Barrett-Joyner-Halenda) analysis of the samples were quantified by total surface area and pore size analyser (Autosorb-IQ MP, Quantachrome, USA).

2.1.7. Batch adsorption experiments

Variables influencing the biosorption efficiency of the biosorbents (RAA, SAA and SAAC) were optimised in batch mode experiments performed using 250 mL Erlenmeyer flasks; incubating in a shaker incubator (Orbitek, Scigenics Biotech, India) at fixed temperatures and rpm. The parameters optimised that majorly influenced the biosorption capacity were biosorbent (RAA, SAA and SAAC) dose (0.2-2.0 $mgmL^{-1}$), pH of Cr(VI) aqueous solution (2-10), incubation temperature (303-330 K) and initial Cr(VI) concentration (100-1000 mgL^{-1}). The limits for the variables that were opted for the present studies were based on the literature survey and feasible enough to perform at the industrial scale. After adsorption, the remaining Cr(VI) species in the filtrate were evaluated using a UV-Visible spectrophotometer at a wavelength of 540 nm (GeneQuant 1300, GE, USA) by complexing the filtrate with 1, 5-diphenyl carbazide (DPC) in acidic pH (Rangabhashiyam et al., 2015). The removal efficiency of Cr(VI) species by the adsorbents was evaluated using the following equation:

$$\%\text{Removal} = \frac{(C_0 - C_t)}{C_0} \times 100 \qquad (2.1)$$

TH-3150_176106114

where C_0 represents the initial Cr(VI) concentration (mgL^{-1}), C_t represents equilibrium Cr(VI) concentration at specific time 't' (mgL^{-1}). Biosorption capacity (q_t) of biosorbent was evaluated using the following:

$$q_t = \frac{(C_0 - C_t)V}{m} \tag{2.2}$$

where 'm' is the biosorbent dose (mg) and 'V' represents the volume of Cr(VI) solution (mL) (Fu et al., 2015).

2.1.8. Recyclability studies

Recyclability studies attribute to repeated adsorption-desorption phenomenon using 0.1 N NaOH (sodium hydroxide) solution as the desorbing agent. After a single run of adsorption, the efficiency of the biosorbent in removing Cr(VI) decreases as the adsorbent surface gets saturated and thereby making the process not so cost-effective for the long run. It also makes the process depend on continuous supplying of the biomass in the process. Therefore, analysing the potential of used biomass to reuse plays an important role in commercialising a biosorbent. The adsorbent was desorbed with 0.1 N NaOH for regaining the sorbent surface. The adsorbents (RAA, SAA and SAAC) were then thoroughly rinsed with distilled water to wash away any residual NaOH or HCl. The adsorbents are dried and reused for four consecutive adsorption-desorption processes for the recyclability analysis. The desorption efficiency was evaluated using the following equation:

$$\%\text{Desorption} = \frac{C_{de}}{C_{ad}} \times 100 \tag{2.3}$$

where C_{de}, C_{ad} are the Cr(VI) concentrations during desorption and after adsorption, respectively for time 't' (mgL^{-1}) (Moharem et al., 2019).

TH-3150_176106114

2.2. Results and discussion

2.2.1. Characterization of biosorbents

The biosorbents (RAA, SAA and SAAC) were characterized for various morphological and functional features and modifications; before and after biosorption of Cr(VI) species. The following describes the various analysis.

2.2.1.1. BET/BJH total pore analysis

The specific surface area of the biosorbents and their pore distribution properties was evaluated using N_2 adsorption-desorption isotherm at a degassing temperature of 393 K (for 3 hours). The amount of nitrogen gas adsorbed and desorbed onto the biosorbent surface during the process was measured to determine the adsorption isotherm. The raw biosorbent (RAA) has a surface area of 1.901 m^2g^{-1} whereas the acid-activated sample (SAA) has a hugely increased surface area of 891.39 m^2g^{-1}. SAAC also showed a higher surface area than RAA with a value of 789.35 m^2g^{-1} which may be due to the incorporation of chelating agent on the surface. Table 2.1 showed the pore diameter, total pore volume and specific surface area of RAA, SAA and SAAC. As observed from the data, the surface modification did play a pivotal role in enhancing the biosorbent efficiency by making the active functional groups like carboxyl, hydroxyl groups available to interact with the metal ions. The BET analysis proved acid activation showed an elevated specific surface area (m^2g^{-1}) of the biosorbent SAA, thus verifying the number of available sites for Cr(VI) sorption.

Table 2.1: BET pore analysis of RAA, SAA and SAAC

	RAA	**SAA**	**SAAC**
Total pore volume (cm^3g^{-1})	0.009	0.543	0.531
Pore diameter (nm)	4.675	4.987	4.789
Specific surface area (m^2g^{-1})	1.901	891.39	789.35

2.2.1.2. Electron microscopy analysis

Scanning electron microscopy was done for evaluating the morphological characteristics of the biosorbents (RAA, SAA and SAAC) as shown in fig. 2.1 (a, b, c, d, e, f). It's evident from fig. 2.1a that RAA shows dense surface morphology with relatively low pore density. SAA (fig. 2.1b) being acid-activated and pyrolysed showed better porosity with enhanced and distinct micro and macro-pores over the heterogeneous surface.

TH-3150_176106114

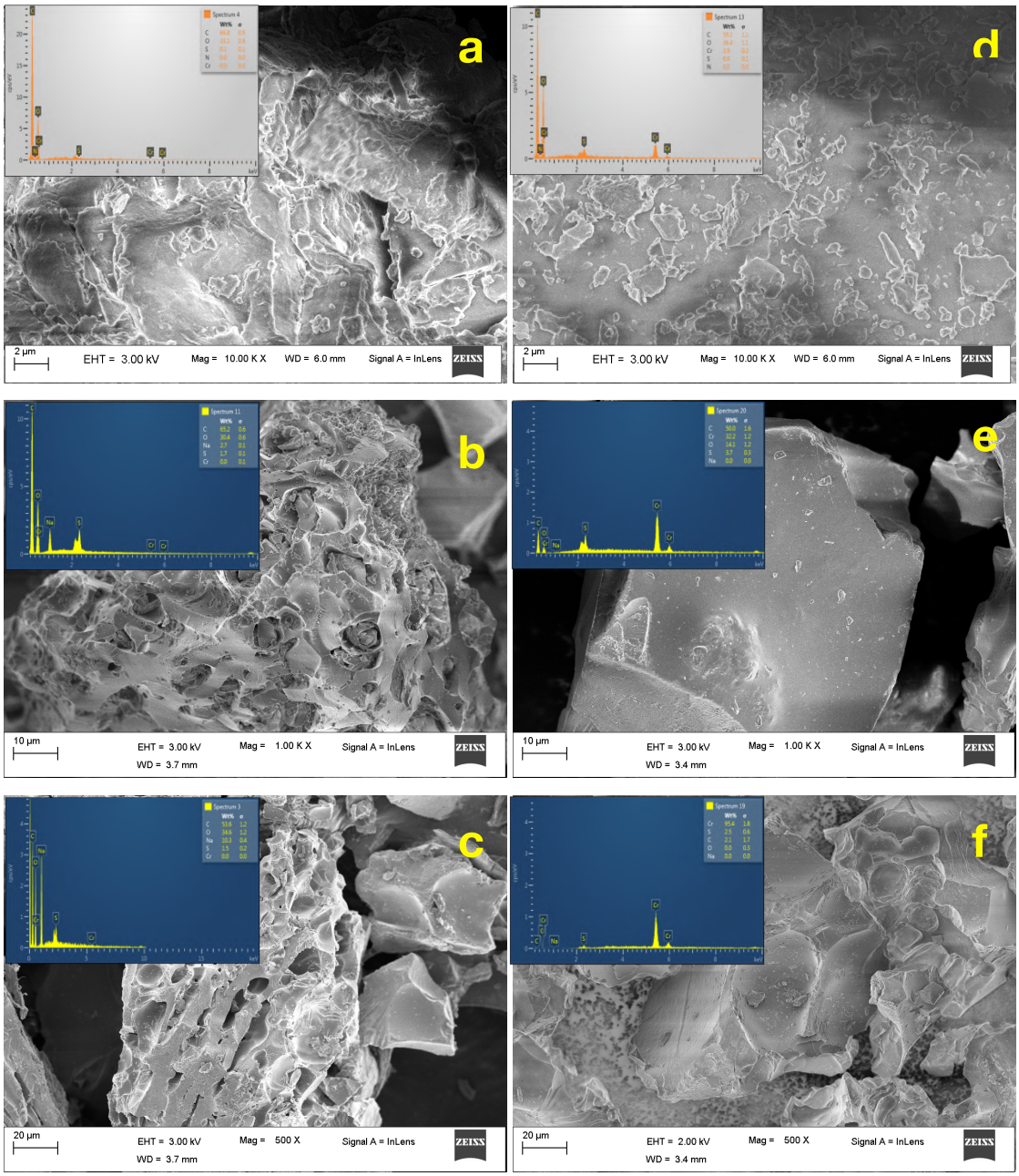

Fig. 2.1: Scanning electron micrographs and EDX images of biosorbents RAA, SAA and SAAC (a, b, c) before and (d, e, f) after Chromium biosorption

SEM images for SAAC (fig. 2.1c) revealed a more intense heterogeneous surface with elevated surface irregularities. Conclusively, the surface heterogeneity increased with acid modification followed by pyrolysis, which was further enhanced with complexation. This behaviour of the biosorbents can be verified with the experimental data. RAA (fig. 2.1d), SAA (fig. 2.1e) and SAAC (fig. 2.1f) showed relatively homogenous, flat and low intensity

TH-3150_176106114

ridges and unevenness after Cr(VI) adsorption. This characterisation is about the change in the morphology of the outer surface.

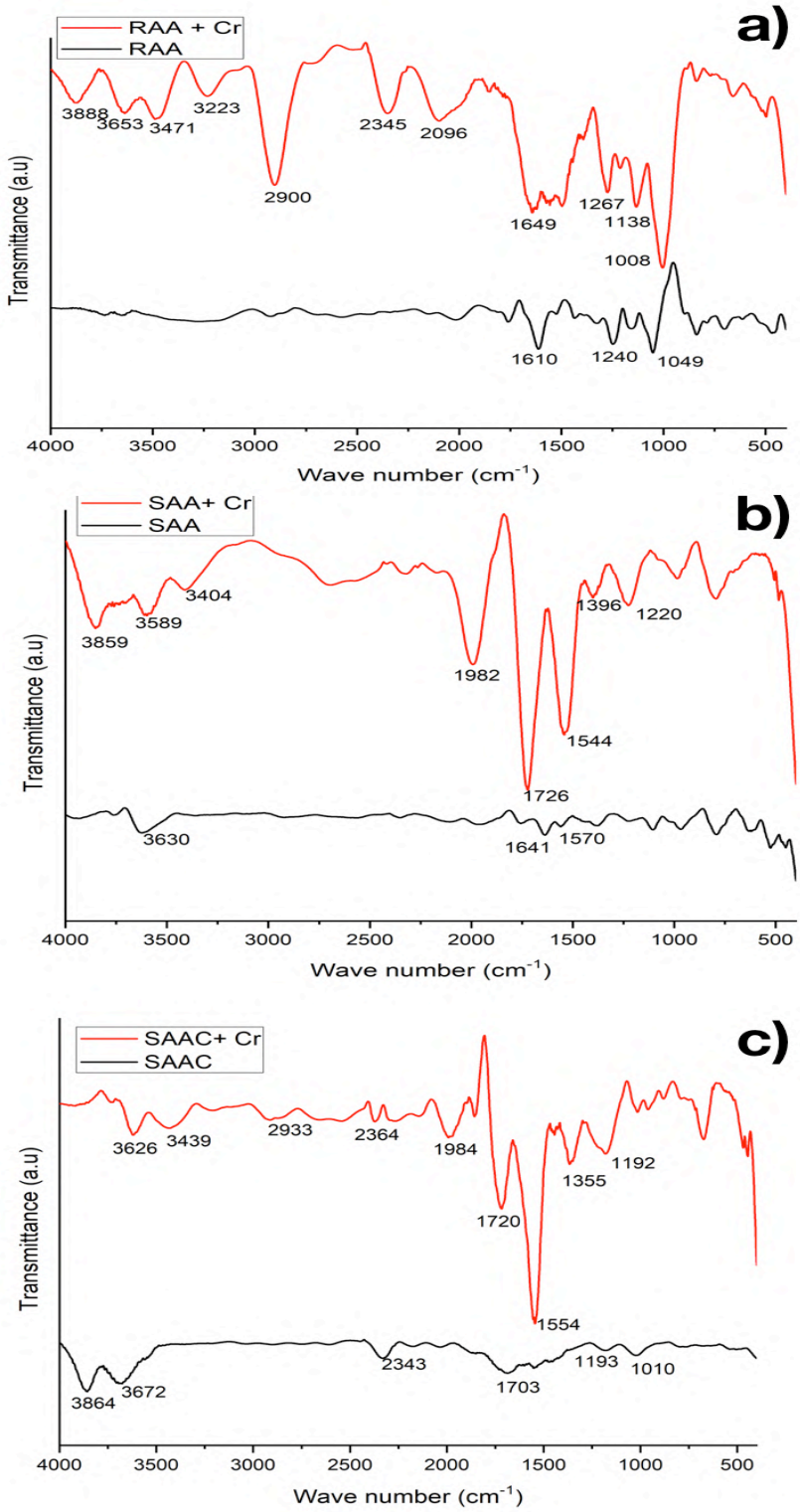

Fig. 2.2: FTIR spectral analysis of biosorbent (a) RAA, (b) SAA, (c) SAAC with and without chromium

TH-3150_176106114

2.2.1.3. Energy dispersive X-ray spectrometry analysis

Surface elemental analysis of the biosorbents (RAA, SAA and SAAC) was done to evaluate their adsorption capabilities. The spectra for chromium molecules as depicted in fig. 2.1(d, e and f) and show the chromium peaks in the order: RAA<SAA<SAAC. This trend was likely to occur since Cr(VI) species adsorption increased with elevated surface area and heterogeneity as affirmed by pore analysis and SEM analysis. Complexation (SAAC) further showed Cr(VI) peak elevation as compared to RAA and SAA. Contrary to after Cr(VI) adsorption, fig. 2.1(a, b and c) show no peak for Cr(VI). EDS results confirmed direct affirmation of Cr(VI) biosorption over the sorbent's surface (Saleh et al., 2012).

2.2.1.4. Fourier transform infrared spectrometry analysis

FTIR spectral analysis gives information about biosorption effects through shifting in the surface functional groups in a molecule on the original as well as in the residual sample. The FTIR spectra (4000-400 cm^{-1}) of RAA, SAA and SAAC prior to and after Cr(VI) adsorption is as represented in Fig. 2.2. In raw biosorbent (RAA) there are peaks at 1610 and 1049 cm^{-1} suggesting C=C stretching and CO-O-CO stretching for anhydride compound respectively. When RAA was adsorbed with Cr, some distinguished peaks emerged. Peaks at 3888, 3653, 3471 and 3223 cm^{-1} are due to -OH stretching vibration. Spectra at 2900 cm^{-1} attributed to the formation of -H bonds between -OH groups of RAA and Cr(VI) after the biosorption. Another peak at 2345 cm^{-1} can be attributed to O=C=O stretching. Spectral changes observed in the FTIR spectra of RAA after the biosorption is due to a shift or complete disappearance of peaks. Spectra after 1650 are due to mostly C=C stretching that is retained after biosorption. For SAA, there is a single peak at 3630 cm^{-1} suggesting O-H stretching of alcohol, whereas 1641 and 1570 cm^{-1} peaks are attributed to alkene C=C vibrational stretching. After Cr biosorption on SAA, new peaks at 3859, 3589, 3404 cm^{-1} are due to the interaction of Cr with the sample and thereby emerging these functional groups viz. -OH, -NH, -CO etc. C-H bending is also observed for a peak at 1982 cm^{-1}.

Now especially for SAAC, before adsorption, it has many functional groups present at 3864, 3672 cm^{-1} which are for -OH stretching and amine group. Peaks at 2343, 1703 and 1193 cm^{-1} are due to strong O-C-O, aldehyde (C=O) and amine stretching respectively. 1010 cm^{-1} can be attributed to C-H bending. After Cr biosorption, there are shifting of some peaks to 3626, 2364, 1720 and 1192 cm^{-1} but falls in the same functional group range which may be due to

TH-3150_176106114

the binding of the metal ion. Some peaks are observed at 3439, 2933, 1984 cm^{-1} suggesting -OH stretching and -CH bending. Nitro and sulfonic stretching at 1554 and 1355 cm^{-1} are found in the SAAC biosorbent (Moharem et al., 2019) which could be possibly due to the presence of a chelating agent EDTA. The overall large number of peaks were observed in SAA and SAAC before and after chromium biosorption which is attributed to the acid treatment and chelation with EDTA that largely increased the adsorbent capacity of the biosorbent.

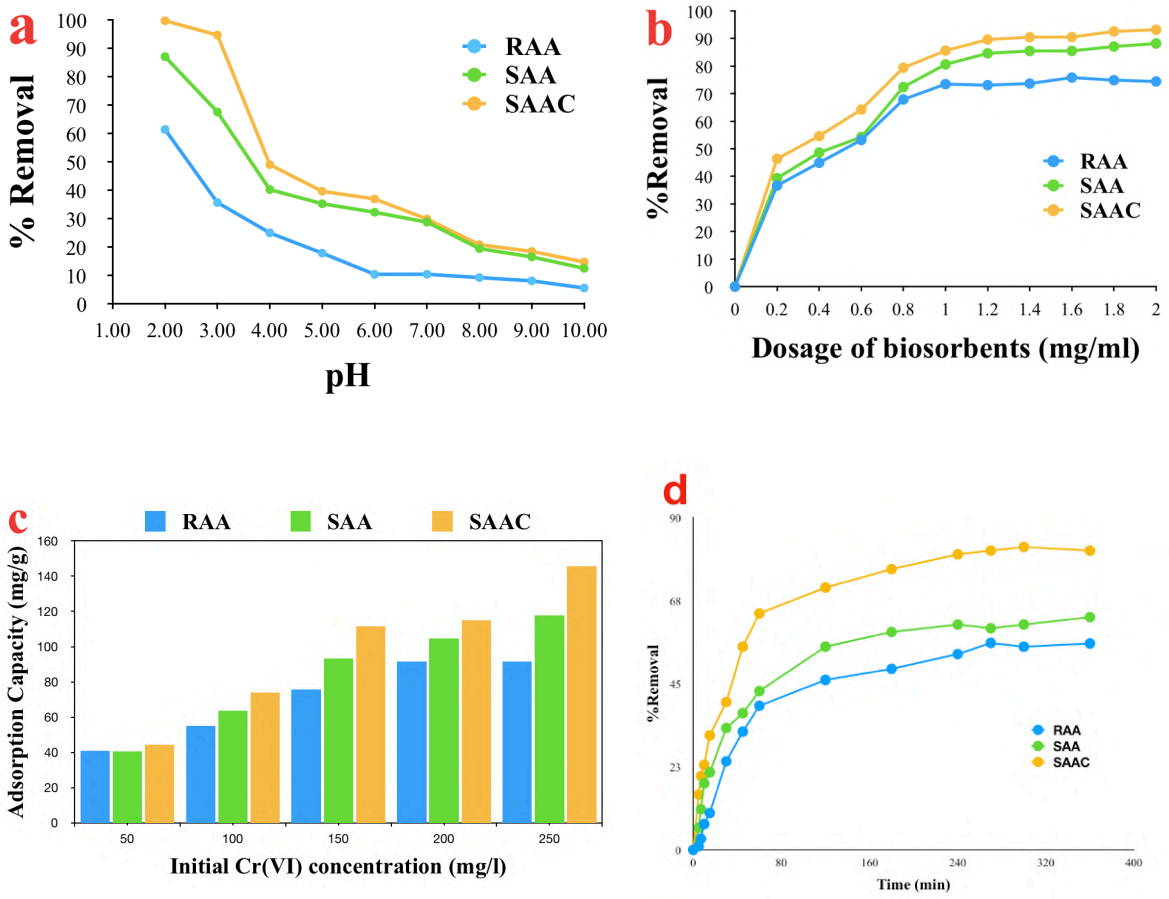

Fig. 2.3: Effect of (a) pH; (b) variable dosage of biosorbents over adsorption efficiency; (c) variable initial Cr(VI) concentration and (d) contact time on adsorption capacity and efficiency by RAA, SAA and SAAC

2.2.2. Effect of pH

The effect of the initial pH of the metal solution was evaluated from 2.0 to 10.0 at 303 K considering 0.5 mgl^{-1} of biosorbent and 200 mgl^{-1} of Cr(VI) solution. The maximum removal

TH-3150_176106114

percentage was observed at pH 2.0 for RAA, SAA and SAAC with a magnitude of 61.38%, 87.02% and 99.68% respectively as shown in fig. 2.3(a). With the increase in pH, all the biosorbents showed a gradual decline in biosorption capacity. The reason behind this could be that in an aqueous solution Cr(VI) is present in anionic forms viz. $HCrO^{4-}$, CrO_4^{2-} and $Cr_2O_7^{2-}$ and thus they show increased electrostatic pull towards heavily protonated biosorbent's surface at lower pH. As the pH gradually increases, the protonation intensity of the biosorbent decreases and so does the electrostatic pull of the Cr(VI) species (Priya et al., 2014).

Table 2.2: Thermodynamic parameters of RAA, SAA and SAAC for Cr(VI) removal

		RAA			SAA			SAAC		
Ci	T	ΔG°	ΔH°	ΔS°	ΔG°	ΔH°	ΔS°	ΔG°	ΔH°	ΔS°
50	303	-3.390	5.239	5.062	-3.149	3.837	22.886	-4.152	60.767	183.683
	313	-4.410			-7.692			-4.600		
	323	-3.095			-3.102			-1.884		
	333	-3.631			-4.055			-4.051		
100	303	-1.933	3.847	4.539	-1.275	10.506	26.100	-3.129	13.428	35.502
	313	-3.555			-4.923			-2.026		
	323	-1.815			-1.080			-1.021		
	333	-2.311			-1.545			-2.382		
150	303	-0.874	10.155	28.200	-0.235	12.552	37.172	-2.259	22.478	68.736
	313	-2.816			-3.067			-0.235		
	323	-0.385			-0.441			-0.244		
	333	-0.671			-0.062			-0.233		
200	303	-0.166	9.183	28.556	-0.803	7.124	23.634	-1.236	23.905	76.493
	313	-1.564			-1.266			-0.795		
	323	-0.476			-1.180			-0.923		
	333	-0.515			-0.853			-1.196		
250	303	-0.813	6.051	21.300	-1.529	4.463	12.699	-0.543	13.317	43.708
	313	-0.684			-0.191			-1.772		
	323	-1.078			-1.881			-1.802		

TH-3150_176106114

333	-1.158	-1.673	-2.102

2.2.3. Effect of adsorbent dosage

The amount of biosorbent could influence the efficient removal capacity of the metal ions. The optimal dosage was inspected by using 0.2-2.0 $mgml^{-1}$ of biosorbent (size range 0.150-0.300 mm) with 25 mL working solution and 200 mgL^{-1} of initial Cr(VI) concentration. The pH of Cr(VI) aqueous solution was kept at 2 at 303 K temperature and agitation speed 120 rpm. The removal efficiency increased gradually with increasing dosage for all the biosorbents as depicted in Fig. 2.3(b). The trend followed for raw (RAA) as well as

Table 2.3: Adsorption isotherm parameters, constants and coefficient of determination for Cr(VI) species biosorption by RAA, SAA and SAAC at variable temperatures (K)

Isotherms		RAA			SAA			SAAC		
		303 K	313 K	323 K	303 K	313 K	323 K	303 K	313 K	323 K
Langmuir	Q_L	98.24	135.38	91.84	120.22	171.42	115.72	168.56	88.96	102.12
	L	0.05	0.16	0.05	0.04	0.04	0.04	0.04	0.12	0.03
	R^2	0.99	0.99	0.99	0.99	0.99	0.99	0.99	0.99	0.99
Freundlich	K_F	0.536	0.490	0.556	19.09	40.67	18.93	18.02	29.06	11.72
	n	3.492	3.205	3.603	3.13	3.83	3.39	2.32	4.48	2.46
	R^2	0.98	0.98	0.97	0.92	0.95	0.98	0.95	0.94	0.94
Dubinin–Radushkevich	Q_{DR}	82.19	114.15	73.85	84.54	121.21	87.36	107.31	79.75	78.50
	K_{DR}	16.31	1.21	16.61	14.74	11.75	21.01	11.26	6.02	40.20
	E_{DR}	0.18	0.64	0.17	0.18	0.21	0.15	0.21	0.29	0.11
	R^2	0.89	0.89	0.89	0.69	0.90	0.91	0.83	0.94	0.95
Redlich-Peterson	Arp	6.18	8.27	5.21	5.21	22.03	4.41	6.61	10.51	3.23
	Brp	0.053	0.050	0.046	0.053	0.162	0.048	0.039	0.118	0.032
	g	0.75	0.86	0.69	0.7	0.85	0.63	0.65	0.57	0.61
	R^2	0.98	0.98	0.97	0.99	0.97	0.96	0.96	0.99	0.98

TH-3150_176106114

Table 2.4: Kinetic rate constants related to the biosorption of Cr(VI) onto RAA, SAA and SAAC

		Pseudo-first order			Pseudo-second order			Intra-particle diffusion		
Ci (mgL^{-1})	qe mgg^{-1} (exp.)	qe mgg^{-1}	K_1 (min^{-1})	R^2	qe (mgg^{-1})	K_2 (gmg^{-1} min^{-1})	R^2	K_{id} (mgg^{-1} $min^{0.5}$)	C (mgg^{-1})	R^2
RAA										
50	41.13	20.82	-0.04	0.80	42.89	0.0018	0.98	2.18	13.33	0.72
100	55.21	34.56	-0.03	0.83	59.59	0.0008	0.99	3.18	13.24	0.84
150	75.71	43.26	-0.03	0.87	80.86	0.0003	0.97	4.30	10.57	0.93
200	91.74	35.65	-0.03	0.64	92.93	0.0006	0.99	4.60	26.90	0.73
250	91.48	62.37	-0.02	0.85	101.83	0.0004	0.97	5.41	21.29	0.82
SAA										
50	40.46	30.75	-0.03	0.95	49.07	0.0003	0.99	2.59	2.07	0.97
100	63.76	59.70	-0.03	0.95	88.83	0.0001	0.98	4.47	-0.62	0.97
150	93.30	63.66	-0.04	0.95	104.39	0.0002	0.98	5.59	8.83	0.96
200	104.59	74.85	-0.05	0.96	112.48	0.0005	0.99	6.10	26.84	0.82
250	117.75	102.70	-0.05	0.83	128.45	0.0002	0.98	7.30	8.25	0.93
SAAC										
50	44.58	28.63	-0.05	0.95	47.48	0.0013	0.99	2.53	12.17	0.79
100	74.11	56.86	-0.07	0.99	78.63	0.0010	0.97	4.18	22.11	0.76
150	111.44	63.41	-0.04	0.91	117.29	0.0006	0.99	6.24	32.08	0.76
200	115.13	71.99	-0.05	0.93	121.48	0.0007	0.98	6.47	34.73	0.75
250	145.72	105.21	-0.06	0.95	157.01	0.0004	0.99	8.81	34.86	0.80

the acid-activated (SAA) sample in quite the same way with efficiency however less than the SAAC.

An explanation for this could be the availability of the reactive functional groups with the modified biosorbent (Shahnaz et al., 2020, Gupta et al., 2011). All the biosorbents viz. RAA (74.44%), SAA (88.20%) and SAAC (93.20%), showed maximum Cr(VI) adsorption efficiencies at a maximum dosage value of 2 $mgml^{-1}$; which is possibly because of the elevation of available sites with the elevation in dosage for fixed Cr(VI) concentration.

TH-3150_176106114

2.2.4. Effect of initial chromium concentration and contact time

With the increase in initial Cr(VI) concentration (50 to 250 mgl^{-1}), the adsorption capacity of the biosorbent (fixed dose) gradually increases until equilibrium; considering pH 2 at 303 K and incubated for 240 mins. The study with contact time revealed that the rate of Cr(VI) species uptake gradually increases logarithmically for the first 10-15 mins, after which it starts to decline and finally attains equilibrium (Fig. 2.3d). The possible reason for this is due to saturation of adsorption sites over the due course of time. As shown in fig. 2.3c with the increase in initial Cr(VI) concentration, the adsorption capacity of the biosorbents also elevated from 41.13 mgg^{-1} (50 mgl^{-1}) to 91.48 mgg^{-1} (250 mgl^{-1}) for RAA, 40.46 mgg^{-1} (50 mgl^{-1}) to 117.75 mgg^{-1} (250 mgl^{-1}) for SAA and 44.58 mgg^{-1} (50 mgl^{-1}) to 145.72 mgg^{-1} (250 mgl^{-1}) for SAAC at pH 2 and 303K (Ihsanullah et al., 2015).

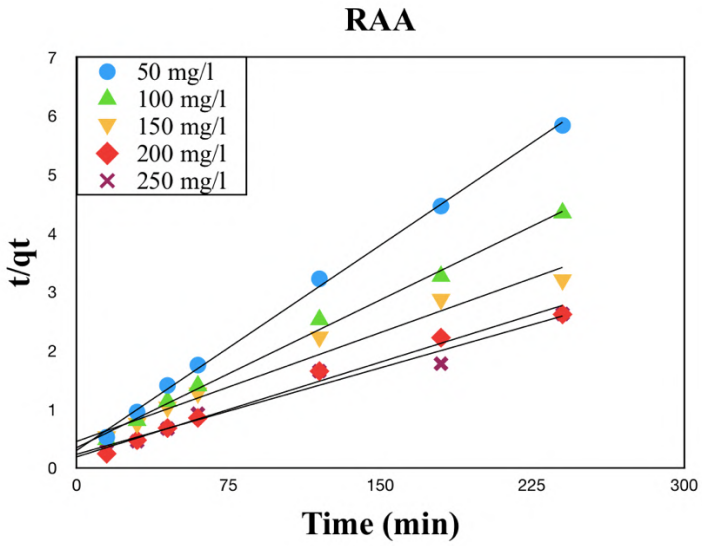

TH-3150_176106114

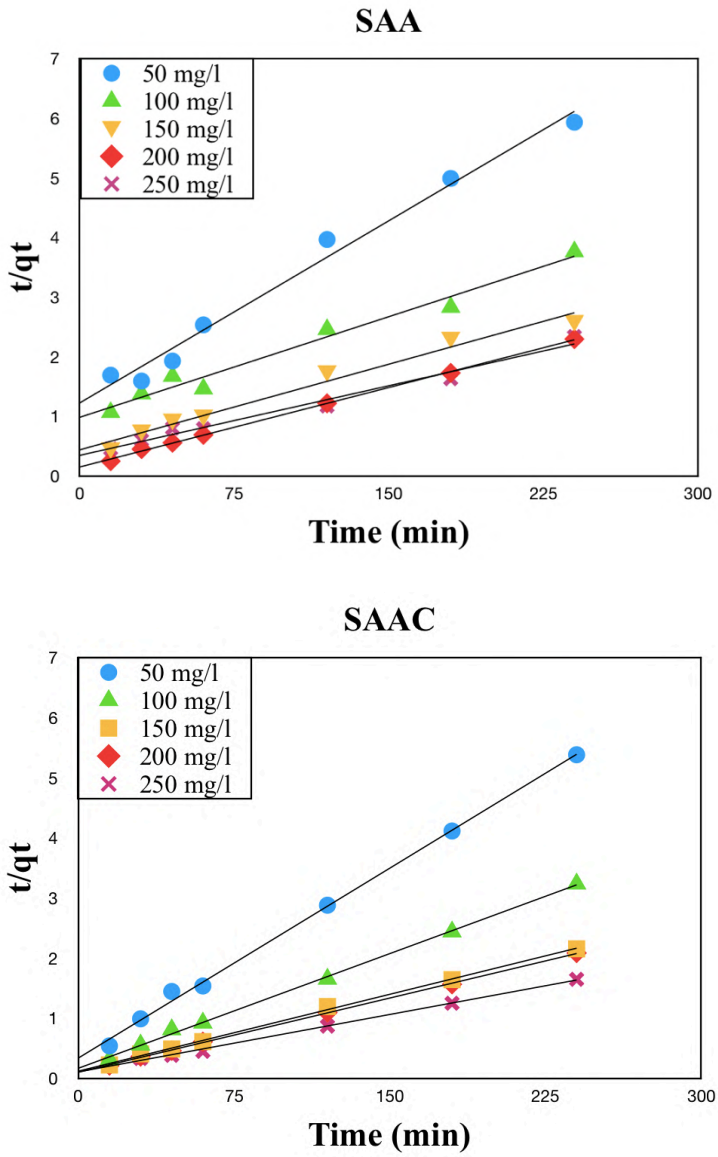

Fig. 2.4: Pseudo-second-order kinetics for biosorption of Cr(VI) on RAA, SAA and SAAC respectively

2.2.5. Effect of temperature and related thermodynamic studies

Temperature played a dominating role in the sorption process and the same has been exploited from 303K to 323K. With the increase in temperature, the adsorption process increased to 313 K for RAA and SAA, after which the sorption efficiency decreased to 323K. However, SAAC performed the reverse of RAA and SAA owing to a splitting of chelating agents with increased temperature. For SAAC, the maximum removal was found to be at 303 K. Table 2.2 presents the calculated values of ΔG^0, ΔH^0 and ΔS^0 at variable temperatures and Cr(VI) concentrations. Negative ΔG^0 values by RAA, SAA and SAAC confirmed spontaneity and thermodynamic favourability towards sorbate-sorbent

TH-3150_176106114

interactions. Positive ΔH^0 values verified the endothermic biosorption process and positive ΔS^0 values verified the rise in the degree of disorderliness and randomness favouring the biosorption process (Mohammadi et al., 2011).

2.2.6. Biosorption isotherm studies

Two-parameter (Langmuir, Freundlich, Dubinin-Radushkevich) and three-parameter (Redlich-Peterson) isotherm models were evaluated using experimental data to obtain the co-relation between Cr(VI) species and biosorbent molecules. Table 2.3 represents the different isotherm models evaluated along with the constants, coefficients and regression (R^2) values. Langmuir adsorption isotherm showed the best fit (R^2) for the interaction of Cr(VI) molecules with the biosorbent's surface; for all the biosorbents (RAA, SAA, SAAC) at all temperatures (303 K to 323 K). Thus, it could be concluded that Cr(VI) species formed a mono-layer over the adsorbent's surface. Langmuir maximum adsorption capacity (Q_L) for RAA, SAA and SAAC was 135.38 mgg^{-1} (313K), 171.42 mgg^{-1} (313 K) and 168.56 mgg^{-1} (303 K) respectively.

With this, it can be verified that acid-activation of the RAA to SAA and complexation of SAA to SAAC caused an elevation in the monolayer adsorption. The separation factor (R_L) for the biosorbents were between 0 to 1, hence favouring the monolayer adsorption process. Regression (R^2) values for other isotherms viz. Freundlich and Dubinin-Radushkevich isotherm showed a low fit as compared to Langmuir adsorption isotherm. Freundlich isotherm model empirical parameter (n) values for all the adsorbents were greater than 1, thus favouring the biosorption phenomenon at all temperatures. Redlich-Peterson isotherm model presented relatively good regression (R^2>0.95) values, thus conforming to its accuracy in verifying Cr(VI) sorption by all the biosorbents. Values for g (Redlich-Peterson exponent) are approximately close to unity thus suggesting monolayer formation by Cr(VI) species over the adsorbent's surface as hypothesized by the Langmuir isotherm model (Gupta et al., 2002, Shahbeig et al., 2013).

2.2.7. Kinetic studies

Various kinetic models like pseudo-first-order, pseudo-second-order and intra-particle diffusion were studied to evaluate the involved mechanism for Cr(VI) species biosorption and the rate-limiting step in the mechanism. Table 2.4 presents the estimated parameters from the studied kinetic models and their regression values (R^2). The comparative

TH-3150_176106114

assessment showed low regression values for the pseudo-first-order model, and hence the acceptability of the model with the biosorption process by RAA, SAA and SAAC is low. Pseudo-second order kinetics showed high regression values (R^2>0.99), thus giving the best fit for Cr(VI) sorption by the biosorbents. Experimental adsorption capacities [q_e (expt.)] thus obtained were almost equal to the pseudo-second-order model theoretical adsorption capacity, as presented in table 2.4. Results thus obtained relate the rate-limiting step for Cr(VI) biosorption by RAA, SAA and SAAC and also confirm that the process is governed by chemisorption. Regression (R^2) values for the intraparticle diffusion model fitted the least, thus affirming intraparticle diffusion is not the only one to determine the rate of sorbate-sorbent interaction (Saleh et al., 2014). Fig. 2.4 shows the best fit for Cr(VI) biosorption by RAA, SAA and SAAC by pseudo-second-order kinetics.

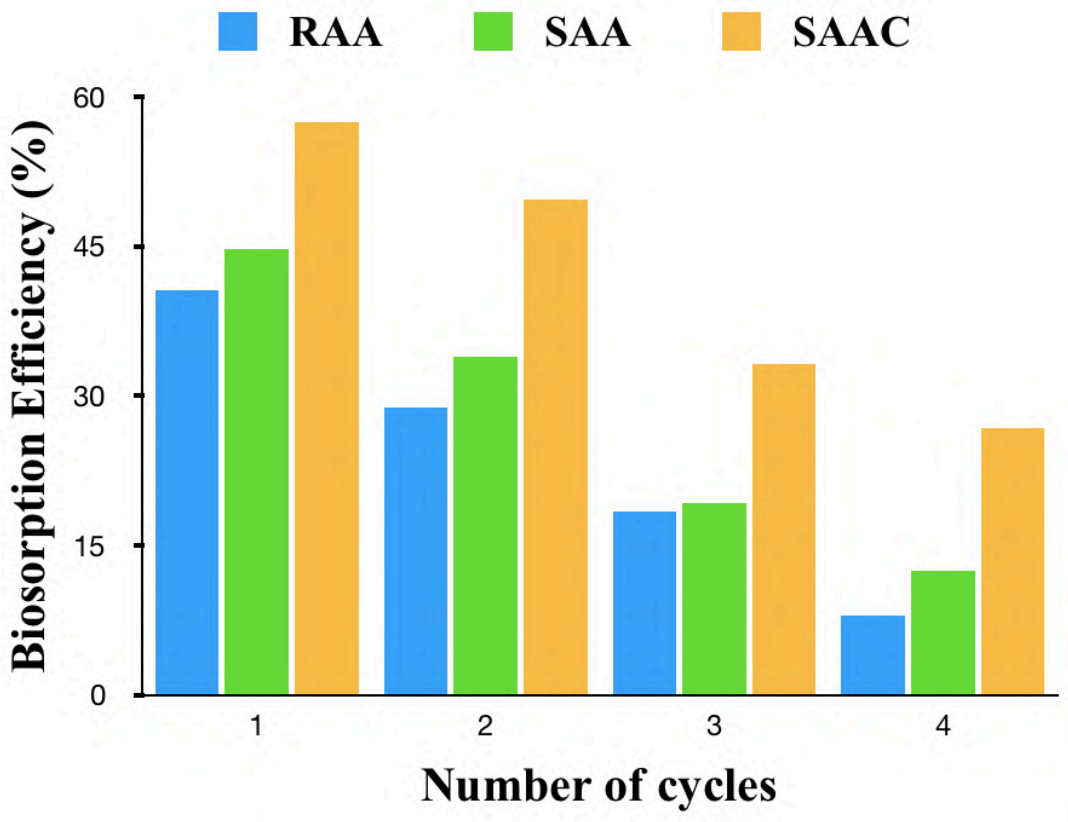

Fig. 2.5: Effect of desorption and re-adsorption of Cr(VI) by the biosorbents for 4 cycles

2.2.8. Recyclability analysis

To evaluate the reuse potential of the biosorbents (RAA, SAA, SAAC), the biosorbents had to undergo desorption after each biosorption process. 0.1 M NaOH was used as a suitable

TH-3150_176106114

desorbing agent and the biosorbents were desorbed for 4 continuous cycles after every cycle of adsorption. After 4 cycles the removal efficiency of the biosorbents was not very relevant. RAA showed a gradual decrement in Cr(VI) removal efficiency in the order; 40.65 %, 28.82%, 18.38% and 7.95%. Similarly, for SAA the Cr(VI) removal efficiency was in the order of 44.73%, 33.93%, 19.20% and 12.47%. In the case of SAAC, the removal efficiency was in the order 57.51%, 49.65%, 33.23% and 26.81%. Consecutive desorption, regeneration and biosorption studies revealed that RAA, SAA and SAAC are effectively reusable for up to some cycles (as illustrated in fig. 2.5). The possible reason for this decline with consecutive cycles may be due to morphological modifications of the biosorbent. Another possible reason could be the presence of some Cr(VI) molecule remnants on the biosorbent's surface and thus failed to desorb even after the desorption step. Such results of RAA, SAA and SAAC regeneration and reusability conclude that the studied biosorbents can be reused for limited series of sorption-desorption cycles. This is an essential characteristic owing to long-term use for Cr(VI) removal from wastewater (Mittal et al., 2010, Saravanan et al., 2013).

2.3. Significant findings

Acacia auriculiformis waste biomass was studied as a biosorbent in its raw (RAA), acid-activated (SAA) and complexed (SAAC) form. Biosorption efficiency for the raw biosorbent (RAA) elevated with acid-activation (SAA), which further increased after complexing with EDTA (SAAC). Experimental parameters viz. pH, incubation temperature, biosorbent dosage, and initial metal ion concentration influenced very much the adsorption efficiency for all the biosorbents in batch mode. The kinetics of sorbate-sorbent interactions can be represented by the pseudo-second-order model. Langmuir isotherm model showed the best fit for Cr(VI) biosorption by all the biosorbents. Thermodynamic studies reveal the biosorption process as spontaneous, favourable and endothermic with an elevated degree of disorderedness. The primary reason for the interaction between the metal ion and the biosorbent can be inferred due to be the electrostatic interaction between them. Desorption, regeneration and reuse of the biosorbents indicated its favourability for their reusability. Overall *Acacia auriculiformis* waste biomass and its different forms proved efficient in sequestration of Cr(VI) from industrial effluent with minimal expense.

TH-3150_176106114

Chapter 3
Facile preparation of nanocellulose embedded polypyrrole for dye removal: unary and binary process optimization and seed toxicity

The work embodied in this chapter is published in

TASRIN SHAHNAZ, Mohamed Madhar Fazil S, Senthilmurugan S and Selvaraju Narayanasamy*, Facile preparation of nanocellulose embedded polypyrrole composite for bromophenol blue and direct blue 6 removal: unary and binary process optimisation and seed toxicity, **International Journal of Environmental Science and Technology, 2020, (Springer, SCI IF: 3.519)**

TH-3150_176106114

Abstract

A fundamental understanding of cellulose fibre composite with tailor-made personalization has contributed to a diverse range of high-end engineering applications. In this study, nanocellulose was synthesised from cellulose via the top-down method and chemical polymerization of pyrrole to make nanocellulose embedded polypyrrole composite. This modification provides superior properties, enhanced functionality, and application in dye removal. This work may serve as an alternative to the conventional method for removing dye from industrial effluent providing an essential, fascinating field of cellulose-based nanocomposites application. The goal is to study the application of the composite for the removal of Direct Blue 6 and Bromophenol blue in a unary and binary system. The results show satisfactory removal of the dyes with 99.18, 96.32 and 98.77% for Direct blue, Bromophenol blue and binary system respectively. To provide evidence about the clarity of the effluent after treatment with the synthesized adsorbent, seed toxicity is performed where root length and % germination was used as key metric. The graphical abstract is shown in scheme 3.1.

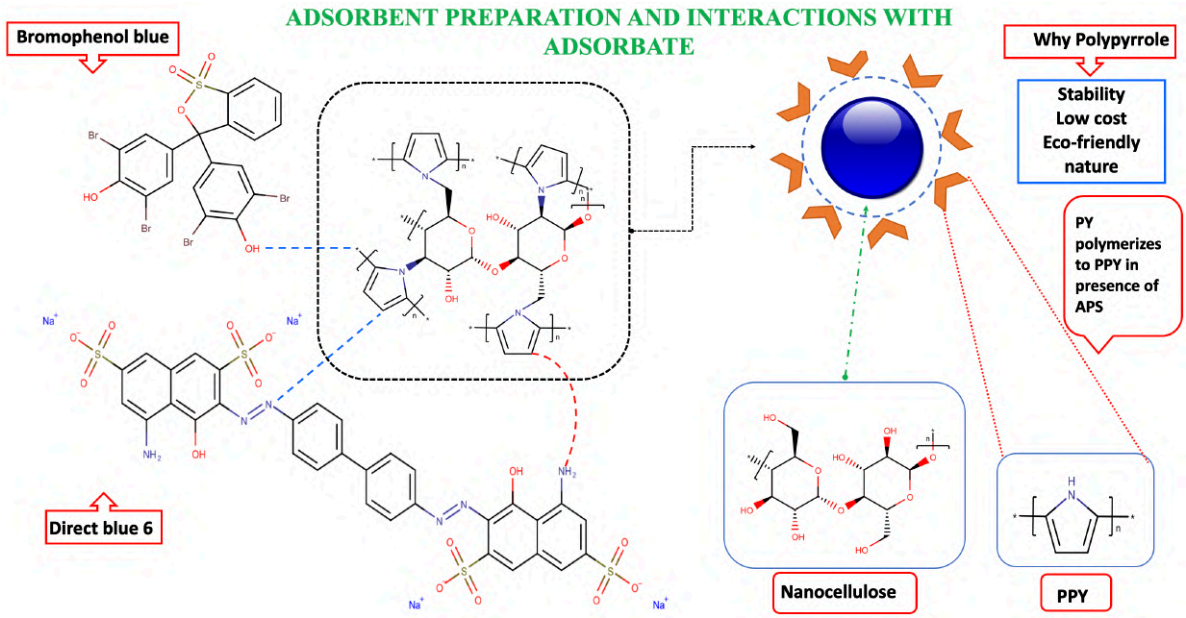

Scheme 3.1: Graphical abstract

TH-3150_176106114

3.1. Materials and methods

3.1.1. Chemicals

Analytical grade and high purity cellulose, direct blue 6, bromophenol blue, ammonium persulphate, pyrrole, sodium hydroxide were obtained from HiMedia and sulphuric acid and hydrochloric acid from Thermo-Fisher Scientific.

3.1.2. Sorbate specifications

The dye Bromophenol blue (BB) and Direct blue 6 (DB 6) were used in the experiments in the unary and binary system. They were supplied from Hi-Media with purity >95% as received.

3.1.3. Preparation of nanocellulose

20 g of cellulose powder was suspended in water to form a colloidal solution. 50-70 ml of 64% (w/v) sulphuric acid was added gradually and stirred vigorously for 30 min at 45 °C (Sharma et al. 2020). Sulphuric acid hydrolysis was quenched by adding ice-cold water. Obtained nanocellulose gel was washed and then centrifuged for 10 mins at 5000 rpm at room temperature. The cellulose nanocrystal suspension was dialyzed with cellulose dialysis membranes having 12,000-14,000 molecular weight cut off against deionized water until it reached neutral pH. The neutral pH suspension was sonicated in an ice bath for 45 mins (Lu and Hsieh 2012). The suspension in its original wet state was stored at a temperature of 4 °C.

3.1.4. Preparation of nanocellulose polypyrrole (NCPPY) composite

The nanocellulose suspension was sonicated for 40 minutes. In 25 ml of the suspension, 1.34 ml of pyrrole in 200 ml of distilled water was added and stirred. Slowly 0.15 M in 40 ml of ammonium persulphate (APS) was added to the solution and continued stirring. The colour changes from white to green, dark green and finally black with time as the polymerization of pyrrole to polypyrrole. The product was kept at 3 ^{0}C for some time and removed the upper layer. After keeping it at -80 ^{0}C it was lyophilized to get the NCPPY. To show a comparative study simultaneously 25 g of cellulose was taken and the same procedure was followed to obtain cellulose polypyrrole composite (CPPY).

3.1.5. Characterization

CPPY and NCPPY were characterized by FESEM images with before and after adsorption (Pramanik et al. 2019; Tan et al. 2019), FETEM, AFM, and functional groups were identified with FTIR spectra (Yang et al. 2018). Arrangement of the samples was determined by XRD,

TH-3150_176106114

Delsa Nano; to determine the surface charge, the results of characterization showed that NCPPY has a well-developed nanocellulose layer on the polypyrrole matrix containing abundant oxygen-containing functional groups such as hydroxyl and carboxyl groups. Thermal stability was checked with thermogravimetric analysis (Vakili et al. 2019).

3.1.6. Sorption experiments

The DB 6 and BB were estimated using an ultraviolet spectrophotometer (model: Tecan Infinite multimode plate reader, make: Switzerland) at the wavelength of 590 and 545 nm, respectively. In a binary mixture, the same method was applied which was feasible due to the difference in the absorption wavelength of the two dyes. All the experiments were performed thrice, and the average values were reported throughout the work (Ajmani et al. 2019).

3.1.7. Unary adsorption of dyes

Anionic dye DB 6 and BB were used as the model pollutant for the adsorption experiments. The effect of the initial pH varied from 2 to 9 with 5 mgL^{-1} of adsorbent (NCPPY) and with an initial concentration of 10-500 mgL^{-1} through 25-55 °C with a 5 °C increase was examined. The solution pH was set as required using 1 M HCl or NaOH. The effect of temperature from 25-55 °C on dye removal was investigated using 20 mL of dye solution with the optimal conditions found in the previous experiment and the same initial dye concentration. For studying the effect of contact time, optimal initial pH and temperature were used with initial concentrations of 40 mgL^{-1} for both DB 6 and BB. Adsorption isotherm experiments were conducted under optimal conditions of dye solutions with varying initial dye concentrations from 10-500 mgL^{-1}. The system was shaken at 140 rpm for 3 h to as the equilibrium reached for that time. The adsorption capacity of the adsorbent (q_e, mgg^{-1}) and removal percentage (R %) were calculated as follows:

$$q_{\mathrm{e}} = \frac{C_0 - C_{\mathrm{e}} \times V}{m} \tag{3.1}$$

$$R\% = \frac{(C_0 - C_{\mathrm{e}})}{C_0} \times 100\% \tag{3.2}$$

TH-3150_176106114

where C_0 (mgL^{-1}) is the initial concentration and C_e (mgL^{-1}) is the equilibrium concentration of the dye. V is the volume of the solution and m is the mass of the adsorbent used (g) (Elgarahy et al. 2019; Elwakeel et al. 2016; Elwakeel 2009).

3.1.8. Competitive adsorption of dyes in the binary system

The adsorption capacity has also been checked in the binary system to evaluate their behaviour in a more complex system. The adsorption towards DB 6/BB in binary systems with a 1:1 ratio was carried out using 10 mg of NCPPY at the initial pH 3 in 10 mgL^{-1} solution. After 3 h of shaker incubation at 40 °C, the final concentration was measured and took the average reading was after repeating the experiments thrice. The absorbance additive principle has been used to detect the individual dye concentration for a binary system of components p and q as follows (Liu et al. 2015):

$$W_{\lambda 1p,q} = \varepsilon_{\lambda 1p} l C_p + \varepsilon_{\lambda 1p} l C_q \quad (3.3)$$

$$W_{\lambda 2p,q} = \varepsilon_{\lambda 2p} l C_p + \varepsilon_{\lambda 2p} l C_q \quad (3.4)$$

where $W_{\lambda 1p,q}$ and $W_{\lambda 2p,q}$ are the total absorbance of the mixture solution at 590 and 545 nm, for DB 6 and BB, respectively, and l is the thickness of the well in the 96 well plates. The molar absorption coefficients $\varepsilon_{\lambda 1p}$, $\varepsilon_{\lambda 1q}$, $\varepsilon_{\lambda 2p}$ and $\varepsilon_{\lambda 2q}$, and C_p and C_q are the equilibrium concentrations of DB 6 and BB.

3.1.9. Toxicological tests and effect of NCPPY on *Vigna mungo*

Seed germination study is a method for the environmental toxicity evaluation of pollutants. This assay is based on US EPA 1996 guidelines considering seed germination rate and plant growth with few modifications (Ecological Effects Test Guidelines, OPPTS 850.4025, Target Area Phytotoxicity). Test concentration of two unary and one binary mixture was 10 and 40 mgL^{-1}, and their toxic effect on physiological characteristics of *Vigna mungo* seed was evaluated. Organic *V. Mungo* seeds were purchased from a local market. High germination rate and long shelf life are two key measures of a good phytotoxicity test, so the higher the germination in control water, the less the error in the test sample (Haq and Raj 2018; Dhaouuefi et al., 2019, Wang et al., 2022). The selected seeds were washed properly with

TH-3150_176106114

distilled water, and ten seeds were spread evenly on 7.5 cm diameter Petri plates with 25 mL of 10 mgL^{-1} and 40 mgL^{-1} for each unary and binary mixture. The role of NCPPY in decreasing the dye toxicity was evaluated with 12 treatment groups as follows: Blank (DI water), BB, DB 6, binary (10 mgL^{-1} dye), BB, DB 6 (40 mgL^{-1} dye), BB, DB 6 (10 mgL^{-1} dye + NCPPY), BB, DB 6 (40 mgL^{-1} dye + NCPPY). The Petri plates were kept in dark conditions for four days and then placed indoors one day with the irradiance of natural light. After 4 days of conditioning, seed germination (%) and root length were measured. The germination rate was determined using the formula as follows (3.5) (Nagia and El-Mohamedy 2007; Wang 1985).

$$\%G = \left(\text{Number of germinated seed} / \text{Total seed used}\right) * 100 \quad (3.5)$$

3.1.10. Recyclability studies

Recyclability studies is an important parameter and are performed to check the repeated use of the adsorbent and its efficiency after several cycles. After the very use, the adsorption capacity decreases due to the saturation of the adsorbent surface, thereby making the process not so cost-effective for the long run. Also, this requires a continuous supply of the adsorbent; therefore, to analyse the absorbent it is a must in commercializing a novel adsorbent. Mostly 0.1 N NaOH (sodium hydroxide) solution is used as the desorbing agent. NCPPY was desorbed with 0.1 N NaOH for regaining the sorbent surface for further adsorption. After that, it was rinsed thoroughly with distilled water to remove residual NaOH and used for 3 cycles after the first adsorption. The desorption efficiency was determined with the following equation 3.6,

$$\%\ \text{Desorption} = \frac{C_{de} * 100}{C_{ad}} \quad (3.6)$$

C_{de} and C_{ad} are the dye concentration during desorption and after adsorption, respectively, for time "*t*" (mgL^{-1}).

TH-3150_176106114

3.2. Results and Discussion

3.2.1. FESEM analyses

CPPY, NCPPY and adsorption of NCPPY with Bromophenol Blue, Direct Blue and Binary mixture of the two dyes were analyzed with Field Emission Scanning Electron Microscopy (Make: Zeiss, Model: Sigma 300). The raw CPPY (Fig 3.1a) exhibits a sheet-like, nonuniform appearance and was measured in the range of micrometers whereas the sulphuric acid-treated NCPPY (Fig 3.1b) was observed with a spherical, uniform and homogenous appearance and less than 100 nm. The reduction to the nano range of cellulose due to acid hydrolysis yielded increased surface area and greater exposure to functional groups. The nano cellulose helps to acquire more dye molecules for the greater adsorption of pollutants as compared to cellulose. It is confirmed by analyzing the FESEM images of NCPPY with BB (Fig 3.1c), DB 6 (Fig 3.1d) and a binary mixture of BB and DB 6 (Fig 3.1e).

3.2.2. FETEM analyses

Fig 3.1f shows the FETEM (Model: JEOL, JEM-2100, Make: Japan) transmission micrograph of NCPPY which was prepared on a copper grid by drop-casting a dilute sample. The nanocellulose spheres are separated in some places while in some other places they are agglomerated. The majority of the particle size lies in the nano range with a uniform distribution. The average dimension of a nanocellulose sphere has been indicated as 40-50 nm as shown in Fig 3.1i.

3.2.3. AFM analyses

The surface morphology and topography of CPPY and NCPPY were analyzed with an Atomic Force Microscope (AFM) (Make: Oxford Model: Cypher). On a clean silica surface, the sample was drop cast and dried overnight at room temperature. The AFM image of the CPPY and NCPPY was shown in fig 3.1g and 1h. The height and phase images of the CPPY (Fig 3.1g) and NCPPY (Fig 3.1h) which was taken over a 14.5 µm×14.5 µm and 5µm×5 µm area respectively. The bright contrast dots represent on the left and right images represent cellulose and nanocellulose which are embedded in the polypyrrole matrix. The amplitude and phase images showed the cellulose size after hydrolysis with acid i.e. nanocellulose and polypyrrole polymerization are less than 10 nm whereas cellulose particle was in the range of 2 µm. The roughness data of cellulose and nanocellulose was determined using software named “Gwydion”. For CPPY the root means square roughness average (RMS-Ra) was

TH-3150_176106114

found to be 10.06 nm whereas, for NCPPY, this data was found to be 1.318 nm which verifies the successful conversion of the cellulose to nanocellulose particle of the desired size range.

3.2.4. XRD analyses

Fig 3.2a. showed the X-ray diffraction pattern of native cellulose, polypyrrole, CPPY, and NCPPY. Three major peaks (2Θ = 22.82, 16.43, 34.03) were observed from raw cellulose powder.

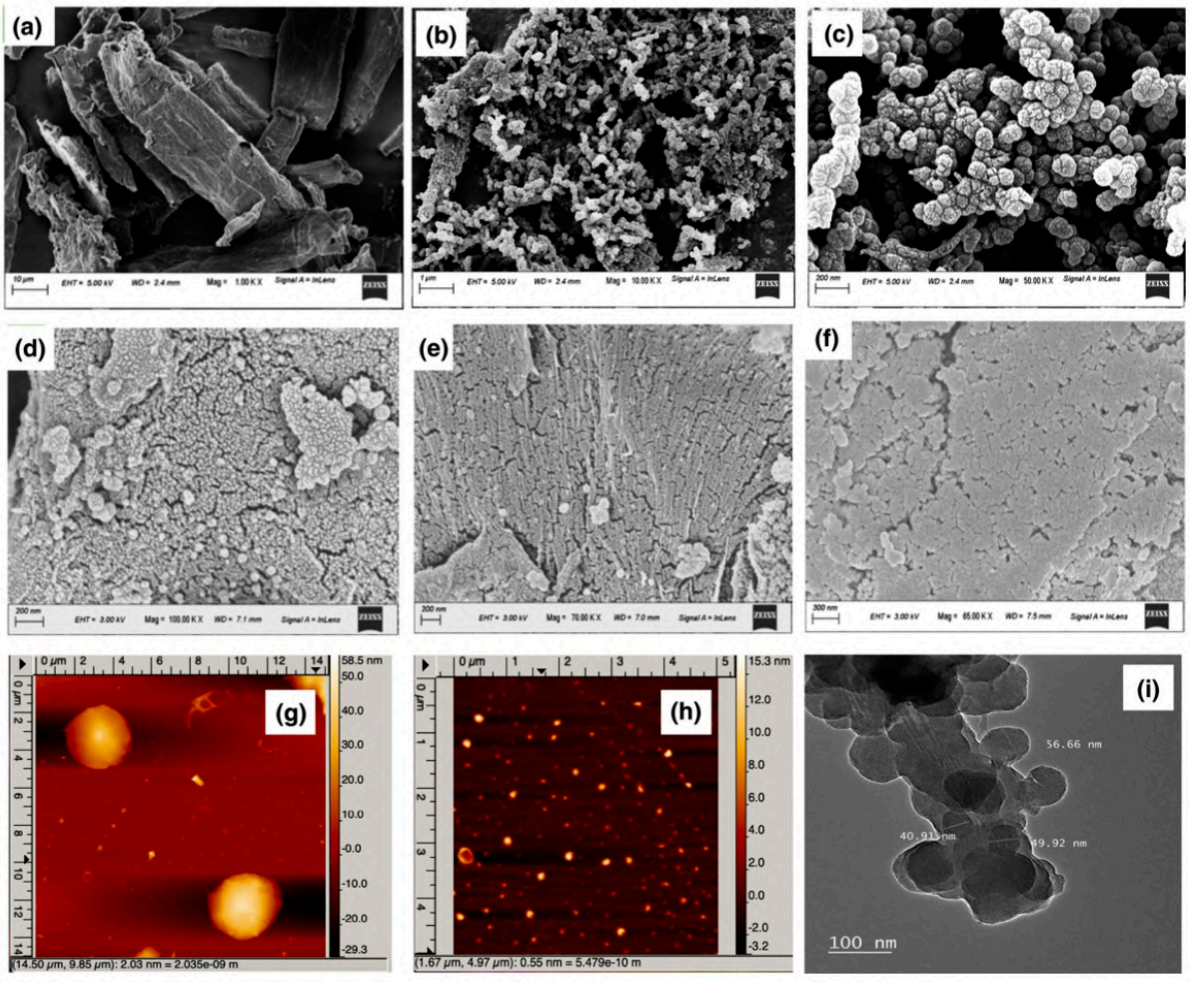

Fig. 3.1: FESEM images of CPPY (a), NCPPY (b), NCPPY (high resolution, 50kX) (c), NCPPY-DB 6 (d), NCPPY-BB (e), NCPPY-binary (f), AFM image of CPPY (g), AFM image of NCPPY (h), FETEM image of NCPPY. Most of the particles lie within the size range of 10-30 nm and <1 nm for CPPY and NCPPY respectively

The CPPY diffractogram pattern was slightly different at an angle of 21 ^{0} (2Θ) from the native cellulose as a small peak appears for polypyrrole confirmed from the polypyrrole diffractogram (Yue et al. 2019). NCPPY almost overlaps with the CPPY. It was also observed

TH-3150_176106114

that the ordered crystalline structure of the cellulose was not disrupted by sulphuric acid hydrolysis (Zhou et al. 2013). In fig 3.2a, a distinct peak was observed at 2Θ = 22 ^{0} which was due to the presence of polypyrrole as confirmed by the result of the pure polypyrrole diffractogram showing the amorphous nature of the sample (Ryan et al. 2018). From the XRD analysis, the crystallinity index of the composite was determined which is a quantitative indicator of the crystalline nature of the sample. This is a hypothesis by Hermans and Weidinger (Gusev 1978) states that diffraction from crystalline and amorphous materials is additive. The composite sample is found to be semi-crystalline in nature.

3.2.5. Thermo Gravimetric analysis

The thermal stability of NCPPY was analyzed at the heating range up to 600 °C with a temperature of 20 °C/10 min in an argon gas atmosphere with a High-Temperature Differential Scanning Calorimetry (DSC)/Thermo Gravimetric (TG) System (Make: Netzsch, Model: STA449F3A00). This Analysis of Nanocellulose polypyrrole was shown in fig 3.2c. The thermal stability of the raw PPY (Fig 3.2b) sample was checked and found that nearly 8% weight loss around 100 °C was due to evaporation of residual water. Whereas for NCPPY, small weight loss (3% wt) was found in the range of 50-200 °C due to the evaporation of water content in the sample. The sharp peak was observed at 225 °C due to the thermal decomposition of the pyrolysis of nanocellulose. Around 250-350 °C, the minor weight loss is due to cellulose and polypyrrole degradation for NCPPY. Introducing polypyrrole into the system enhanced the thermal stability of the composite (ElNahrawy et al. 2017). Above 225 °C, the decomposition of organic matter was initiated up to 600 °C where the complete decomposition happened (52% wt).

3.2.6. The parameters affecting dye adsorption

3.2.6.1. Effect of initial pH

In an efficient adsorption process effect of initial pH plays a very crucial role by altering the degree of ionization of adsorbate and the surface properties of the adsorbent. The effect of initial pH was checked in the range of 2 to 9 with an initial dye concentration of 10 mgL^{-1} for a period of three hours at 35 ^{0}C. The result was graphed as % removal versus initial pH as shown in Fig 3.3a. For BB after initial pH 4, there is a consistent result of more than 75% removal while for DB 6, apart from initial pH 2 at all the pH range removal % was found to be in the range 40-50 %. No considerable variation was observed over the pH range of 2-6 for

TH-3150_176106114

binary mixture and then a slight decrease over initial pH 7 occurred though it is significantly high with a value of 81%. For further studies, the pH of BB, DB 6 and binary dye effluent was adjusted at initial pH 9, 7 and 3 respectively as their best pH evaluated.

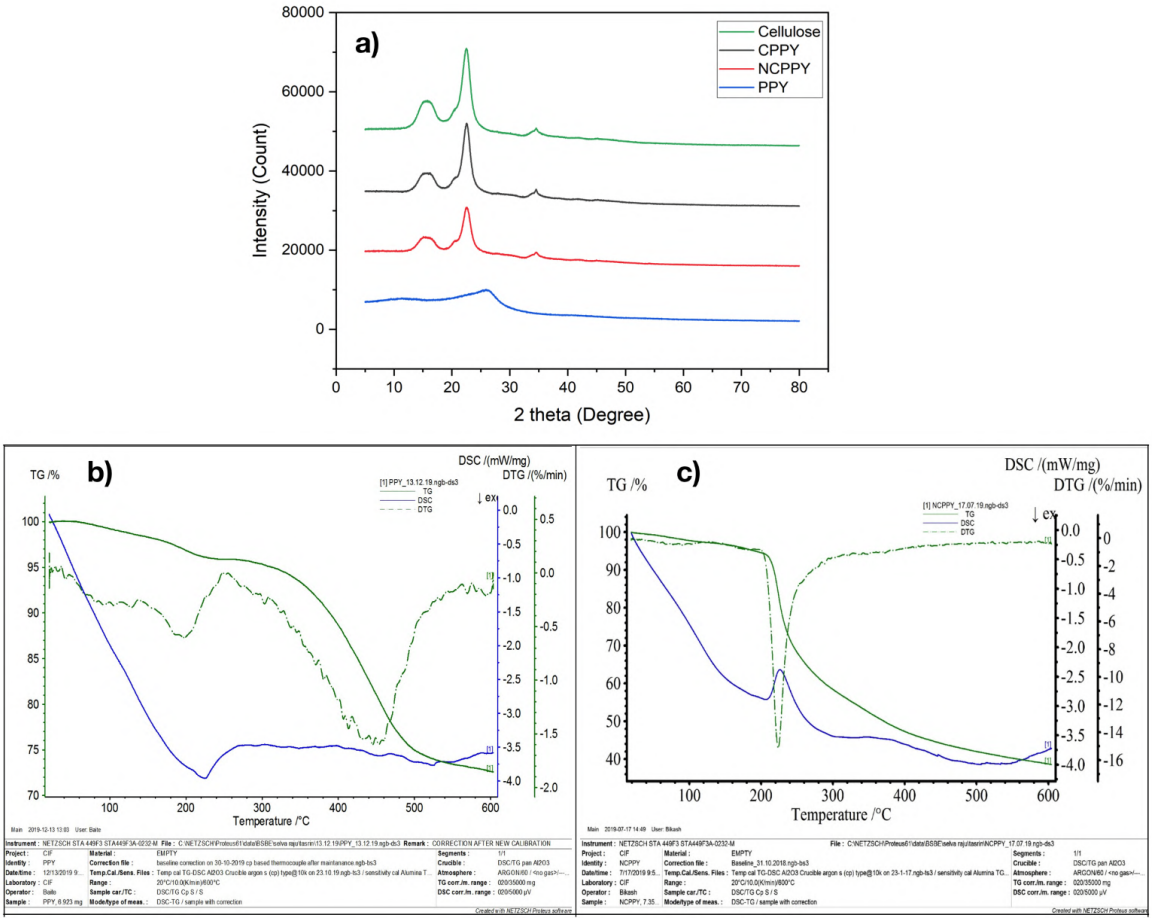

Fig. 3.2. XRD plot of Cellulose, CPPY, NCPPY and PPY (a), TGA of PPY (b), TGA of NCPPY (c) respectively

3.2.6.2. Effect of dosage

To investigate the adsorbent capacity of NCPPY adsorbent dosage was varied from 1 to 10 mg at a concentration of 10 mgL^{-1} and experiments were carried out at 45 ^0C under the best condition for each set of dye in the unary and binary system for 3 hours and the results were shown in Fig 3.3b. The removal efficiency initially increased from 36% to 86.32% for BB and 64.38%-89.67% for DB 6 with an increase in adsorbent dosage from 1 to 7 and 1 to 5 mg respectively. For the binary mixture, with an increase in dosage from 1 to 2 mg the removal % increased very fast from 67.95% to 96.53% and then maintained throughout other dosages with very good removal %. This can be due to increased adsorption surface area and

TH-3150_176106114

availability of active adsorption sites on the adsorbent. Whereas a decrease in removal efficiency was observed over 7 mg per 10 mL for BB and binary that may be attributed to the overcrowding of adsorbate molecules that prevented the diffusion through the actual adsorption sites. The maximum removal efficiency of 86.32% for BB, 89.67% for DB 6 and 97.95% for binary was achieved.

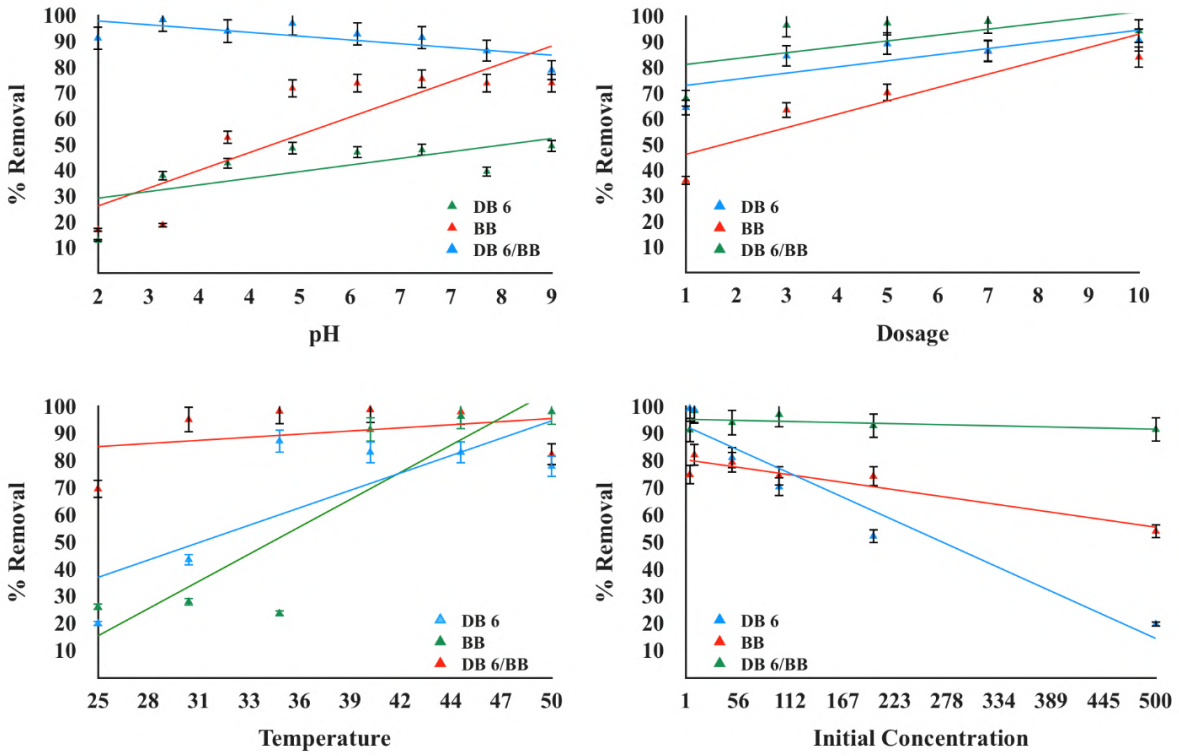

Fig. 3.3: Removal % against pH (a), dosage (b), temperature (c) and initial concentration (d) for DB 6, BB and binary (10 mgL^{-1} of initial concentration, 323 K, pH 9 and 7, dosage 7 and 5 mg for BB and DB 6)

3.2.6.3. Effect of temperature and thermodynamics

Effect of temperature and the thermodynamic study was performed for the simulated solution of BB and DB 6 by NCPPY using 10 mgL^{-1} of initial concentration under optimum conditions for the respective dyes. The results have been shown in Fig 3.3c, where the adsorption capacity of BB increased from 7.24 to 20.98 mgg^{-1} with an increasing temperature from 298 to 323 K. Similarly, the amount of DB 6 adsorbed increased from 4.57 to 20.11 mgg^{-1} as the temperature increased from 298 to 323 K which can be attributed to the expansion of NCPPY composite at elevated temperature. This may be explained as the

TH-3150_176106114

enhanced hydrophobic interactions between alkyl groups of nanocellulose and BB and DB 6 molecules. At relatively high temperatures the mobility of the dye molecules increases with a decrease in solution viscosity (Elgarahy et al. 2019; Elwakeel et al. 2012; Shahnaz et al. 2020; Yakout et al. 2019). Thermodynamic parameters were summarized in Table 3.1. The negative values of ΔG° (Gibbs free energy), suggest that the adsorption process of both the dyes is spontaneous and favourable (Abd El-Ghaffar et al. 2009). The enthalpy calculation suggests the process to be endothermic with a positive value for BB and DB 6. Entropy change, ΔS° confirms the increased randomness with a value of 60.99 and 304.85 $KJmol^{-1}K^{-1}$ for BB and DB 6 respectively at the NCPPY interface. Also, the positive value of entropy for both the dyes implies that an increase in temperature promotes dye adsorption by removing water molecules from the NCPPY surface (Elwakeel 2010) and the feasibility of the process.

Table 3.1 : Thermodynamics parameters for BB and DB 6 on NCPPY (10 mgL^{-1} of initial concentration, pH 9 and 7, dosage 7 and 5 mg for BB and DB 6 respectively)

Dye	T	ΔG^0	ΔH^0	ΔS^0
BB	298	-6.25	13.82	60.99
	303	-1.84		
	308	-2.18		
	313	-7.96		
	318	-10.47		
	323	-1.97		
DB 6	298	-2.50	86.77	304.85
	303	-1.51		
	308	-11.9		
	313	-13.23		
	318	-12.06		
	323	-5.97		

3.2.6.4. Effect of contact time

Contact time is a very important parameter for understanding the kinetics of the adsorption system. Experimental results agreed with pseudo-second-order indicating the process to be chemically dominating and valence forces were involved through electron sharing between NCPPY and dye molecule. As shown in Table 3.2, the maximum adsorption capacity matches

TH-3150_176106114

the experimental data with an R^2 value of 0.999 and 0.9986 for DB 6 and BB respectively. The initial sorption rate was found to be 4.36 and 0.27 for DB 6 and BB respectively.

Table 3.2: Kinetic parameters with PFO, PSO, Elovich and Intraparticle diffusion model (10 mg/L of initial concentration, 323 K, pH 9 and 7, dosage 7 and 5 mg for BB and DB 6 respectively)

Kinetic model	Parameters	Direct Blue	Bromophenol Blue
Pseudo first order	q_e (exp)	6.64	6.04
	q_e	0.18	0.79
	K_1	0.01	0.009
	R^2	0.42	0.356
Pseudo second order	q_e	6.54	6.16
	K	9.81	0.007
	h	4.36	0.27
	R^2	0.99	0.998
Intraparticle diffusion	KID	0.10	0.04
	C	5.21	5.47
	R^2	0.59	0.50
Elovich	β	4.10	5.98
	α	$5.32*10^8$	$5.82*10^{12}$
	R^2	0.822	0.465

3.2.7. Adsorption isotherms in single systems

The effect of initial concentration for unary and binary with removal efficiency is plotted in Fig 3.3d. The maximum adsorption capacities of the adsorbent for the studied dyes were analyzed with the experimental data for the single system to find the best-fitted isotherm model. In Table 3.3, the isotherm additional information has been summarised where Halsey isotherm best fitted with R^2 value exactly 1.

3.2.8. Discussion on the adsorption mechanism

This work follows pseudo-second-order kinetics indicating the adsorption process to be dominated by chemisorption as in the rate-controlling step, the chemical reaction seems significant (Donia et al. 2008; Elwakeel et al. 2009; Shahnaz et al. 2020). Also for isotherm, Halsey provided the best correlation with the experimental data and the adsorption mechanism where the adsorption was found to be multilayer on the heterogeneous surface. The Freundlich isotherm constant 1/n was found between 0 to 1 showing reaction is desirable

TH-3150_176106114

(Elwakeel et al. 2013). Since Langmuir Isotherm was not agreed with the experimental data it interpreted that there is proper interaction between the adsorbed molecules. The thermodynamics data are well agreed with the process to be spontaneous, feasible and endothermic. The increase in the removal efficiency of the binary system could be due to the multilayer adsorption on the resultant affinity of adsorption sites on NCPPY which is known as cooperative adsorption. A combination of dyes in the mixture had the increased affinity of the adsorbent for the dye adsorption possibly by altering the overall surface charge or by a change in orientation of the adsorbed molecules. Another probable reason could be the formation of adsorption sites on NCPPY, which is explained as molecular wedging effects. Besides, it can be interpreted that the adsorbent has important potential for efficient removal of both dyes in unary and binary systems, especially in waste containing DB 6 and BB.

Table 3.3: Isotherm parameters for the adsorption of DB 6 and BB on the NCPPY surface (1-500 mgL^{-1} of initial concentration, 323 K, pH 9 and 7, dosage 7 and 5 mg for BB and DB 6 respectively)

Model	Constant	BB	DB 6
Langmuir	q_m	17.02	17.38
	K	0.145	0.121
	R_2	0.693	0.636
Freundlich	K_f	1.38	1.74
	n	1.331	1.344
	R_2	0.849	0.924
Halsey	n_H	1	1
	K_H	88.49	79.99
	R_2	1	1

3.2.9. Seed germination rate and root length measurement

The germination rate and root length of *Vigna mungo* were measured on the 4th day according to the method of Wang et al (Wang 1985). All the experimental data were presented as mean ± SD after performing in triplicates as shown in Table 3.4. The seed germination in blank was 100 % whereas at 40 mgL^{-1} of different dye control samples was found to be 20-30% only showing a high level of the toxicity of the dye to the *V. mungo* seeds. Though less germination was observed at 10 mgL^{-1} it was comparatively higher than 40 mgL^{-1} with

TH-3150_176106114

50-70%. However, the dye solution after NCPPY treatment at 10 mgL^{-1} showed 60-90% and at 40 mgL^{-1}, 50-80% germination rate as compared to the control. The root length of the seed in the blank system was found to be highest with 9.11 ±0.02 cm on average. The control system with 10 mgL^{-1} was 4.6-5.1 cm and 40 mgL^{-1} was distinctly less with 1.1-2.8 cm only for all the test groups. After the treatment, the BB gave good results with an average root length of 9.35 cm whereas DB 6 and binary also measured 8.2 and 7.1 cm respectively. In a higher concentration, the result was found to be 2.9, 2.6 and 2.2 for BB, DB 6 and binary respectively. This seed toxicity provided measures to get evidence of the efficiency of the treated effluent. Thereby can be concluded that NCPPY could be an alternative to the most expensive wastewater treatment methods.

Table 3.4: Phytotoxicity analysis of dye solution and residual dye using germination of *Vigna Mungo* seeds (25 ^{0}C, 4 days, 25 ml adsorbate)

	Conc. (mgL^{-1})	Treatment	Radicle (cm)	Seed germination (%)
Blank			9.11 ± 0.02	100
Control	10	BB	4.95 ± 0.04	60
		DB 6	5.1 ± 0.16	70
		DB 6/BB	4.6 ± 0.57	50
	40	BB	2.83 ± 1.31	30
		DB 6	2.1 ± 0.94	20
		DB 6/BB	1.1 ± 0.49	30
Effluent	10	BB	9.35 ± 0.20	60
		DB 6	8.2 ± 0.24	80
		DB 6/BB	7.1 ± 0.12	90
	40	BB	2.9 ± 0.95	80
		DB 6	2.66 ± 1.17	70
		DB 6/BB	2.23 ± 0.89	50

3.2.10. Recyclability analysis

NCPPY was desorbed with 0.1 M NaOH after every cycle and for 3 continuous cycles after every cycle of adsorption. The removal efficiency after the first cycle was 84.6, 81.2 and 65 % for BB. Whereas for DB 6, the gradual decrease was seen as 78, 63 and 48.1 %. However, the binary mixture showed a removal efficiency of 77 % after the first cycle which decreased

TH-3150_176106114

to 58 and 31 %. After 3 cycles, the removal efficiency of the adsorbents was not very significant. These consecutive desorption, regeneration and adsorption studies revealed that NCPPY is effectively reusable for up to some cycles (as shown in fig. 3.4). After desorption, the probability of dye molecule presence on the surface limits this phenomenon. The morphological change of NCPPY and saturation of the active adsorbent site could be the possible reason for the gradual decrease of dye removal capacity. Therefore it can be concluded from the regeneration studies that the present adsorbent can be effectively reused for a series of sorption-desorption cycles.

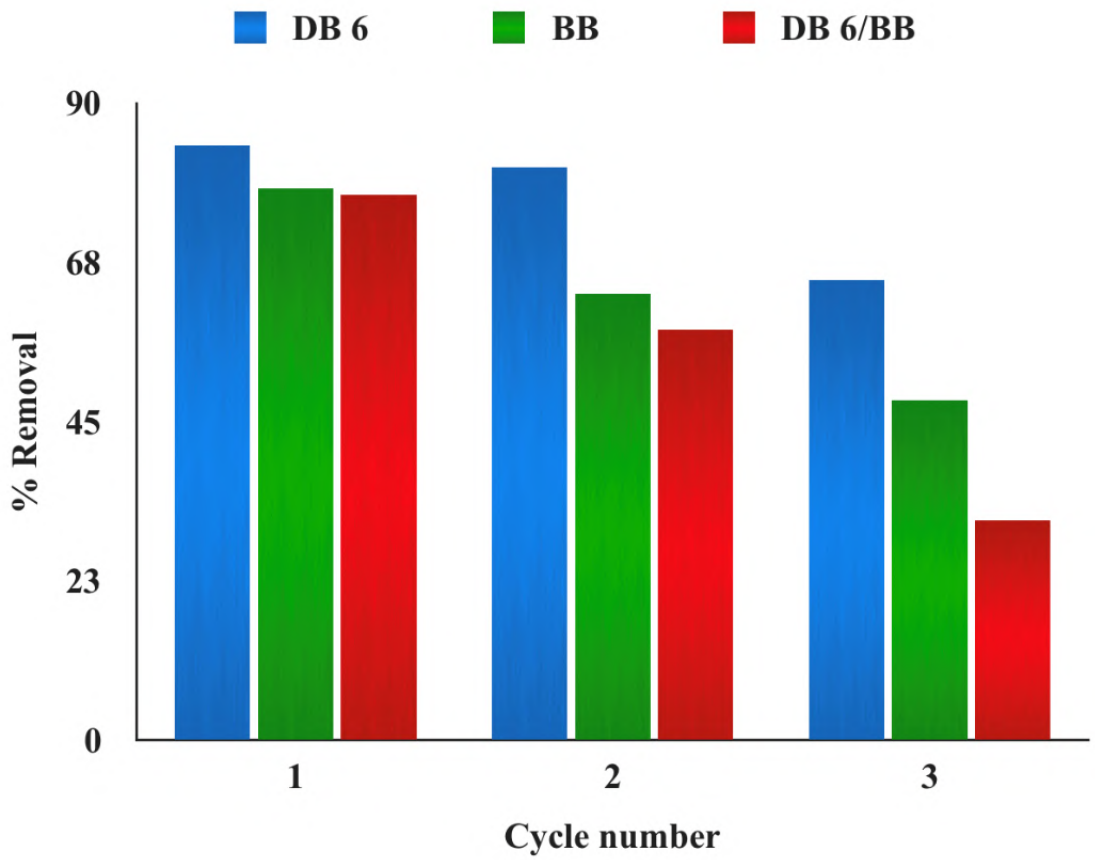

Fig. 3.4: Desorption study for BB and DB 6 using NCPPY(500 mgL^{-1} of initial concentration, 323 K, pH 9, 7 and 3, dosage 5, 7 and 5 for the reaction volume of 20 mL for BB, DB 6 and binary mixture respectively)

3.3 Significant findings

In this study, the synthesis of nanocellulose polypyrrole composite by chemical polymerization of pyrrole coating on the nanocellulose spheres is reported. This incorporation has greatly enhanced the adsorption of the studied dyes viz. BB and DB 6 on the adsorbent in

TH-3150_176106114

both single and binary systems. Moreover, this method demonstrated that it was possible to produce a nanocellulose-based adsorbent that was more efficient than the raw cellulose, allowing an improved adsorption capacity which follows pseudo-second-order and Halsey isotherm was best agreed. Furthermore, the biodegradable character could also reduce solid sludge production in a water treatment plant and this new nanocellulose polypyrrole adsorbent appears as an interesting alternative to the classic treatment used. The use of seed to analyse the biosorbent practical capability provides evidence about the clarity of the effluent in a real scenario. Further studies would be performed for the removal of actual textile effluent with a mixture of toxic dyes to evaluate the efficiency of the adsorbent.

TH-3150_176106114

Chapter 4

Surface modification of nanocellulose using polypyrrole for the adsorptive removal of Congo red dye and Chromium in binary mixture

The work embodied in this chapter is published in

TASRIN SHAHNAZ, Mohamed Madhar Fazil S, Padmanaban V C, and Selvaraju Narayanasamy*, Surface Modification of Nanocellulose Using Polypyrrole for the Adsorptive Removal of Congo red Dye and Chromium in Aqueous Binary Mixture: Studies on Composite Characterisation and Process Kinetics, **International Journal of Biological Macromolecules, 2020, (Elsevier, SCI IF: 8.025)**

Abstract:

In this study, nanocellulose was synthesised by acid hydrolysis of cellulose and was coupled with a polypyrrole supporting matrix. The synthesised nanocellulose polypyrrole composite (NCPPY) was characterised by FESEM, XRD, FTIR, BET, and TGA/DSC. These analyses showed the conversion of cellulose to a nano-sized crystalline structure with excellent thermal stability and higher surface area. The effect of different parameters like pH, temperature, contact time, adsorbent dosage and initial concentration of chromium (Cr(VI)) and Congo Red (CR) were optimised in batch mode. Response Surface Methodology (RSM) has been employed as an optimization tool for the efficient removal of Cr(VI) and CR and the maximum removal efficiency was found to be 80% and 85% respectively. The Langmuir and Freundlich isotherm well fitted the equilibrium data for CR and Cr(VI) respectively. Thermodynamic data showed that the adsorption of Cr(VI) and CR on NCPPY is an endothermic, spontaneous, and entropy-driven process. The adsorption kinetic followed pseudo-second-order for Cr(VI) and intraparticle diffusion for CR. The effect of co-existing ions was checked using several common salts and heavy metals. Results indicated that NCPPY has great potential to remove Cr(VI) and CR binary mixture under simulated conditions.

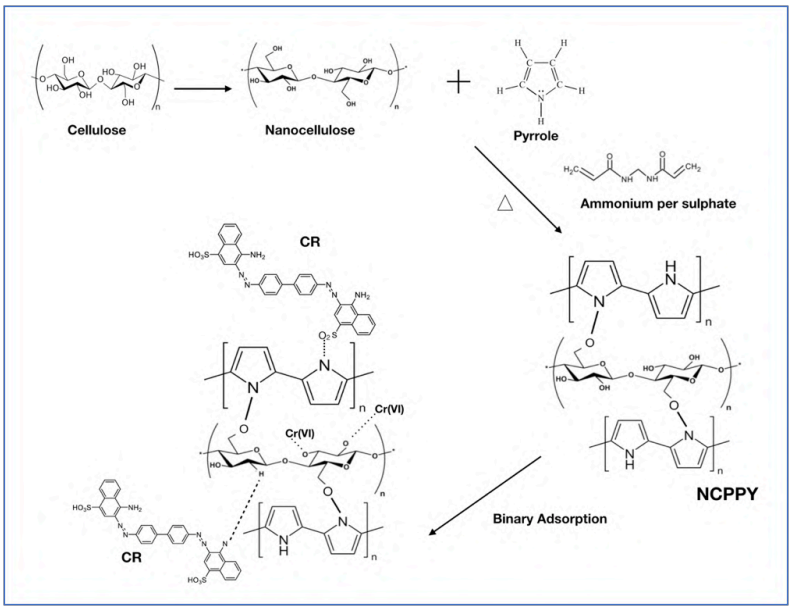

Scheme 4.1 Mechanism for synthesis of NCPPY and CR and Cr(VI) adsorption on it

4.1. Materials and Methods

4.1.1 Materials

Congo red (HiMedia, CAS no.: 573-58-0) (azo dye with molecular formula- $C_{32}H_{22}N_6Na_2O_6S_2$, molecular weight 696.7 g.mol^{-1}, λ_{max}= 495 nm (red colour at basic pH), 565 nm (blue colour at acidic pH)) and potassium dichromate (HiMedia, CAS no.: 7778-5-9) (molecular formula: $K_2Cr_2O_7$, molecular weight 294.18 gmol^{-1}) were used as adsorbate. Cellulose (CAS no.: 9004-34-6) and pyrrole (CAS no.: 109-97-7) used in the adsorbent were purchased from HiMedia and Avra respectively. The pH of the mixtures was adjusted using sodium hydroxide (HiMedia, CAS no.: 1310-73-2), hydrochloric acid (SRL, CAS no.: 7647-01-0) and sulphuric acid (HiMedia, CAS no.: 7664-93-9). Another chemical used in this study is Ammonium persulphate procured from HiMedia (CAS no.: 7727-54-0).

4.1.2 Preparation of the Nanocellulose (NC)

20 g of cellulose powder was suspended in water to form a colloidal solution. Cellulose nanocrystal was obtained by treating the colloidal suspension of cellulose with 65% sulphuric acid at 40 °C under stirring conditions for 3 hours. The hydrolysis reaction was followed by centrifugation at 8000 rpm for 10 mins. To remove excess acid, the obtained suspension was dialyzed against deionized water with the help of a dialysis membrane having a molecular weight cut off of 12000-14000. The resultant suspension was further subjected to ultra-sonication for 45 mins in an ice bath (Lu et al., 2012).

4.1.3 Preparation of Nanocellulose-Polypyrrole composite

0.67% (v/v) of pyrrole was used for the synthesis of the NCPPY composite. The conversion of pyrrole to polypyrrole is facilitated by the addition of 0.15M ammonium persulphate under stirring conditions. The polymerisation of pyrrole to polypyrrole is observed by the change in colour from white to green and then finally to black. The sonicated cellulose nanocrystal suspension was mixed with PPY and kept at 3°C for 30 mins and the top layer is removed from the solution. The NCCPY composite powder was obtained by lyophilisation and was stored at room temperature.

4.1.4. Characterization

The structure of sulphuric acid hydrolyzed NCPPY composite was analyzed by Field Emission Scanning Microscopy (Zeiss, Sigma 300). The surface area was analyzed using a BET analyzer (Quantachrome, Autosorb-IQ MP). Functional groups were studied with

Fourier transform infrared (FTIR) spectroscopy (PerkinElmer, USA). The crystallinity of the NCPPY composite was analyzed by an X-ray diffractometer (Rigaku, Micromax-007HF). The thermal stability of NCPPY was analyzed at the heating range up to 600 °C with a temperature of 20 °C/10 min in an argon gas atmosphere with a high-temperature Differential Scanning Calorimetry (DSC)/Thermo Gravimetric (TG) System (Netzsch, STA449F3A00).

4.1.5. Polynomial equation-based modelling using response surface methodology

The removal of CR and Cr(VI) was studied with Central Composite Design (CCD) based modelling using Design-Expert(11) using a four-factor CCD model with CR concentration (A), Cr(VI) concentration (B), the dosage of NCPPY (C), temperature (D) as variable parameters. A total of 30 runs of experiments were carried out to acquire an optimal condition in CR/Cr adsorption process as shown in Table 4.1. The data were analyzed by multiple regression to fit the second-order polynomial model according to the following equation 4.1.

$$y = \beta_0 + \sum_{i=1}^{4} \beta_i x_i + \sum_{i=1}^{4} \sum_{j=1}^{4} \beta_{ij} x_i x_j + \sum_{i=1}^{4} \beta_{ii} x_i^2 \quad (4.1)$$

where y is the predicted response (% adsorption), X_i and X_j are the independent variables, β_0 is the model constant, β_i is the linear coefficient, β_{ii} is the quadratic coefficient, β_{ij} is the interaction coefficient (Torrades et al., 2014).

Table 4.1 Central composite model design matrix for RSM

Factors	Low (-1)	Center (0)	High (1)
A: CR Concentration (mgL^{-1})	10	30	50
B: Cr(VI) Concentration (mgL^{-1})	10	30	50
C: NCPPY Dosage (mg)	10	20	30
D: Temperature (°C)	30	40	50

4.2. Results and Discussion

4.2.1 Synthesis and Characterization of NCPPY composites

Scheme. 1 shows the proposed mechanism for the synthesis of the NCPPY. Nanocellulose is a polysaccharide having -OH and -NH_2 groups which are acting as a base and provide active sites for the polypyrrole on it. The addition of ammonium persulphate generates free radicals and helps in the cross-linking of nanocellulose and polypyrrole. The synthesised NCPPY composites were characterised using FESEM, BET Surface area, FTIR, XRD, and TGA.

4.2.2. FESEM, roughness and surface area analysis

Fig. 4.1 illustrates the FESEM, roughness analysis of NCPPY composite before and after adsorption of CR, Cr(VI) and their binary mixture. The sulphuric acid hydrolysed NC are spherical, clustered morphology with the PPY matrix and sized around 10-100 nm. After adsorption, the surface became smooth as compared to NCPPY bare surface. The roughness plots indicated the evidence of the FESEM result which showed the total height (R_a) of the adsorbent before and after adsorption. From the BET surface area analysis, the specific surface area of NC and NCPPY and their pore distribution properties were evaluated using N_2 adsorption-desorption isotherm at a degassing temperature of 393 K (for 3h). The pristine NC has a surface area of 197 m^2g^{-1} whereas NCPPY has a hugely increased surface area of 488 m^2g^{-1}. As the data showed that surface modification enhanced the adsorbent efficiency by making the active functional groups like carboxyl, and hydroxyl groups available to interact with the dye and metal ions.

4.2.3. Thermal stability

From the thermogravimetric (TG) and Differential Scanning Calorimetry (DSC) analysis of NCPPY in Fig. 4.2, a weight loss of 8% wt was observed as the temperature was increased from 50 to 200°C. A sharp decline was observed at 225 °C due to the thermal decomposition of the pyrolysis of NC. Above 225°C, the decomposition of organic matter was initiated up to 600 °C where the complete decomposition happened (52% wt). This can be concluded as the higher thermal stability of the NCPPY composite.

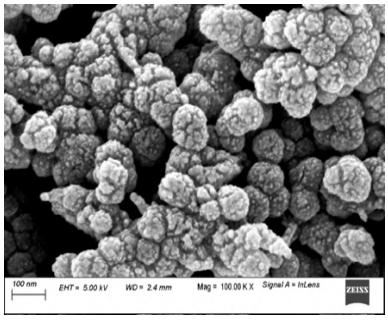
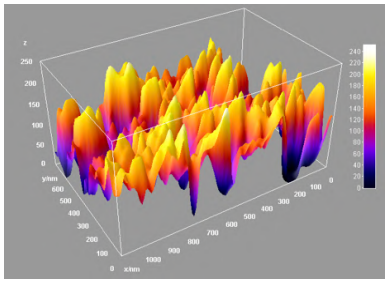

NCPPY Before adsorption

R_q - 125.418 nm

R_a - 101.559 nm

R_{sk} - 1.416

R_{ku} - 2.156

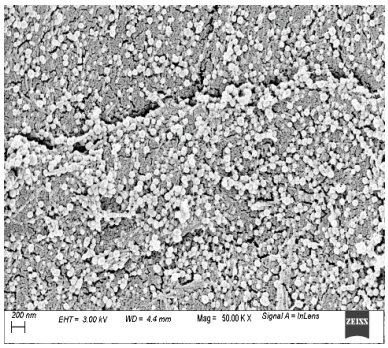
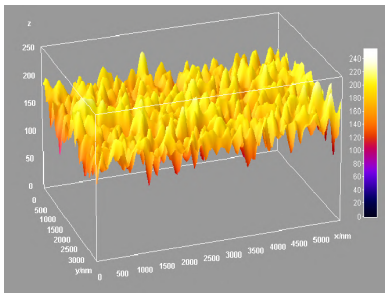

NCPPY after CR Dye adsorption

R_q - 181.417 nm

R_a - 169.255 nm

R_{sk} - 1.134

R_{ku} - 1.337

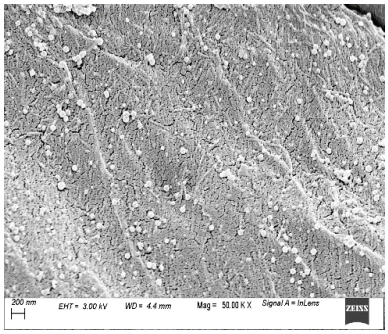
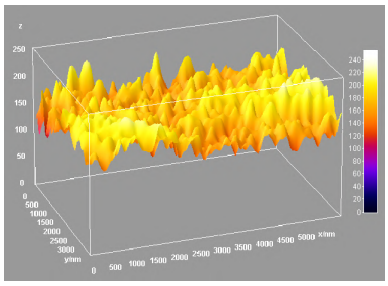

NCPPY after Cr metal adsorption

R_q - 175.634 nm

R_a - 168.525 nm

R_{sk} - 1.092

R_{ku} - 1.238

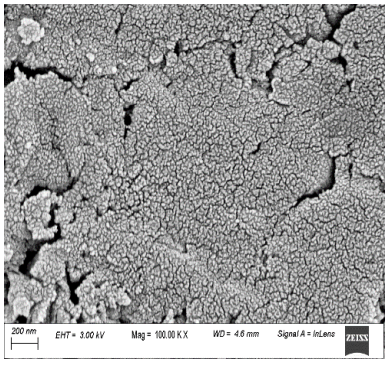
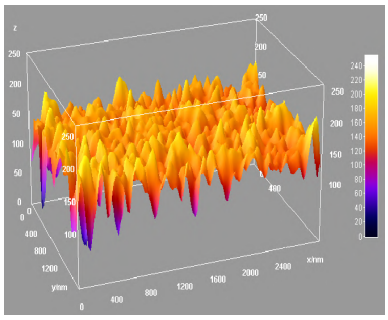

NCPPY after adsorption in binary mixture

R_q - 154.025 nm

R_a -144.906 nm

R_{sk} - 1.138

R_{ku} - 1.364

Fig. 4.1: Roughness Imaging of FESEM images of NCPPY under different conditions

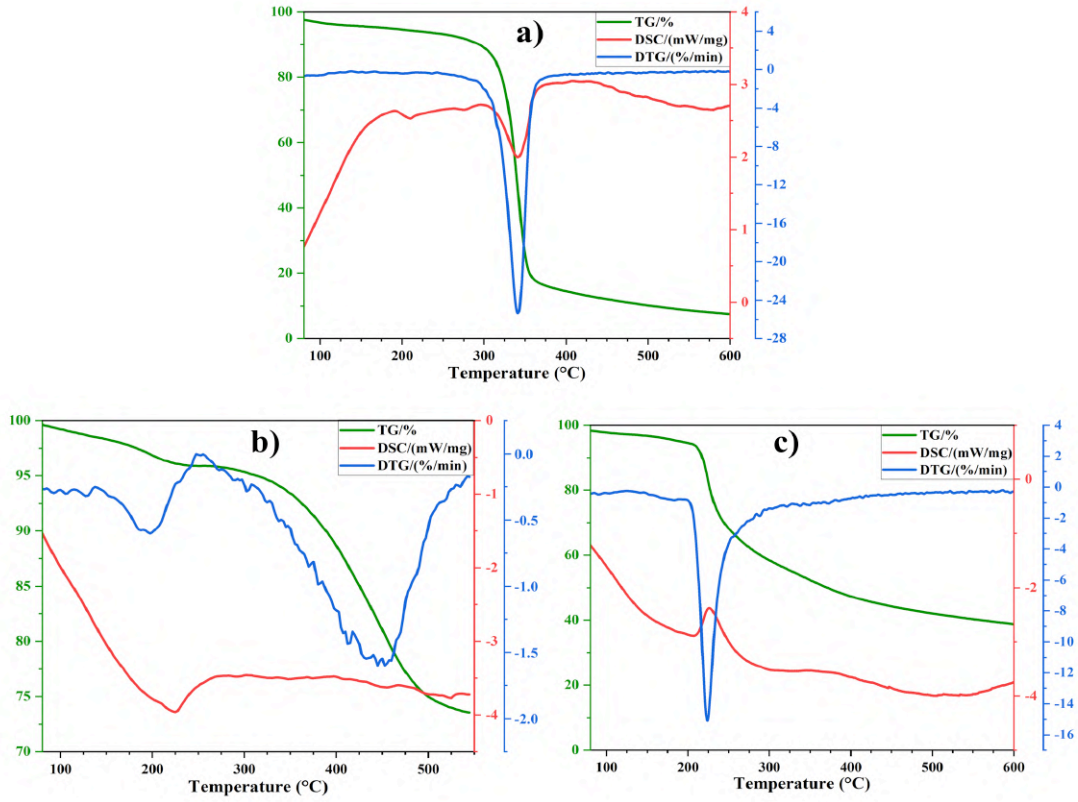

Fig. 4.2: Thermogravimetric analysis of a) NC, b) PPY and c) NCPPY

4.2.4. XRD analysis

The X-ray diffraction pattern of raw cellulose and NCPPY was illustrated in Fig. 4.3a. Two sharp crystalline peaks, namely 2Θ = 22.82°, 34.03° were observed in both raw cellulose and NCPPY (Aichour et al., 2020). A broad peak at 15.4° has been found and it denotes the amorphous region of the sample. From the literature, Polypyrrole has a distinct peak at 26.88° (Dahiru et al., 2008) which is merged with cellulose in Fig. 4.3a which showed the ordered crystalline structure was not disrupted by the sulphuric acid hydrolysis (Gu et al., 2020).

4.2.5. FTIR analysis

Fig. 4.3b illustrates the FTIR analysis of PPY, NC, and NCPPY before and after adsorption of CR and Cr(VI). The broad peak between 3500-3100 cm^{-1} corresponds to the -OH stretch of cellulose. The peak at 2900 cm^{-1} is related to asymmetrically stretching vibrations of C-H groups. The sharp peaks at 1427 cm^{-1} and 1369 cm^{-1} signify -CH_2 deformation of cellulose and -CH deformation of PPY and cellulose molecules respectively. The PPY band at 1513

cm^{-1} denotes C=N stretching vibrations, C-C asymmetric inter-ring, and C-C asymmetric inter-ring while the band at 1260 cm^{-1} corresponds to the C-N in-plane bending (Bober et al., 2014, Zhang et al., 2013). The band at 1130 cm^{-1} is related to ring in-phase stretching of the PPY ring structure. The band between 1140-930 cm^{-1} involves a C-O stretch of COH/COC where a sharp peak at 898 cm^{-1} denotes a ring semi-circle stretch of the cellulose molecule. The peak at 1640 cm^{-1} corresponds to the presence of the water molecule (Ahamad et al., 2019).

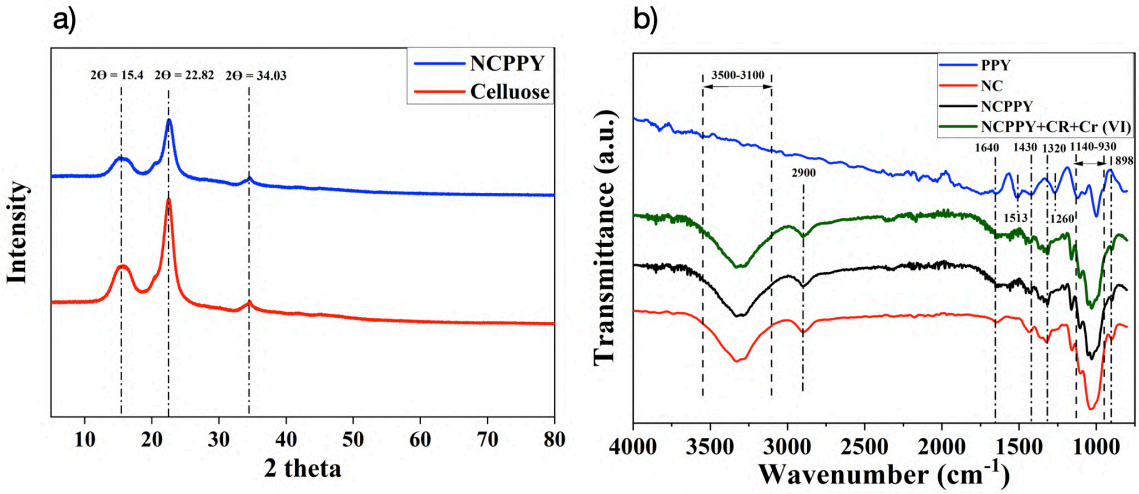

Fig. 4.3: XRD (a) (NCPPY and cellulose) and FTIR analysis (b) of PPY, NC, NCPPY and NCPPY after adsorption

4.2.6. Effect of pH on removal studies of CR and Cr(VI)

The NCPPY composites were used for the adsorptive removal of CR and Cr(VI) from the binary aqueous solution. Further, the interaction of CR and Cr(VI) has also been depicted in scheme 4.1. The solution pH plays an important role in affecting the efficiency of adsorption by altering the degree of ionisation, adsorbent-adsorbate interactions and surface properties of NCPPY adsorbent. The influence of pH was tested with a pH range of 2 to 9 with the initial dye concentration of 10 $mgmL^{-1}$ of CR/Cr(VI) binary mixture. It was observed that as pH decreases, the sulfonated groups of the dissolved dye molecule are dissociated generating anions in the solution in aqueous solution and Cr(VI) predominantly occurs in anionic forms showing affinity towards protonated NCPPY adsorbent. As pH increases the rate of adsorption decreases due to a reduction in the protonation on the adsorbent surface (Zhang et al., 2019, Patra et al., 2019).

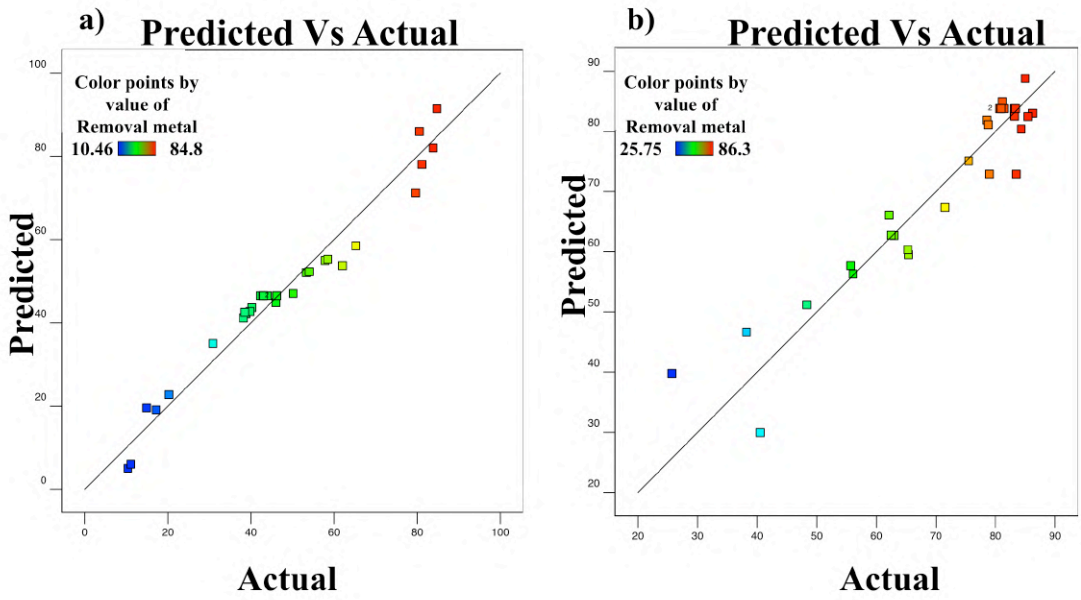

Fig. 4.4: Plot of predicted data versus experimental data for a) Cr(VI) and b) CR adsorption

4.2.7. Polynomial Equation-based Modelling using Response Surface Methodology

CCD model was employed for the experimental design, regression and graphical analysis. Total, 30 experiments were carried out to complete RSM Model to study the interaction of CR (A) and Cr(VI) (B) concentration, NCPPY dosage (C), and temperature (D) on the efficiency of removal of the pollutants individually. From Fig. 4.4, the closer values of actual and predicted "data of fit" provide evidence for reliability. The second-order polynomial model equations (Equation 4.2, 4.3) were made to define the influence of four independent variables. F-test, Analysis of variance (ANOVA), and regression give a better understanding of the interaction between the mathematical model and reaction parameters. ANOVA modelling, depicting the F value of 25.84 for Cr(VI) and 9.78 for CR, implies model terms are significant. When the p-value is less than 0.001, it denotes the model terms are substantial while the p-value greater than 0.001 means that the model terms are not significant (Dahiru et al., 2008). By observing p values and 3D surface plots (Fig. 4.5), Initial Cr(VI) concentration (B) and dosage of NCPPY (C) act as the main influential parameters of adsorption of Cr(VI) whereas initial dye concentration (A) plays an essential role in determining the adsorption efficiency of CR on NCPPY adsorbent. From the results, under acidic environment, the optimised conditions were as follows: CR concentration 50 mgL^{-1},Cr(VI) 10mgL^{-1}, NCPPY

dosage 30mg, temperature 50°C. With these optimised conditions, removal of Cr(VI) and CR increases by up to 80 % and 85 % respectively.

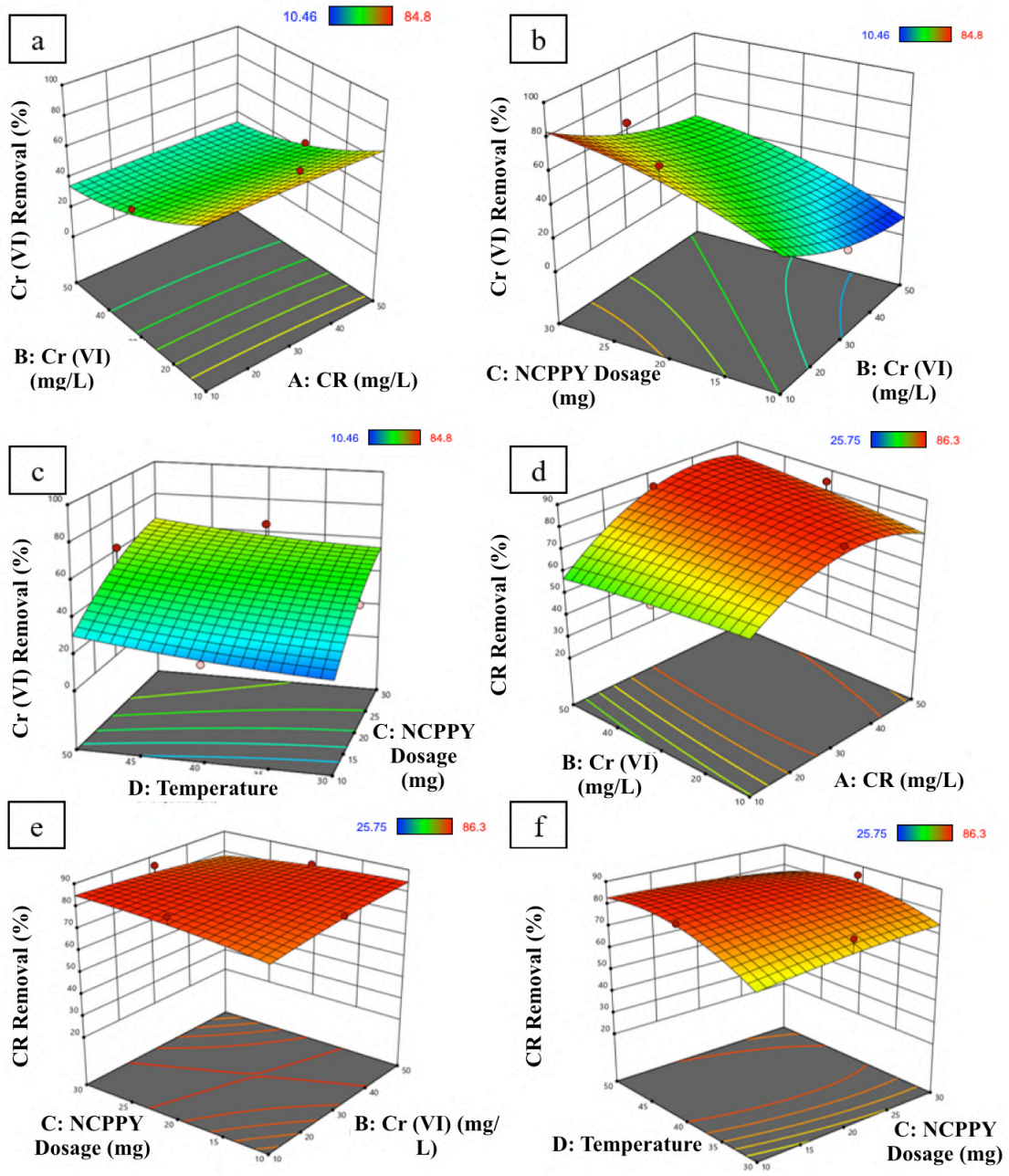

Fig. 4.5: Response surface plots for Cr (VI) adsorption a) A-B b) B-C c) C-D and CR adsorption d) A-B e) B-C f) C-D on NCPPY adsorbent

$$RCR\ \% = 83.73 + 8.81A - 0.16B - 0.031C + 4.11D + 4.34AB + 7.70AC + 6.63AD - 3.21BC - 2.89BD - 2.92CD - 12.20A^2 - 0.93B^2 - 1.29C^2 - 6.77368D^2 \quad (4.2)$$

$$RCr\ \% = 46.45 - 1.11A - 18.06B + 17.88C + 5.61D + 0.61AB - 0.63AC - 0.37AD - 0.19BC + 0.80BD - 0.49CD - 0.57A^2 + 6.58B^2 - 5.92C^2 + 1.59702D^2 \quad (4.3)$$

4.2.8. Effect of Ionic Strength

Real wastewater contains several common salts like NaCl, $KH_2PO_4^{3-}$, $MgCl_2$, KCO_3^{2-}, $CaCl_2$ etc. in the ionic form. To check the effect of these ions, we have studied the adsorption of CR and Cr(VI) onto NCPPY in the presence of a 20 ppm solution of each metal and dye with 0.1 M aqueous solutions of each salt. The results are shown in Fig. 4.6. Adsorption of CR onto NCPPY was 86.5% before the addition of any ionic salt. On addition of these ionic salts, the adsorption of CR was slightly decreased in the order KCO_3^{2-}(86.33%)>$ZnSO_4$(81.62%)> $FeSO_4$(78%)>NaCl(77.53%)>$CaCl_2$(76.53%)>$CuSO_4$(74.08%)>KH_2PO_4(73.52%)> $MgNO_3$(71%). For Cr(VI), Control experiment without salt (87%)>NaCl(75.36)> $CaCl_2$(70.50%)>$ZnSO_4$(66.26%)>$CuSO_4$(60.81%)>$MgNO_3$(60.90%)>KCO_3^{2-}(57.36%)> KH_2PO_4(53.96%)>$FeSO_4$(78%). This decrease in removal percentage was due to the difference in hydrated ionic radii. Ions with smaller hydro radii can compete with large-sized pollutant and easily gets adsorbed resulting in decreased removal of CR and Cr(VI). From this study of the effect of co-existing ions it can be concluded that even in the presence of ionic salts, NCPPY could be used efficiently for the removal of CR and Cr(VI) from an aqueous medium (Sharma et al., 2017, El-Bayaa et al., 2009).

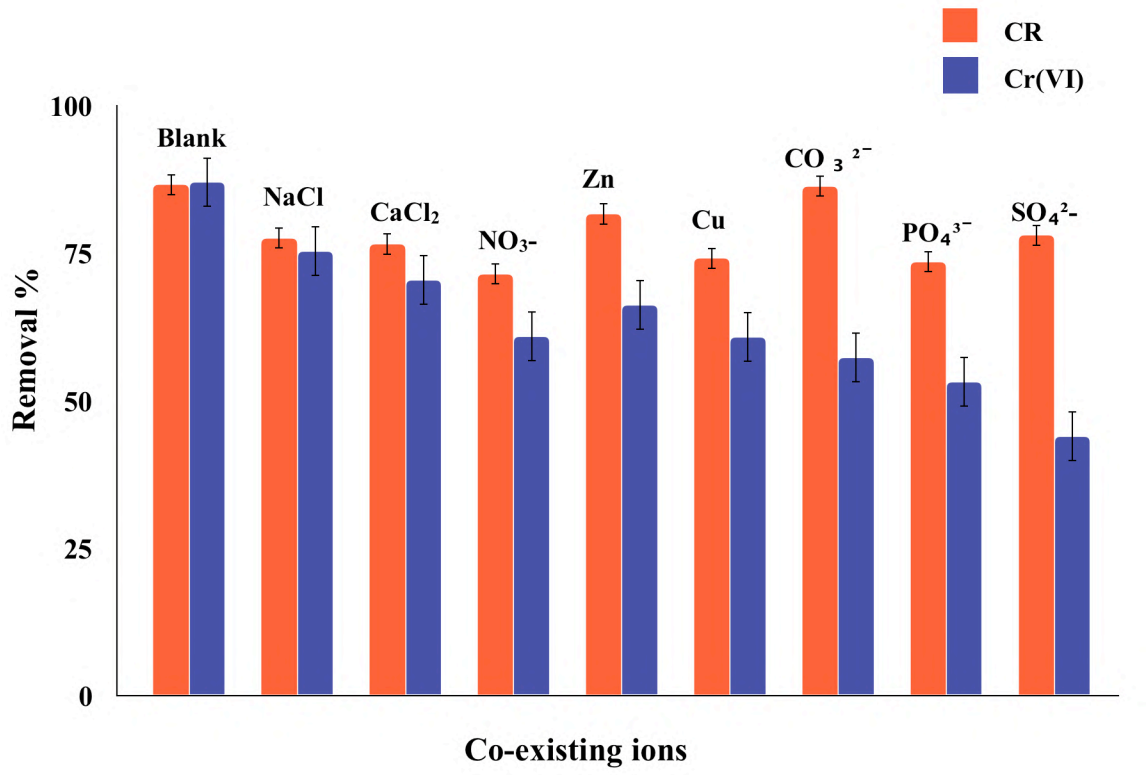

Fig. 4.6: Effect of co-existing ions on Cr(VI) and CR adsorption to NCPPY

4.2.9. Thermodynamic Studies

Thermodynamic studies were performed by observing the change in enthalpy (ΔH°), change in entropy (ΔS°), and change in free energy (ΔG°) with the temperature range within 30-50 °C. The adsorption capacity increases with the increase in temperature. This may be due to an increase in active sites and an increase in the mobility of the adsorbate molecules. A positive ΔH° value for both CR and Cr indicates that the adsorption follows an endothermic reaction with the increase in temperature. A positive ΔS° value suggests an increase in the randomness at the internal structure of the adsorption and hence the feasibility of the process. The negative ΔG° value indicates the adsorption is more spontaneous and energetically more favourable (Table 4.2) (Wu et al., 2020).

Table 4.2: Thermodynamic Parameters

Pollutant	Temperature	ΔG°	ΔH°	ΔS°
Cr(VI)	303	-2.045	31.238	0.109
	313	-2.417		
	318	-4.113		
	323	-3.958		
CR	303	-5.444	78.062	0.277
	313	-9.599		
	318	-10.342		
	323	-10.788		

4.2.10. Isotherm Studies

The experimental data were fitted into three different models viz. Langmuir, Freundlich and Dubinin-Radushkevich (D-R). From Table 4.3, the R_L values for Cr(VI) and CR adsorption is less than 1 which indicates energetically favourable biosorption (Langmuir, 1918).

The slopes and intercepts determined the values of Langmuir isotherm constants by plotting $1/q_e$ vs $1/C_e$. The q_m and k_L values were listed in Table 4.3. R_L values for both Cr(VI) and CR lie below 1 indicating the viability of biosorption in NCPPY biosorbent. The examination of the coefficient of determination (R^2) reported in Table 4.3 shows that experimental data well

fitted to Langmuir isotherm. Based on the coefficient of determination (R^2), the Langmuir model matched the adsorption of CR on NCPPY so, that the possibility of monolayer adsorption is more. The Freundlich plots of ln q_e vs ln C_e for biosorption on NCCPY were generated for determining k_F and n values. The n values were greater than 1, indicating the favourable biosorption of Cr(VI) and CR onto NCPPY. Moreover, K_L values at 50°C (CR=22.56, Cr(VI)=4.90) are greater compared to 30°C (CR=5.96, Cr(VI)=1.44) which indicates the easy uptake of pollutants and multilayer formation (especially Cr(VI)) from aqueous solution by NCPPY (Rangabhashiyam et al., 2015). D-R constants were calculated using the plots ln q_e vs ε^2 and it is listed in Table 4.3. The E values for both Cr(VI) and CR lie less than 16 $kJmol^{-1}$ which indicated that the adsorption process might be physical since the coefficient of determination values (R^2) are less, and the experimental model cannot be well interpreted with D-R isotherm.

Table 4.3: Isotherm constants of Cr (VI) and CR biosorption on NCPPY

Isotherm Models	**CR**		**Cr(VI)**	
	273 K	**323 K**	**273 K**	**323K**
Langmuir				
q_m	74.87	46.78	12.67	25.35
k_L	0.094	1.603	0.066	0.1832
R_L	<0.1	<0.1	<0.6	<0.3
Coefficient of determination (R^2)	0.9410	0.949	0.9638	0.9351
Freundlich				
K_F	5.96	22.56	1.44	4.90
n	1.17	3.07	1.934	2.09
Coefficient of determination (R^2)	0.94	0.886	0.9934	0.9788
Dubinin Radushkevich				
q_m	91.63	39.71	264.21	67.37
β	0.11	0.0047	0.44	0.1509
E	2.105	10.32	1.05	1.819
Coefficient of determination (R^2)	0.7668	0.9058	0.888	0.792

4.2.11. Kinetic Studies

Table 4.4: Kinetics models of biosorption of CR and Cr(VI)

Kinetic Models	Parameters	CR	Cr(VI)
	q_e (exp.)	12.02	5.33
Pseudo first order	q_e	11.5895	4.3121
	K_1	0.0230	0.0142
	R^2	0.7154	0.9134
Pseudo second order	q_e	11.38	3.634
	K_2	0.0048	-0.0555
	h	0.6231	-0.7338
	R^2	0.897	0.978
Intraparticle diffusion	K_{ID}	1.084	0.626
	C	0.260	1.194
	R^2	0.9555	0.8906
Elovich	α	1.6468	1.9179
	β	0.5087	0.733
	R^2	0.8477	0.9885

Four models namely pseudo-first-order, pseudo-second-order, elovich and intraparticle diffusion models were applied to express the kinetics of the adsorption process. The values of pseudo-first-order constants were calculated by plotting log (q_e-q) vs t. Low values of the coefficient of determination for both Cr(VI) and CR indicate the insufficiency of the pseudo-first-order model to fit the equilibrium data. The second-order kinetics values such as k_2 and q_e were calculated by the plot between t/q_t against t. Elovich model describes the chemical adsorption mechanism in nature (Wu et al., 2009). The intraparticle diffusion plot of q_t vs $t^{0.5}$ for CR shows that the rate-limiting step may be the diffusion of CR onto the NCPPY layer. Since the regression of a plot of q_t vs $t^{0.5}$ for CR passes through the origin, the involvement of the diffusional barrier is a vital factor for the adsorption of CR onto the NCPPY surface (Allafchian et al., 2019). From Table 4.4, based upon the coefficient of determination (R^2)

values, it was observed that Cr(VI) biosorption followed elovich kinetics and CR biosorption developed intraparticle diffusion model.

4.3. Significant findings

NCPPY was prepared using sulphuric acid hydrolysis through polymerisation of pyrrole on NC. FESEM analysis clearly showed the cellulose conversion to nano size. X-Ray Diffraction pattern confirmed that acid hydrolysed nanocellulose is crystalline. The thermogravimetric study showed that the thermal decomposition point of NCPPY is 210 °C. BET analysis supported the increased surface area of NCPPY after modification of the bare components. The effect of co-existing ions showed CR removal did not show much decrease but Cr(VI) removal decreased up to 25-50% after the addition of different salts due to the competitive adsorption of some salts with Cr(VI) ions. At pH 2, the biosorption of CR and Cr(VI) was highest. Using RSM studies, the optimum conditions were found at initial CR concentration of 30 mgL^{-1}, initial Cr(VI) concentration of 10 mgL^{-1}, NCPPY dosage of 20 mg, and temperature of 30°C for 40 mL of the reaction volume for efficient biosorption. This NCPPY showed an excellent efficiency for both dye and metal in simultaneous adsorptive removal. Hopefully, this work will provide a new approach to the research and development of new adsorbents.

Chapter 5

Use of Nanocellulose extracted from grass for adsorption abatement of Ciprofloxacin and Diclofenac removal with phyto, and fish toxicity studies

The work embodied in this chapter is published in

TASRIN SHAHNAZ, Vishnu Priyan V., Sivakumar Pandian. and Selvaraju Narayanasamy*, Nanocellulose extracted from grass for adsorption abatement of Ciprofloxacin and Diclofenac removal with phyto, and fish toxicity studies, **Environmental Pollution, 2021, (Elsevier, SCI IF: 9.988)**

TH-3150_176106114

Abstract:

The present study deals with the adsorption of antibiotic Ciprofloxacin (CPXO) and anti-inflammatory agent Diclofenac (DCF) on Grass nanocellulose (GNC) extracted from *Cyprus rotundas* grass. The adsorbent GNC was characterized with various microscopic, elemental and spectroscopic analyses to monitor physicochemical alterations of the surface before and after adsorption. The size of the converted nanocellulose was found to be 40-50 nm. Experimental measures influencing the adsorption of CPXO and DCF that were optimized are initial solution pH, GNC dosage, temperature and initial concentration of adsorbate. Halsey isotherm model and the pseudo-second-order kinetic model agreed best with the experimental outcome for both the adsorbate. The maximum adsorption capacity of GNC was 227.223 and 192.307 mgg^{-1} for CPXO and DCF respectively. Phytotoxicity studies were performed using 6 different types of seeds to evaluate the effect of GNC-treated effluent on plants. Similarly, acute fish toxicity on zebrafish analysis showed to have a lesser mortality rate of the effluent after adsorption of CPXO and DCF on GNC. The overall work has been represented in Scheme 5.1.

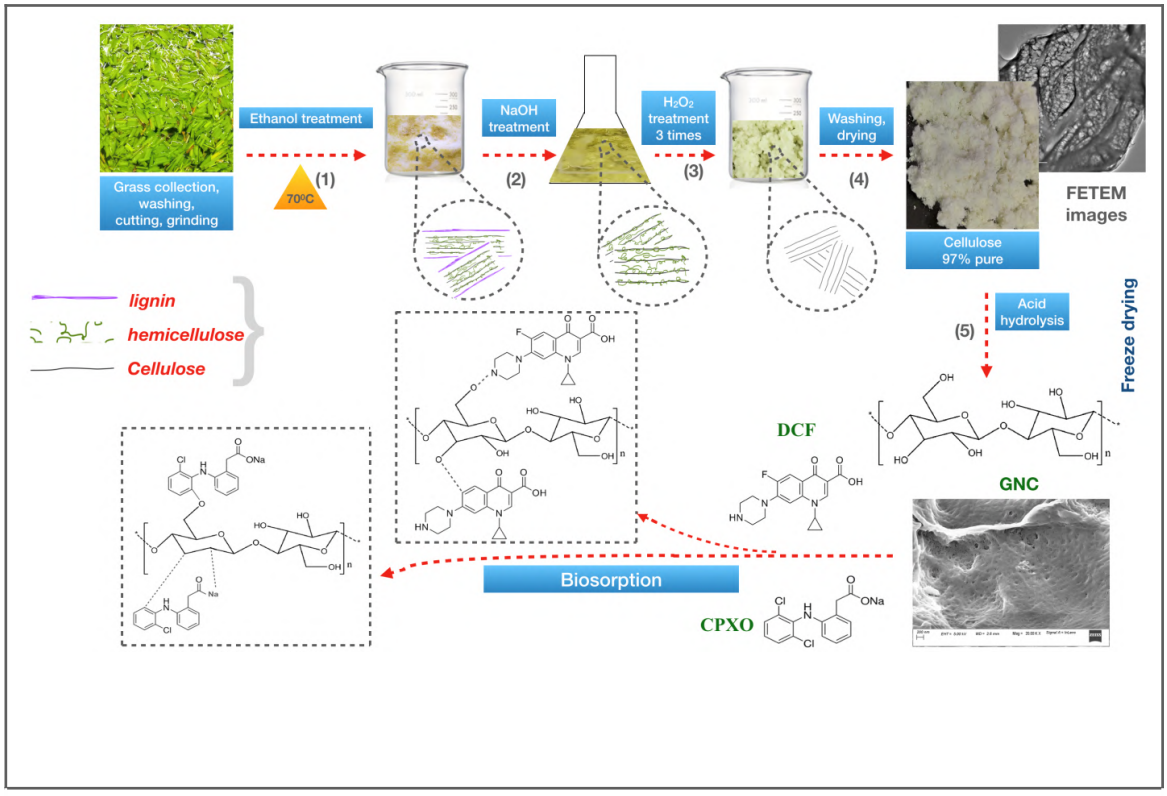

Scheme 5.1: Preparation of GNC and biosorption process

TH-3150_176106114

5.1. Materials and methods

5.1.1. Reagents

CPXO and DCF of analytical grade were procured from Sigma Aldrich (Table 5.1). A stock solution of 1000 mgL^{-1} was prepared for CPXO and DCF separately and diluted with deionised water as needed. Sulphuric acid, hydrogen peroxide, sodium hydroxide, ammonia solution, ferric chloride hexahydrate, ferrous chloride heptahydrate and other chemicals were obtained from HiMedia and were of analytical standard grade. Required solutions were prepared in Mili Q distilled water.

Table 5.1: Specification of the adsorbates used

Chemicals	Molecular formula	MW ($gmol^{-1}$)	Solubility (mgL^{-1})
Ciprofloxacin (CPXO)	$C_{17}H_{18}FN_3O_3$	331.35	6.19 × 103 (at 37 °C)
Diclofenac (DCF)	$C_{14}H_{11}Cl_2NO_2$	296.148	2.37 mgL^{-1} (at 25 °C)

5.1.2. Preparation of GNC

Grass (*Cyperus rotundus*), commonly found in North East India (26°11′14″N 91°41′30″E) was collected in bulk which was then washed and cut into small pieces of approximately 1 inch. Proper grinding was followed by 90% ethanol treatment at 70 ^{0}C in shaking conditions to remove dirt and other impurities present outside. The treated grass was then rinsed with 1N NaOH solution to remove the lignin content. It was again rinsed with water and finally treated with H_2O_2 (hydrogen peroxide) three times consecutively. The colour turns from green to white as H_2O_2 dissolves the hemicellulose leaving only the cellulose in the mixture. On drying the cellulose, purity was 97%. 5 g of cellulose powder was suspended in 250 mL water to form a colloid and to this 98% sulphuric acid was added drop-wise under constant stirring conditions for 3 h. After the addition of sulphuric acid, the suspension was heated at 50 ^{0}C for 2 h and then diluted 10 times with ice-cooled distilled water to prevent the acid hydrolysis reaction. The obtained white colloidal suspension was centrifuged at 8000 rpm for 20 min. This process was followed by dialysis to remove excess acid (membrane of molecular weight cut off 12,000-14000) after which ultra sanitation was carried out for 45 min in ice-cooled condition and lyophilised till further use (Shahnaz et al., 2020).

TH-3150_176106114

5.1.3. Adsorbent characterisation

To study the surface morphology of GNC and the elements present, an energy dispersive spectroscopy equipped with scanning electron microscopy (Zeiss-Gemini, Germany) was used. Transmission electron microscopy (JEOL, JEM-2100, Japan) further confirmed the adsorbent surface and dimension to be in the nano range. SAED pattern was checked to know the crystal arrangement type of the sample. Radiator-equipped Atomic Force Microscope (Cypher, Oxford) was utilised to describe the dimensional properties as well as roughness parameters of the GNC surface. Raman microscopy was used to check the structural fingerprint of GNC before and after adsorption for which a Laser Micro Raman microscope from Horiba Jobin Vyon, LabRam HR was utilised at an excitation wavelength of 633 nm with 400 lines per mm grating. With a 10 microscope objective and 20 mW laser power each sample was exposed for 10 s and scanned from 400 to 3500 cm^{-1}. An X-Ray diffractometer from Rigaku, Micromax-007HF was used to study the crystallinity of GNC before and after the adsorption of CPXO and DCF.

5.1.4. Detection of CPXO and DCF

The CPXO and DCF concentration before and after adsorption was measured using high-performance liquid chromatography (HPLC, Shimadzu LC-20A) with an XDB-C18 column from Agilent Model Eclipse to perform the chromatographic separation. The column was conditioned at 30 °C, with a wavelength of 278 nm and 280 nm for CPXO and DCF respectively. The mobile phase for CPXO is acetic acid:acetonitrile:distilled water (8.4:80:411.6, v/v) while phosphate buffer (pH 7):0.1% trifluoroacetic acid-acetonitrile (65:35 v/v) for DCF. Every time 10 µL of the sample was injected at the flow rate of 1 mL per minute.

5.1.5. Phytotoxicity studies

To evaluate the environmental toxicity of pollutants, seed germination is a method based on the U.S. EPA, 1982 guidelines about the seed germination % and plant growth inhibitions with a few modifications. Two key measures for a phytotoxicity test are good germination % and long shelf life (Kalidhasan et al., 2016). Therefore, there is a lesser error in the test sample for higher germination in the control group. Phytotoxicity studies of the untreated and GNC treated CPXO and DCF effluent were performed using six different types of seeds viz. *Vigna mungo* (black gram), *Vigna radiata* (green gram), *Macrotyloma uniflorum* (horse gram), *Cicer arietinum* (Bengal gram), *Pennisetum glaucum* (pearl millet) and *Triticum aes-*

TH-3150_176106114

tivum (wheat) seeds. All the experiments were carried out for a week in dark incubation and one day indoors in natural light (Dhaouefi et al., 2019, Nouren et al., 2017) at 25 ^{0}C in the Petri plates of 7.5 cm diameter. The seeds were pretreated with 1% sodium hypochlorite solution for 10 min and then rinsed with distilled water to avoid any possible fungal growth. 10 seeds were spread evenly in each Petri plate containing distilled water as control, CPXO and DCF solutions before and after adsorption at different test concentrations (10, 30 and 50 mgL^{-1}). A total 7 treatment groups viz. blank (Deionised Water), CPXO and DCF (10 mgL^{-1}), CPXO and DCF (30 mgL^{-1}), CPXO and DCF (50 mgL^{-1}), CPXO and DCF [(10 mgL^{-1})+GN)], CPXO and DCF [(30 mgL^{-1})+GNC] CPXO and DCF [(50 mgL^{-1})+GNC] for each seed type were studied to evaluate the role of GNC in decreasing the pollutant toxicity. After 8 days of the conditioning, the seeds were checked for % germination, shoot and root length for growth inhibition to determine phytotoxicity.

5.1.6. Acute fish toxicity studies

Acute fish toxicity was studied using zebrafish (*Danio rerio*) according to the Test Guideline No. 231, 2009 Fish acute toxicity testing of OECD (Hossam Mahmoud et al., 2020). The tests were done for 96 h for CPXO and DCF solutions and untreated and treated with GNC. The model organism was purchased from a licensed market and the fishes were sorted according to size and age. Two different test groups were performed for each pollutant. The untreated CPXO solutions were prepared in concentrations of 1, 5, 10, 50, 100, 120 and 150 mgL^{-1}. For DCF, the concentration level was taken up to 100 mgL^{-1}. External conditioning was a photoperiod of (14:10, Light: Dark), the temperature of 25 ^{0}C, oxygen concentration (>75% of air saturation) and the solutions were maintained at pH in the range of 6.5-7.5 throughout the experiments. A total of 16 and 12 test groups (before and after adsorption) were evaluated for CPXO and DCF respectively with 10 fishes for each treatment. The solution with 0 mgL^{-1} was kept as the control. After 24, 48 and 96 h of treatment, each group was checked for the total number of dead fish and the mortality % was calculated. The lethal concentration 50 (LC_{50}) is often used as a general indicator of acute toxicity which is the amount of a particular substance needed to kill half the population of a test organism during a specific incubation period. From the data generated periodically, the LC_{50} value was determined for CPXO and DCF.

TH-3150_176106114

5.2. Results and Discussion

5.2.1. Characterisation

The SEM images of GNC were shown in Fig. 5.1(i-iii) with various magnifications clearly showing the thread-like structure and porous sheet mostly in nano dimension. Then broken layers of the nanocellulose are seen in Fig. 5.1(ii) increasing the adsorption capacity of the fibrous adsorbent. Under a higher magnification of up to 50 kx FESEM images reveal several foldings of GNC. Fig. 5.1 (iv and v) reveals the nanocellulose with dimensions of 40-50 nm and with some particles in aggregated form. The accurate size was also confirmed by FETEM analysis. The SAED pattern (Fig. 5.1(vii)) revealed the sample to be semi-crystalline in nature. AFM enabled to analyse of the sample for its surface morphology and topography. The sample was drop cast on a silica surface and dried at room temperature. Over 10x5 mm area was checked for height and phase plane as shown in Fig. 5.2 for GNC. The roughness data was checked with a software called “Gwyddion” where different parameters viz. average roughness, RMS roughness, height, peak, and waviness can be obtained. Fig. 5.2 shows evenly spread spots with an average roughness of 0.155 nm and a height of 1.5 nm that confirm the successful conversion of cellulose to nanocellulose. Some additional parameters are also tabulated in Table 5.2 from the AFM images. Raman spectroscopy was analysed for the characteristic fingerprint from 400 to 3500 cm^{-1} Raman shift. For GNC raw sample, the peaks at 608, 1050, 1470, and 2731 cm^{-1} denote the cellulose characteristics band (Lu et al., 2020). For GNC+CPXO, the peaks at 1344, 1389, 1467, 1547, 1624 cm^{-1} correspond to the fluorine present in CPXO (Stiles et al., 2008). The appearance of the peak at 857, 1120, 1790 cm^{-1} confirm the adsorption of chlorine which is the key element in DCF (Fig. 5.3) (Graouer-Bacart et al., 2016). XRD pattern from 5 to 50 (2θ) for GNC before and after adsorption is depicted in Fig. 5.4. Three major peaks (2θ= 16, 22.5, 35.03) seen from raw GNC correspond to the significant peaks of cellulose. It also specifies the semi-crystalline nature of cellulose. GNC with CPXO and DCF diffractogram pattern slightly shift at angles 11.3, 14.85, and 20.8 from the GNC as some peaks appear and amend for F and Cl as confirmed from the literature report (Maia et al., 2019). Furthermore, the crystallinity index for GNC was checked which quantifies the semi-crystalline nature of GNC. Gusev hypothesised the state that diffraction patterns are additive. Energy Dispersive X-Ray of GNC before and after adsorption with

TH-3150_176106114

CPXO and DCF was analysed (Gusev et al.,1978). In Fig. 5.5(a), the raw GNC has only C and O in its elemental presence after adsorption with CPXO. In Fig. 5.5(b), significant peaks for F were observed with 0.4 wt %. Similarly, for DCF as shown in Fig. 5.5(c), the adsorbed GNC was seen with a distinguished peak for Cl with 0.3 wt %. The aluminium peak seen was due to the reason the sample was prepared on aluminium foil paper (Fig. 5.5).

Table 5.2: AFM data for GNC

Parameters	**GNC**
Roughness average (R_a), nm	0.155
Root mean square roughness (R_q), nm	0.205
Maximum height of the roughness (R_t), nm	1.563
Maximum roughness peak height (R_p), nm	0.705
Waviness average (W_a), nm	4.335
Waviness maximum height ($W_y = W_{max}$), nm	5.566

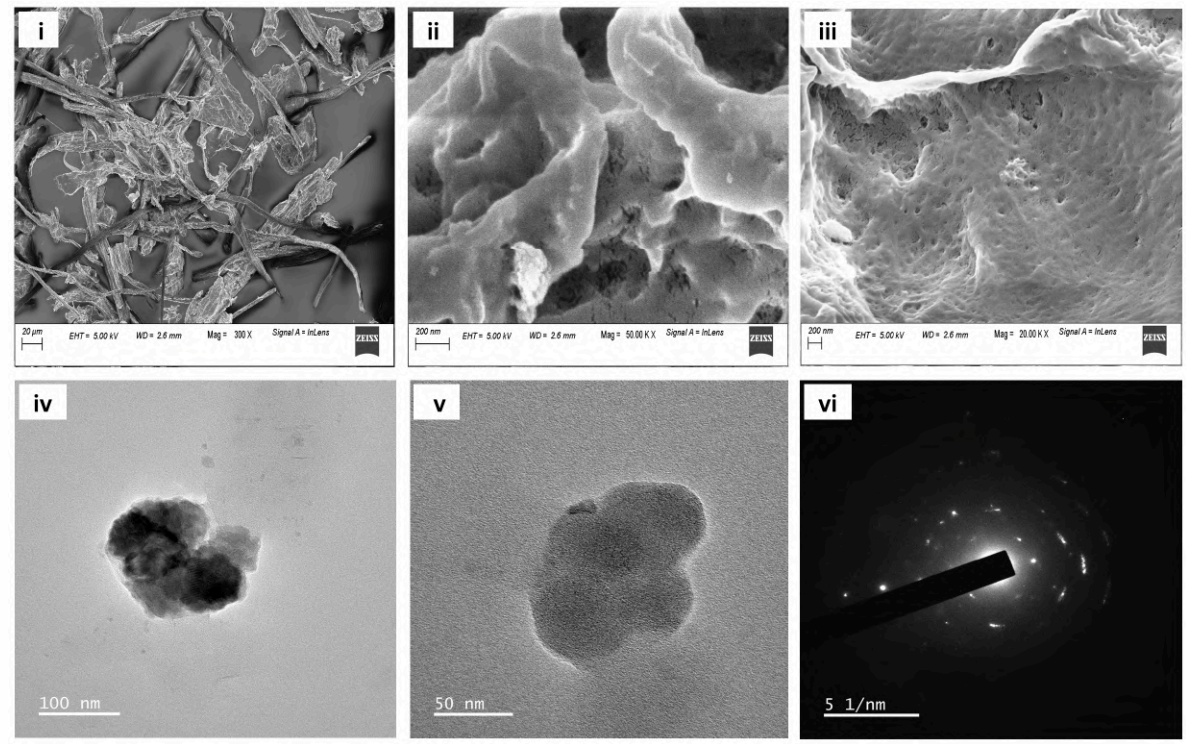

Fig. 5.1: GNC (i-iii) FESEM, (iv-v) FETEM (high resolution), (vi) SAED pattern

TH-3150_176106114

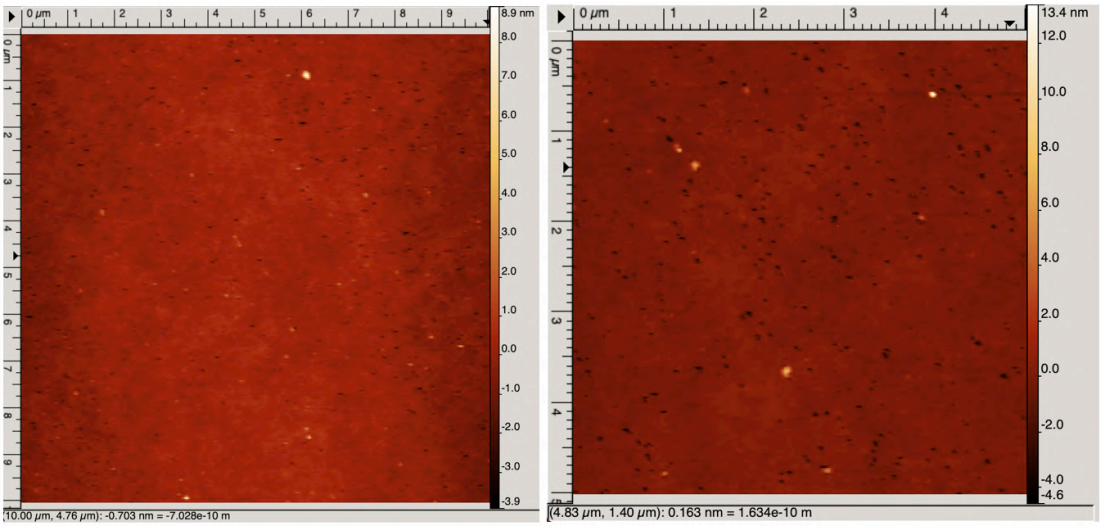

Fig. 5.2: AFM images of GNC

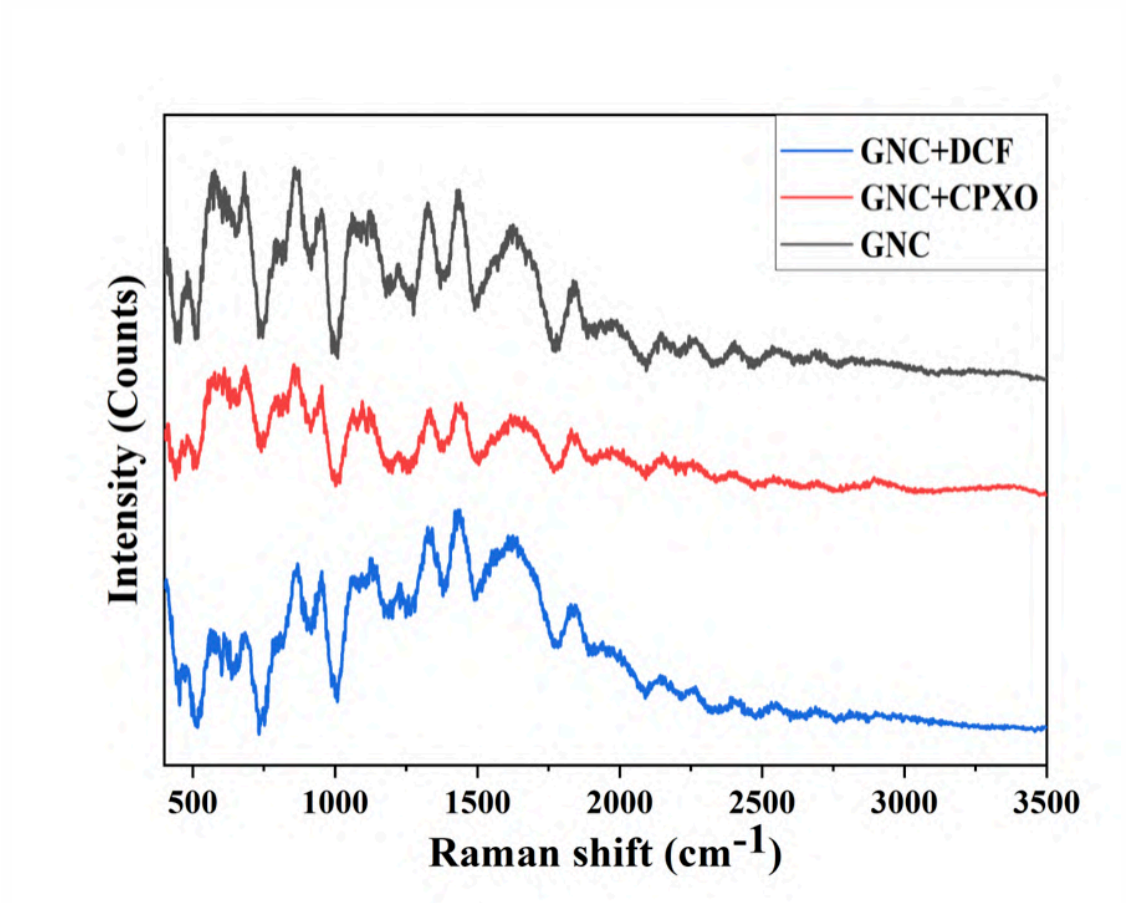

Fig. 5.3: Raman spectroscopy of GNC, GNC+CPXO and GNC+DCF

TH-3150_176106114

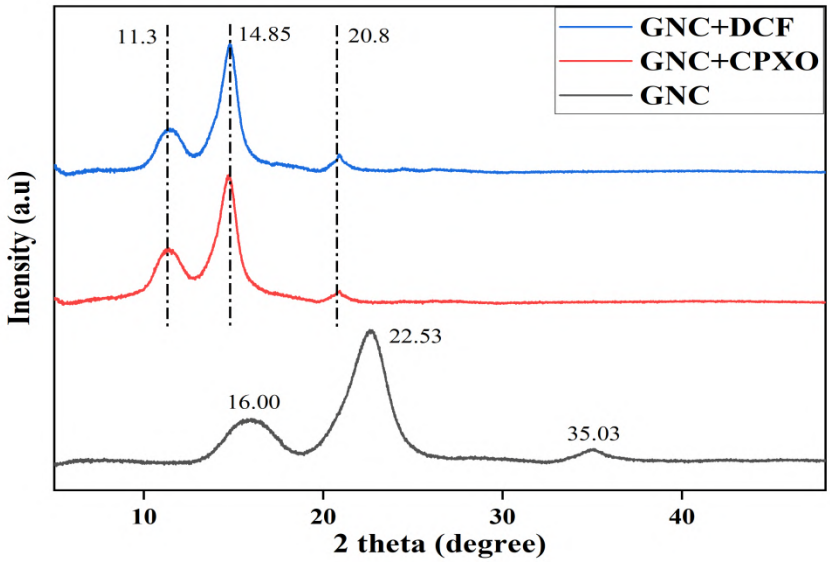

Fig. 5.4: XRD plot of GNC, GNC+CPXO and GNC+DCF

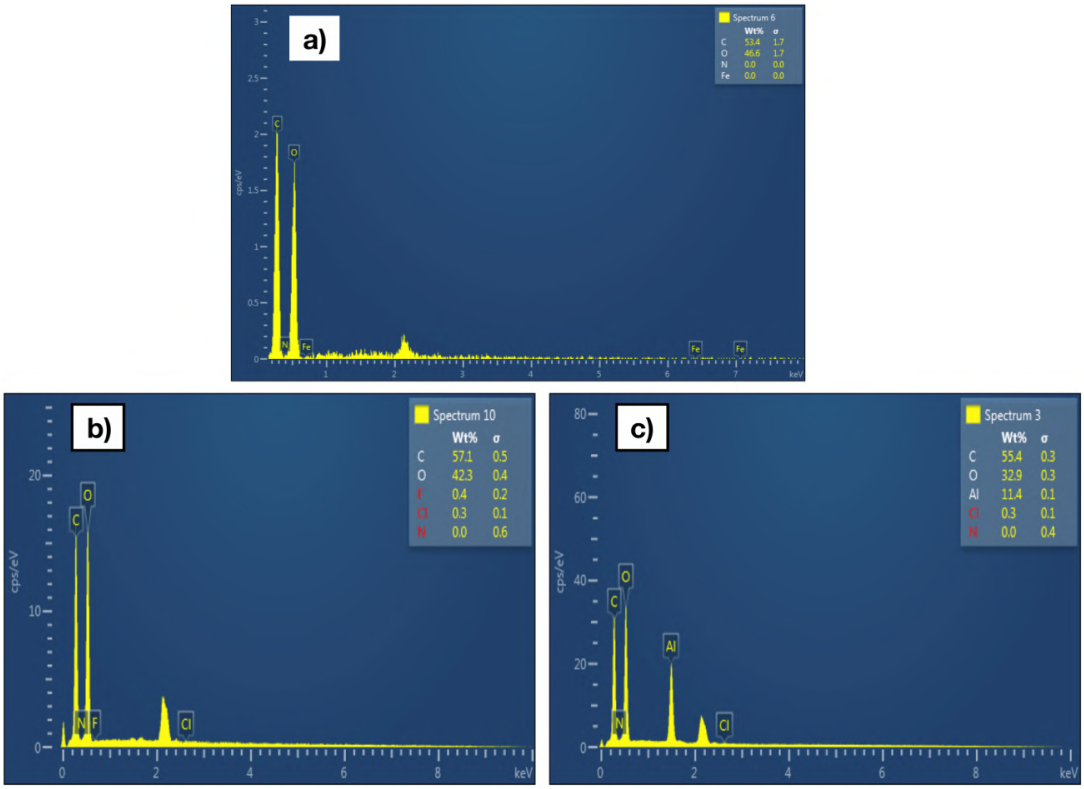

Fig. 5.5: EDX (a) GNC (b) GNC+CPXO and (c) GNC+DCF

TH-3150_176106114

5.2.2. Influence of experimental parameters

To obtain the highest removal efficiency, any treatment method needs to be optimised carefully. Hence, all the operating conditions including the adsorbent dosage, pH, temperature, initial CPXO and DCF concentrations were optimised (Trache et al., 2020).

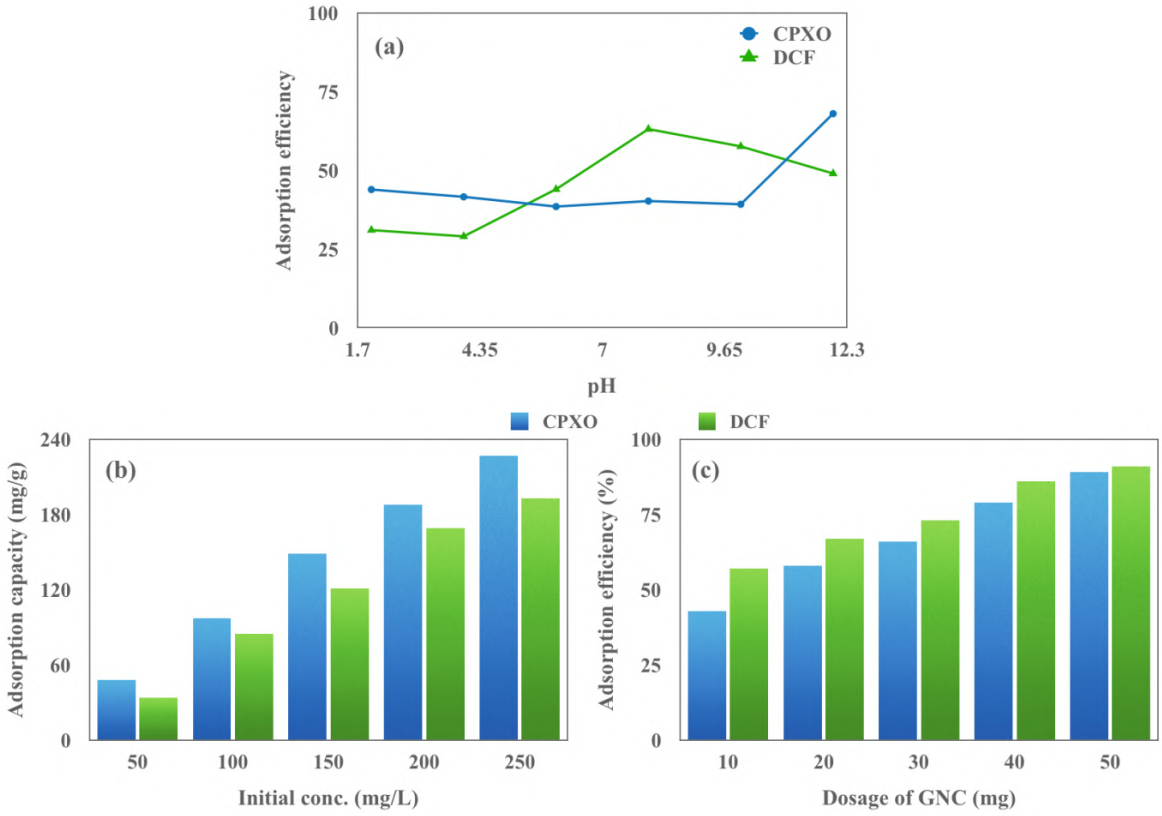

Fig. 5.6: Effect of pH (a), different initial concentrations (b) of adsorbate solution and dosage of GNC (c) over adsorption efficiency of GNC

5.2.2.1. Effect of pH

In an efficient adsorption process, pH always plays a crucial role as it affects the solution ion concentration and the solid surface properties. At 35 C for 3 h, an initial CPXO and DCF concentration of 5 mgL^{-1} was checked for pH influence ranging from 2 to 12. In Fig. 5.6(a) plots are shown for pH vs. adsorption efficiency (%) (Priya et al., 2014). For CPXO, the removal % was observed to be only 50% from pH 2 to 10 which gradually increased through pH 10 and finally at pH 12, the efficiency showed a maximum of 73%. For DCF, the efficiency first increased after pH 4 and a maximum of pH 8 with 63% adsorption efficiency which later decreased to 50% at pH 12. For further studies, the pH of CPXO and DCF was

TH-3150_176106114

adjusted to 12 and 8 respectively.

5.2.2.2. Influence of initial concentration

For the influence of the initial concentration of CPXO and DCF, a 50-250 mgL^{-1} simulated solution was checked separately at a fixed dose of GNC with a pH of 12 and 8 respectively at 313 K and incubated for 180 min. With a rise in the initial CPXO and DCF concentration, the adsorption capacity of GNC gradually increased and reached the maximum after attaining equilibrium with a decrease in the removal % (Fig. 5.6(b)). Similar results were obtained by other researchers as well (Bizi and El Bachra, 2020). The probable reason may be the saturation of the adsorption sites with time. The adsorption capacity for CPXO increased from 48 mgg^{-1} (50 mgL^{-1}) to 227.2 mgg^{-1} (250 mgL^{-1}) and for DCF from 38 mgg^{-1} (50 mgL^{-1}) to 192.3 mgg^{-1} (250 mgL^{-1}) at pH 12 and 8 respectively.

Table 5.3: Isotherm parameters of CPXO and DCF adsorption on GNC

	Parameter	CPXO	DCF
Langmuir	Q_0	227.273	192.307
	K	0.097	0.242
	R^2	0.913	0.911
Freundlich	n	0.47	0.44
	K_F	0.0395	0.0232
	R^2	0.958	0.959
Halsey	n_H	-1	-1
	K_H	0.019	0.032
	R^2	1	0.973
Redlich-Peterson	K_{rp}	5.12	3.87
	Arp	0.081	0.054
	Brp	0.57	0.60
	R^2	0.917	0.923

TH-3150_176106114

5.2.2.3. Effect of dosage

Adsorbent dosage is yet another key parameter to be optimised for an efficient adsorption process (Nekouei et al., 2015). In this study, GNC dosage was varied from 10 to 50 mg for a 50 mgL^{-1} concentration of CPXO and DCF separately under the best condition for each pollutant for 3 h. Fig. 5.6(c) shows a removal efficiency of CPXO that increased from 43 to 89% and 57 to 91% for DCF which may be due to the rise in the adsorption surface area and the active adsorption sites present on GNC (Abu-Danso et al., 2019).

5.2.3. Adsorption isotherms

The experimental data for CPXO and DCF agreed well with the Halsey isotherm as shown in Table 5.3 with a maximum coefficient of determination (R^2) of 1 and 0.973 respectively. The linear fitting of the isotherm plotted for $\ln(1/C_e)$ vs. $\ln(q_e)$ confirms the heterogeneous distribution of active sites and the multilayer adsorption at a relatively greater distance from the adsorbent for both the pollutants studied. This model also determined the heteroporosity of the GNC surface and its interaction with CPXO and DCF molecules. Moreover, though the Freundlich isotherms have lesser fitting (but have R^2 0.95) the constant “n” values from the plots of $\log q_e$ vs $\log C_e$ were 0.47 and 0.44 lying between 0 to 10 indicating the favourable chemisorption of CPXO and DCF onto GNC (Mittal et al., 2010, IhsanullahAsmaly et al., 2015, Ghaedi et al., 2015) (Table 5.3).

5.2.4. Adsorption kinetics

From the kinetic models, it was evaluated that the PSO model standard error values (0.09) when checked with three concentrations viz. 5, 50 and 100 mgL^{-1}. Furthermore, the equilibrium adsorption capacity found with this model [q_e (cal)] is close to the experimental values [q_e (exp)], which show the correlation between the PSO model and the adsorption that is driven by chemical reaction rate. Hence, sharing and exchange of electrons at the GNC surface for the adsorption of CPXO and DCF could be the key factor driving the process. Different Kinetic parameters of CPXO and DCF biosorption onto GNC are tabulated in Table 5.4.

5.2.5 Thermodynamics

The adsorption reaction is observed to be exothermic for both CPXO and DCF with the negative values for enthalpy suggesting that the process is more feasible and more efficient at a

TH-3150_176106114

lower temperature ranging from 25 to 30 ^{0}C and it does not require external heat. Positive entropy value suggests the increased randomness in the sorbent interface and the feasibility of the adsorption process (Mohammadi et al., 2011). Moreover, both the reactions are spontaneous with negative free energy values which are energetically favourable as well (Table 5.5).

Table 5.4: Different Kinetic parameters of CPXO and DCF adsorption onto CNC

Kinetics	**CPXO**	**DCF**
Pseudo-first-order model		
q_e (mgg^{-1})	60.49	110.90
k_1 (min^{-1})	0.02	0.03
R^2	0.9216	0.8913
Std. Error.	0.1764	0.2689
Pseudo-second-order model		
q_e (mgg^{-1})	201.07	100.01
k_2 (gmg^{-1}min^{-1})	0.0023	0.57
R^2	0.9954	1
Std. Error.	0.0982	0.0966
Elovich model		
α (gmg^{-1}min^{-1})	74.17	-
β (mgg^{-1})	0.06	14.69
R^2	0.9123	0.9423
Std. Error.	7.626	0.369
Intra particle diffusion		

TH-3150_176106114

k_i ($mgg^{-1}min^{-1/2}$)	10.40	0.626
d	18.48	1.194
R^2	0.7673	0.8906
Std. Error.	2.0828	0.6480

Table 5.5: Thermodynamic parameters of CPXO and DCF adsorption on GNC

C_i	T(K)	CPXO			DCF		
		ΔG°	**ΔH°**	**ΔS°**	**ΔG°**	**ΔH°**	**ΔS°**
50	303	-6.7940	-91.6630	282.7950	-9.9700	(56.17)	154.1310
	308	-2.8750			-9.0120		
	313	-2.0590			-9.2290		
	318	-1.9480			-5.8720		
	323	-0.8310			-4.9720		
100	303	-3.6080	-33.7250	100.7710	-8.4450	(60.63)	173.9330
	308	-2.2250			-5.9330		
	313	-1.9780			-6.2050		
	318	-1.1120			-5.4200		
	323	-1.5210			-4.9700		
150	303	-3.0030	-7.3300	17.6180	-7.6500	(78.53)	232.0510
	308	-2.8460			-5.9100		
	313	-1.2970			-5.5300		
	318	-1.2970			-4.4910		

TH-3150_176106114

	323	-0.9020			-4.4530		
200	303	-1.9540	-23.4060	71.3710	-7.5360	(46.72)	134.8210
	308	-1.6310			-5.6580		
	313	-1.7070			-4.6040		
	318	-0.6740			-3.9640		
	323	-0.9780			-4.1680		
250	303	-0.6440	-25.2990	80.0850	-6.9310	(59.93)	183.9460
	308	-0.9660			-5.1200		
	313	-1.8450			-4.5140		
	318	-0.4090			-3.3850		
	323	-0.8580			-3.7230		

5.2.6. Phytotoxicity

Seed germination is a key parameter to check the afterwards effect of the adsorbent treated effluent by measuring seed germination (%) and inhibition of growth (%). In this study before and after adsorption of GNC with CPXO and DCF was checked with 6 different types of seeds. Distilled water was taken as the control to carry out a comparative study on the actual growth of the seeds whereby its growth was found to be 100%. It is evident from Fig. 5.7(a) that with an increase in the solution concentration for CPXO when untreated, the seed germination decreases from 76% (10 mgL^{-1}) to 53% (50 mgL^{-1}) for black gram (BG) while it reduces from 93% (10 mgL^{-1}) to 78% (50 mgL^{-1}) when CPXO was treated with GNC validating a good amount to be adsorbed. Similar results were obtained for green gram (GG), horse gram (HG), Bengal gram (BgG), pearl millet (PM) and wheat (W) with reduced seed germination that varies from a maximum reduction of 82% to a minimum reduction till 11% for untreated CPXO with an increase in concentration from 10 to 50 mgL^{-1}. However, when CPXO was treated, a minimum reduction of 50% was observed even at 50 mgL^{-1}. When DCF was untreated, seed germination reduced from a maximum of 76% to a minimum of 21% with a gradual increase in concentration from 10 to 50 mgL^{-1} while it reduced from 94% (10 mgL^{-1}) to 52% (50 mgL^{-1}). A drastic difference can be observed in both the test sets of all the

TH-3150_176106114

seed groups in their % germination rate because of the removal of CPXO and DCF from the solution. Another observation was done for the inhibition of growth (%) as depicted in Fig. 5.7. Growth inhibition % was calculated from the difference of the average shoot and root length in the control solution to the teated solution which was found to follow the concentration-dependent manner. It is obvious that with increased test concentration, the shoot and root length will be lesser due to cellular disruption by toxic pollutants and hence their metabolic process. The quantitative data were presented in Fig. 5.8. This shows that the increase in % inhibition from 19% to a very high value of 88% for CPXO untreated drastically affects seed growth. In the case of DCF untreated, this increases to 34% in 10 mgL^{-1}. When the treated solutions were checked, the minimum reduction was found to be 51% and 52% for CPXO and DCF respectively. Similar results are reported in the literature (Dhaouefi et al., 2019).

5.2.7 Acute Fish toxicity

In the current study, the toxicity of the pharmaceuticals CPXO and DCF before and after biosorption was examined using zebrafish (*Danio rerio*) (Hossam Mahmoud et al., 2020). The pharmaceuticals before and after the biosorption process showed the highest toxicity when compared to the pharmaceuticals after biosorption. It was observed that there was no death and abnormal behaviour in the control groups. At concentrations above 100 mgL^{-1} of CPXO and 50 mgL^{-1} of DCF showed some abnormal symptoms like staying at the bottom of the tank, and unusual and rapid swimming were observed which are also reported in the literature (Kim et al., 2019). After 96 h at a concentration of 120 mgL^{-1} of CPXO, the mortality percentage was found to be 90% and at 100 mgL^{-1} of DCF, the mortality rate was 100% causing all fishes to die. These pharmaceuticals were subjected to adsorption and they were tested again for toxicity using zebrafish. After adsorption, the mortality rate of zebrafish was much reduced to 40% at a concentration of 150 mgL^{-1} of CPXO and 40% at the concentration of DCF. No mortality was observed till the 10 mgL^{-1} concentration of CPXO and DCF after adsorption. This shows that adsorption helps to reduce the toxicity caused due to pharmaceuticals. 96 h LC_{50} value of CPXO on *Danio rerio* were found to be 100 mgL^{-1} for untreated tests while the treated group showed an increased value at 150 mgL^{-1} which is a good measure. Moreover, for DCF 96 h and LC_{50} value was found to be 50 mgL^{-1} for untreated tests while the treated group showed an increased value at 100 mgL^{-1}. Also, test groups exposed to 1, 5

TH-3150_176106114

and 10 mgL^{-1} of CPXO and DCF showed no mortality rate with the normal behaviour of the fishes. A graph has been plotted for easy comprehension as shown in Fig. 5.9 with the data tabulated in Table 5.6.

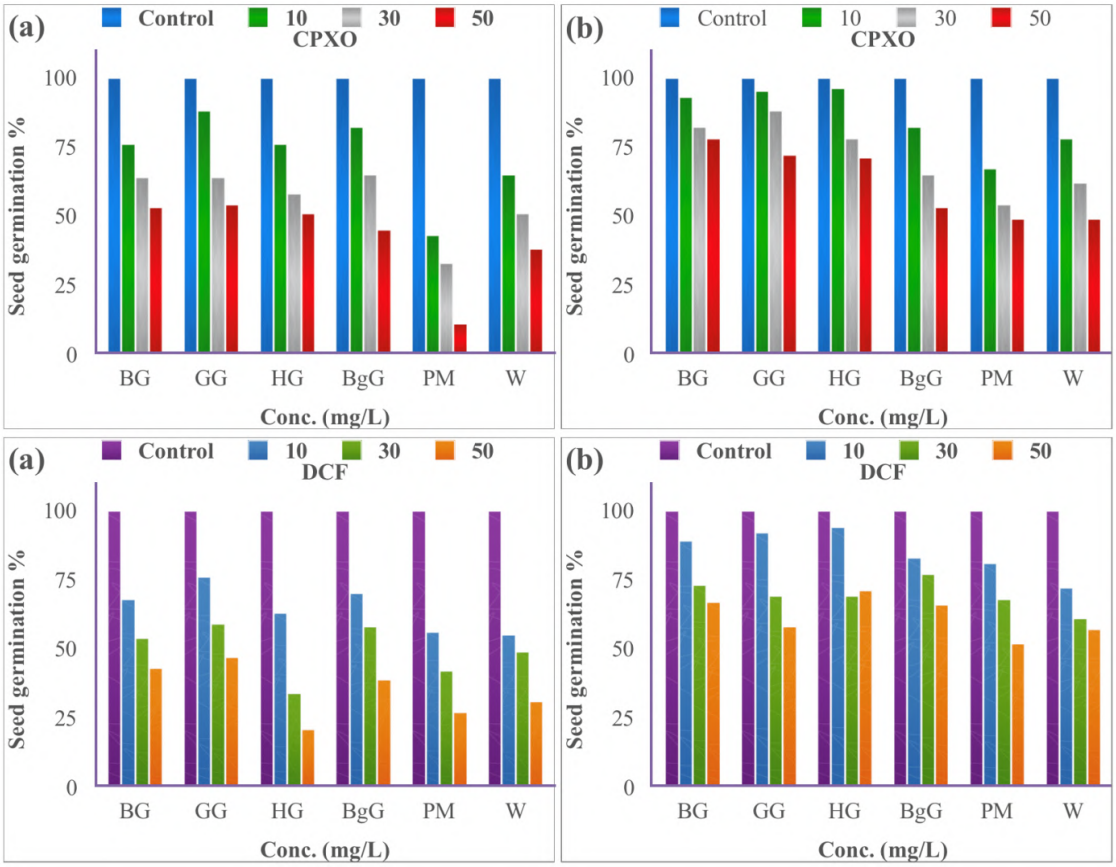

Fig. 5.7: Seed germination (%) of black gram, green gram, horse gram, Bengal gram, pearl millet and wheat seeds at various concentrations of CPXO and DCF a) before and b) after adsorption

TH-3150_176106114

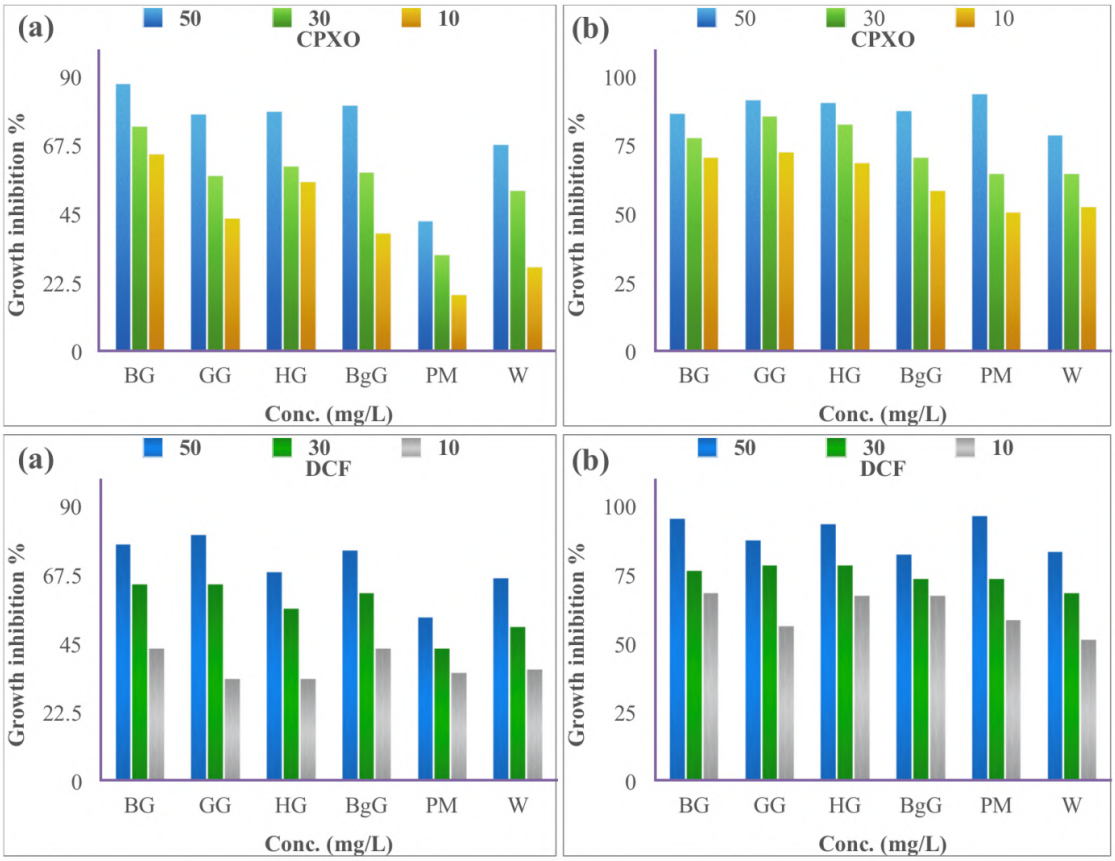

Fig. 5.8: Inhibition of growth (%) of black gram, green gram, horse gram, Bengal gram, pearl millet and wheat seeds at various concentrations of CPXO and DCF a) before and b) after adsorption

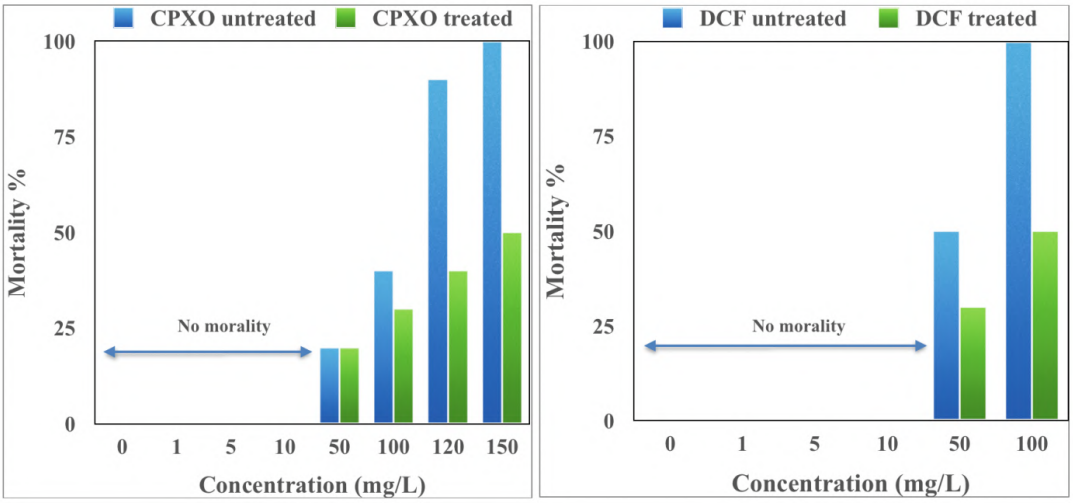

Fig. 5.9: Mortality (%) of *Danio rerio* (Zebra fish) to various concentrations of CPXO and DCF before and after adsorption

TH-3150_176106114

Table 5.6: Fish toxicity data of GNC on CPXO and DCF adsorption

Sl. No.	Conc. (mgL^{-1})	96 h no. of fish alive	Mortality %	96 h no. of fish alive	Mortality %
		For CPXO control		**For CPXO test**	
1	0	10	0	10	0
2	1	10	0	10	0
3	5	10	0	10	0
4	10	10	0	10	0
5	50	8	20	8	20
6	100	6	40	7	30
7	120	1	90	6	40
8	150	0	100	5	50
		LC_{50} = 100 mgL^{-1}		LC_{50} = 150 mgL^{-1}	
		For DCF control		**For DCF test**	
1	0	10	0	10	0
2	1	10	0	10	0
3	5	10	0	10	0
4	10	10	0	10	0
5	50	5	50	7	30
6	100	0	100	5	50
		LC_{50} = 50 mgL^{-1}		LC_{50} = 100 mgL^{-1}	

TH-3150_176106114

5.3. Significant findings

As an approach toward green nanotechnology, cellulose extracted from *Cyperus rotundus* grass was scaled down to nanocellulose for efficient removal of antibiotic Ciprofloxacin (CPXO) and anti-inflammatory agent Diclofenac (DCF). Different characterization analyses showed the conversion of nano-sized GNC which was used as a great adsorbent in a maximum of 3 hours with 91 and 89% removal for CPXO and DCF respectively under optimized experimental conditions. Adsorption kinetics fitted well with PSO and Halsey adsorption isotherm for both the pollutant. Thermodynamics study showed the process is exothermic, feasible and spontaneous in nature. Phytotoxicity studies with 6 different seeds showed a lesser effect of GNC-treated effluent on them as compared to control groups that were not treated with GNC. Further acute fish toxicity was revealed to have very little effect of the treated CPXO and DCF solution on model zebra fishes with tolerance levels up to 120 and 150 mgL^{-1} respectively. This GNC showed excellent efficiency for these emerging pollutants with great adsorptive capacity and could be commercialized with its high and cheap availability as well as conversion to the final product.

TH-3150_176106114

Chapter 6

Magnetic nanocellulose from *Cyperus rotundas* grass in the absorptive removal of rare earth element cerium (III): Toxicity studies and interpretation

The work embodied in this chapter is published in

TASRIN SHAHNAZ, Vishnu Priyan V., Anjali J. and Selvaraju Narayanasamy*, Magnetic nanocellulose from *Cyperus rotundas* grass in the absorptive removal of rare earth element Cerium (III): toxicity studies and interpretation. **Chemosphere, 2021, (Elsevier, SCI IF: 8.943)**

TH-3150_176106114

Abstract

In this study, a very common grass named *Cyperus rotundas* was used to extract cellulose which was converted to magnetic grass nano cellulose (MGNC) to adsorb the rare earth element Cerium (Ce(III)). The prepared MGNC was analyzed with sophisticated techniques to determine the alteration in physical and chemical properties before and after adsorption with the pollutant Cerium. Parameters like pH, temperature, MGNC dosage and initial concentration of Ce were optimized to check parameters influencing the adsorption of Ce(III). The optimized experimental data were perfectly modelled into the Langmuir model with an adsorption capacity of 353.04 mgg^{-1} for Ce(III). For kinetics, the data fitted into a pseudo-second-order model. To check the efficacy of MGNC in a real scenario, untreated and treated Ce was used for phototoxicity studies with 4 different plant seeds. Apart from this, model fish, *Danio rerio* was used to check the toxicity level on aquatic organisms before and after adsorption of Ce(III) with MGNC. This study showed the efficient use of MGNC and maximum removal of Cerium from wastewater and the magnetic behaviour incorporated the advantage of easy retrieval. Graphical representation is shown in Scheme 6.1.

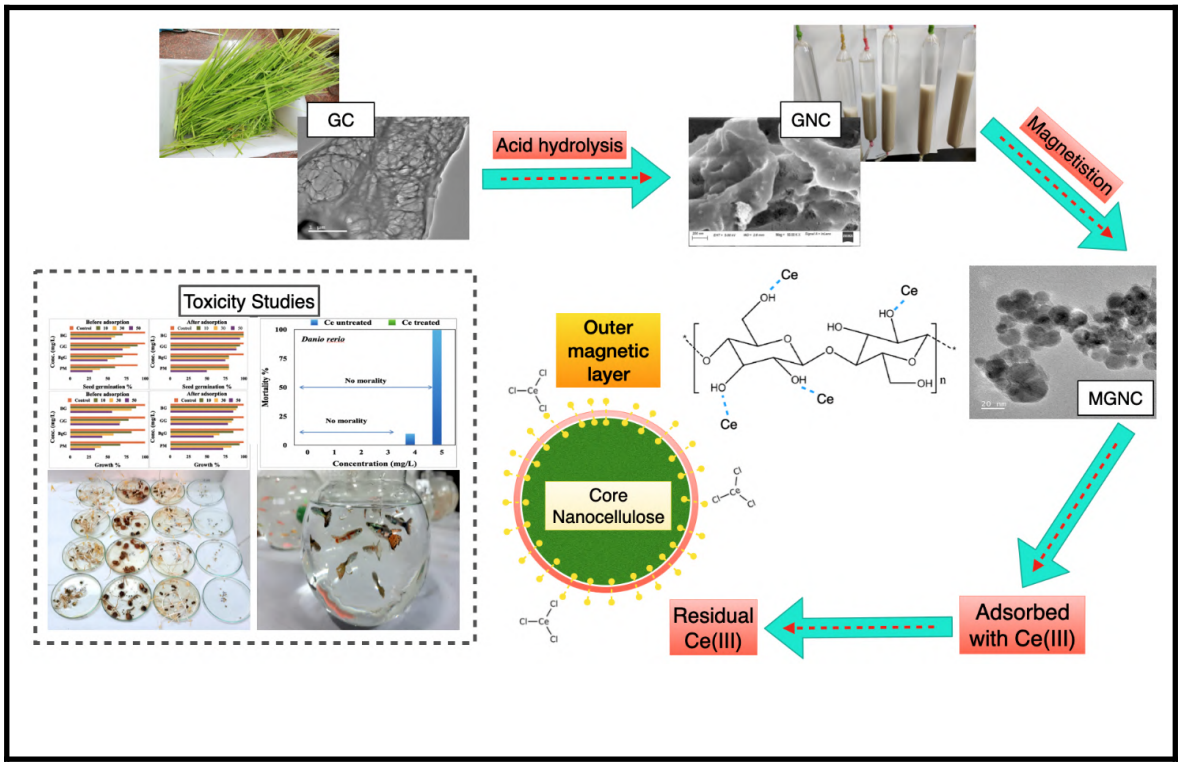

Scheme 6.1: Graphical Abstract

TH-3150_176106114

6.1. Materials and methods

6.1.1 Chemicals

Analytical grade Cerous trichloride heptahydrate from Sigma Aldrich was procured and the stock solution of 1000 mgL^{-1} was prepared. Further experiments were done by diluting the stock with deionized water as needed. Other chemicals such as ammonia solution, hydrogen peroxide, ferrous chloride heptahydrate, sulphuric acid, ferric chloride hexahydrate, and sodium hydroxide were purchased from HiMedia (analytical grade). All the experiments except fish toxicity studies were done in a solution prepared in distilled water (Mili Q) (Shahnaz et al., 2021).

6.1.2. Preparation of MGNC

Cyperus rotundus grass was used to extract cellulose with $NaOH/H_2O_2$ method and converted it to nano cellulose. The process to convert cellulose to nano cellulose involves sulphuric acid hydrolysis and dialysis with a membrane of 12000-14000 molecular weight cut off against deionised water until the solution reached neutral pH. The detailed method has already been published in a previously published study by the author group (Tasrin et. al, 2020). The nanocellulose suspension in its original wet form after bath sonication was used to prepare Magnetic Nanocellulose (MGNC). In 100 mL of distilled water $FeCl_3.6H_2O$, and $FeCl_2.4H_2O$ were added in a 2:1 ratio and stirred continuously in a magnetic stirrer. To this solution, the nanocellulose mixture was added and again stirred for 16 h at 80 °C. To that 10% ammonia solution was mixed very slowly and let the colour of the solution turn bluish-black and further stirred at 60 °C for 1 hour. Later the suspension was filtered and washed with ethyl alcohol several times. Then the prepared MGNC was dried at 60 °C for 24 h in an oven and stored for further study.

6.1.3. Characterization

To get detailed properties of biosorbent MGNC before and after adsorption, various morphological, elemental and fingerprinting characterisations were used with sophisticated techniques. To study the surface morphology of MGNC and the elements present, an energy dispersive spectroscopy equipped with scanning electron microscopy (Make: Zeiss, Model: Sigma) was used. Transmission electron microscopy (Make: JEOL, Model: 2100F) further confirmed the adsorbent surface and dimension to be in the nano range. SAED pattern was checked to know the crystal arrangement type of the sample. Radiator-equipped Atomic

TH-3150_176106114

Force Microscope (Make: Oxford, Model: Cypher) was utilized to describe the dimensional properties as well as roughness parameters of the MGNC surface. An X-ray diffractometer (Make: Rigaku, Model: Micromax-007HF) was used to study the crystallinity of MGNC before and after the adsorption of Ce(III). The thermal stability of the MGNC was examined by a thermogravimetric analyzer (Make: Netzsch, Model: STA449F3A00). Magnetization of the sample was characterized by Vibrating Sample Magnetometer (Make: Lakeshore, Model: 7410 series).

6.1.4. Detection of Ce(III)

The cerium concentration before and after adsorption was measured with Atomic Emission Spectroscopy (Make: India, Model: Agilent Technologies, 4210 MP-AES) equipped with a 4107 Nitrogen Generator.

6.1.5. Effect of Co-existing ions

Common ions that are present in real wastewater are salts of NaCl, KCO_3^{2-}, $MgCl_2$, $KHP_2O_4^{3-}$, $CaCl_2$ etc. The effect of these ions on Ce(III) adsorption onto MGNC was checked using 10 ppm of Ce(III) solution with 0.1 M aqueous salt solution separately (Shahnaz et al., 2020).

6.1.6. Phytotoxicity

Seed germination rate and growth % of fast-growing plants are used to determine the environmental toxicity of Ce(III) following the guidelines of U.P. EPA, 1982 with a few changes (Xie et al., 2019). For phytotoxicity studies, two important measures include longer shelf life along with a good germination rate. This is to avoid errors in the control test group and to ensure a higher germination rate. In the present study four varieties of seeds viz. *Vigna mungo* (black gram/BG), *Vigna radiata* (green gram/ GG), *Pennisetum glaucum* (pearl millet/ PM), and *Cicer arietinum* (Bengal gram/BgG), were taken and incubated with treated and untreated Ce(III) solution. A total of 16 test groups with 10 properly rinsed and pre-treated seeds were spread evenly in separate Petriplates of 7.5 cm diameter for a week in dark conditions at 25 ^{0}C (Nouren et al., 2017, Dhaouefi et al., 2019). Test groups contained 0, 10, 30 and 50 mgL^{-1} of Ce(III) solution before and after adsorbed with MGNC where 0 mgL^{-1} was taken as blank. Other 6 groups were Ce(III) (10), Ce(III) (30), Ce(III) (50), Ce(III) [(10) +MGNC)], Ce(III) [(30) +MGNC], Ce(III) [(50) +MGNC] for each seed variety to check the

TH-3150_176106114

capacity of MGNC to reduce the toxicity of the pollutant. Below equation (6.1) was used to calculate the germination rate of the seeds after 7 days along with growth % by measuring the average root and shoot length of each seed.

$$\% G = (\text{No. of germinated seeds/Total seeds used}) \times 100 \quad (6.1)$$

6.1.7. Acute fish toxicity

Zebrafish (*Danio rerio*) procured from a market (licensed) were used to perform acute fish toxicity and followed the Test Guideline No. 231, 2009 Fish acute toxicity testing of OECD. Fish were sorted according to approximate size and age and acclimatized for 1 week in a laboratory environment at 25 ^{0}C. Treated and untreated Ce(III) solutions were taken and 10 fish were exposed to each experimental set for 96 h. With solution pH maintained around 6.5-7.5, oxygen concentration (>75% of air saturation) concentrations of 1,2,3,4,5 mgL^{-1} at room temperature were started gradually from lower concentration. A total of 10 test groups for the fish with treated and untreated Ce(III) were analyzed for mortality % with a solution without Ce(III) kept as a control. After every 24 h, each treatment group were monitored for fish death and noted. As a widely used measure of acute toxicity LC_{50} (lethal concentration 50) denotes the concentration of a particular substance capable of killing half the population of an experimental group in a specific incubation period. Ce(III) LC_{50} value was determined for the fish from the data generated periodically (Hossam Mahmoud et al., 2020).

6.2. Results and Discussion

6.2.1. Characterization of MGNC

MGNC was characterized to view the surface morphology with FESEM, FETEM, and AFM. From Fig. 6.1 (GC), the raw grass cellulose (GC) looks like a highly fibrous material that takes a sheet-like structure after successful conversion into grass nano cellulose (GNC) and can be seen in Fig 6.1 (GNC). After this, the GNC was magnetized (MGNC) to incorporate the advantage of easy retrieval after application. The FESEM image (Fig. 6.1 (MGNC)) and FETEM (Fig. 6.1 (MGNC TEM)) of MGNC showed the sponge-like highly porous structure and increased surface area. The same MGNC after adsorbed with Ce(III) is shown in the next image with a smooth surface indicating maximum adsorption on MGNC (Fig. 6.1 (MGNC-Ce)). The sample was confirmed to be polycrystalline in nature as shown in Fig. 6.1 (MGNC

TH-3150_176106114

SAED) of the SAED pattern. The elemental composition of MGNC before and after adsorption was checked with EDS where the relative weight % of the rare earth element Ce(III) was calculated in comparison to Fe, C and O and found to be 0.7% (Fig. 6.2.A, 6.2.B). A high-performance Atomic Force Microscope was used to check the roughness, texture and waviness of the MGNC surface and put in Fig. 6.2.C. In Fig. 6.2.C, an image derived from a software called Gwydion (64 bit) showed the nano range dimension of MGNC which lie on the scale of 0.5 to 0.7 nm. Thermogravimetric analysis is a method where the mass of a sample is measured concerning time and temperature along with various physical and chemical alterations like a phase transition, adsorption/desorption, decomposition, phase reaction etc. can be evaluated (Patra et al., 2020). To understand the thermal stability of MGNC, TGA measurements were carried out and plotted in Fig. 6.2.E. The initial 10% weight loss was due to the evaporation of water molecules from MGNC. From the TG% curve, it can be seen that a sharp decrease in weight of 55% around 300-340 ^{0}C occurred due to various processes such as depolymerization or decomposition of glycosyl unit of nano cellulose to charred residual compound. The last degradation of the TGA run was seen after 650 ^{0}C which is probably due to the conversion of residue into gaseous form (Khan et al., 2020) with a residual weight of 19%. The DSC plot signifies the thermal response of MGNC where a peak from 90 to 300 ^{0}C shows an endothermic reaction as water takes heat to evaporate. Then 380-650 ^{0}C another broad endothermic peak prevailed where the nanocellulosic components degrade with the onset temperature of 355 ^{0}C and these obtained values are perfectly in line with TGA data. This results again in sequential behaviour with the DTG analysis where peak decomposition temperature was observed in two stages. Magnetization of MGNC was measured as a function of magnetic field and temperature. In Fig. 6.2.F the magnetization graph for the MGNC at room temperature shows ferromagnetic behaviour with magnetic saturation (M_s) at 0.18064 emu g $^{-1}$ with a coercivity (H_{ci}) value of 13.150 Oe.

TH-3150_176106114

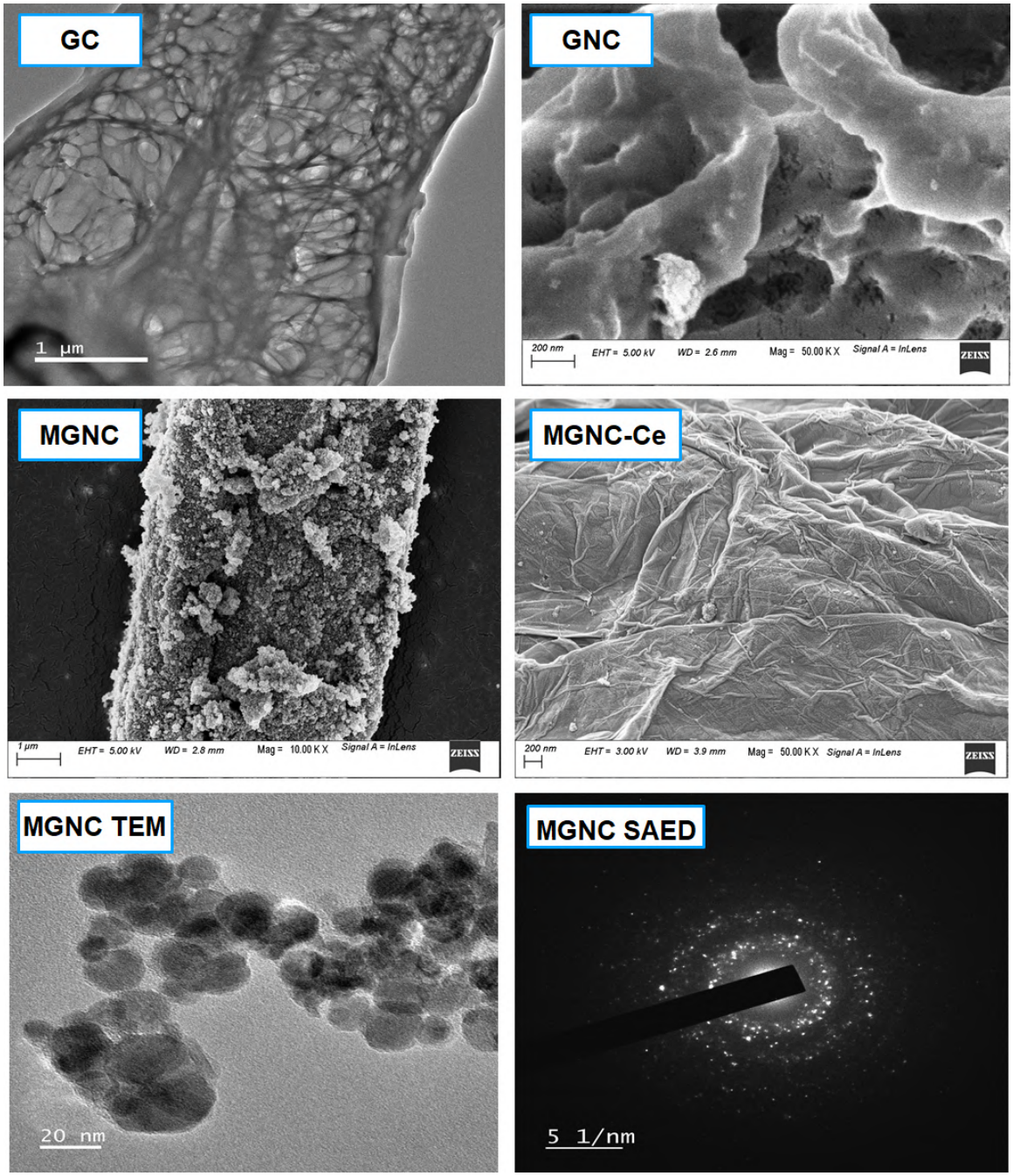

Fig. 6.1: FESEM spectroscopy of GC, GNC, MGNC, MGNC after treating Ce, FETEM spectroscopy of MGNC, and SAED pattern of MGNC

The purpose of applying magnetism in MGNC is to facilitate easy removal from the solution after treating the Ce(III), which also allows the sample to be used again after retrieving. Another efficient nondestructive analytical method called XRD that employs the principle of Bragg's law was utilized to determine the crystallinity of MGNC using copper k alpha

TH-3150_176106114

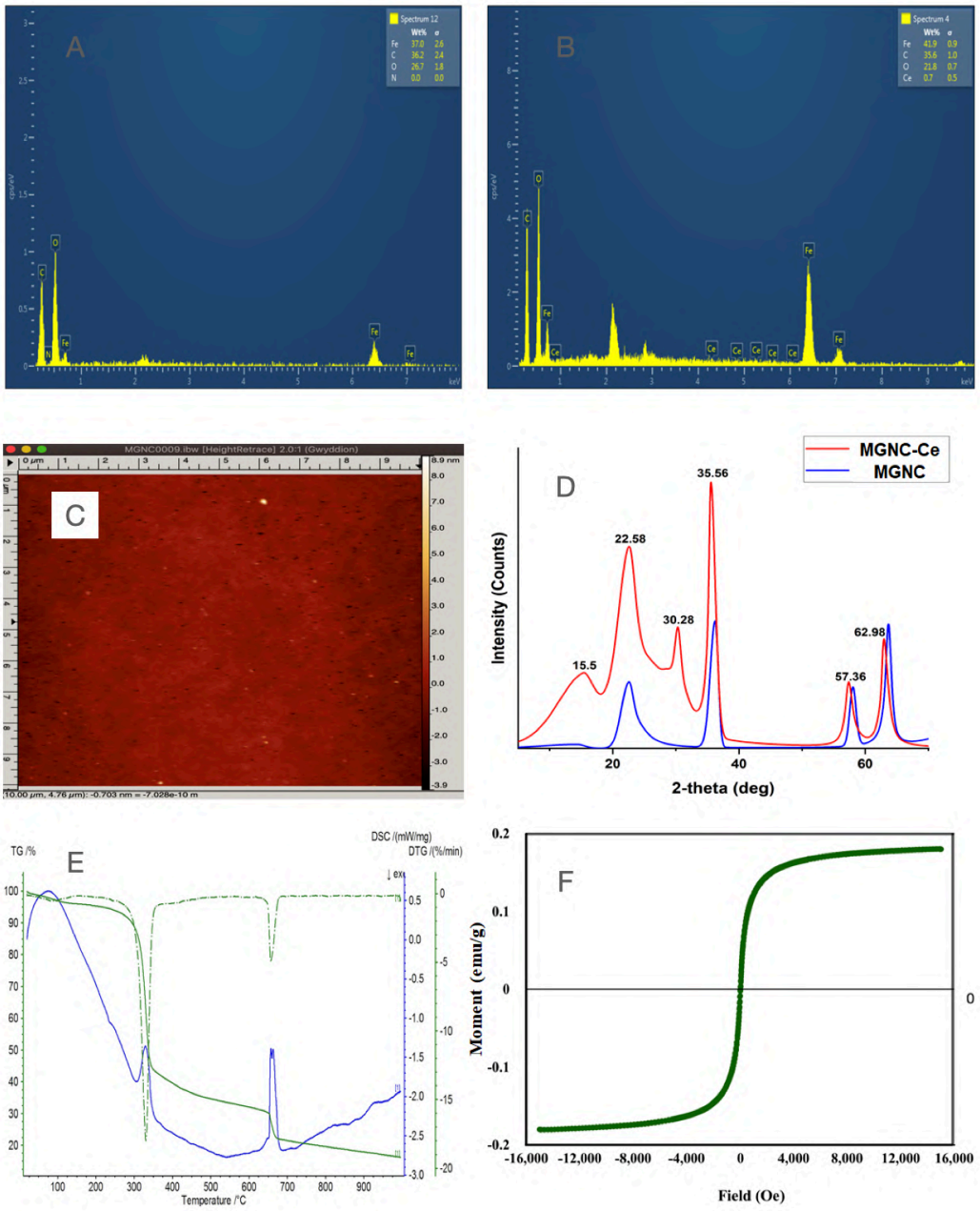

Fig. 6.2: EDS before Ce adsorption (A), EDS after Ce adsorption (B), AFM (C), XRD (D), TGA (E) and Magnetic hysteresis (F)

radiation (Xu and Wang, 2017, Hosseynizadeh Khezri et al., 2012). Both pre and post Ce(III) biosorption data were plotted in Fig. 6.2.D where three sharp peaks observed at 15.5, 22.58 and 35.56 signify nanocellulose components whereas after magnetizing the sample additional peaks for the iron particle as magnetite showed up at 35.56, 57.36 and 62.98 which are by literature report as well. In the graph MGNC with Ce peaks specific for cerium can be seen at angles 35.56, 57.36, and 62.98 which overlaps with the peak observed from magnetite as well. One peak only for cerium at 30.28 was observed (Hosseynizadeh Khezri et al., 2012).

TH-3150_176106114

The phase of the metal in the XRD profile can be predicted by the qualitative phase identification method where single-phase cubic cerium oxide formation can be seen for the MGNC-Ce sample.

6.2.2. Influence of experimental parameters

Optimization of experimental parameters is crucial for any adsorption study. In the present experimental conditions, MGNC dosage, pH, temperature and initial Ce(III) concentration were optimized to obtain maximum removal efficiency.

6.2.2.1. Influence of pH

Among all the other experimental parameters, pH influences the most as variation in solution pH changes the overall ionic concentration along with surface properties of the adsorbent used. The initial concentration of 10 mgL^{-1} was checked from 1 to 9 pH at a temperature of 35 °C with an MGNC dosage of 5 mg in a shaking condition of 160 rpm for 3 h. It was found that from pH 1 to 4% removal increases gradually from 32 to 76% and reached a maximum at 89% for pH 5 and again drops till pH 9. Further experiments were carried out at pH 5 as considered optimum for Ce(III) (Huang et. al, 2021).

6.2.2.2. Initial concentration influence

To check the optimal initial concentration of Ce(III) simulated solution from 20-120 mgL^{-1} was taken and checked at pH 5 and 35 °C with a fixed dose of 10 mg MGNC under shaking incubation for 240 min (Tasrin et. al, 2021). As the initial concentration rises the removal reduces to 30%, however, the adsorption capacity increases. This happens as the adsorption site becomes saturated with the pollutant. The maximum adsorption capacity was found at 353.04 (400 mgL^{-1}) mgg^{-1}.

6.2.2.3. Effect of dosage

Lastly, MGNC dosage was selected from 10 mg to 50 mg and optimized for maximum removal efficiency of Ce(III) under the experimental condition of pH 5, in 20 mgL^{-1} Ce(III) solution and at the optimum temperature of 35 °C. Removal efficiency increased from 24 to 78% as the dosage was increased. It could be interpreted as the amount of MGNC exposed to Ce(III) was increased the adsorption surface and active functional sites for adsorption were increased (Zhao et. al, 2019).

TH-3150_176106114

6.2.2.4. Effect of ionic strength

Since all the laboratory experiments were carried out in simulated Ce(III) solution a separate test set where common salts present in real wastewater were taken into account. The purpose of this is to analyse the altered behaviour of MGNC towards Ce(III) in presence of these salt viz. KCO_3^{2-}, $ZnSO_4$, NaCl, $CaCl_2$, $CuSO_4$, KH_2PO_4, $MgNO_3$. In separate experiments where the salt solution in ionic form was mixed with Ce(III) solution in a 1:1 ratio (by strength) and allowed in shaking incubation with optimized pH, temperature and time. The data analyzed were plotted in Fig. 6.3 for easy comprehension. The removal of the control sample before adding any ionic salt was 79.42%.

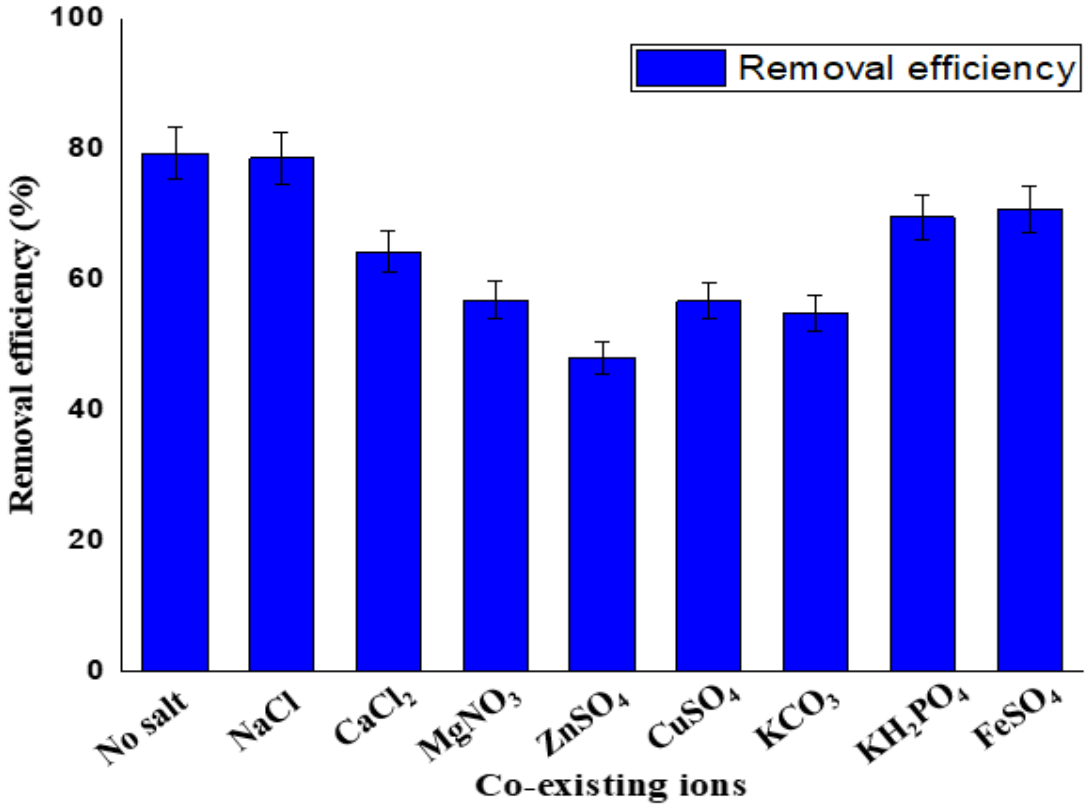

Fig. 6.3: Effect of co-existing ions on Ce(III) adsorption on MGNC

The descending order of removal after addition of ionic salts was as shown: NaCl(78.70%)>KH_2PO_4(69.65%)>$CaCl_2$(64.32%)>$MgNO_3$(56.91%)>$CuSO_4$(56.82%)> KCO_3^{2-}(54.89%)>$ZnSO_4$(48.12%). This order of decreased removal of Ce(III) can be explained by the phenomenon of hydration where either a cation or an anion attracts water

TH-3150_176106114

molecules to its vicinity. The smaller the size of the metal ion the greater will be the hydrated radii due to their more intense electric field. Therefore, when a solution with smaller hydrated radii ions competes with large pollutants they get selectively adsorbed resulting in less adsorption of Ce(III). However, after studying this effect of co-existing ions it can be concluded that MGNC could be used even in the presence of common ionic salts as it can effectively remove a minimum of half of the studied pollutant with just 10 mg of dosage.

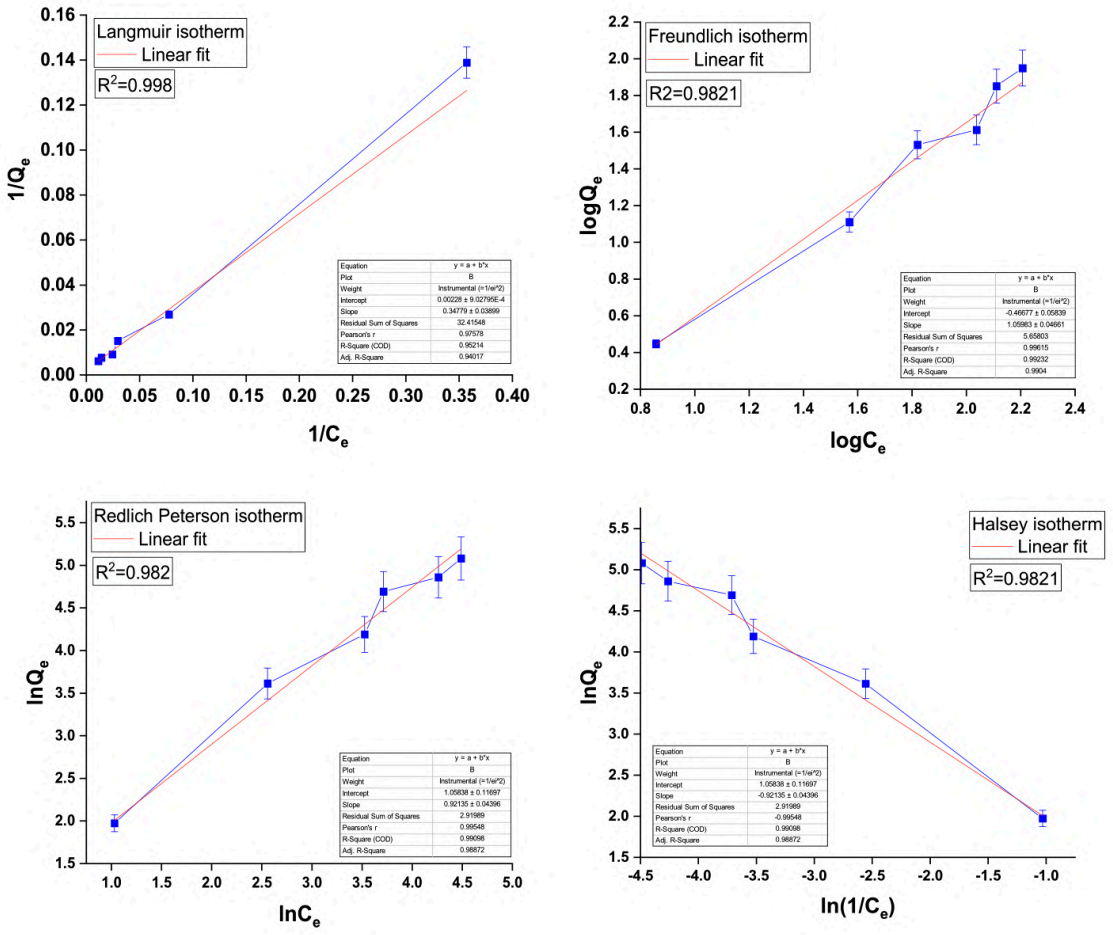

Fig. 6.4: Isotherm modelling plot

6.2.3. Isotherms

The optimized value of Ce(III) is fitted with four isotherms, among them Langmuir model agreed well with a maximum coefficient of determination (R^2) of 0.998 and standard error of 0.02 minimum (Fig. 6.4) with detailed statistical analysis. Langmuir isotherm suggests the adsorption to be monolayer with the presence of finite identical sites on MGNC for Ce(III) to adsorb. However, though the Freundlich model has a lesser fitting than Langmuir (with R^2

TH-3150_176106114

0.9821) the constant “n” values from the plots of $logq_e$ vs $logC_e$ were 0.91 lying between 0 to 10 indicating the chemisorption of Ce(III) onto MGNC is favourable.

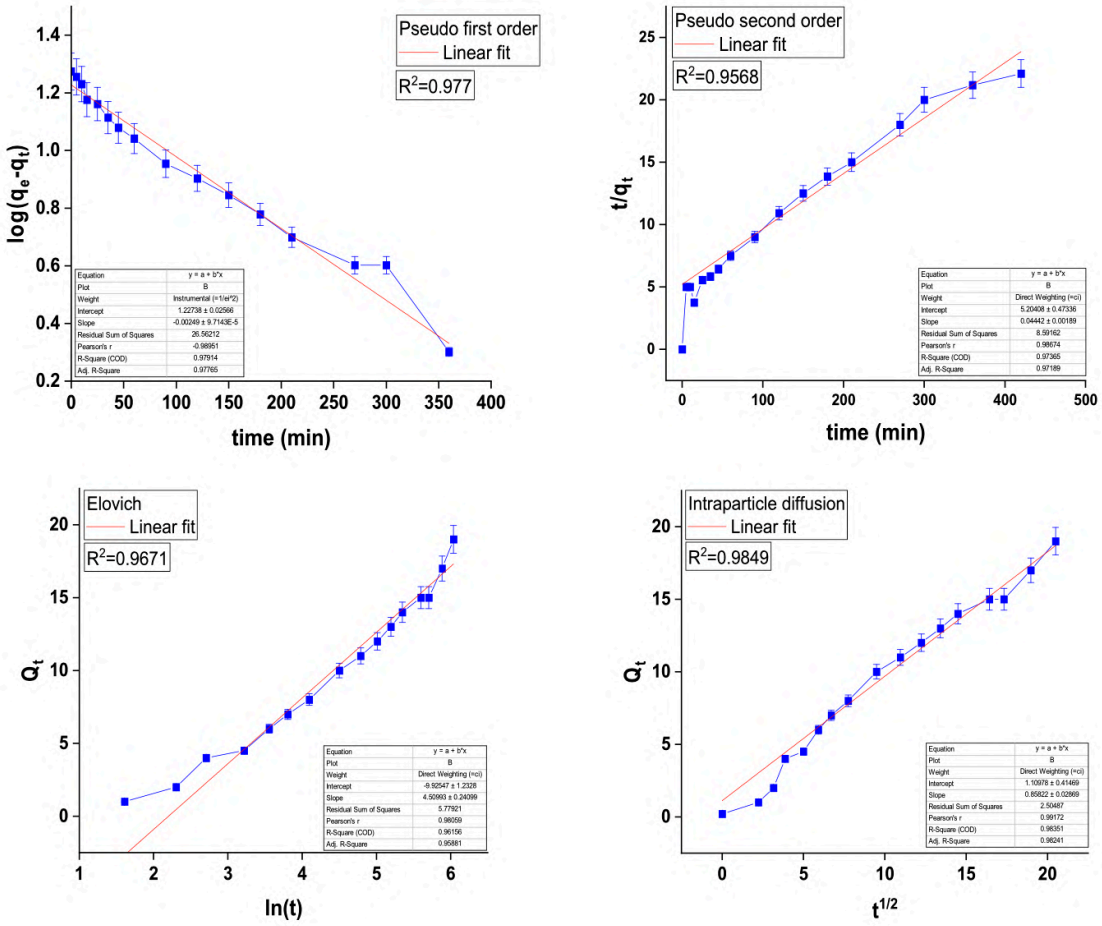

Fig. 6.5: Kinetics modelling plot

6.2.4. Kinetics

The kinetic models were fitted with the optimized data of Ce(III) adsorption on MGNC and analysed that Intra-particle diffusion (IPD) was the dominant model with a coefficient of determination (R^2) of 0.9849 maximum and standard error values (1.41) minimum when evaluating for a period of 420 min. The adsorption process is driven by diffused Ce(III) from the bulk solution to the film surrounding MGNC and then entering through the micropores of MGNC. This also supports the mechanism of the present adsorption study where MGNC was confirmed to have the magnetic outer layer covering the nano cellulose extracted from grass.

TH-3150_176106114

In Fig. 6.5, the regression plot of all the four kinetic models has been plotted with detailed statistical analysis.

6.2.5. Thermodynamics

Temperature plays a crucial role in the real scenario for the proper functioning of a biosorbent and hence a detailed study was performed to analyse the thermodynamics. A reaction that occurs without an external heat supply is said to be exergonic/spontaneous and is desirable. In this present study, the negative value of Gibb's free energy suggested the spontaneity of the reaction at all temperatures irrespective of concentration. It also confirms the energetically favourable nature of Ce(III) adsorption on MGNC. The enthalpy of the reaction being negative signifies that no external heat was required and the process is exothermic. The entropy value was found to be positive suggesting the increase in randomness of the biosorbent at the sorbate-sorbent interface (Table 6.1).

Table 6.1: Different thermodynamic parameters of Ce(III) biosorption onto MGNC

C_i (mgL $^{-1}$)	T	Ce(III)		
		ΔG°	ΔH°	ΔS°
1	303	-5.8280	-100.6103	306.1240
	308	-1.4490		
	313	-1.0210		
	318	-2.9040		
	323	-1.8990		
5	303	-6.3560	-123.8330	399.2900
	308	-0.4170		
	313	-2.2050		
	318	-3.2940		
	323	-2.4580		
10	303	-7.9070	-77.8486	249.0670
	308	-1.0890		
	313	-1.0890		
	318	-1.7810		

TH-3150_176106114

	323	-1.4290		
50	303	-6.8000	-48.7584	149.9260
	308	-1.0130		
	313	-1.1230		
	318	-1.1230		
	323	-1.2380		
100	303	-2.3460	-20.7120	61.1510
	308	-8.7990		
	313	-3.8380		
	318	-0.2220		
	323	-1.0080		

6.2.6. Phytotoxicity

The phytotoxic effects of Ce(III) before and after biosorption on various seeds of different plant species were investigated in this study. The toxicity was evaluated based on the rate of seed germination (%) and the growth of the seedlings (%) at different concentrations of Ce(III) solutions (10, 30, 50 mgL^{-1}). The seeds with distilled water are taken as a control for all groups. It is observed that control groups before the adsorption process showed 90 to100% of seed germinations. The seeds of BG, and GG shows a 100% germination rate and the seeds of BgG, PM show about 90% of germination. The reduction in seed germination may be due to the unhealthy seeds. At 10 mgL^{-1} of Ce(III) the germination of seeds is 70% (BG), 90% (GG), 70% (BgG) and 60% (PM). As the concentration of the cerium solution increases to 50 mgL^{-1}, the rate of seed germination of the various decreases rapidly to 55% for BG, 70% for GG, 50% for BgG and 30% for PM. The reduction in seed germination was due to the closure of stomata, damage in the membrane of seeds, and inhibition of certain enzymes and metabolic pathways by Ce(III) ions. After biosorption of Ce(III) by MGNC, we can observe that the rate of seed germination increases in all concentrations as seen in the. 6.7. At 50 $mgL^{-1,}$ the germination rate was found to be 95% for BG, 90% for GG, 75% for BgG and 50% for PM. Fig. 6.6 represents the growth (%) of seedlings of various plant species. In the control groups, we can observe 100% of growth in all seedlings. Before biosorption of

TH-3150_176106114

Ce(III), the growth of seedlings decreases as the concentration increases. At 50 mgL^{-1} of Ce(III) growth (%) was found to be 56% for BG, 66% for GG, 43% for BgG and 33% for PM respectively. The growth was inhibited due to ROS production and apoptosis in seedlings induced by high Ce(III) concentrations (Zicari et al., 2018). After the biosorption process, the growth of the seedlings tends to increase to 85.68% for BG, 78.54% for GG, 59% for BgG and 72.28% for PM. This confirms that MGNC effectively removed the Ce(III) ions present in the water and made the water toxic-free from Ce(III).

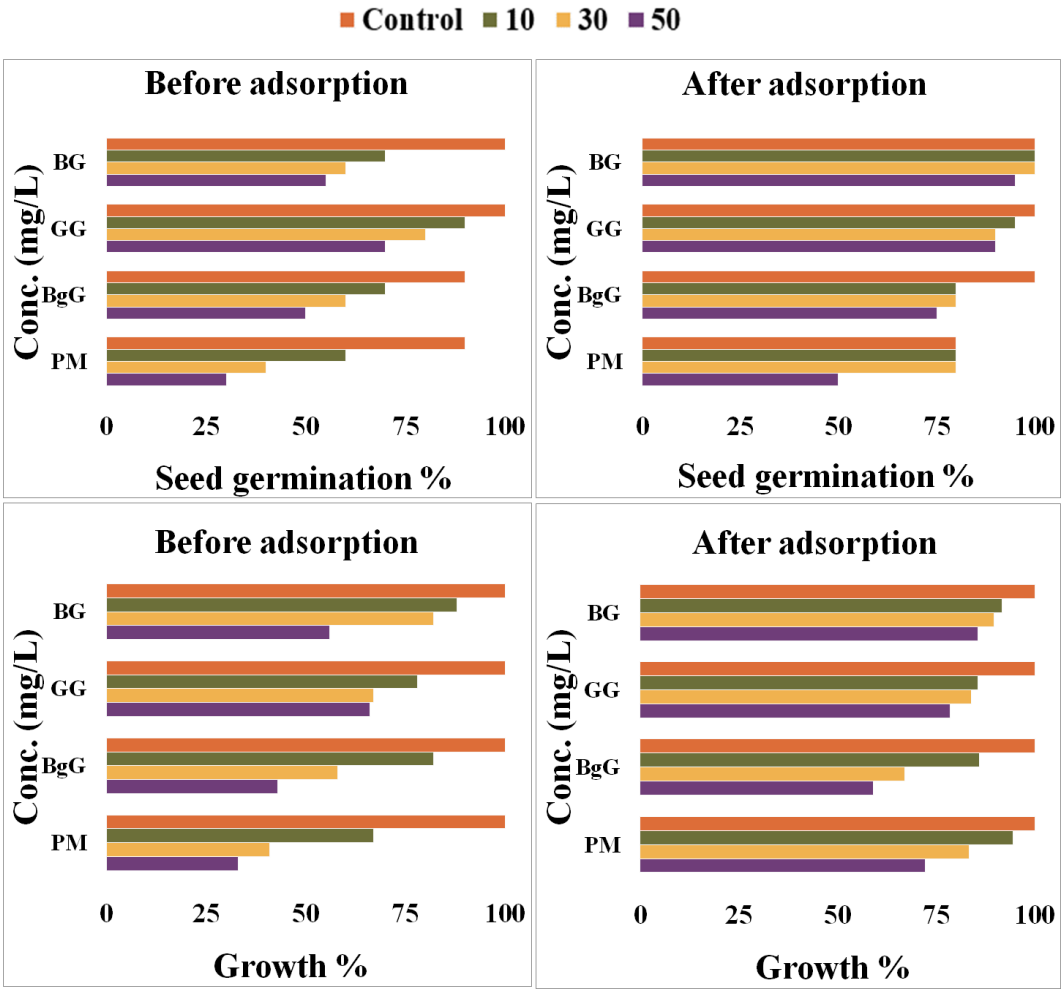

Fig. 6.6: Seed germination and growth (%) of black gram, green gram, Bengal gram and pearl millet seeds at various concentrations of Ce(III) before and after adsorption

6.2.7. Acute toxicity in fish

In this current study, treated and untreated Ce(III) was examined using zebrafish (*Danio rerio*) to analyse the level of toxicity. Untreated solutions at different concentrations showed toxicity at a higher level than the treated ones. In control group for zebrafish showed no

TH-3150_176106114

mortality till 3 mgL^{-1} of Ce(III) solution up to 96 h of incubation. At 4 mgL^{-1} after 72 h, the fish started showing abnormal behaviour like unusual swimming patterns with rapid movement, staying at the bottom of the tank and after 96 h 10% mortality rate was found. When the concentration was increased to 5 mgL^{-1} total mortality was observed in just 48 h causing all fish to die. Similarly, treated Ce(III) of the same set of concentrations with MGNC was also checked and found that after adsorption no fish death was seen for 5 mgL^{-1} with a mortality rate reduced to 100% (Fig. 6.7). Thereby assessing the efficacy of MGNC which can be utilized in the wastewater treatment process as an alternative.

After performing experiments on fish with test and control groups lethal concentration (LC_{50}) was determined using the probit model which is a unit measurement of statistical probability based on the deviation from the normal distribution mean. LC_{50} values for 24, 48, 72 and 96 h for zebrafish were found to be 4.607, 4.607, 3.940, and 3.940 mgL^{-1} when checked for the untreated control group. Whereas with the treated test group there was no mortality observed. From the derived data of the probit model graphs were prepared for easy understanding as shown in Fig. 6.7. The interpretation of the whole experiments with acute fish toxicity was to evaluate the reduced level of toxicity of Ce(III) when treated with biosorbent MGNC.

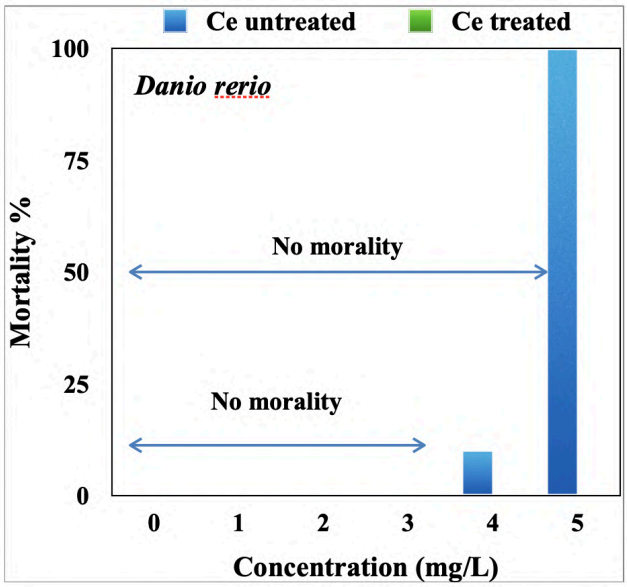

Fig. 6.7: Mortality (%) of Danio rerio (zebra fish) to various concentrations of Ce before and after adsorption

TH-3150_176106114

6.3. Significant findings

GNC was prepared using sulphuric acid hydrolysis of cellulose extracted from *Cyperus rotundas* grass and then magnetization using ferrous sulphate and ferric chloride co-precipitation on the GNC surface. This step facilitates the easy retrieval of the sample after adsorption. The successful conversion of grass cellulose to nanocellulose was confirmed with FESEM, FETEM and AFM analysis. The vibrating sample magnetometer showed the ferromagnetic behaviour of the prepared adsorbent MGNC whereas the crystallinity of MGNC was confirmed by the X-ray Diffraction pattern. The effect of common ion present in the real sample showed little alteration of Ce(III) removal which is desirable. The highest adsorption efficiency was found at pH 5 which is 353.04 mgg^{-1} which shows MGNC to be an excellent alternative to removing the rare earth element Cerium. Isotherm, kinetics and thermodynamics study further support the favourability of the present work. This work is expected to provide a new approach to studying and developing a more effective waste removal method and further study with different pollutants is underway.

TH-3150_176106114

Chapter 7

Cyperus rotundus as a new cellulose source for remediation of Basic Fuchsine dye: A static and flow adsorptive approach

Abstract:

Dye concentration even if accumulates in a very low amount cause a severe impact on the aquatic flora and fauna and eventually end up in human through the food chain. Among various classes of dyes, basic dyes are classified as the most harmful due to their toxic, allergenic, carcinogenic and resistant behaviour to biodegradation. In the present study "basic fuchsine" dye was used to adsorb on cellulose extracted from a commonly found grass species *Cyperus rotundus* in both batch and column mode. Experimental conditions were optimised and isotherm, kinetics, and thermodynamics of the process were analysed for batch mode. Further, in continuous mode, a fixed column was used to study the real-time behaviour of the adsorbent towards the adsorbate. The data derived were fitted in models such as Thomas, Adams, Yoon Nelson and Bed Depth Service Time model and found that maximum adsorption capacity to be 318.45 mgg^{-1} with a maximum of 97% removal efficiency. Additionally, the main mechanism of the dye adsorption onto the adsorbate was discussed.

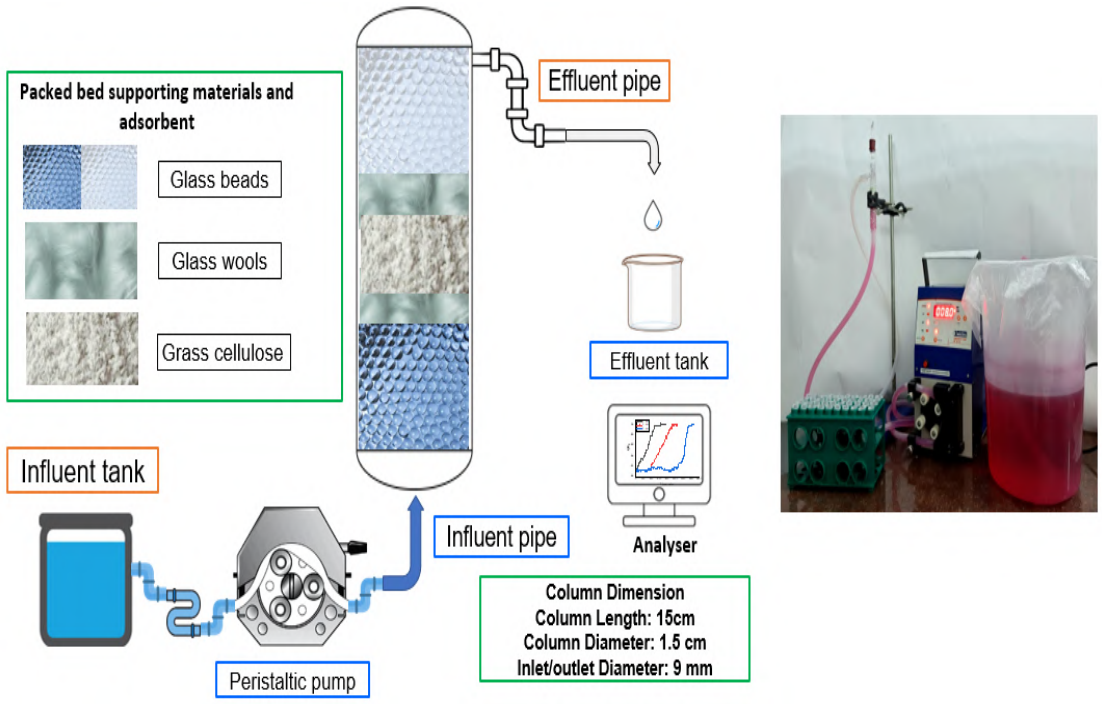

Scheme 7.1: Graphical abstract

7.1. Materials and methods

7.1.1. Materials

Analytical grade dye Basic Fuchsine (BF), hydrochloric acid, sodium hydroxide, ethanol, and hydrogen peroxide were procured from HiMedia and 1000 mgL^{-1} BF was prepared as a stock solution. All the experiments were conducted in MiliQ distilled water.

7.1.2. Preparation of Grass Cellulose (GC)

The grass sample was prepared by the literature reported by the same author group previously (Shahnaz et al., 2021). This commonly available grass (*Cyperus rotundus*) was collected in bulk and treated with ethanol, sodium hydroxide and finally hydrogen peroxide to remove lignin and hemicellulose parts leaving behind only cellulose part. The dried cellulose when analysed was found to be 97% pure which was used for all the experimental procedures.

7.1.3. Water regain experiment

This is an important study to check the fibrous network of GC water holding capacity. First, the dry GC was weighed accurately and for around 120 min submerged in deionised water. The excess water was filtered through a filter paper and then weighed. The water regain capacity was checked with the formula below:

$$Water\ regain = \frac{(W_\omega - W_d)}{W_d} * 100\% \quad (1)$$

where W_d is the weight of the dry sample and W_w is the wet sample weight (Li et al., 2021).

7.1.4. Detection of Basic Fuchsine

The dye concentration was measured with a UV-Visible Spectroscopy before and after adsorption (Model: Tecan Infinite multimode plate reader, Make: Switzerland) with a unique band of adsorption at a wavelength (λ =) 620 nm.

7.2. Results and discussion

7.2.1. Morphological and textural analyses of the adsorbent

7.2.1.1. FESEM analyses

GC and adsorption of the GC with basic fuchsine dye were analysed for the surface morphology as shown in Fig. 7.1a. The raw sample exhibits a rough texture and long channel-type appearance (Shahnaz et al., 2021). While the dye-treated sample (Fig. 7.1b) can be observed with a much smoother and homogeneous surface. The natural form of cellulose is capable of adsorbing larger dye molecules due to their greater exposure to evenly distributed functional groups (Wang et al., 2021; Wu et al., 2021; H. Yang et al., 2021).

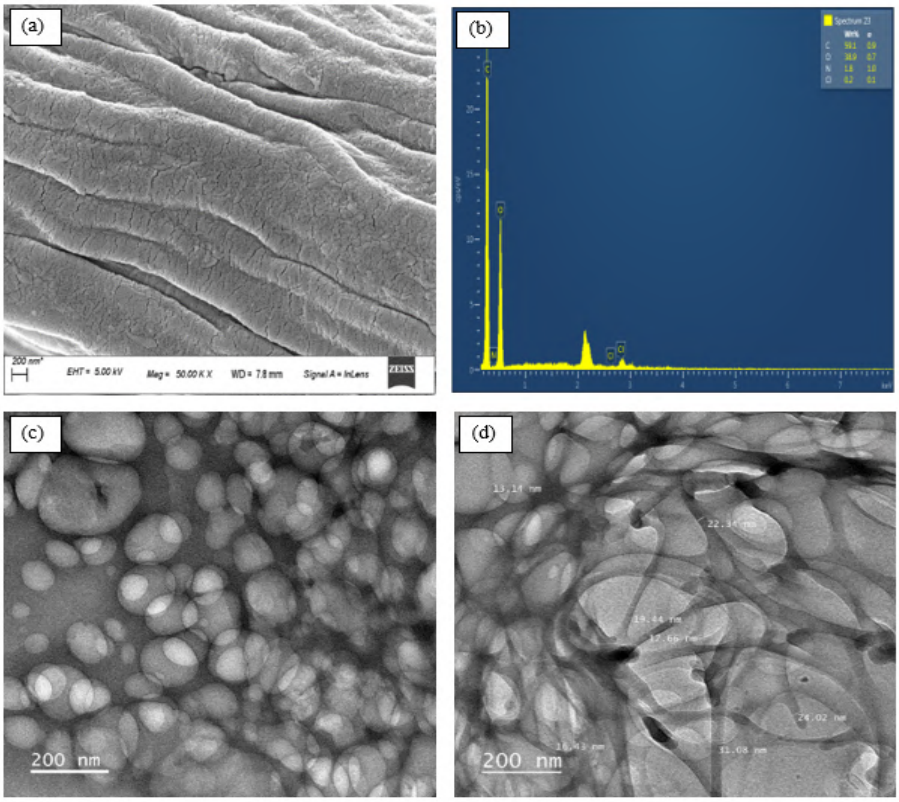

Fig. 7.1: FESEM, EDX and TEM spectroscopy of GC

7.2.1.2. FETEM analyses

The high-resolution morphology of the adsorbent was obtained from a transmission micrograph where the sample was prepared through drop-casting of diluted GC on a copper mesh (Vishnu Priyan et al., 2021). The perfect fibrous network can be seen in Fig.

7.1c and 7.1d where the cellulose fibres form a spherical network and thereby providing extra sites for the dye particle to get adsorbed. The majority of the fibre breadth dimension lies from 13 to 30 nm.

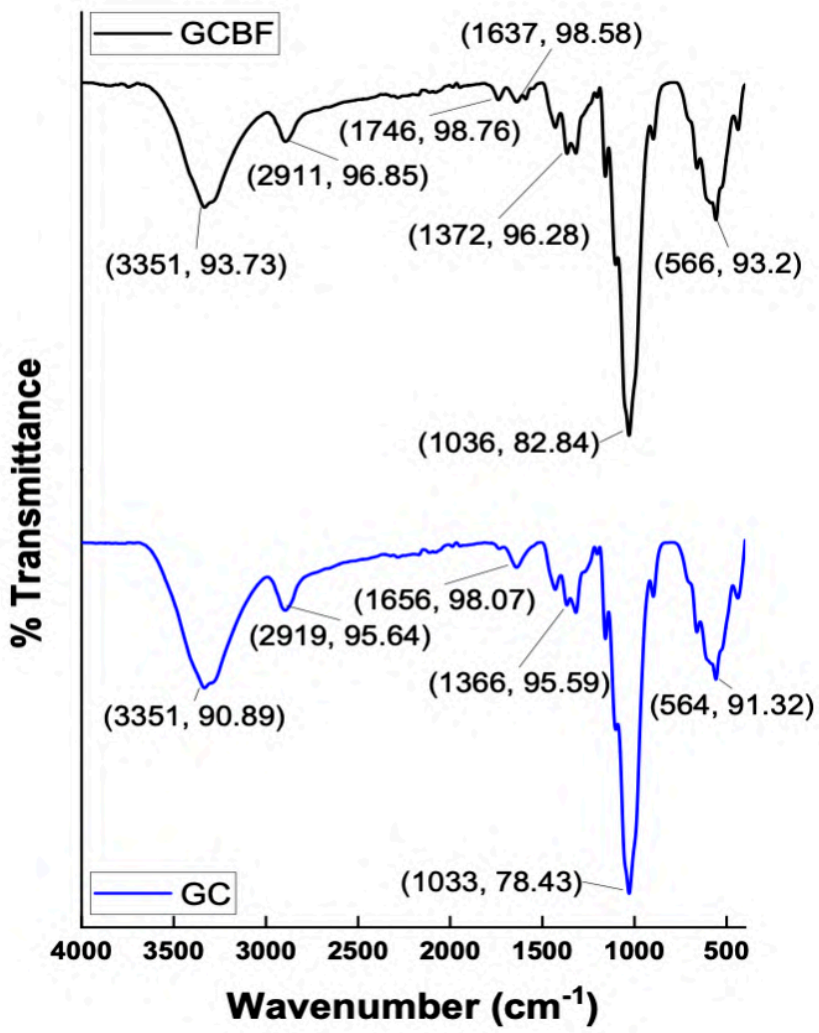

Fig. 7.2: FTIR analysis of GC (before and after) BF adsorption

7.2.1.3. Energy Dispersive Spectroscopy

Before and after adsorption of BF onto GC were checked with Energy Dispersive Spectroscopy where significant peaks of chlorine and nitrogen were observed with 0.2 and 1.8 wt % respectively which are the component of basic fuchsine dye (Sun et al., 2017). A relatively higher % of N as compared to Cl is also observed due to the presence of N

molecules in the complex aromatic ring structure. Whereas raw GC has only carbon and oxygen in its elemental presence.

7.2.1.4. FTIR analysis

Fig. 7.2 presents the FTIR analysis of GC before and after adsorption of BF. The broad peak around 3350 cm^{-1} was attributed to the -OH stretch of cellulose in both the samples in an intermolecular fashion. The peaks at 2911, and 2919 cm^{-1} are related to asymmetrically stretching vibrations of C-H groups and also weak -OH bending in an intramolecular fashion. The peak at 1656 cm^{-1} is due to C=C stretching in GC whereas peaks at 1746 cm^{-1} correspond to strong C=O stretching, -CH bending and 1637 cm^{-1} involves -NH bending for adsorbed aromatic basic fuchsine structure. The peak at 1637 cm^{-1} also corresponds to the presence of the water molecule in GCBF. Weak peaks around 1366 cm^{-1} and 1372 cm^{-1} in GC and GCBF respectively are due to -OH bending. A very sharp peak at 1033 cm^{-1}, and 1036 cm^{-1} are observed due to C-O stretching in GC and GCBF (Shahnaz et al., 2020).

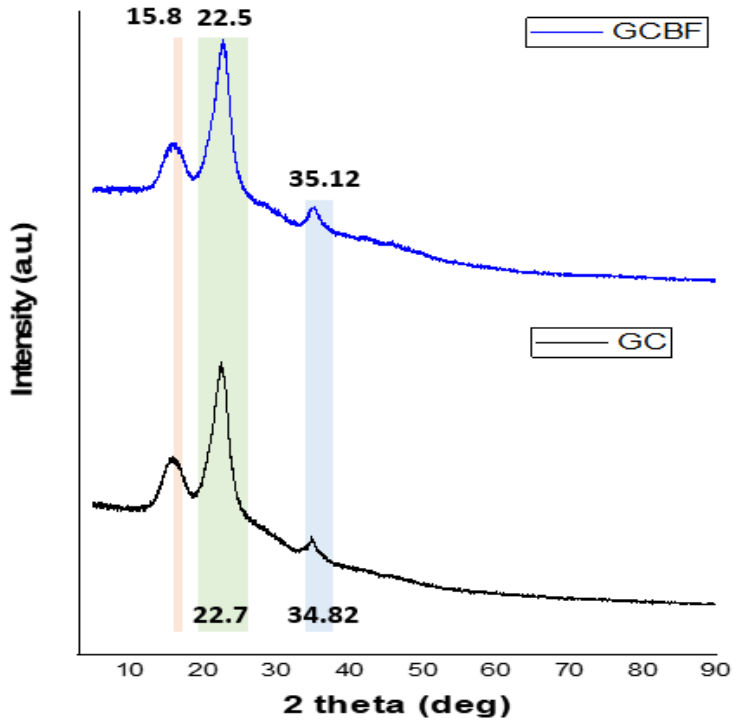

Fig. 7.3: XRD analysis of GC and GCBF

7.2.1.5. XRD analysis

The X-ray diffraction pattern was analysed by irradiating the raw GC and GCBF with CuKa1 with a wavelength of 1.54 nm. Prominent peaks were found in the range 2Θ =11.71 to 43.92°. The crystalline structure was found to be monoclinic with cell parameters a = 7.87, b = 10.31 and c = 10.13. The peaks found around 15°, 22.5° and 35° are common in both raw cellulose and GCBF. The characteristic broad peak at 15.8° indicates the amorphous type of the sample. From various works reported previously, basic fuchsine is known to have a distinguished peak at 26.88° which is expected to be merged with cellulose as shown in Fig. 7.3. This analysis verified that the ordered crystalline structure remained the same after adsorption which is desirable for the reuse of the adsorbent (H. Yang et al., 2021).

7.2.2. Static adsorption studies

To obtain the correlation between BF dye and GC molecules, five isotherm models viz. Langmuir, Freundlich, Dubinin-Radushkevich, Temkin and Halsey were fitted to the experimental data (Hu and Wang, 2019) (Fig. 7.4a). Isotherm models give the mechanism of the adsorption process and thereby hold a significant place in evaluating any sorption process. Halsey isotherm fits the data well which signifies the heterogeneous distribution of active sites and multilayer adsorption of BF molecules on GC. Regression (R^2) values for Langmuir, Freundlich and Dubinin-Radushkevich isotherm, showed a low fit as compared to Halsey adsorption isotherm. Empirical parameter (n) values of the Freundlich isotherm model for all the adsorbents were greater than 1, thus favouring the adsorption phenomenon at all temperatures. Moreover, the Temkin model also showed a closer regression coefficient confirming the decrease in heat of adsorption by GC linearly with the increase in the GC surface. It also suggests the uniform distribution of binding energy. From the rate of the process studies, it was observed that PSO kinetics fitted well with the experimental data and also the standard error value for this was the minimum as compared to the other models checked (Zhao et al., 2017, Ajmani et al., 2019). The plot showing PFO, PSO, and Elovich were shown in Fig. 7.4b. The equilibrium adsorption capacity determined through this model [q_e (cal)] is closer to the experimental values [q_e (exp)], which shows that the adsorption is controlled by the chemical reaction rate. Further, the

regression value of the plot of t/q_t vs t passes through the origin, the driving force behind the adsorption of BF onto the GC surface might be due to the sharing and exchange of electrons. From the thermodynamics analysis, it was found that when the temperature was increased from 30 to 50 ^{0}C there will be increased mobility of the molecule of BF along with decreased viscosity of the reaction solution which further enhances the process of adsorption. The positive enthalpy suggests the endothermic nature of the adsorption system whereas increased randomness at the adsorbent structure confirms the positive entropy and feasibility of the process. The negative Gibbs free energy indicates the spontaneity of the sorption process which is energetically favourable (Bessashia et al., 2020).

7.2.3. Fixed bed flow studies

For designing an operational fixed-bed column set-up, satisfactory modelling of the breakthrough curve is important which provides information about the effect of flow rate (Q, mLmin^{-1}), initial concentration (C_0, mgL^{-1}), bed height (Z, cm) on the adsorption capacity and yield % of the adsorbent (Adeniyi et al., 2019; Bhoumik et al., 2013; Meneses et al., 2022). Figure 7.5 shows the influence of these parameters on the breakthrough curve of BF adsorption onto GC along with a table listing all the numerical findings of the key experimental parameters viz. breakthrough time (t_b, min), BF adsorption amount (q_{total}, mg), effective volume ($V_{eff,}$ L), and yield rate (Y, %) obtained from the breakthrough curves.

Table 7.1: Evaluation of column data at various conditions for adsorption of BF removal using GC

w	u	Z	F	C_o	time	m_{total}	q_{total}	q_e (exp.)	V_{eff}	Y
Wt. of GC	($cmmin^{-1}$)	(cm)	($mL\ min^{-1}$)	(mgL^{-1})	(min)	(mg)	(mg)	(mgg^{-1})	(L)	(%)
0.50	0.0010	1.00	8	10.00	920	79.60	75.86	151.72	7.96	95.30
0.50	0.0007	1.00	8	15.00	695	169.80	159.23	318.45	11.32	93.77
0.50	0.0014	1.00	8	5.00	1335	27.80	27.02	54.03	5.56	97.18
1.00	0.0014	2.00	6	10.00	1430	113.20	110.45	110.45	11.32	97.57
1.00	0.0014	2.00	8	10.00	1275	84.90	81.56	81.56	8.49	96.07
1.00	0.0022	2.00	10	10.00	815	89.00	83.13	83.12	8.90	93.39
1.50	0.0021	3.00	8	10.00	1415	113.20	110.43	73.62	11.32	97.55

7.2.3.1. Influence of flow rate

The influence of flow rate was analysed by varying the flow rate at 6 $mLmin^{-1}$, 8 $mLmin^{-1}$, 10 $mLmin^{-1}$ while keeping the bed height constant at 2 cm and the initial dye concentration at 10 mgL^{-1} (Fig. 7.5a). The breakthrough time and total time got reduced with an increased flow rate (Ajmani et al., 2020). Table 7.1 can be referred for the decrease in removal from 97.18 to 93.77% with an increase in flow rate which can be explained as there was less exposure of BF onto the GC with a higher rate of flow for a shorter period.

7.2.3.2. Influence of initial concentration

For this set of experiments flow rate and bed, height was kept constant at 8 $mlmin^{-1}$ and 1 cm respectively and initial concentrations were varied at 5, 10 and 15 mgL^{-1}. Breakthrough time, as well as total time, was observed to be decreased with increased dye concentration (Khadri et al., 2019; Santoso et al., 2020) as shown in Fig. 7.5b. This trend is observed as the amount of BF adsorbed on GC increased in a lesser amount of time making the bed saturated faster owing to the increased driving force between BF and GC surface site functional groups.

7.2.3.3. Influence of GC loading amounts i.e. bed height

Effect of GC loading amount i.e. bed height was performed at 1 cm, 2 cm, and 3 cm by influenting 10 mgL^{-1} of dye solution at a constant flow rate of 8 $mlmin^{-1}$ for all the three columns set up. As the bed height was increased the volume necessary for the column to saturate along with the breakthrough time increased (Ajmani et al., 2020; Salehi et al., 2021; Yin et al., 2022). With this total time was also observed to be increased as shown in Fig. 7.5c. The dye removal percentage increased from 93.77 to 97.55% when the bed height was increased from 1 to 3 cm (data has been shown in Table 7.1). The reason behind this is due to more GC amount that corresponds to a greater site of adsorption availability.

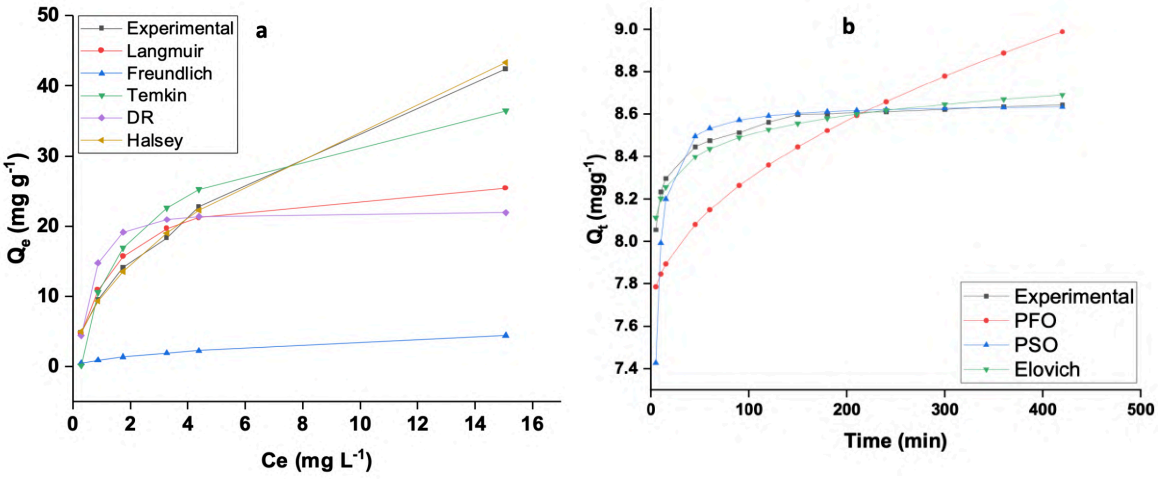

Fig. 7.4: Isotherm (a) and kinetics (b) modelling plot

7.2.4. Breakthrough curve and modelling

7.2.4.1. Thomas model

Data derived are presented in Table 7.2. However, this model does not give a good fit as the regression values (R^2) of this model range from 0.5038 to 0.7584. When the bed height was increased adsorption capacity also increased with a drop in K_{TH} value. Again with an increase in the dye initial concentration Q_0 increased with reduced K_{TH} values. The major force driving the adsorption process is the difference in dye concentration on the GC and that of the dye solution. Additionally, elevated volumetric flow rate resorted in decreased adsorption capacity and increased $K_{TH.}$ This could be explained as the residence time of

BF on the adsorbent bed in the packed bed column was less. These results can also be supported by (Ashokan et al., 2021; Chen et al., 2021).

7.2.4.2. Adams-Bohart model

Data derived were presented in Table 7.2. With the increased adsorbent bed height as well as flow rate there has been an observed decrease value of N_{AB} and K_{AB}. Further elevated initial dye concentration resulted in decreased K_{AB} and increased N_{AB} values respectively. These findings can be attributed to the external mass transfer in BF adsorption in the column initial part. The regression coefficient showed a maximum value of 0.8086 which is acceptable in predicting the fixed bed column behaviour.

7.2.4.3. Yoon-Nelson model

The slope and intercept of the plot linearized between ln $Ct/(C_0-C_t)$ and t give the values of K_{YN} and τ and the collected data from the column run are tabulated in Table 7.2. With the increase in column bed height, the time needed to reach 50% breakthrough (τ) is increased while the rate constant is reduced. When the flow rate was increased rate constant K_{YN} increased along with decreased τ. With this analysis, quick saturation of the packed bed column can be attributed to the less residual time of dye on the adsorbent. Similar works have been reported by various author groups (Yahya et al., 2022, Maleki et al., 2021, Ameh et al., 2021). However, this model did not give good regression values for the applicability of the experimental data fitting.

Table 7.2: Parameters of various models for BF adsorption by GC in packed bed at various conditions

Column parameters			Thomas model			Adams-Bohart model			Yoon-Nelson model		
Z	F	C_o	Q_o	k_{TH}	R^2	N_{AB}	k_{AB}	R^2	k_{YN}	τ	R^2
(cm)	($mLmin^{-1}$)	(mgL^{-1})	(mgg^{-1})	($mLmg^{-1}$ min^{-1})		(mgL^{-1})	($mLmg^{-1}$ min^{-1})		(min^{-1})	(min)	
1	8	10	2046.42	0.00923	0.7584	3398.78	0.0033	0.7892	0.0451	118.98	0.3487
1	8	15	4323.32	0.00458	0.5038	4659.48	0.0026	0.6824	0.0292	198.43	0.2283
1	8	5	1715.4	0.00966	0.6216	1777.2	0.0067	0.6332	0.0752	85.85	0.342
2	6	10	3123.66	0.00623	0.5649	3132.1	0.0031	0.6636	0.0184	324.84	0.32
2	8	10	2983.86	0.00862	0.7260	2765.9	0.0028	0.6732	0.0345	236.98	0.2987
2	10	10	2113.48	0.00923	0.7368	1768.34	0.0024	0.8086	0.0465	206.07	0.2236
3	8	10	4327.45	0.00505	0.7162	1097.06	0.0021	0.7182	0.0191	284.2	0.114

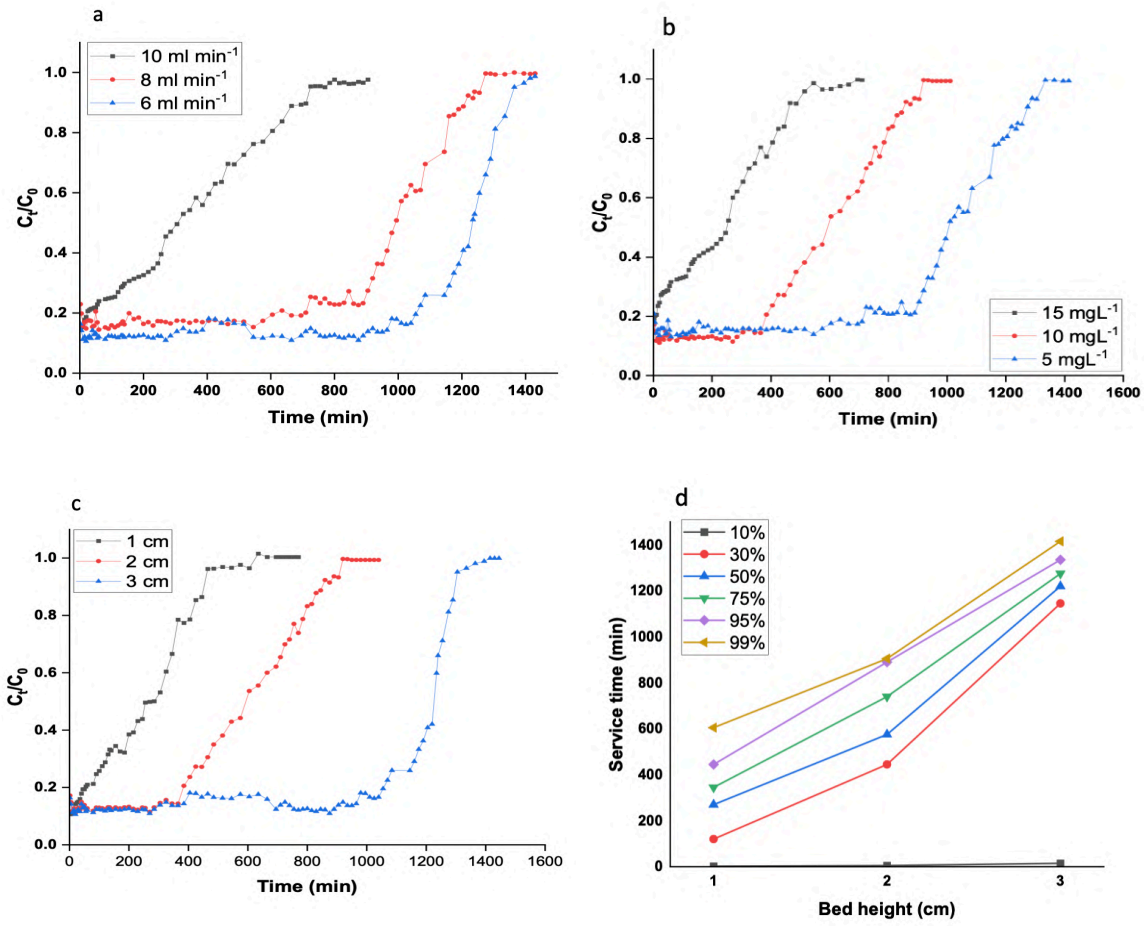

Fig. 7.5: Influence of flow rate (a), initial dye concentration (b) and bed height (c) and Linear plots of Bed Depth Service Time model (d)

7.2.4.4. Bed Depth Service Time (BDST) model

The standard form of the linearized plot usually gives a straight line for service time versus bed height which is shown in Figure 7.5d. Linear regression gives a value of 0.9925 suggesting a better fit of the BDST model for the packed bed column. Rate constant (K_a) and sorption capacity (N_0) were calculated and the data thus calculated are shown in Table 7.3. N_0 and K_a were found to be 24780 mgL^{-1} which is a quite good result and 0.002 ($Lmg^{-1}min^{-1}$) respectively. To mention, if the K_a value is small it suggests increasing the bed height to avoid the breakthrough and vice versa. These findings can be used in the implementation of the further pilot set-up of the experimental design.

Table 7.3: Bed Depth Service Time model parameters

Column parameters			Bed Depth Service Time model		
u ($cmmin^{-1}$)	**C_o** (mgL^{-1})	**C_o/C_t**	**N_o** (mgL^{-1})	**K_a** ($Lmg^{-1}min^{-1}$)	**R^2**
5.33	10	1.0526	24780	0.002	0.9925

7.2.4.5. Key findings of continuous column studies

Major evidence from the adsorptive removal of BF dye onto GC when studied in a dynamic column showed the influencing experimental parameters were flow rate, bed height (initial weight for the loaded GC) and initial dye concentration. The key findings of this column experiments are:

1. Breakthrough time and total time decreases when the flow rate was increased. The uptake capacity was achieved at a flow rate of 6 $mLmin^{-1}$ with a bed height of 2 cm and an initial dye concentration of 10 mgL^{-1} which proved to be the most effective combination for the column studied. The reduced exposure of BF onto GC with increased flow rate till 10 $mLmin^{-1}$ lowers the yield % to 93.77%.

2. With increasing bed height, breakthrough time increased which is due to more amount of GC providing more adsorption sites to be utilized however the dye inlet concentration decreases with an increase. The breakthrough curve got steeper when bed height was low.

3. When dye concentration at the inlet was increased the breakthrough time decreased as the bed gets saturated faster due to the high amount of BF molecules adsorbed onto GC in a lesser amount of time.

7.2.5. Mechanism of BF adsorption onto GC

All the experimental findings indicated that grass extracted cellulose showed a very good removal efficiency of Basic fuchsine dye from simulated wastewater which is possibly feasible to use on large scale. It gave good adsorption capacity within a very short period. In any adsorptive remediation technique, especially dye pollutant on adsorbent from polysaccharide/biomass origin is dependent on various factors viz. pH of an aqueous

solution, available sites for adsorption, the interaction of sorbent-sorbate molecules, the surface morphology of adsorbent, temperature etc. In general, dye species go and bind to adsorbents via electrostatic, H-bond and diffusion mechanisms. In this section probable mechanism of the dye adsorption onto GC has been stated:

1. Due to the availability of an enormous anionic functional group (-OH) on cellulose, the cationic dye strongly binds via electrostatic interaction. The interaction has been depicted in Fig. 7.6. FTIR was performed before and after adsorption of BF onto GC to better comprehend the interaction. In the FTIR spectrum presence of the -OH group is observed at the position 3350 cm^{-1} in both the samples in an intermolecular fashion which after adsorption showed a difference in peak intensity. Further weak peaks around 1366 cm^{-1} shifted to 1372 cm^{-1} after adsorbing BF possibly due to -OH bending.

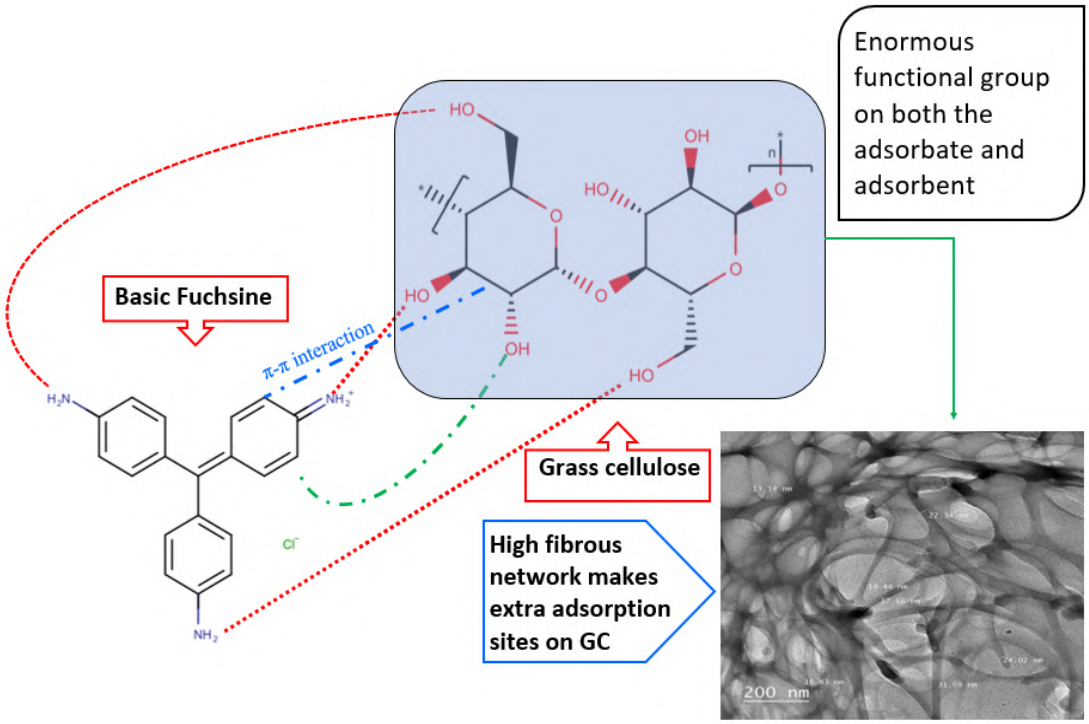

Fig. 7.6: Mechanism of Basic Fuchsine dye adsorption on Grass Cellulose

2. From the surface morphology observed from FESEM and FETEM images, the highly fibrous network formed with the interconnected channel-type cellulose

threads provides extra adsorption sites for the adsorption of dye molecules through the pore diffusion mechanism.

3. Basic fuchsine has polar nitrogen atoms which form H bonds with GC functional groups which however provides a minor contribution to the interaction between sorbate-sorbent.

4. Another probable reason might be the π-π interaction where π-electron of the aromatic ring structure of BF dye interacts with C=C bond of cellulose molecule as shown in the schematic fig. 7.6.

7.3. Significant findings

In the present work, cellulose extracted from grass in a very efficient way was identified as a better adsorbent for the elimination of basic fuchsine dye in both batch and continuous modes. The experimental conditions were optimized for pH, adsorbent dosage, initial dye concentration and temperature. The experimental data gave the best fit to the Halsey isotherm owing to the heterogeneous distribution of active sites and multilayer adsorption on GC and pseudo-second-order kinetics. In continuous column studies, the adsorption was found to be affected by experimental parameters such as flow rate, bed height (initial amount of GC loaded) and initial concentration of dye solution. The lower flow rate was the most beneficial parameter for the higher yield up to 97%. Among the column models studied, Adams-Bohart showed the best fitting and BDST model further verified the correlation between the processing time and column bed height. The maximum removal efficiency was found to be 318.45 mgg^{-1} in static and 110 mgg^{-1} in the column. The raw materials used for cellulose extraction were grass which is available throughout the year and considered a substitute for costly activated carbon.

Chapter 8
Summary and Conclusion

8.1. Summary and conclusion

8.1.1. Overall conclusion of the work

Lignocellulosic waste biomass is increasingly used as a potent biosorbent for the biosorption of hexavalent chromium. Not only these biosorbents are cheap and easily available but they are recyclable too. The current study uses a novel plant-based biosorbent prepared from *Acacia auriculiformis* shells and two of its modified forms. Results verified that the chelated biosorbent has higher adsorption capacities as compared to the raw biosorbent. The primary reason for the interaction between the metal ion and the biosorbent can be inferred due to the electrostatic interaction between them. Desorption, regeneration and reuse of the biosorbents indicated its favourability for their reusability. Overall *A. auriculiformis* waste biomass and its different forms proved efficient in the sequestration of chromium with minimal expense.

As the major part of lignocellulose consists of cellulose, the next study deals with the use of cellulose in nano dimension and further preparation of a composite by chemical polymerization of pyrrole coating on the nanocellulose spheres. This adsorbent was used for the adsorptive removal of two common dyes in both single and binary systems. This incorporation has greatly enhanced the adsorption of the studied dyes and demonstrated that it was possible to produce a nanocellulose-based adsorbent that was more efficient than raw cellulose. Further, the use of seed to analyse the adsorbent capability provides evidence about the clarity of the effluent in a real scenario.

The same nanocellulose polypyrrole composite was used for a dye and a metal in a simultaneous system. Response Surface Methodology was implemented to determine the optimum experimental conditions. Here, the effect of co-existing ions was another addition to the standard experimental work and it showed the dye removal did not show much decrease but the metal removal decreased up to 25-50% after the addition of different salts due to the competitive adsorption of some salts with the metal species. This adsorbent showed excellent efficiency for both dye and metal removal. This work will provide a new approach to the research and development of new adsorbents.

The next approach was the extraction of cellulose from a widely distributed perennial grass species “*Cyperus rotundus*”, as a green initiative. This fibrous adsorbent showed very good adsorption capacity owing to its natural composite and arrangement. However, despite their advantage in bioremediation, this waste biomass carries a downside of accumulating

pollutants in large amounts due to the macro size. Therefore, grass cellulose was scaled down to nanocellulose and used as a potent candidate for adsorptive removal of antibiotic Ciprofloxacin (CPXO) and anti-inflammatory agent Diclofenac (DCF) from simulated wastewater. The nano dimensional property facilitates easy and huge coverage over GNC after treating with CPXO and DCF. An extended toxicity study was performed using six various plant seeds and zebrafish. The experimental findings implied the feasibility of GNC for the efficient removal of CPXO and DCF and reduced toxicity of the treated pollutant on the model organisms.

Another modification was incorporated through co-precipitation of ferrous sulphate and ferric chloride on the GNC surface where the cellulose source was *Cyperus rotundas* grass. This newly prepared adsorbent was named Magnetic grass nano cellulose (MGNC) and was used for the removal of a rare earth element cerium. The magnetization step facilitates the easy retrieval of the sample after adsorption. The effect of common ion present in the real sample showed little alteration of cerium removal which is desirable. The highest adsorption efficiency was found at pH 5 which is 353.04 mgg^{-1} which shows MGNC to be an excellent alternative to remove cerium. Isotherm, kinetics and thermodynamics study further support the favourability of the present work.

In the final work, cellulose extracted from the grass was used for the elimination of basic fuchsine dye in both batch and continuous mode. All the experimental findings indicated that grass cellulose showed a very good removal efficiency which is feasible to use on large scale. It gave good adsorption capacity within a very short period. In general, dye species go and bind to adsorbent via electrostatic, H-bond and function through diffusion mechanism. The raw materials used for cellulose extraction were grass which is available throughout the year and considered a substitute for activated carbon.

8.1.2. Significance of the work

Water being the most vital element of all life forms has the utmost attention due to the global scarcity it is facing for the past few decades with a rapid decrease in the available water for drinking, agriculture, and industrial and domestic usage. Among the roots of water pollution, industrialization tops the list with mostly heavy metals, dyes, pharmaceutical pollutants, and rare earth elements contaminated by waste effluents. Pollutants like antibiotics are categorised as emerging contaminants (EC) as they could potentially end up in drinking water in future. Remediation of these toxic pollutants has become of particular concern due to their persistence in the ecosystem. Several techniques such as adsorption, coagulation, chemical precipitation, membrane filtration, photocatalytic degradation, and electrochemical treatment have been used with their respective pros and cons. However, the technique of clean-up through adsorption has its advantage over other mechanical processes, being a passive metabolic process it does not require external energy. This has been practised for a long with lignocellulosic plant biomass, activated carbon, clay, algae etc. But they suffer from low sorption and low selectivity towards pollutants. To circumvent this issue, novel synthetic materials have been explored and tailor-made composite adsorbent is a new star candidate in this area of adsorption with their high efficiency, recyclability, temperature and pH stability, and easy separation from waste after treatment. The present thesis work has tried to imply surface tuned adsorbents for the removal of various pollutants by fabricating lignocellulosic/ cellulosic composites with other materials. The use of polymer and cross-linking agents were a few modifications that allowed the resulting adsorbent to exhibit better adsorption capacity. This current thesis could be a foundation for developing potential adsorbents or modifications of existing adsorbents to eliminate/minimize one of the global problems mankind is facing.

Bibliography

[1] K.Z. Elwakeel, A.A. El-Bindary, A. Ismail, A.M. Morshidy, Sorptive removal of Remazol Brilliant Blue R from aqueous solution by diethylenetriamine functionalized magnetic macro-reticular hybrid material, RSC Adv. 6 (2016) 22395–22410. https://doi.org/10.1039/C5RA26508H.

[2] B. Gulen, P. Demircivi, B. Gulen, P. Demircivi, Adsorption properties of flouroquinolone type antibiotic ciprofloxacin into 2:1 dioctahedral clay structure: Box-Behnken experimental design, JMoSt. 1206 (2020) 127659. https://doi.org/10.1016/J.MOLSTRUC.2019.127659.

[3] T. Shahnaz, M.M.F. S., P. V.C., S. Narayanasamy, Surface modification of nanocellulose using polypyrrole for the adsorptive removal of Congo red dye and chromium in binary mixture, Int. J. Biol. Macromol. 151 (2020). https://doi.org/10.1016/j.ijbiomac.2020.02.181.

[4] G.S. Maia, J.R. de Andrade, M.G.C. da Silva, M.G.A. Vieira, Adsorption of diclofenac sodium onto commercial organoclay: Kinetic, equilibrium and thermodynamic study, Undefined. 345 (2019) 140–150. https://doi.org/10.1016/J.POWTEC.2018.12.097.

[5] H. Fakhri, A.R. Mahjoub, H. Aghayan, Effective removal of methylene blue and cerium by a novel pair set of heteropoly acids based functionalized graphene oxide: Adsorption and photocatalytic study, Chem. Eng. Res. Des. 120 (2017) 303–315. https://doi.org/10.1016/J.CHERD.2017.02.030.

[6] B. Priya, V.K. Gupta, D. Pathania, A.S. Singha, Synthesis, characterization and antibacterial activity of biodegradable starch/PVA composite films reinforced with cellulosic fibre, Carbohydr. Polym. 109 (2014) 171–179. https://doi.org/10.1016/j.carbpol.2014.03.044.

[7] L. Wang, C. Yang, A. Lu, S. Liu, Y. Pei, X. Luo, An easy and unique design strategy for insoluble humic acid/cellulose nanocomposite beads with highly enhanced adsorption performance of low concentration ciprofloxacin in water, Bioresour. Technol. 302 (2020). https://doi.org/10.1016/j.biortech.2020.122812.

[8] V. Sharma, T. Shahnaz, S. Subbiah, S. Narayanasamy, New Insights into the Remediation of Water Pollutants using Nanobentonite Incorporated Nanocellulose Chitosan Based Aerogel, J. Polym. Environ. 28 (2020) 2008–2019. https://doi.org/10.1007/S10924-020-01740-9.

[9] P. Lu, Y. Lo Hsieh, Preparation and characterization of cellulose nanocrystals from rice straw, Carbohydr. Polym. 87 (2012) 564–573. https://doi.org/10.1016/j.carbpol.2011.08.022.

[10] F. Torrades, J. García-Montaño, Using central composite experimental design to optimize the degradation of real dye wastewater by Fenton and photo-Fenton reactions, Dye. Pigment. 100 (2014) 184–189. https://doi.org/10.1016/j.dyepig.2013.09.004.

[11] T. Shahnaz, M.M.F. S., P. V.C., S. Narayanasamy, Surface modification of nanocellulose using polypyrrole for the adsorptive removal of Congo red dye and chromium in binary mixture, Int. J. Biol. Macromol. 151 (2020) 322–332. https://doi.org/10.1016/J.IJBIOMAC.2020.02.181.

[12] J. Gu, A. Dichiara, Hybridization between cellulose nanofibrils and faceted silver nanoparticles used with surface enhanced Raman scattering for trace dye detection, Int. J. Biol. Macromol. 143 (2020) 85–92. https://doi.org/10.1016/j.ijbiomac.2019.12.018.

[13] P. Bober, J. Liu, K.S. Mikkonen, P. Ihalainen, M. Pesonen, C. Plumed-Ferrer, A. Von Wright, T. Lindfors, C. Xu, R.M. Latonen, Biocomposites of Nanofibrillated cellulose, polypyrrole, and silver nanoparticles with electroconductive and antimicrobial properties, Biomacromolecules. 15 (2014) 3655–3663. https://doi.org/10.1021/BM500939X.

[14] Y. Sun, Y. Chu, W. Wu, H. Xiao, Nanocellulose-based lightweight porous materials: A review, Carbohydr. Polym. 255 (2021). https://doi.org/10.1016/j.carbpol.2020.117489.

[15] T. Ahamad, M. Naushad, Ruksana, A.N. Alhabarah, S.M. Alshehri, N/S doped highly porous magnetic carbon aerogel derived from sugarcane bagasse cellulose for the removal of bisphenol-A, Int. J. Biol. Macromol. 132 (2019) 1031–1038. https://doi.org/10.1016/j.ijbiomac.2019.04.004.

[16] C. Patra, R.M.N. Medisetti, K. Pakshirajan, S. Narayanasamy, Assessment of raw, acid-modified and chelated biomass for sequestration of hexavalent chromium from aqueous solution using Sterculia villosa Roxb. shells, Environ. Sci. Pollut. Res. 26 (2019) 23625–23637. https://doi.org/10.1007/S11356-019-05582-4.

[17] Y. Zhang, X. Shen, H. Qian, L. Song, K. Xie, M. Zhang, H. Wang, 2D NMR assisted structure elucidation of three cyanoethylated cellulose derivatives and correlated with their properties, Carbohydr. Res. 487 (2020). https://doi.org/10.1016/j.carres.2019.107861.

[18] G. Sharma, M. Naushad, A.H. Al-Muhtaseb, A. Kumar, M.R. Khan, S. Kalia, Shweta, M. Bala, A. Sharma, Fabrication and characterization of chitosan-crosslinked-poly(alginic acid) nanohydrogel for adsorptive removal of Cr(VI) metal ion from aqueous medium, Int. J. Biol. Macromol. 95 (2017) 484–493. https://doi.org/10.1016/j.ijbiomac.2016.11.072.

[19] A.A. El-Bayaa, N.A. Badawy, E.A. AlKhalik, Effect of ionic strength on the adsorption of copper and chromium ions by vermiculite pure clay mineral, J. Hazard. Mater. 170 (2009) 1204–1209. https://doi.org/10.1016/j.jhazmat.2009.05.100.

[20] I. Langmuir, The adsorption of gases on plane surfaces of glass, mica and platinum, J. Am. Chem. Soc. 40 (1918) 1361–1403. https://doi.org/10.1021/JA02242A004.

[21] A. Allafchian, Z.S. Mousavi, S.S. Hosseini, Application of cress seed musilage magnetic nanocomposites for removal of methylene blue dye from water, Int. J. Biol. Macromol. 136 (2019) 199–208. https://doi.org/10.1016/j.ijbiomac.2019.06.083.

[22] T. Shahnaz, V. Sharma, S. Subbiah, S. Narayanasamy, Multivariate optimisation of Cr (VI), Co (III) and Cu (II) adsorption onto nanobentonite incorporated nanocellulose/chitosan aerogel using response surface methodology, J. Water Process Eng. 36 (2020). https://doi.org/10.1016/j.jwpe.2020.101283.

[23] S. Kalidhasan, A. Santhana Krishna Kumar, V. Rajesh, N. Rajesh, The journey traversed in the remediation of hexavalent chromium and the road ahead toward greener alternatives-A perspective, Coord. Chem. Rev. 317 (2016) 157–166. https://doi.org/10.1016/j.ccr.2016.03.004.

[24] Z. Dhaouefi, A. Toledo-Cervantes, K. Ghedira, L. Chekir-Ghedira, R. Muñoz, Decolorization and phytotoxicity reduction in an innovative anaerobic/aerobic photobioreactor treating textile wastewater, Chemosphere. 234 (2019) 356–364. https://doi.org/10.1016/j.chemosphere.2019.06.106.

[25] S. Nouren, H.N. Bhatti, M. Iqbal, I. Bibi, S. Kamal, S. Sadaf, M. Sultan, A. Kausar, Y. Safa,

By-product identification and phytotoxicity of biodegraded Direct Yellow 4 dye, Chemosphere. 169 (2017) 474–484. https://doi.org/10.1016/j.chemosphere.2016.11.080.

[26] A. Hossam Mahmoud, N.M. Darwish, Y. Ock Kim, P. Viayaraghavan, J.T. Kwon, S. Won Na, J. Chul Lee, H.J. Kim, Fenvalerate induced toxicity in Zebra fish, Danio rerio and analysis of biochemical changes and insights of digestive enzymes as important markers in risk assessment, J. King Saud Univ. - Sci. 32 (2020) 1569–1580. https://doi.org/10.1016/j.jksus.2019.12.013.

[27] M. Graouer-Bacart, S. Sayen, E. Guillon, Adsorption and co-adsorption of diclofenac and Cu(II) on calcareous soils, Ecotoxicol. Environ. Saf. 124 (2016) 386–392. https://doi.org/10.1016/j.ecoenv.2015.11.010.

[28] G. V. Gusev, Hermans-Weidinger X-ray diffraction technique for determining polymer crystallinity and the use of the Ruland ratio, Polym. Sci. U.S.S.R. 20 (1978) 1295–1297. https://doi.org/10.1016/0032-3950(78)90270-8.

[29] M. Bizi, F.E. El Bachra, Evaluation of the ciprofloxacin adsorption capacity of common industrial minerals and application to tap water treatment, Powder Technol. 362 (2020) 323–333. https://doi.org/10.1016/j.powtec.2019.11.047.

[30] F. Nekouei, S. Nekouei, I. Tyagi, V.K. Gupta, Kinetic, thermodynamic and isotherm studies for acid blue 129 removal from liquids using copper oxide nanoparticle-modified activated carbon as a novel adsorbent, J. Mol. Liq. 201 (2015) 124–133. https://doi.org/10.1016/j.molliq.2014.09.027.

[31] E. Abu-Danso, A. Bagheri, A. Bhatnagar, Facile functionalization of cellulose from discarded cigarette butts for the removal of diclofenac from water, Carbohydr. Polym. 219 (2019) 46–55. https://doi.org/10.1016/j.carbpol.2019.04.090.

[32] A. Mittal, J. Mittal, A. Malviya, V.K. Gupta, Removal and recovery of Chrysoidine Y from aqueous solutions by waste materials, J. Colloid Interface Sci. 344 (2010) 497–507. https://doi.org/10.1016/j.jcis.2010.01.007.

[33] M. Ghaedi, S. Hajjati, Z. Mahmudi, I. Tyagi, S. Agarwal, A. Maity, V.K. Gupta, Modeling of competitive ultrasonic assisted removal of the dyes - Methylene blue and Safranin-O using Fe3O4 nanoparticles, Chem. Eng. J. 268 (2015) 28–37. https://doi.org/10.1016/j.cej.2014.12.090.

[34] Ihsanullah, H.A. Asmaly, T.A. Saleh, T. Laoui, V.K. Gupta, M.A. Atieh, Enhanced adsorption of phenols from liquids by aluminum oxide/carbon nanotubes: Comprehensive study from synthesis to surface properties, J. Mol. Liq. 206 (2015) 176–182. https://doi.org/10.1016/j.molliq.2015.02.028.

[35] N. Mohammadi, H. Khani, V.K. Gupta, E. Amereh, S. Agarwal, Adsorption process of methyl orange dye onto mesoporous carbon material-kinetic and thermodynamic studies, J. Colloid Interface Sci. 362 (2011) 457–462. https://doi.org/10.1016/j.jcis.2011.06.067.

[36] D. Trache, A.F. Tarchoun, M. Derradji, T.S. Hamidon, N. Masruchin, N. Brosse, M.H. Hussin, Nanocellulose: From Fundamentals to Advanced Applications, Front. Chem. 8 (2020) 392. https://doi.org/10.3389/FCHEM.2020.00392/BIBTEX.

[37] P.L. Stiles, J.A. Dieringer, N.C. Shah, R.P. Van Duyne, Surface-enhanced Raman spectroscopy, Annu. Rev. Anal. Chem. (Palo Alto. Calif). 1 (2008) 601–626. https://doi.org/10.1146/

ANNUREV.ANCHEM.1.031207.112814.

[38] A. Aichour, H. Zaghouane-Boudiaf, Single and competitive adsorption studies of two cationic dyes from aqueous mediums onto cellulose-based modified citrus peels/calcium alginate composite, Int. J. Biol. Macromol. 154 (2020) 1227–1236. https://doi.org/10.1016/J.IJBIOMAC.2019.10.277.

[39] T. Dahiru, P-Value, a true test of statistical significance? a cautionary note, Ann. Ibadan Postgrad. Med. 6 (2011) 21–26. https://doi.org/10.4314/aipm.v6i1.64038.

[40] T. Shahnaz, V. Vishnu Priyan, S. Pandian, S. Narayanasamy, Use of Nanocellulose extracted from grass for adsorption abatement of Ciprofloxacin and Diclofenac removal with phyto, and fish toxicity studies, Environ. Pollut. 268 (2021). https://doi.org/10.1016/j.envpol.2020.115494.

[41] T. Shahnaz, V. Sharma, S. Subbiah, S. Narayanasamy, Multivariate optimisation of Cr (VI), Co (III) and Cu (II) adsorption onto nanobentonite incorporated nanocellulose/chitosan aerogel using response surface methodology, J. Water Process Eng. 36 (2020). https://doi.org/10.1016/j.jwpe.2020.101283.

[42] C. Patra, T. Shahnaz, S. Subbiah, S. Narayanasamy, Comparative assessment of raw and acid-activated preparations of novel Pongamia pinnata shells for adsorption of hexavalent chromium from simulated wastewater, Environ. Sci. Pollut. Res. 27 (2020) 14836–14851. https://doi.org/10.1007/S11356-020-07979-Y.

[43] M.N. Khan, N. Rehman, A. Sharif, E. Ahmed, Z.H. Farooqi, M.I. Din, Environmentally benign extraction of cellulose from dunchi fiber for nanocellulose fabrication, Int. J. Biol. Macromol. 153 (2020) 72–78. https://doi.org/10.1016/j.ijbiomac.2020.02.333.

[44] C.L. Xu, Y.Z. Wang, One-Step Approach to the Growth of ZnO Nano-/Microrods on Cellulose toward Its Durable Superhydrophobicity, Adv. Mater. Interfaces. 4 (2017). https://doi.org/10.1002/ADMI.201700550.

[45] T. Huang, S. wen Zhang, J. Xie, L. Zhou, L. fei Liu, Effective adsorption of quadrivalent cerium by synthesized laurylsulfonate green rust in a central composite design, J. Environ. Sci. (China). 107 (2021) 14–25. https://doi.org/10.1016/J.JES.2021.01.028.

[46] S. Tasrin, S. Mohamed Madhar Fazil, S. Senthilmurugan, N. Selvaraju, Facile preparation of nanocellulose embedded polypyrrole for dye removal: unary and binary process optimization and seed toxicity, Int. J. Environ. Sci. Technol. 18 (2021) 365–378. https://doi.org/10.1007/S13762-020-02814-W.

[47] L. Zhao, M.R. Azhar, X. Li, X. Duan, H. Sun, S. Wang, X. Fang, Adsorption of cerium (III) by HKUST-1 metal-organic framework from aqueous solution, J. Colloid Interface Sci. 542 (2019) 421–428. https://doi.org/10.1016/J.JCIS.2019.01.117.

[48] M.A. Zicari, L. d'Aquino, A. Paradiso, S. Mastrolitti, F. Tommasi, Effect of cerium on growth and antioxidant metabolism of Lemna minor L., Ecotoxicol. Environ. Saf. 163 (2018) 536–543. https://doi.org/10.1016/j.ecoenv.2018.07.113.

[49] S. Hosseynizadeh Khezri, A. Yazdani, R. Khordad, Pure iron nanoparticles prepared by electric arc discharge method in ethylene glycol, Eur. Phys. J. - Appl. Phys. 59 (2012). https://doi.org/10.1051/EPJAP/2012110303.

[50] X. Xie, C. Chen, X. Wang, J. Li, S. Naraginti, Efficient detoxification of triclosan by a S–Ag/TiO2@g-C3N4 hybrid photocatalyst: process optimization and bio-toxicity assessment, RSC Adv. 9 (2019) 20439–20449. https://doi.org/10.1039/C9RA03279G.

[51] Q. Han, M. Du, Y. Guan, G. Luo, Z. Zhang, T. Li, Y. Ji, Removal of simulated radioactive cerium (III) based on innovative magnetic trioctylamine-polystyrene composite microspheres, Chem. Phys. Lett. 741 (2020). https://doi.org/10.1016/j.cplett.2020.137092.

[52] Y. Hao, Y. Cui, J. Peng, N. Zhao, S. Li, M. Zhai, Preparation of graphene oxide/cellulose composites in ionic liquid for Ce (III) removal, Carbohydr. Polym. 208 (2019) 269–275. https://doi.org/10.1016/j.carbpol.2018.12.068.

[53] C.F. Carolin, P.S. Kumar, A. Saravanan, G.J. Joshiba, M. Naushad, Efficient techniques for the removal of toxic heavy metals from aquatic environment: A review, J. Environ. Chem. Eng. 5 (2017) 2782–2799. https://doi.org/10.1016/j.jece.2017.05.029.

[54] H.J. Hong, J.S. Lim, J.Y. Hwang, M. Kim, H.S. Jeong, M.S. Park, Carboxymethlyated cellulose nanofibrils(CMCNFs) embedded in polyurethane foam as a modular adsorbent of heavy metal ions, Carbohydr. Polym. 195 (2018) 136–142. https://doi.org/10.1016/j.carbpol.2018.04.081.

[55] R. Saravanan, S. Karthikeyan, V.K. Gupta, G. Sekaran, V. Narayanan, A. Stephen, Enhanced photocatalytic activity of ZnO/CuO nanocomposite for the degradation of textile dye on visible light illumination, Mater. Sci. Eng. C. 33 (2013) 91–98. https://doi.org/10.1016/j.msec.2012.08.011.

[56] E. Nakkeeran, C. Patra, T. Shahnaz, S. Rangabhashiyam, N. Selvaraju, Continuous biosorption assessment for the removal of hexavalent chromium from aqueous solutions using Strychnos nux vomica fruit shell, Bioresour. Technol. Reports. 3 (2018). https://doi.org/10.1016/j.biteb.2018.09.001.

[57] A. Banerjee, A. Roychoudhury, Differential lead-fluoride and nickel-fluoride uptake in co-polluted soil variably affects the overall physiome in an aromatic rice cultivar, Environ. Pollut. 268 (2021). https://doi.org/10.1016/j.envpol.2020.115504.

[58] Y. Benmassaoud, M.J. Villaseñor, R. Salghi, S. Jodeh, M. Algarra, M. Zougagh, Á. Ríos, Magnetic/non-magnetic argan press cake nanocellulose for the selective extraction of sudan dyes in food samples prior to the determination by capillary liquid chromatograpy, Talanta. 166 (2017) 63–69. https://doi.org/10.1016/j.talanta.2017.01.041.

[59] J. Supramaniam, R. Adnan, N.H. Mohd Kaus, R. Bushra, Magnetic nanocellulose alginate hydrogel beads as potential drug delivery system, Int. J. Biol. Macromol. 118 (2018) 640–648. https://doi.org/10.1016/j.ijbiomac.2018.06.043.

[60] H. Ibrahim, N. Sazali, W.N.W. Salleh, M.N. Zainal Abidin, A short review on recent utilization of nanocellulose for wastewater remediation and gas separation, Mater. Today Proc. 42 (2019) 45–49. https://doi.org/10.1016/J.MATPR.2020.09.245.

[61] N. Amiralian, M. Mustapic, M.S.A. Hossain, C. Wang, M. Konarova, J. Tang, J. Na, A. Khan, A. Rowan, Magnetic nanocellulose: A potential material for removal of dye from water, J. Hazard. Mater. 394 (2020). https://doi.org/10.1016/j.jhazmat.2020.122571.

[62] Y. Chu, Y. Sun, W. Wu, H. Xiao, Dispersion Properties of Nanocellulose: A Review, Carbohydr. Polym. 250 (2020). https://doi.org/10.1016/j.carbpol.2020.116892.

[63] A.G. Adeniyi, J.O. Ighalo, Biosorption of pollutants by plant leaves: An empirical review, J. Environ. Chem. Eng. 7 (2019). https://doi.org/10.1016/j.jece.2019.103100.

[64] S.H. Peng, R. Wang, L.Z. Yang, L. He, X. He, X. Liu, Biosorption of copper, zinc, cadmium and chromium ions from aqueous solution by natural foxtail millet shell, Ecotoxicol. Environ. Saf. 165 (2018) 61–69. https://doi.org/10.1016/j.ecoenv.2018.08.084.

[65] M. Li, X. Xiao, S. Wang, X. Zhang, J. Li, S.G. Pavlostathis, X. Luo, S. Luo, G. Zeng, Synergistic removal of cadmium and organic matter by a microalgae-endophyte symbiotic system (MESS): An approach to improve the application potential of plant-derived biosorbents, Environ. Pollut. 261 (2020). https://doi.org/10.1016/j.envpol.2020.114177.

[66] A. Blanco, M.C. Monte, C. Campano, A. Balea, N. Merayo, C. Negro, Nanocellulose for industrial use: Cellulose nanofibers (CNF), cellulose nanocrystals (CNC), and bacterial cellulose (BC), Handb. Nanomater. Ind. Appl. (2018) 74–126. https://doi.org/10.1016/B978-0-12-813351-4.00005-5.

[67] P. Phanthong, P. Reubroycharoen, X. Hao, G. Xu, A. Abudula, G. Guan, Nanocellulose: Extraction and application, Carbon Resour. Convers. 1 (2018) 32–43. https://doi.org/10.1016/j.crcon.2018.05.004.

[68] L.K. Kian, N. Saba, M. Jawaid, M.T.H. Sultan, A review on processing techniques of bast fibers nanocellulose and its polylactic acid (PLA) nanocomposites, Int. J. Biol. Macromol. 121 (2019) 1314–1328. https://doi.org/10.1016/j.ijbiomac.2018.09.040.

[69] E. Allahkarami, B. Rezai, Removal of cerium from different aqueous solutions using different adsorbents: A review, Process Saf. Environ. Prot. 124 (2019) 345–362. https://doi.org/10.1016/j.psep.2019.03.002.

[70] B.T. Kilbourn, Cerium and Cerium Compounds, Kirk-Othmer Encycl. Chem. Technol. (2011). https://doi.org/10.1002/0471238961.0305180911091202.A01.PUB3.

[71] J.T. Dahle, Y. Arai, Environmental geochemistry of cerium: Applications and toxicology of cerium oxide nanoparticles, Int. J. Environ. Res. Public Health. 12 (2015) 1253–1278. https://doi.org/10.3390/IJERPH120201253.

[72] K. Dashtian, R. Zare-Dorabei, Synthesis and characterization of functionalized mesoprous SBA-15 decorated with Fe3O4 nanoparticles for removal of Ce(III) ions from aqueous solution: ICP–OES detection and central composite design optimization, J. Colloid Interface Sci. 494 (2017) 114–123. https://doi.org/10.1016/j.jcis.2017.01.072.

[73] C. Lin, W. Luo, J. Chen, Q. Zhou, Rice husk grafted PMAA by ATRP in aqueous phase and its adsorption for Ce3+, Chem. Phys. Lett. 690 (2017) 68–73. https://doi.org/10.1016/j.cplett.2017.10.029.

[74] S.F. Chua, A. Nouri, W.L. Ang, E. Mahmoudi, A.W. Mohammad, A. Benamor, M. Ba-Abbad, The emergence of multifunctional adsorbents and their role in environmental remediation, J. Environ. Chem. Eng. 9 (2021). https://doi.org/10.1016/j.jece.2020.104793.

[75] D. Lu, S. Xu, W. Qiu, Y. Sun, X. Liu, J. Yang, J. Ma, Adsorption and desorption behaviors of antibiotic ciprofloxacin on functionalized spherical MCM-41 for water treatment, J. Clean. Prod. 264 (2020). https://doi.org/10.1016/j.jclepro.2020.121644.

[76] A.M. Ares, R. Muiño, A. Costoya, R.A. Lorenzo, A. Concheiro, A.M. Carro, C. Alvarez-

Lorenzo, Cyclodextrin-functionalized cellulose filter paper for selective capture of diclofenac, Carbohydr. Polym. 220 (2019) 43–52. https://doi.org/10.1016/j.carbpol.2019.05.055.

[77] S. Álvarez, R.S. Ribeiro, H.T. Gomes, J.L. Sotelo, J. García, Synthesis of carbon xerogels and their application in adsorption studies of caffeine and diclofenac as emerging contaminants, Chem. Eng. Res. Des. 95 (2015) 229–238. https://doi.org/10.1016/j.cherd.2014.11.001.

[78] Y. Zhao, F. Liu, X. Qin, Adsorption of diclofenac onto goethite: Adsorption kinetics and effects of pH, Chemosphere. 180 (2017) 373–378. https://doi.org/10.1016/j.chemosphere.2017.04.007.

[79] M. Cantarella, S.C. Carroccio, S. Dattilo, R. Avolio, R. Castaldo, C. Puglisi, V. Privitera, Molecularly imprinted polymer for selective adsorption of diclofenac from contaminated water, Chem. Eng. J. 367 (2019) 180–188. https://doi.org/10.1016/j.cej.2019.02.146.

[80] V.K. Gupta, N. Atar, M.L. Yola, Z. Üstündağ, L. Uzun, A novel magnetic Fe@Au core-shell nanoparticles anchored graphene oxide recyclable nanocatalyst for the reduction of nitrophenol compounds, Water Res. 48 (2014) 210–217. https://doi.org/10.1016/j.watres.2013.09.027.

[81] A. Avcı, İ. İnci, N. Baylan, Adsorption of ciprofloxacin hydrochloride on multiwall carbon nanotube, J. Mol. Struct. 1206 (2020). https://doi.org/10.1016/j.molstruc.2020.127711.

[82] R.G. Silva, C.A. Morais, É.D. Oliveira, Selective cerium removal by thermal treatment of mixed rare earth oxalates or carbonates obtained from non-purified rare earth sulphate liquor, Miner. Eng. 139 (2019). https://doi.org/10.1016/j.mineng.2019.105865.

[83] Q.P. Hu, X.M. Cao, D.L. Hao, L.L. Zhang, Chemical Composition, Antioxidant, DNA Damage Protective, Cytotoxic and Antibacterial Activities of Cyperus rotundus Rhizomes Essential Oil against Foodborne Pathogens, Sci. Rep. 7 (2017). https://doi.org/10.1038/SREP45231.

[84] A.A. Al-Gheethi, Q.M. Azhar, P. Senthil Kumar, A.A. Yusuf, A.K. Al-Buriahi, R.M.S. Radin Mohamed, M.M. Al-shaibani, Sustainable approaches for removing Rhodamine B dye using agricultural waste adsorbents: A review, Chemosphere. 287 (2022). https://doi.org/10.1016/j.chemosphere.2021.132080.

[85] T. Shahnaz, V. Vishnu Priyan, S. Pandian, S. Narayanasamy, Use of Nanocellulose extracted from grass for adsorption abatement of Ciprofloxacin and Diclofenac removal with phyto, and fish toxicity studies, Environ. Pollut. 268 (2021) 115494. https://doi.org/10.1016/J.ENVPOL.2020.115494.

[86] H. Li, H. Huang, X. Yan, C. Liu, L. Li, A Calix[4]arene-crosslinked polymer for rapid adsorption of cationic dyes in water, Mater. Chem. Phys. 263 (2021) 124295. https://doi.org/10.1016/J.MATCHEMPHYS.2021.124295.

[87] Q. Yang, Y. Sun, W. Sun, Z. Qin, H. Liu, Y. Ma, X. Wang, Cellulose derived biochar: Preparation, characterization and Benzo[a]pyrene adsorption capacity, Grain Oil Sci. Technol. 4 (2021) 182–190. https://doi.org/10.1016/J.GAOST.2021.10.001.

[88] H. Yang, J. Sun, Y. Zhang, Q. Xue, S. Xia, Preparation of hydrophobic carbon aerogel using cellulose extracted from luffa sponge for adsorption of diesel oil, Ceram. Int. 47 (2021) 33827–33834. https://doi.org/10.1016/J.CERAMINT.2021.08.294.

[89] V. Vishnu Priyan, T. Shahnaz, E. Suganya, S. Sivaprakasam, S. Narayanasamy,

Ecotoxicological assessment of micropollutant Diclofenac biosorption on magnetic sawdust: Phyto, Microbial and Fish toxicity studies, J. Hazard. Mater. 403 (2021). https://doi.org/10.1016/J.JHAZMAT.2020.123532.

[90] Z. Sun, G. Yao, M. Liu, S. Zheng, In situ synthesis of magnetic MnFe2O4/diatomite nanocomposite adsorbent and its efficient removal of cationic dyes, J. Taiwan Inst. Chem. Eng. 71 (2017) 501–509. https://doi.org/10.1016/J.JTICE.2016.12.013.

[91] T. Shahnaz, M.M.F. S., P. V.C., S. Narayanasamy, Surface modification of nanocellulose using polypyrrole for the adsorptive removal of Congo red dye and chromium in binary mixture, Int. J. Biol. Macromol. 151 (2020) 322–332. https://doi.org/10.1016/J.IJBIOMAC.2020.02.181.

[92] D. Hu, H. huang, R. Jiang, N. Wang, H. Xu, Y.G. Wang, X. kun Ouyang, Adsorption of diclofenac sodium on bilayer amino-functionalized cellulose nanocrystals/chitosan composite, J. Hazard. Mater. 369 (2019) 483–493. https://doi.org/10.1016/j.jhazmat.2019.02.057.

[93] A. Ajmani, T. Shahnaz, S. Narayanan, S. Narayanaswamy, Equilibrium, kinetics and thermodynamics of hexavalent chromium biosorption on pristine and zinc chloride activated Senna siamea seed pods, Chem. Ecol. 35 (2019) 379–396. https://doi.org/10.1080/02757540.2019.1584614.

[94] W. Bessashia, Y. Berredjem, Z. Hattab, M. Bououdina, Removal of Basic Fuchsin from water by using mussel powdered eggshell membrane as novel bioadsorbent: Equilibrium, kinetics, and thermodynamic studies, Environ. Res. 186 (2020) 109484. https://doi.org/10.1016/J.ENVRES.2020.109484.

[95] I.P. Meneses, S.D. Novaes, R.S. Dezotti, P.V. Oliveira, D.F.S. Petri, CTAB-modified carboxymethyl cellulose/bagasse cryogels for the efficient removal of bisphenol A, methylene blue and Cr(VI) ions: Batch and column adsorption studies, J. Hazard. Mater. 421 (2022) 126804. https://doi.org/10.1016/J.JHAZMAT.2021.126804.

[96] M. Bhaumik, K. Setshedi, A. Maity, M.S. Onyango, Removal from water using fixed bed column of polypyrrole/Fe 3O4 nanocomposite, Sep. Purif. Technol. 110 (2013) 11–19. https://doi.org/10.1016/j.seppur.2013.02.037.

[97] A. Ajmani, T. Shahnaz, S. Subbiah, S. Narayanasamy, Hexavalent chromium adsorption on virgin, biochar, and chemically modified carbons prepared from Phanera vahlii fruit biomass: equilibrium, kinetics, and thermodynamics approach, Environ. Sci. Pollut. Res. 26 (2019). https://doi.org/10.1007/s11356-019-06335-z.

[98] E. Santoso, R. Ediati, Y. Kusumawati, H. Bahruji, D.O. Sulistiono, D. Prasetyoko, Review on recent advances of carbon based adsorbent for methylene blue removal from waste water, Mater. Today Chem. 16 (2020) 100233. https://doi.org/10.1016/J.MTCHEM.2019.100233.

[99] M.D. Yahya, I.A. Imam, S.A. Abdulkareem, Column adsorption studies for the removal of chemical oxygen demand from fish pond wastewater using waste alum sludge, Adv. Remediat. Tech. Polluted Soils Groundw. (2022) 21–48. https://doi.org/10.1016/B978-0-12-823830-1.00006-7.

[100] F. Maleki, M. Gholami, R. Torkaman, M. Torab-Mostaedi, M. Asadollahzadeh, Cobalt(II) removal from aqueous solution by modified polymeric adsorbents prepared with induced-graft polymerization: Batch and continuous column study with analysis of breakthrough behaviors, Environ. Technol. Innov. 24 (2021). https://doi.org/10.1016/J.ETI.2021.102054.

[101] A.E. Ameh, O.O. Oyekola, L.F. Petrik, Column adsorption of Rhodamine 6G over Na–P/SOD zeolite synthesised from aluminosilicate secondary waste, J. Clean. Prod. 338 (2022) 130571. https://doi.org/10.1016/J.JCLEPRO.2022.130571.

[102] N. Khadhri, M. El Khames Saad, M. Ben Mosbah, Y. Moussaoui, Batch and continuous column adsorption of indigo carmine onto activated carbon derived from date palm petiole, J. Environ. Chem. Eng. 7 (2019). https://doi.org/10.1016/J.JECE.2018.11.020.

[103] P. Ashokan, M. Asaithambi, V. Sivakumar, P. Sivakumar, Batch and column mode adsorption studies of reactive red 195 dye using Adenanthera paronina L seed activated carbon, Groundw. Sustain. Dev. 15 (2021). https://doi.org/10.1016/J.GSD.2021.100671.

[104] Y. Yin, G. Xu, Y. Xu, M. Guo, Y. Xiao, T. Ma, C. Liu, Adsorption of inorganic and organic phosphorus onto polypyrrole modified red mud: Evidence from batch and column experiments, Chemosphere. 286 (2022) 131862. https://doi.org/10.1016/J.CHEMOSPHERE.2021.131862.

[105] C. Chen, Z. Chen, J. Shen, J. Kang, S. Zhao, B. Wang, Q. Chen, X. Li, Dynamic adsorption models and artificial neural network prediction of mercury adsorption by a dendrimer-grafted polyacrylonitrile fiber in fixed-bed column, J. Clean. Prod. 310 (2021). https://doi.org/10.1016/J.JCLEPRO.2021.127511.

[106] E. Salehi, M. Askari, Y. Darvishi, Novel combinatorial extensions to breakthrough curve modeling of an adsorption column — Depth filtration hybrid process, J. Ind. Eng. Chem. 86 (2020) 232–243. https://doi.org/10.1016/J.JIEC.2020.03.015.

[107] M. Beyki, M. Bayat, F.S.-B. technology, undefined 2016, Fabrication of core–shell structured magnetic nanocellulose base polymeric ionic liquid for effective biosorption of Congo red dye, Elsevier. (n.d.). https://www.sciencedirect.com/science/article/pii/S0960852416308860.

[108] S. Archin, S. Sharifi, G.A.-J. of C. Production, undefined 2019, Optimization and modeling of simultaneous ultrasound-assisted adsorption of binary dyes using activated carbon from tobacco residues: response surface, Elsevier. (n.d.). https://www.sciencedirect.com/science/article/pii/S0959652619330069.

[109] G. Eshaq, A.E. ElMetwally, Bmim[OAc]-Cu2O/g-C3N4 as a multi-function catalyst for sonophotocatalytic degradation of methylene blue, Ultrason. Sonochem. 53 (2019) 99–109. https://doi.org/10.1016/J.ULTSONCH.2018.12.037.

[110] Z. yuan YANG, Kinetics and mechanism of the adsorption of methylene blue onto ACFs, J. China Univ. Min. Technol. 18 (2008) 437–440. https://doi.org/10.1016/S1006-1266(08)60090-5.

[111] V. Katheresan, J. Kansedo, S.Y. Lau, Efficiency of various recent wastewater dye removal methods: A review, J. Environ. Chem. Eng. 6 (2018) 4676–4697. https://doi.org/10.1016/J.JECE.2018.06.060.

[112] L. Gong, H. Wu, X. Shan, Z. Li, Facile fabrication of phosphorylated alkali lignin microparticles for efficient adsorption of antibiotics and heavy metal ions in water, J. Environ. Chem. Eng. 9 (2021). https://doi.org/10.1016/J.JECE.2021.106574.

[113] L. Liu, S. Liu, H. Peng, Z. Yang, L. Zhao, A. Tang, Surface charge of mesoporous calcium silicate and its adsorption characteristics for heavy metal ions, Solid State Sci. 99 (2020). https://doi.org/10.1016/J.SOLIDSTATESCIENCES.2019.106072.

[114] J. Pires, V. Souza, A.F.-I.C. and Products, undefined 2019, Valorization of energy crops as a source for nanocellulose production–current knowledge and future prospects, Elsevier. (n.d.). https://www.sciencedirect.com/science/article/pii/S0926669019306521.

[115] J. Li, Z. Wu, Q. Duan, A. Alsaedi, T. Hayat, C. Chen, Decoration of ZIF-8 on polypyrrole nanotubes for highly efficient and selective capture of U(VI), J. Clean. Prod. 204 (2018) 896–905. https://doi.org/10.1016/J.JCLEPRO.2018.09.050.

[116] P. Lu, Y.H.-C. Polymers, undefined 2012, Preparation and characterization of cellulose nanocrystals from rice straw, Elsevier. (n.d.). https://www.sciencedirect.com/science/article/pii/S0144861711007016.

[117] R. Pramanik, B. Ganivada, … F.R.-J. of the, undefined 2019, Influence of nanocellulose on mechanics and morphology of polyvinyl alcohol xerogels, Elsevier. (n.d.). https://www.sciencedirect.com/science/article/pii/S1751616118311044.

[118] K. Tan, S. Heo, M. Foo, I. Chew, C.Y.-S. of T. Total, undefined 2019, An insight into nanocellulose as soft condensed matter: Challenge and future prospective toward environmental sustainability, Elsevier. (n.d.). https://www.sciencedirect.com/science/article/pii/S0048969718333734.

[119] Y. Yang, N. Chen, C. Feng, M. Li, Y. Gao, Chromium removal using a magnetic corncob biochar/polypyrrole composite by adsorption combined with reduction: Reaction pathway and contribution degree, Colloids Surfaces A Physicochem. Eng. Asp. 556 (2018) 201–209. https://doi.org/10.1016/J.COLSURFA.2018.08.035.

[120] M. Vakili, S. Deng, G. Cagnetta, W. Wang, P. Meng, D. Liu, G. Yu, Regeneration of chitosan-based adsorbents used in heavy metal adsorption: A review, Sep. Purif. Technol. 224 (2019) 373–387. https://doi.org/10.1016/J.SEPPUR.2019.05.040.

[121] K.Z. Elwakeel, Removal of As(V) from aqueous solution using glycidyl methacrylate resin immobilized with Cu(II)-tetraethylenepentamine complex, Water Supply. 9 (2009) 181–190. https://doi.org/10.2166/WS.2009.227.

[122] A.M. Elgarahy, K.Z. Elwakeel, G.A. Elshoubaky, S.H. Mohammad, Untapped Sepia Shell–Based Composite for the Sorption of Cationic and Anionic Dyes, Water. Air. Soil Pollut. 230 (2019) 1–23. https://doi.org/10.1007/S11270-019-4247-1/TABLES/7.

[123] I. Haq, A.R.- Chemosphere, undefined 2018, Biodegradation of Azure-B dye by Serratia liquefaciens and its validation by phytotoxicity, genotoxicity and cytotoxicity studies, Elsevier. (n.d.). https://www.sciencedirect.com/science/article/pii/S0045653517321318.

[124] F. Nagia, R.E.-M.-D. and pigments, undefined 2007, Dyeing of wool with natural anthraquinone dyes from Fusarium oxysporum, Elsevier. (n.d.). https://www.sciencedirect.com/science/article/pii/S0143720806002853.

[125] W.W.-E. international, undefined 1985, The use of plant seeds in toxicity tests of phenolic compounds, Elsevier. (n.d.). https://www.sciencedirect.com/science/article/pii/0160412085901011.

[126] Y. Zhou, M. Zhang, X. Hu, X. Wang, J. Niu, T. Ma, Adsorption of Cationic Dyes on a Cellulose-Based Multicarboxyl Adsorbent, J. Chem. Eng. Data. 58 (2013) 413–421. https://doi.org/10.1021/JE301140C.

[127] Y. Yue, X. Wang, J. Han, L. Yu, J. Chen, Q. Wu, J. Jiang, Effects of nanocellulose on sodium alginate/polyacrylamide hydrogel: Mechanical properties and adsorption-desorption capacities, Carbohydr. Polym. 206 (2019) 289–301. https://doi.org/10.1016/J.CARBPOL.2018.10.105.

[128] E.M. Ryan, C.B. Breslin, Formation of polypyrrole with dexamethasone as a dopant: Its cation and anion exchange properties, J. Electroanal. Chem. 824 (2018) 188–194. https://doi.org/10.1016/J.JELECHEM.2018.07.052.

[129] A.M. ElNahrawy, A.A. Haroun, I. Hamadneh, A.H. Al-Dujaili, S. kamel, Conducting cellulose/TiO2 composites by in situ polymerization of pyrrole, Carbohydr. Polym. 168 (2017) 182–190. https://doi.org/10.1016/J.CARBPOL.2017.03.066.

[130] A.M. Elgarahy, K.Z. Elwakeel, G.A. Elshoubaky, S.H. Mohammad, Microwave-accelerated sorption of cationic dyes onto green marine algal biomass, Environ. Sci. Pollut. Res. 26 (2019) 22704–22722. https://doi.org/10.1007/S11356-019-05417-2/FIGURES/3.

[131] K.Z. Elwakeel, M.A. Abd El-Ghaffar, S.M. El-kousy, H.G. El-Shorbagy, Synthesis of new ammonium chitosan derivatives and their application for dye removal from aqueous media, Chem. Eng. J. 203 (2012) 458–468. https://doi.org/10.1016/J.CEJ.2012.07.001.

[132] K.Z. Elwakeel, A.M. Yousif, Adsorption of malathion on thermally treated egg shell material, Water Sci. Technol. 61 (2010) 1035–1041. https://doi.org/10.2166/WST.2010.005.

[133] A.A. Yakout, M.A. Shaker, K.Z. Elwakeel, W. Alshitari, Lauryl sulfate@magnetic graphene oxide nanosorbent for fast methylene blue recovery from aqueous solutions, J. Dispers. Sci. Technol. 40 (2019) 707–715. https://doi.org/10.1080/01932691.2018.1477604/SUPPL_FILE/LDIS_A_1477604_SM7904.DOC.

[134] M.A. Abd El-Ghaffar, M.H. Mohamed, K.Z. Elwakeel, Adsorption of silver(I) on synthetic chelating polymer derived from 3-amino-1,2,4-triazole-5-thiol and glutaraldehyde, Chem. Eng. J. 151 (2009) 30–38. https://doi.org/10.1016/J.CEJ.2009.01.039.

[135] A.M. Donia, A.A. Atia, K.Z. Elwakeel, Selective separation of mercury(II) using magnetic chitosan resin modified with Schiff's base derived from thiourea and glutaraldehyde, J. Hazard. Mater. 151 (2008) 372–379. https://doi.org/10.1016/J.JHAZMAT.2007.05.083.

[136] K.Z. Elwakeel, Removal of Reactive Black 5 from aqueous solutions using magnetic chitosan resins, J. Hazard. Mater. 167 (2009) 383–392. https://doi.org/10.1016/J.JHAZMAT.2009.01.051.

[137] K.Z. Elwakeel, M.A. Abd El-Ghaffar, S.M. El-Kousy, H.G. El-Shorbagy, Enhanced Remediation of Reactive Black 5 from Aqueous Media Using New Chitosan Ion Exchangers, Http://Dx.Doi.Org/10.1080/01932691.2012.695943. 34 (2013) 1008–1019. https://doi.org/10.1080/01932691.2012.695943.

[138] G. Wang, Y. Yang, Y. Kong, R. Ma, J. Yuan, G. Li, Key factors affecting seed germination in phytotoxicity tests during sheep manure composting with carbon additives, J. Hazard. Mater. 421 (2022) 126809. https://doi.org/10.1016/J.JHAZMAT.2021.126809.

[139] L. Liu, Z.Y. Gao, X.P. Su, X. Chen, L. Jiang, J.M. Yao, Adsorption removal of dyes from single and binary solutions using a cellulose-based bioadsorbent, ACS Sustain. Chem. Eng. 3 (2015) 432–442. https://doi.org/10.1021/SC500848M/SUPPL_FILE/SC500848M_SI_001.PDF.

[140] A. Asfaram, M. Ghaedi, S. Agarwal, I. Tyagi, V.K. Gupta, Removal of basic dye Auramine-O by ZnS:Cu nanoparticles loaded on activated carbon: Optimization of parameters using response surface methodology with central composite design, RSC Adv. 5 (2015) 18438–18450. https://doi.org/10.1039/C4RA15637D.

[141] S. Rangabhashiyam, N.S.-J. of the T.I. of, undefined 2015, Evaluation of the biosorption potential of a novel Caryota urens inflorescence waste biomass for the removal of hexavalent chromium from aqueous solutions, Elsevier. (n.d.). https://www.sciencedirect.com/science/article/pii/S1876107014003009.

[142] J. Fu, Z. Chen, M. Wang, S. Liu, J. Zhang, … J.Z.-C.E., undefined 2015, Adsorption of methylene blue by a high-efficiency adsorbent (polydopamine microspheres): kinetics, isotherm, thermodynamics and mechanism analysis, Elsevier. (n.d.). https://www.sciencedirect.com/science/article/pii/S1385894714010055.

[143] M. Moharem, E. Elkhatib, M.M.-E. research, undefined 2019, Remediation of chromium and mercury polluted calcareous soils using nanoparticles: Sorption–desorption kinetics, speciation and fractionation, Elsevier. (n.d.). https://www.sciencedirect.com/science/article/pii/S0013935118306893.

[144] T.A. Saleh, V.K. Gupta, Synthesis and characterization of alumina nano-particles polyamide membrane with enhanced flux rejection performance, Sep. Purif. Technol. 89 (2012) 245–251. https://doi.org/10.1016/j.seppur.2012.01.039.

[145] V.K. Gupta, R. Jain, A. Nayak, S. Agarwal, M. Shrivastava, Removal of the hazardous dye-Tartrazine by photodegradation on titanium dioxide surface, Mater. Sci. Eng. C. 31 (2011) 1062–1067. https://doi.org/10.1016/j.msec.2011.03.006.

[146] T. Shahnaz, V. Sharma, S. Subbiah, S. Narayanasamy, Multivariate optimisation of Cr (VI), Co (III) and Cu (II) adsorption onto nanobentonite incorporated nanocellulose/chitosan aerogel using response surface methodology, J. Water Process Eng. 36 (2020). https://doi.org/10.1016/J.JWPE.2020.101283.

[147] N. Mohammadi, H. Khani, V. Gupta, … E.A.-J. of colloid and, undefined 2011, Adsorption process of methyl orange dye onto mesoporous carbon material–kinetic and thermodynamic studies, Elsevier. (n.d.). https://www.sciencedirect.com/science/article/pii/S002197971100806X.

[148] V.K. Gupta, C.K. Jain, I. Ali, S. Chandra, S. Agarwal, Removal of lindane and malathion from wastewater using bagasse fly ash - A sugar industry waste, Water Res. 36 (2002) 2483–2490. https://doi.org/10.1016/S0043-1354(01)00474-2.

[149] H. Shahbeig, N. Bagheri, S.A. Ghorbanian, A. Hallajisani, S. Poorkarimi, A new adsorption isotherm model of aqueous solutions on granular activated carbon, Citeseer. 1 (2013) 243–254. http://citeseerx.ist.psu.edu/viewdoc/download?doi=10.1.1.571.6718&rep=rep1&type=pdf.

[150] A. Mittal, J. Mittal, A. Malviya, V.G.-J. of colloid and interface, undefined 2010, Removal and recovery of Chrysoidine Y from aqueous solutions by waste materials, Elsevier. (n.d.). https://www.sciencedirect.com/science/article/pii/S002197971000038X.

[151] R. Saravanan, V. Gupta, … T.P.-J. of M., undefined 2013, Synthesis, characterization and photocatalytic activity of novel Hg doped ZnO nanorods prepared by thermal decomposition method, Elsevier. (n.d.). https://www.sciencedirect.com/science/article/pii/

S0167732212004114.

[152] K.Z. ELwakeel, S. El-Kousy, H.G. El-Shorbagy, M.A.A. El-Ghaffar, Comparison between the removal of Reactive Black 5 from aqueous solutions by 3-amino-1,2,4 triazole,5-thiol and melamine grafted chitosan prepared through four different routes, J. Environ. Chem. Eng. 4 (2016) 733–745. https://doi.org/10.1016/J.JECE.2015.12.015.

[153] K.Z. Elwakeel, A.A. El-Bindary, A.Z. El-Sonbati, A.R. Hawas, Adsorption of toxic acidic dye from aqueous solution onto diethylenetriamine functionalized magnetic glycidyl methacrylate-N,N′-methylenebisacrylamide, RSC Adv. 6 (2016) 3350–3361. https://doi.org/10.1039/C5RA24035B.

[154] H. Fakhri, A.R. Mahjoub, H. Aghayan, Effective removal of methylene blue and cerium by a novel pair set of heteropoly acids based functionalized graphene oxide: Adsorption and photocatalytic study, Chem. Eng. Res. Des. 120 (2017) 303–315. https://doi.org/10.1016/j.cherd.2017.02.030.

[155] B. Luo, G. Huang, Y. Yao, C. An, P. Zhang, K. Zhao, Investigation into the influencing factors and adsorption characteristics in the removal of sulfonamide antibiotics by carbonaceous materials, J. Clean. Prod. 319 (2021). https://doi.org/10.1016/J.JCLEPRO.2021.128692.

[156] H.J. Hong, H. Yu, M. Park, H.S. Jeong, Recovery of platinum from waste effluent using polyethyleneimine-modified nanocelluloses: Effects of the cellulose source and type, Carbohydr. Polym. 210 (2019) 167–174. https://doi.org/10.1016/J.CARBPOL.2019.01.079.

[157] M. Banerjee, R. Basu, S.D.-P.S. and Environmental, undefined 2018, Cr (VI) adsorption by a green adsorbent walnut shell: adsorption studies, regeneration studies, scale-up design and economic feasibility, Elsevier. (n.d.). https://www.sciencedirect.com/science/article/pii/S0957582018300922.

[158] V. Pakade, L. Maremeni, … T.N.-S.A.J. of, undefined 2016, Application of quaternized activated carbon derived from Macadamia nutshells for the removal of hexavalent chromium from aqueous solutions, Scielo.Org.Za. (n.d.). http://www.scielo.org.za/scielo.php?pid=S0379-43502016000100021&script=sci_arttext&tlng=es.

[159] D. Pradhan, L. Sukla, B. Mishra, N.D.-J. of C. Production, undefined 2019, Biosorption for removal of hexavalent chromium using microalgae Scenedesmus sp., Elsevier. (n.d.). https://www.sciencedirect.com/science/article/pii/S0959652618333213.

[160] L. Maremeni, S. Modise, … F.M.-B., undefined 2018, Adsorptive removal of hexavalent chromium by diphenylcarbazide-grafted Macadamia nutshell powder, Hindawi.Com. (n.d.). https://www.hindawi.com/journals/bca/2018/6171906/.

[161] V.K. Gupta, I. Ali, T.A. Saleh, M.N. Siddiqui, S. Agarwal, Chromium removal from water by activated carbon developed from waste rubber tires, Environ. Sci. Pollut. Res. 20 (2013) 1261–1268. https://doi.org/10.1007/S11356-012-0950-9.

[162] M. Dakiky, M. Khamis, A. Manassra, M.M.-A. in environmental, undefined 2002, Selective adsorption of chromium (VI) in industrial wastewater using low-cost abundantly available adsorbents, Elsevier. (n.d.). https://www.sciencedirect.com/science/article/pii/S109301910100079X.

[163] X. Wang, Z. Li, S.T.-J. of E. Management, undefined 2009, Removal of chromium (VI) from aqueous solution using walnut hull, Elsevier. (n.d.). https://www.sciencedirect.com/science/

article/pii/S0301479708000194.

[164] L. Li, H. Ren, Y. Liu, X. Liu, Y. Zhao, X. Zhou, W. Kang, X. Zhuang, B. Cheng, Facile construction of hierarchical porous ultrafine alumina fibers (HPAFs) and its application for dye adsorption, Microporous Mesoporous Mater. 308 (2020). https://doi.org/10.1016/J.MICROMESO.2020.110544.

[165] F. Marrakchi, B.H. Hameed, E.H. Hummadi, Mesoporous biohybrid epichlorohydrin crosslinked chitosan/carbon–clay adsorbent for effective cationic and anionic dyes adsorption, Int. J. Biol. Macromol. 163 (2020) 1079–1086. https://doi.org/10.1016/J.IJBIOMAC.2020.07.032.

[166] A.A. Atia, A.M. Donia, K.Z. Elwakeel, Adsorption behaviour of non-transition metal ions on a synthetic chelating resin bearing iminoacetate functions, Sep. Purif. Technol. 43 (2005) 43–48. https://doi.org/10.1016/J.SEPPUR.2004.09.012.

[167] D. Zhao, C. Cai, Cerium-based UiO-66 metal-organic framework for synergistic dye adsorption and photodegradation: A discussion of the mechanism, Dye. Pigment. 185 (2021). https://doi.org/10.1016/J.DYEPIG.2020.108957.

[168] Document Display | NEPIS | US EPA, (n.d.). https://nepis.epa.gov/Exe/ZyNET.exe/P100XGVV.TXT?ZyActionD=ZyDocument&Client=EPA&Index=1995+Thru+1999&Docs=&Query=&Time=&EndTime=&SearchMethod=1&TocRestrict=n&Toc=&TocEntry=&QField=&QFieldYear=&QFieldMonth=&QFieldDay=&IntQFieldOp=0&ExtQFieldOp=0&XmlQuery=&File=D%3A%5Czyfiles%5CIndexData%5C95thru99%5CTxt%5C00000041%5CP100XGVV.txt&User=ANONYMOUS&Password=anonymous&SortMethod=h%7C-&MaximumDocuments=1&FuzzyDegree=0&ImageQuality=r75g8/r75g8/x150y150g16/i425&Display=hpfr&DefSeekPage=x&SearchBack=ZyActionL&Back=ZyActionS&BackDesc=Results page&MaximumPages=1&ZyEntry=1&SeekPage=x&ZyPURL.

[169] Ground Water and Drinking Water | US EPA, (n.d.). https://www.epa.gov/ground-water-and-drinking-water.

[170] N.H. Mthombeni, S. Mbakop, S.C. Ray, T. Leswifi, A. Ochieng, M.S. Onyango, Highly efficient removal of chromium (VI) through adsorption and reduction: A column dynamic study using magnetized natural zeolite-polypyrrole composite, J. Environ. Chem. Eng. 6 (2018) 4008–4017. https://doi.org/10.1016/J.JECE.2018.05.038.

[171] O.C. Iheanacho, J.T. Nwabanne, C.C. Obi, C.E. Onu, Packed bed column adsorption of phenol onto corn cob activated carbon: linear and nonlinear kinetics modeling, South African J. Chem. Eng. 36 (2021) 80–93. https://doi.org/10.1016/J.SAJCE.2021.02.003.

[172] F.B. Hussein, B.K. Mayer, Fixed-bed column study of phosphate adsorption using immobilized phosphate-binding protein, Chemosphere. 295 (2022) 133908. https://doi.org/10.1016/J.CHEMOSPHERE.2022.133908.

[173] V. Javanbakht, Z. Rafiee, Fibrous polyester sponge modified with carboxymethyl cellulose and Zeolitic imidazolate frameworks for methylene blue dye removal in batch and continuous adsorption processes, J. Mol. Struct. 1249 (2022). https://doi.org/10.1016/J.MOLSTRUC.2021.131552.

[174] S.S. Madan, B.S. De, K.L. Wasewar, Adsorption performance of packed bed column for benzylformic acid removal using CaO2 nanoparticles, Chem. Data Collect. 23 (2019). https://doi.org/10.1016/J.CDC.2019.100267.

[175] P. Patel, S. Gupta, P. Mondal, Modeling of continuous adsorption of greywater pollutants onto sawdust activated carbon bed integrated with sand column, J. Environ. Chem. Eng. 10 (2022). https://doi.org/10.1016/J.JECE.2022.107155.

[176] K.H. Chu, Breakthrough curve analysis by simplistic models of fixed bed adsorption: In defense of the century-old Bohart-Adams model, Chem. Eng. J. 380 (2020). https://doi.org/10.1016/J.CEJ.2019.122513.

[177] K.C. Lai, B.Y.Z. Hiew, W.T. Tee, S. Thangalazhy-Gopakumar, S. Gan, L.Y. Lee, Usage of a new macro-hierarchical graphene sponge in batch adsorption and packed column configuration for efficient decontamination of cadmium in aqueous environment, J. Environ. Chem. Eng. 9 (2021). https://doi.org/10.1016/J.JECE.2021.106057.

[178] D.M. Juela, Comments on “Treatment of malachite green dye containing solution using biodegradable sodium alginate/NaOH treated activated sugarcane baggsse charcoal beads: Batch, optimization using response surface methodology and continuous fixed bed column study” and “Adsorption and oxidation of ciprofloxacin in a fixed bed column using activated sludge derived activated carbon,” J. Environ. Manage. 281 (2021). https://doi.org/10.1016/J.JENVMAN.2020.111815.

[179] A.B.V. de Farias, T.B. da Costa, M.G.C. da Silva, M.G.A. Vieira, Cerium recovery from aqueous solutions by bio/adsorption: A review in a circular economy context, J. Clean. Prod. 326 (2021). https://doi.org/10.1016/J.JCLEPRO.2021.129395.

[180] F. Feizi, A.K. Sarmah, R. Rangsivek, Adsorption of pharmaceuticals in a fixed-bed column using tyre-based activated carbon: Experimental investigations and numerical modelling, J. Hazard. Mater. 417 (2021). https://doi.org/10.1016/J.JHAZMAT.2021.126010.

[181] S. Kumar, T. Shahnaz, N. Selvaraju, P.V. Rajaraman, Kinetic and thermodynamic studies on biosorption of Cr(VI) on raw and chemically modified Datura stramonium fruit, Environ. Monit. Assess. 192 (2020). https://doi.org/10.1007/s10661-020-8181-x.

[182] S. Mishra, S.S. Sahoo, A.K. Debnath, K.P. Muthe, N. Das, P. Parhi, Cobalt ferrite nanoparticles prepared by microwave hydrothermal synthesis and adsorption efficiency for organic dyes: Isotherms, thermodynamics and kinetic studies, Adv. Powder Technol. 31 (2020) 4552–4562. https://doi.org/10.1016/J.APT.2020.10.001.

[183] T. Van Tran, D.T.C. Nguyen, H.T.N. Le, D.V.N. Vo, V.D. Doan, V.P. Dinh, H.T.T. Nguyen, T.D. Nguyen, L.G. Bach, Amino-functionalized MIL-88B(Fe)-based porous carbon for enhanced adsorption toward ciprofloxacin pharmaceutical from aquatic solutions, Comptes Rendus Chim. 22 (2019) 804–812. https://doi.org/10.1016/j.crci.2019.09.003.

[184] T. Shahnaz, D. Bedadeep, S. Narayanasamy, Investigation of the adsorptive removal of methylene blue using modified nanocellulose, Int. J. Biol. Macromol. 200 (2022) 162–171. https://doi.org/10.1016/J.IJBIOMAC.2021.12.081.

[185] F.C. Wu, R.L. Tseng, R.S. Juang, Characteristics of Elovich equation used for the analysis of adsorption kinetics in dye-chitosan systems, Chem. Eng. J. 150 (2009) 366–373. https://doi.org/10.1016/j.cej.2009.01.014.

[186] A.B. Albadarin, M.N. Collins, M. Naushad, S. Shirazian, G. Walker, C. Mangwandi, Activated lignin-chitosan extruded blends for efficient adsorption of methylene blue, Chem. Eng. J. 307 (2017) 264–272. https://doi.org/10.1016/j.cej.2016.08.089.

[187] F.A. Ngwabebhoh, N. Mammadli, U. Yildiz, Bioinspired modified nanocellulose adsorbent for enhanced boron recovery from aqueous media: Optimization, kinetics, thermodynamics and reusability study, J. Environ. Chem. Eng. 7 (2019). https://doi.org/10.1016/J.JECE.2019.103281.

[188] L. Lonappan, T. Rouissi, S. Kaur Brar, M. Verma, R.Y. Surampalli, An insight into the adsorption of diclofenac on different biochars: Mechanisms, surface chemistry, and thermodynamics, Bioresour. Technol. 249 (2018) 386–394. https://doi.org/10.1016/j.biortech.2017.10.039.

[189] F. Wu, R. Tseng, R.J.-C. engineering journal, undefined 2009, Initial behavior of intraparticle diffusion model used in the description of adsorption kinetics, Elsevier. (n.d.). https://www.sciencedirect.com/science/article/pii/S138589470900312X.

[190] Y. Ho, G.M.-P. biochemistry, undefined 1999, Pseudo-second order model for sorption processes, Elsevier. (n.d.). https://www.sciencedirect.com/science/article/pii/S0032959298001125.

[191] A.A. Alqadami, M. Naushad, M.A. Abdalla, M.R. Khan, Z.A. Alothman, Adsorptive removal of toxic dye using Fe3O4−TSC nanocomposite: Equilibrium, kinetic, and thermodynamic studies, J. Chem. Eng. Data. 61 (2016) 3806–3813. https://doi.org/10.1021/ACS.JCED.6B00446.

[192] A. Chandrasekaran, C. Patra, S. Narayanasamy, S. Subbiah, Adsorptive removal of Ciprofloxacin and Amoxicillin from single and binary aqueous systems using acid-activated carbon from Prosopis juliflora, Environ. Res. 188 (2020). https://doi.org/10.1016/j.envres.2020.109825.

[193] N. Ballav, R. Das, S. Giri, A.M. Muliwa, K. Pillay, A. Maity, L-cysteine doped polypyrrole (PPy@L-Cyst): A super adsorbent for the rapid removal of Hg+2 and efficient catalytic activity of the spent adsorbent for reuse, Chem. Eng. J. 345 (2018) 621–630. https://doi.org/10.1016/J.CEJ.2018.01.093.

[194] E.H. Chafyq, K. Legrouri, M. Aghrouch, M. Oumam, S. Mansouri, E. Hassane Khouya, H. Hannache, Adsorption of ciprofloxacin antibiotic on materials prepared from Moroccan oil shales, Chem. Phys. Lett. 778 (2021). https://doi.org/10.1016/J.CPLETT.2021.138707.

[195] T.S. Anirudhan, S.R. Rejeena, Adsorption and hydrolytic activity of trypsin on a carboxylate-functionalized cation exchanger prepared from nanocellulose, J. Colloid Interface Sci. 381 (2012) 125–136. https://doi.org/10.1016/J.JCIS.2012.05.024.

[196] S. Noreen, H.N. Bhatti, M. Iqbal, F. Hussain, F.M. Sarim, Chitosan, starch, polyaniline and polypyrrole biocomposite with sugarcane bagasse for the efficient removal of Acid Black dye, Int. J. Biol. Macromol. 147 (2020) 439–452. https://doi.org/10.1016/j.ijbiomac.2019.12.257.

[197] M. Hachemaoui, B. Boukoussa, A. Mokhtar, A. Mekki, M. Beldjilali, M. Benaissa, F. Zaoui, A. Hakiki, W. Chaibi, M. Sassi, R. Hamacha, Dyes adsorption, antifungal and antibacterial properties of metal loaded mesoporous silica: Effect of metal and calcination treatment, Mater. Chem. Phys. 256 (2020). https://doi.org/10.1016/J.MATCHEMPHYS.2020.123704.

[198] M. Naushad, Surfactant assisted nano-composite cation exchanger: Development, characterization and applications for the removal of toxic Pb2+ from aqueous medium, Chem. Eng. J. 235 (2014) 100–108. https://doi.org/10.1016/j.cej.2013.09.013.

[199] R. Kumar, Mixed phase lamellar titania-titanate anchored with Ag2O and polypyrrole for enhanced adsorption and photocatalytic activity, J. Colloid Interface Sci. 477 (2016) 83–93. https://doi.org/10.1016/J.JCIS.2016.05.039.

[200] C.V.T. Rigueto, M. Rosseto, M.T. Nazari, B.E.P. Ostwald, I. Alessandretti, C. Manera, J.S. Piccin, A. Dettmer, Adsorption of diclofenac sodium by composite beads prepared from tannery wastes-derived gelatin and carbon nanotubes, J. Environ. Chem. Eng. 9 (2021). https://doi.org/10.1016/j.jece.2021.105030.

[201] H. Freundlich, W. Heller, The Adsorption of cis- and trans-Azobenzene, J. Am. Chem. Soc. 61 (1939) 2228–2230. https://doi.org/10.1021/JA01877A071.

[202] X. Song, X. Lü, Y. Shen, S. Guo, Y.G.-I.J. of Coal, undefined 2018, A modified supercritical Dubinin–Radushkevich model for the accurate estimation of high pressure methane adsorption on shales, Elsevier. (n.d.). https://www.sciencedirect.com/science/article/pii/S0166516217308881.

[203] N.H. Mthombeni, S. Mbakop, A. Ochieng, M.S. Onyango, Vanadium (V) adsorption isotherms and kinetics using polypyrrole coated magnetized natural zeolite, J. Taiwan Inst. Chem. Eng. 66 (2016) 172–180. https://doi.org/10.1016/J.JTICE.2016.06.016.

[204] Z. Bian, Y. Feng, H. Li, H. Yu, H. Wu, Adsorption-photocatalytic degradation and kinetic of sodium isobutyl xanthate using the nitrogen and cerium co-doping TiO2-coated activated carbon, Chemosphere. 263 (2021). https://doi.org/10.1016/J.CHEMOSPHERE.2020.128254.

[205] K.H. Chu, The Kiselev isotherm for adsorption at the liquid-solid interface: Solving the mystery of negative equilibrium constants, J. Mol. Liq. 343 (2021). https://doi.org/10.1016/J.MOLLIQ.2021.117674.

[206] M. Stylianou, A. Christou, C. Michael, A. Agapiou, P. Papanastasiou, D. Fatta-Kassinos, Adsorption and removal of seven antibiotic compounds present in water with the use of biochar derived from the pyrolysis of organic waste feedstocks, J. Environ. Chem. Eng. 9 (2021) 105868. https://doi.org/10.1016/J.JECE.2021.105868.

[207] A. Fouda, S.E.D. Hassan, E. Saied, M.F. Hamza, Photocatalytic degradation of real textile and tannery effluent using biosynthesized magnesium oxide nanoparticles (MgO-NPs), heavy metal adsorption, phytotoxicity, and antimicrobial activity, J. Environ. Chem. Eng. 9 (2021) 105346. https://doi.org/10.1016/J.JECE.2021.105346.

[208] R. Li, L. Liu, F. Yang, Removal of aqueous Hg(II) and Cr(VI) using phytic acid doped polyaniline/cellulose acetate composite membrane, J. Hazard. Mater. 280 (2014) 20–30. https://doi.org/10.1016/j.jhazmat.2014.07.052.

[209] I. Santos Sauceda, M.M. Castillo Ortega, G. Tiburcio Munive, J.M. Quiroz Castillo, T. del Castillo Castro, M.A. Encinas Romero, M. Aguilar Vega, J.Z. Ramírez, L.S. Quiroz Castillo, Selective adsorption of metallic complex using polyaniline or polypyrrole, Mater. Chem. Phys. 182 (2016) 39–48. https://doi.org/10.1016/J.MATCHEMPHYS.2016.07.003.

[210] M.C. Sichinga, R. Koshani, T.G.M. van de Ven, Chemisorption of basic fuchsine in packed beds of dialdehyde cellulose fibres, Colloids Surfaces A Physicochem. Eng. Asp. 632 (2022)

127726. https://doi.org/10.1016/J.COLSURFA.2021.127726.

[211] R. Brandes, D. Belosinschi, F. Brouillette, B. Chabot, A new electrospun chitosan/phosphorylated nanocellulose biosorbent for the removal of cadmium ions from aqueous solutions, J. Environ. Chem. Eng. 7 (2019). https://doi.org/10.1016/J.JECE.2019.103477.

[212] V. Medri, E. Papa, M. Mor, A. Vaccari, A. Natali Murri, L. Piotte, C. Melandri, E. Landi, Mechanical strength and cationic dye adsorption ability of metakaolin-based geopolymer spheres, Appl. Clay Sci. 193 (2020). https://doi.org/10.1016/J.CLAY.2020.105678.

[213] R. Curvello, V.S. Raghuwanshi, G. Garnier, Engineering nanocellulose hydrogels for biomedical applications, Adv. Colloid Interface Sci. 267 (2019) 47–61. https://doi.org/10.1016/J.CIS.2019.03.002.

[214] Y. Yue, X. Wang, J. Han, L. Yu, J. Chen, Q. Wu, J. Jiang, Effects of nanocellulose on sodium alginate/polyacrylamide hydrogel: Mechanical properties and adsorption-desorption capacities, Carbohydr. Polym. 206 (2019) 289–301. https://doi.org/10.1016/J.CARBPOL.2018.10.105.

[215] T. Yao, W. Jia, X. Tong, Y. Feng, Y. Qi, X. Zhang, J. Wu, One-step preparation of nanobeads-based polypyrrole hydrogel by a reactive-template method and their applications in adsorption and catalysis, J. Colloid Interface Sci. 527 (2018) 214–221. https://doi.org/10.1016/J.JCIS.2018.05.052.

[216] P.L. Yap, Y.L. Auyoong, K. Hassan, F. Farivar, D.N.H. Tran, J. Ma, D. Losic, Multithiol functionalized graphene bio-sponge via photoinitiated thiol-ene click chemistry for efficient heavy metal ions adsorption, Chem. Eng. J. 395 (2020). https://doi.org/10.1016/J.CEJ.2020.124965.

[217] I. Mironyuk, I. Mykytyn, H. Vasylyeva, K. Savka, Sodium-modified mesoporous TiO2: Sol-gel synthesis, characterization and adsorption activity toward heavy metal cations, J. Mol. Liq. 316 (2020). https://doi.org/10.1016/J.MOLLIQ.2020.113840.

[218] M. Choi, J. Jang, Heavy metal ion adsorption onto polypyrrole-impregnated porous carbon, J. Colloid Interface Sci. 325 (2008) 287–289. https://doi.org/10.1016/j.jcis.2008.05.047.

[219] S.M. Kharrazi, N. Mirghaffari, M.M. Dastgerdi, M. Soleimani, A novel post-modification of powdered activated carbon prepared from lignocellulosic waste through thermal tension treatment to enhance the porosity and heavy metals adsorption, Powder Technol. 366 (2020) 358–368. https://doi.org/10.1016/J.POWTEC.2020.01.065.

[220] Jumina, Y. Priastomo, H.R. Setiawan, Mutmainah, Y.S. Kurniawan, K. Ohto, Simultaneous removal of lead(II), chromium(III), and copper(II) heavy metal ions through an adsorption process using C-phenylcalix[4]pyrogallolarene material, J. Environ. Chem. Eng. 8 (2020). https://doi.org/10.1016/J.JECE.2020.103971.

[221] S.D. Kalme, G.K. Parshetti, S.U. Jadhav, S.P. Govindwar, Biodegradation of benzidine based dye Direct Blue-6 by Pseudomonas desmolyticum NCIM 2112, Bioresour. Technol. 98 (2007) 1405–1410. https://doi.org/10.1016/j.biortech.2006.05.023.

[222] V. Gupta, R. Jain, A. Nayak, … S.A.-M. science and, undefined 2011, Removal of the hazardous dye—tartrazine by photodegradation on titanium dioxide surface, Elsevier. (n.d.). https://www.sciencedirect.com/science/article/pii/S0928493111000749.

[223] P. Sirajudheen, P. Karthikeyan, S. Vigneshwaran, M. Nikitha, C.A.A. Hassan, S. Meenakshi,

Ce(III) networked chitosan/β-cyclodextrin beads for the selective removal of toxic dye molecules: Adsorption performance and mechanism, Carbohydr. Polym. Technol. Appl. 1 (2020) 100018. https://doi.org/10.1016/J.CARPTA.2020.100018.

[224] V.N. Priya, M. Rajkumar, J. Mobika, S.P.L. Sibi, Adsorption of As (V) ions from aqueous solution by carboxymethyl cellulose incorporated layered double hydroxide/reduced graphene oxide nanocomposites: Isotherm and kinetic studies, Environ. Technol. Innov. 26 (2022). https://doi.org/10.1016/J.ETI.2022.102268.

[225] X. Fan, R. Gan, J. Liu, Y. Xie, D. Xu, Y. Xiang, J. Su, Z. Teng, J. Hou, Adsorption and desorption behaviors of antibiotics by tire wear particles and polyethylene microplastics with or without aging processes, Sci. Total Environ. 771 (2021). https://doi.org/10.1016/J.SCITOTENV.2021.145451.

[226] C. Du, Z. Zhang, G. Yu, H. Wu, H. Chen, L. Zhou, Y. Zhang, Y. Su, S. Tan, L. Yang, J. Song, S. Wang, A review of metal organic framework (MOFs)-based materials for antibiotics removal via adsorption and photocatalysis, Chemosphere. 272 (2021). https://doi.org/10.1016/J.CHEMOSPHERE.2020.129501.

[227] W. Ma, X. Xu, B. An, K. Zhou, K. Mi, M. Huo, H. Liu, H. Wang, Z. Liu, G. Cheng, L. Huang, Single and ternary competitive adsorption-desorption and degradation of amphenicol antibiotics in three agricultural soils, J. Environ. Manage. 297 (2021). https://doi.org/10.1016/J.JENVMAN.2021.113366.

[228] G.H.-T.J. of chemical physics, undefined 1948, Physical adsorption on non-uniform surfaces, Aip.Scitation.Org. 16 (1948) 520. https://doi.org/10.1063/1.1746689.

[229] O. Redlich, D.L. Peterson, A useful adsorption isotherm, J. Phys. Chem. 63 (1959) 1024. https://doi.org/10.1021/J150576A611.

[230] M.M. Dubinin, The potential theory of adsorption of gases and vapors for adsorbents with energetically nonuniform surfaces, Chem. Rev. 60 (1960) 235–241. https://doi.org/10.1021/CR60204A006.

[231] J. Gustafsson, M. Akram, C.T.- Chemosphere, undefined 2015, Predicting sulphate adsorption/desorption in forest soils: evaluation of an extended Freundlich equation, Elsevier. (n.d.). https://www.sciencedirect.com/science/article/pii/S0045653514007139.

[232] M. Fayazi, D. Afzali, M.A. Taher, A. Mostafavi, V.K. Gupta, Removal of Safranin dye from aqueous solution using magnetic mesoporous clay: Optimization study, J. Mol. Liq. 212 (2015) 675–685. https://doi.org/10.1016/j.molliq.2015.09.045.

[233] X. Feng, O. Onel, M. Council-Troche, A. Noble, R.H. Yoon, J.R. Morris, A study of rare earth ion-adsorption clays: The speciation of rare earth elements on kaolinite at basic pH, Appl. Clay Sci. 201 (2021) 105920. https://doi.org/10.1016/J.CLAY.2020.105920.

APPENDIX

Table A.1. A detailed list of chemicals, reagents and salts

Sl. No.	Chemicals/Reagents/Salts	Purpose
1	Sulphuric acid (98%)	Chemical activation of adsorbent
2	Sulphuric acid (64%)	Preparation of adsorbent
3	Ortho-phosphoric acid (88%)	Chemical activation of adsorbent
4	Phosphoric acid (85%)	Chemical activation of adsorbent
5	Ethylenediaminetetra acetic acid (EDTA)	Chelating agent for acid activated carbon
6	Ethanol (90%)	Preparation of adsorbent
7	Hydrogen peroxide (H_2O_2)	Preparation of adsorbent
8	Sodium bicarbonate ($NaHCO_3$)	For washing prepared carbon
9	1% Sodium Hypochlorite (NaClO)	Rinsing plant seeds
10	Pyrrole (PY)	Preparation of adsorbent
11	Ammonia solution 10%	Preparation of adsorbent
12	Ferric Chloride Hexahydrate ($FeCl_3.6H_2O$)	Preparation of adsorbent
13	Ferrous chloride tetrahydrate ($FeCl_2.4H_2O$)	Preparation of adsorbent
14	Ammonium persulfate (APS)	Preparation of adsorbent
15	0.1 N Sodium Hydroxide (NaOH)	Desorbing agent
16	Congo Red (CR)	Adsorbate
17	Direct Blue 6 (DB)	Adsorbate
18	Bromophenol Blue (BB)	Adsorbate
19	Basic Fuchsine (BF)	Adsorbate
20	Cerium	Adsorbate
21	Ciprofloxacin (CPXO)	Adsorbate
22	Diclofenac (DCF)	Adsorbate
23	Diphenyl carbazide (DPC)	For detecting Cr(VI)
24	Potassium Dichromate ($K_2Cr_2O_7$)	Source of chromium (Cr^{+6}) ion
25	Lead Nitrate ($Pb(NO_3)_2$)	Source of lead (Pb^{+2}) ion
26	0.1 M Sodium Hydroxide (NaOH)	For adjusting pH

27	0.1 M Hydrochloric acid (HCl)	For adjusting pH
28	Iron(III) Chloride ($FeCl_3$)	Source of ferric (Fe^{+3}) ion
29	Cobalt (II) Chloride ($CoCl_2$)	Source of cobalt (Co^{+2}) ion
30	Nickel Sulphate ($NiSO_4$)	Source of Nickel (Ni^{+2}) ion
31	Zinc Chloride ($ZnCl_2$)	Source of zinc (Zn^{+2}) ion
32	Copper(II) Chloride ($CuCl_2$)	Source of copper (Cu^{+2}) ion
33	Sodium Sulphate (Na_2SO_4)	Source of sulphate (SO_4^{-2}) ion
34	Sodium Nitrate ($NaNO_3$)	Source of nitrate (NO_3^{-2}) ion
35	Sodium Carbonate (Na_2CO_3)	Source of carbonate (CO_3^{-2}) ion
36	Sodium Chloride (NaCl)	Source of chloride (Cl^{-1}) ion
37	Sodium Phosphate (Na_3PO_4)	Source of phosphate (PO_4^{-3}) ion

Table A.2. A detailed list of instrumentation used for characterization of the adsorbent

Sl. No.	Instrumentation	Make and model	Purpose
1	Scanning electron microscopy (SEM)	Zeiss, GeminiSEM, Germany	For surface morphology analysis
2	Transmission electron microscopy (TEM)	JEOL, JEM-2100, Japan	For surface morphology analysis
3	Energy-dispersive X-ray spectroscopy (EDS)	Zeiss, SigmaSEM, Germany	For surface elemental analysis
4	Atomic force microscopy (AFM)	Cypher, Oxford, United Kingdom	For surface morphology analysis
5	Powder X-ray diffraction (XRD)	Rigaku, Micromax-007HF, Japan	Analysing substructural modifications caused due to modification
6	Total pore analysis or Brunauer-Emmett- Teller (BET) analysis	Quantachrome- Autosorb-IQ MP, USA	For total pore/porosity analysis of the adsorbent
7	Zeta potential analysis	Delsa nano C, Beckman Coulter, Switzerland	For analysing surface charge of the adsorbent
8	Fourier-transform infrared spectroscopy (FT-IR)	Spectrum two, PerkinElmer, Singapore	For analysing surface functional groups involved in adsorption or modification
9	Raman microscopy	Horiba Jobin Vyon, LabRam HR	For structural fingerprint
10	Thermogravimetric analyser	Netzsch, STA449F3A00	For thermal stability
11	Vibrating Sample Magnetometer	Lakeshore, 7410 series	For magnetiszation

LIST OF PUBLICATIONS AND COMMUNICATIONS

A. PUBLICATIONS FROM THESIS WORK

1. **TASRIN SHAHNAZ,** Vishnu Priyan V., Sivakumar Pandian. and Selvaraju Narayanasamy*, Nanocellulose extracted from grass for adsorption abatement of Ciprofloxacin and Diclofenac removal with phyto, and fish toxicity studies, **Environmental Pollution, 2021,** https://doi.org/10.1016/j.envpol.2020.115494 (Elsevier, SCI IF: 9.988)
2. **TASRIN SHAHNAZ,** Vishnu Priyan V., Anjali J. and Selvaraju Narayanasamy*, Magnetic nanocellulose from *Cyperus rotundas* grass in the absorptive removal of rare earth element Cerium (III): toxicity studies and interpretation. **Chemosphere, 2021,** https://doi.org/10.1016/j.chemosphere.2021.131912 (Elsevier, SCI IF: 8.943)
3. **TASRIN SHAHNAZ**, Mohamed Madhar Fazil S, Padmanaban V C, and Selvaraju Narayanasamy*, Surface Modification of Nanocellulose Using Polypyrrole for the Adsorptive Removal of Congo red Dye and Chromium in Aqueous Binary Mixture: Studies on Composite Characterisation and Process Kinetics, **International Journal of Biological Macromolecules, 2020,** https://doi.org/10.1016/j.ijbiomac.2020.02.181 (Elsevier, SCI IF: 8.025)
4. **TASRIN SHAHNAZ**, Anjali J., Bedadeep D., Selvaraju Narayanasamy*, A Review on tailored graphene material for Industrial Wastewater, **Journal of Environmental Chemical Engineering, 2021,** https://doi.org/10.1016/j.jece.2021.105933 (Elsevier, SCI IF: 7.968)
5. **TASRIN SHAHNAZ**, Vivek Sharma, Senthilmurugan Subbiah and Selvaraju Narayanasamy*, Multivariate Optimisation of Cr (VI), Co (III) and Cu (II) adsorption onto Nanobentonite incorporated Nanocellulose/Chitosan Aerogel using Response Surface Methodology, **Journal of Water Process Engineering, 2020,** https://doi.org/10.1016/j.jwpe.2020.101283 (Elsevier, SCI IF: 7.340) **(Annual best paper award of 2020, Elsevier)**
6. **TASRIN SHAHNAZ**, Mohamed Madhar Fazil S, Senthilmurugan S and Selvaraju Narayanasamy*, Facile preparation of nanocellulose embedded polypyrrole composite for bromophenol blue and direct blue 6 removal: unary and binary process optimisation and seed toxicity, **International Journal of Environmental Science and Technology, 2020,** https://doi.org/10.1007/s13762-020-02814-w (Springer, SCI IF: 3.519)
7. **TASRIN SHAHNAZ**, Chandi Patra, Vivek Sharma, and Selvaraju Narayanasamy*, Biosorption of Chromium from simulated wastewater using activated and chelated *Acacia auriculiformis* as a plausible biosorbent, **Chemistry and Ecology, 2020,** https://doi.org/10.1080/02757540.2020.1723560 (Taylor & Francis, SCI IF: 2.381)
8. **TASRIN SHAHNAZ,** D. Bedadeep# and Selvaraju Narayanasamy*, Investigation of the adsorptive removal of methylene blue using modified nanocellulose: A Response Surface Methodology Approach, **International Journal of Biological Macromolecules, 2022,** https://doi.org/10.1016/j.ijbiomac.2021.12.081 (Elsevier, SCI IF: 8.025)

TH-3150_176106114

B. PUBLICATIONS FROM COLLABORATIVE WORK

1. Vishnu Priyan V., **TASRIN SHAHNAZ**, Suganya E., Senthilkumar Sivaprakasam and Selvaraju Narayanasamy*, Ecotoxicological assessment of micropollutant Diclofenac biosorption on Magnetic sawdust: Phyto, Microbial and Fish toxicity studies, **Journal of Hazardous Materials, 2020,** https://doi.org/10.1016/j.jhazmat.2020.123532 (Elsevier, SCI IF: 14.224)
2. A. Ajmani, **TASRIN SHAHNAZ**, Senthilmurugan S., and Selvaraju Narayanasamy*, Hexavalent chromium adsorption on virgin, biochar, and chemically modified carbons prepared from *Phanera vahlii* fruit biomass: equilibrium, kinetics, and thermodynamics approach, **Environmental Science and Pollution Research, 2019,** https://doi.org/10.1007/s11356-019-06335-z (Springer, SCI IF: 5.190)
3. Chandi Patra, **TASRIN SHAHNAZ**, Senthilmurugan S., and Selvaraju Narayanasamy*, Comparative assessment of crude and acid-activated preparations of novel *Pongamia pinnata* shells for the elimination of Cr(VI) from simulated wastewater: Isotherm, Kinetic and Thermodynamic studies, **Environmental Science and Pollution Research, 2020,** https://doi.org/10.1007/s11356-020-07979-y (Springer, SCI IF: 5.190)
4. Vivek Sharma, **TASRIN SHAHNAZ**, Senthilmurugan S., and Selvaraju Narayanasamy*, Molecular Scale Insights into the Removal of Hazardous Water Pollutants using Nanobentonite Impregnated Nanocellulose- Chitosan Based Aerogel, **Journal of Polymers and Environment, 2020,** https://doi.org/10.1007/s10924-020-01740-9 (Springer, SCI IF: 3.667)
5. Vishnu Priyan V., **TASRIN SHAHNAZ**, and Selvaraju Narayanasamy*, Muthupandian Saravanan, Synthesized Starch Nanocrystals as Biosorbent for Congo red dye removal, **Journal of Cluster Science, 2021,** https://doi.org/10.1007/s10876-020-01905-5 (Springer, SCI IF: 3.061)
6. Shravan Kumar, **TASRIN SHAHNAZ**, Selvaraju Narayanasamy*, and R. Prasanna Venkatesh, Kinetics and thermodynamics study of Cr (VI)on biosorption onto raw and chemically modified *Datura stramonium* Fruit, **Environmental Monitoring and Assessment, 2020,** https://doi.org/10.1007/s10661-020-8181-x (Springer, SCI IF: 2.513)
7. A. Ajmani, **TASRIN SHAHNAZ**, S Narayanan, and Selvaraju Narayanasamy*, Equilibrium, kinetics and thermodynamics of hexavalent chromium biosorption on pristine and zinc chloride activated *Senna siamea* seed pods, **Chemistry and Ecology, 2019,** https://doi.org/10.1080/02757540.2019.1584614 (Taylor & Francis, SCI IF: 2.381)
8. E. Nakkeeran, Chandi Patra, **TASRIN SHAHNAZ**, S Rangabhashiyam, and Selvaraju Narayanasamy*, Continuous biosorption assessment for the removal of hexavalent chromium from aqueous solutions using *Strychnos nux vomica* fruit shell, **Bioresource Technology Reports, 2018,** https://doi.org/10.1016/j.biteb.2018.09.001 **(Elsevier)**
9. K Janani, N Sivarajasekar, S Muthusaravanan, K Ram, J Prakashman, S Sivamani, Nirajan Dhakal, **TASRIN SHAHNAZ**, and Selvaraju Narayanasamy*, Optimization of EDTA enriched phytoaccumulation of zinc by Ophiopogon japonicus: Comparison of Response Surface, Artificial Neural Network and Random Forest models, **Bioresource Technology Reports, 2019,** https://doi.org/10.1016/j.biteb.2019.100265 **(Elsevier)**

C. PATENT

1. **TASRIN SHAHNAZ,** Selvaraju N, "A method for preparing novel adsorbent for removing dyes from wastewater", Applied, **IPO Application no: 202231034656**

D. LIST OF MANUSCRIPTS UNDER REVIEW

1. Ragavan Chandrasekar, Das Bedadeep, **TASRIN SHAHNAZ**, Vishnu Priyan Varadharaj, Ajit Kumar, Harish Kumar, Selvaraju Narayanasamy*, Graphene-based Materials in Effective Remediation of Wastewater (Book Chapter).
2. D. Bedadeep, **TASRIN SHAHNAZ**, Manu Sankar V., Lingaraj Sahooand Selvaraju Narayanasamy*, Organic polymer doped graphene-based composite for the effective elimination of diclofenac: A detailed study with phytotoxic assessments.

E. LIST OF CONFERENCES ATTENDED

1. **TASRIN SHAHNAZ**, Selvaraju Narayanasamy*, International Conference being organized under the broad theme "Recent Advances in Applied Sciences, Technology & Health– RASTH, March 2021.
2. **TASRIN SHAHNAZ**, Selvaraju Narayanasamy*, International Conference on Nanoscience and Nanotechnology (Virtual Conference) SRM Institute of Science and Technology– ICONN, Feb 2021. **(Best poster presentation award)**
3. Anjali Jayakumar, **TASRIN SHAHNAZ** and Selvaraju Narayanasamy*, International Conference being organized under the broad theme "Recent Advances in Applied Sciences, Technology & Health–RASTH, March 2021.
4. **TASRIN SHAHNAZ**, Mohamed Madhar Fazil S and Selvaraju N*, Facile preparation of nanocellulose embedded polypyrrole composite for bromophenol blue and direct blue 6 removal:unary and binary process optimisation and seed toxicity, Reflux 7.0, Chemical Engineering, IITG, Sep 2019.
5. **TASRIN SHAHNAZ**, V. Vishnu Priyan, N. Selvaraju*, Optimisation of Cr (VI), Co (III) and Cu (II) adsorption onto synthesized Nanobentonite incorporated Nanocellulose/ Chitosan Aerogel using Central Composite Design, Water 2020, Centre for Environment, IITG, Jan 2020.
6. Mohamed Madhar Fazil S, **TASRIN SHAHNAZ** and Selvaraju N*, Synthesis of Nanocellulose Embedded Polypyrrole composite and its application in the removal of Congo red and Chromium, Water 2020, Centre for Environment, IITG, Jan 2020.
7. Mohamed Madhar Fazil S, **TASRIN SHAHNAZ** and Selvaraju N*, Preparation and Characterisation of Nanocellulose/Polypyrrole composites and its application in antibiotic removal in wastewater, ICBSEE 2020, NIT Rourkela, March 2020.

TH-3150_176106114

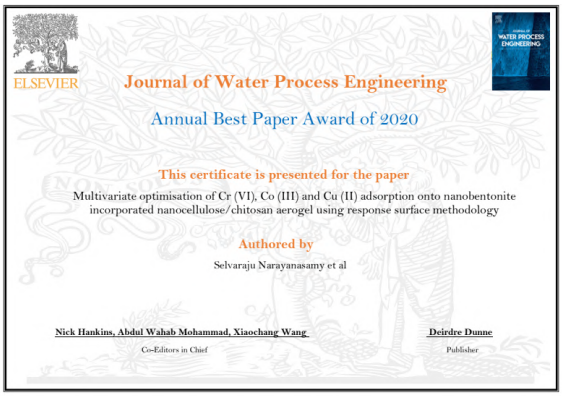
ELSEVIER

Journal of Water Process Engineering

Annual Best Paper Award of 2020

This certificate is presented for the paper

Multivariate optimisation of Cr (VI), Co (III) and Cu (II) adsorption onto nanobentonite incorporated nanocellulose/chitosan aerogel using response surface methodology

Authored by

Selvaraju Narayanasamy et al

Nick Hankins, Abdul Wahab Mohammad, Xiaochang Wang
Co-Editors in Chief

Deirdre Dunne
Publisher

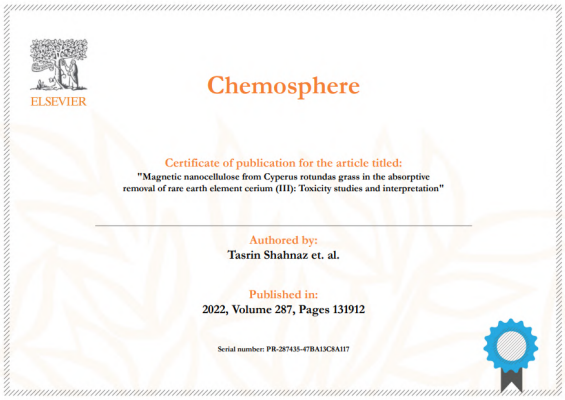
ELSEVIER

Chemosphere

Certificate of publication for the article titled:
"Magnetic nanocellulose from Cyperus rotundas grass in the absorptive removal of rare earth element cerium (III): Toxicity studies and interpretation"

Authored by:
Tasrin Shahnaz et. al.

Published in:
2022, Volume 287, Pages 131912

Serial number: PR-287435-47BA13C8A117


SRM

6th International Conference on Nanoscience and Nanotechnology (Virtual Conference)

SRM Institute of Science and Technology
Kattankulathur - 603203

ICONN 2021

Certificate of Appreciation

The Lecture entitled Synthesis of magnetic nanocellulose composite to treat rare earth element from wastewater and its phytotoxicity studies presented by Mr. / Ms. / Dr. TASRIN SHAHNAZ has received SRM-ICONN Best Poster Presentation Award in the International Conference on Nanoscience and Nanotechnology (ICONN 2021) organized by Department of Physics and Nanotechnology, SRM IST- India during February 01 – 03, 2021, in association with Shizuoka University, Japan; National Chiao Tung University, Taiwan; GNS, New Zealand; University of Rome Tor Vergata, Italy; RMIT University, Australia; Tata Institute of Fundamental Research, India; The Asian Consortium on Computational Materials Science (ACCMS); Indian Physics Association (IPA); Material Research Society of India (MRSI), Indian Carbon Society, Council of Scientific & Industrial Research (CSIR), Indian Science Congress Association (ISCA), Department of Science & Technology (DST) and Springer Nature.

ICONN-2021

Head
Department of Physics and Nanotechnology
SRM IST

Chairperson
School of Applied Sciences
SRM IST


SRM

SRM INSTITUTE OF SCIENCE AND TECHNOLOGY
Directorate of Research
Kattankulathur, Tamil Nadu - 603 203, India

International Conference on Recent Advances in Applied Sciences, Technology & Health - 2021

Presentation Certificate

This is to certify that Tasrin shahnaz of Indian Institute of Technology, Guwahati has made oral / poster entitled Static adsorptive removal of Methylene blue and Basic fuschin on nanocellulose extracted from Cyperus rotundus under the theme "Environmental Science & Technology" in the International Conference on "Recent Advances in Applied Sciences, Technology & Health (RASTH 2021)" held between 3 – 5 "March 2021 (Virtual) at SRM IST, Kattankulathur.

Dr. Paromita Chakraborty
SRM IST, Kattankulathur

Prof. B. Neppolian
Dean (Research)
SRM IST, Kattankulathur

Prof. K. Ramasamy
Director (Research)
SRM IST, Kattankulathur


Certificate of Participation

This certificate is awarded to Tasrin Shahnaz of Indian Institute of Technology Guwahati for attending LaTeX WORKSHOP conducted on 25th and 26th August, 2018

Organized by
Research Scholar Forum, CEE
at
Department of Electronics and Electrical Engineering
Indian Institute of Technology Guwahati

Dr. Arun Tej Mallajosyula
(Faculty Advisor, RSF-EEE)

Atanu Purkayastha
(Chief Executive, RSF-EEE)


Research Conclave'18
An amalgamation of Academia, Industry & Startups
March 8-11, 2018

Certificate of Participation

This is to certify that Tasrin Shahnaz of IIT Guwahati has participated in Advanced Excel/Advanced Origin/~~Image~~/Patent writing and Copyright workshop at Research Conclave'18, organized by Students' Academic Board, Indian Institute of Technology Guwahati, India.

Chairman
Students' Academic Board

Faculty Convener
Research Conclave'18

Faculty Co-Convener
Research Conclave'18

Student Convener
IIT Guwahati

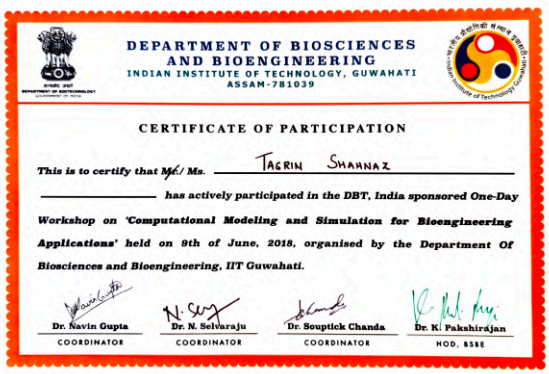
DEPARTMENT OF BIOSCIENCES AND BIOENGINEERING
INDIAN INSTITUTE OF TECHNOLOGY, GUWAHATI
ASSAM-781039

CERTIFICATE OF PARTICIPATION

This is to certify that Mr./ Ms. TASRIN SHAHNAZ has actively participated in the DBT, India sponsored One-Day Workshop on 'Computational Modeling and Simulation for Bioengineering Applications' held on 9th of June, 2018, organised by the Department Of Biosciences and Bioengineering, IIT Guwahati.

Dr. Navin Gupta
COORDINATOR

Dr. N. Selvaraju
COORDINATOR

Dr. Souptick Chanda
COORDINATOR

Dr. K. Pakshirajan
HOD, BSBE

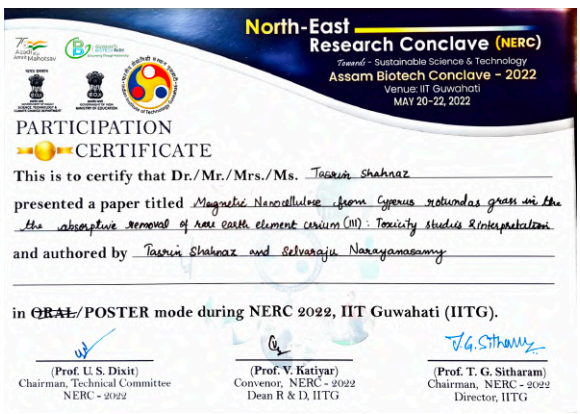
North-East Research Conclave (NERC)
Towards - Sustainable Science & Technology
Assam Biotech Conclave - 2022
Venue: IIT Guwahati
MAY 20-22, 2022

PARTICIPATION CERTIFICATE

This is to certify that Dr./Mr./Mrs./Ms. Tasrin Shahnaz presented a paper titled Magnetic Nanocellulose from Cyperus rotundas grass in the the absorptive removal of rare earth element cerium (III): Toxicity studies & Interpretation and authored by Tasrin Shahnaz and Selvaraju Narayanasamy

in ~~ORAL~~/POSTER mode during NERC 2022, IIT Guwahati (IITG).

(Prof. U. S. Dixit)
Chairman, Technical Committee
NERC - 2022

(Prof. V. Katiyar)
Convenor, NERC - 2022
Dean R & D, IITG

(Prof. T. G. Sitharam)
Chairman, NERC - 2022
Director, IITG

TH-3150_176106114

IHE DELFT

Nuffic

CERTIFICATE

Tailor Made Training on:
Empowerment and Autonomy of Women through a Biobased Circular Economy Design - Resource Recovery from Waste

This is to certify that

Tasrin Shahnaz

born on 4 July 1992 in Jorhat, India

has participated in the tailor made training on: Empowerment and Autonomy of Women through a Biobased Circular Economy Design - Resource Recovery from Waste. The course was held at IIT Guwahati, India from 22 July 2019 to 26 July 2019.

E.L. Ploeger, MSc
Academic Registrar

E.R. Raj, PhD
Course Coordinator

Delft, the Netherlands, 26 July 2019

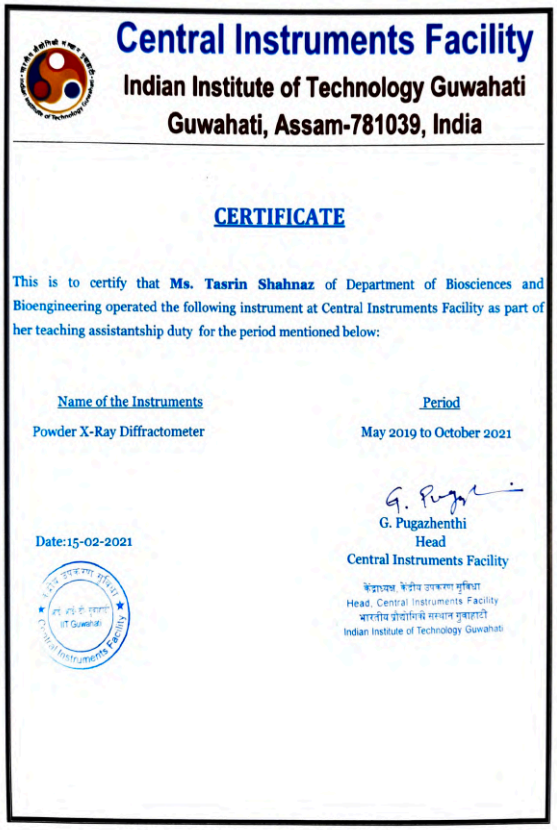

Central Instruments Facility

Indian Institute of Technology Guwahati
Guwahati, Assam-781039, India

CERTIFICATE

This is to certify that **Ms. Tasrin Shahnaz** of Department of Biosciences and Bioengineering operated the following instrument at Central Instruments Facility as part of her teaching assistantship duty for the period mentioned below:

Name of the Instruments	Period
Powder X-Ray Diffractometer	May 2019 to October 2021

Date:15-02-2021

G. Pugazhenthi
Head
Central Instruments Facility

केंद्रप्रमुख केंद्रीय उपकरण सुविधा
Head, Central Instruments Facility
भारतीय प्रौद्योगिकी संस्थान गुवाहाटी
Indian Institute of Technology Guwahati

TH-3150_176106114

VITAE

The author was born on July 4, 1992, in Jorhat, Assam, India. She completed the High School examination conducted by the Board of Secondary Education, Assam in 2008. She completed the Senior Secondary School examination conducted by Assam Higher Secondary Education Council, Assam in 2010. She had done her B. Tech. in Biotechnology from the Department of Bioengineering and Technology, Gauhati University Institute of Science and Technology, Guwahati, Assam in 2015 as a top rank holder with a 9.53/10 Cumulative Grade Point Average (CGPA). She completed her M. Tech. in Biotechnology from the Department of Bioengineering and Technology, Gauhati University Institute of Science and Technology, Guwahati, Assam in 2017 as a top rank holder with a 10/10 Cumulative Grade Point Average (CGPA).

Miss. Tasrin Shahnaz joined the PhD program in January 2018 at the Department of Biosciences and Bioengineering, Indian Institute of Technology Guwahati, Guwahati, Assam, India. She completed her coursework with a 9.13/10 Cumulative Point Index (CPI). She gave the PhD Synopsis seminar on 22nd November 2021. She submitted the thesis on 21st February 2022.

TH-3150_176106114